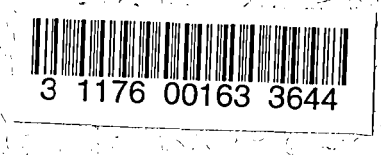

JPL PUBLICATION 42-57

The Telecommunications and Data Acquisition Progress Report

March and April 1980

June 15, 1980

National Aeronautics and
Space Administration

Jet Propulsion Laboratory
California Institute of Technology
Pasadena, California

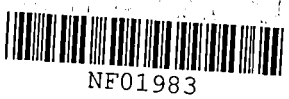

JPL PUBLICATION 42-57

The Telecommunications and Data Acquisition Progress Report

March and April 1980

June 15, 1980

National Aeronautics and
Space Administration

Jet Propulsion Laboratory
California Institute of Technology
Pasadena, California

The research described in this publication was carried out by the Jet Propulsion Laboratory, California Institute of Technology, under NASA Contract No. NAS7-100.

Preface

This publication was formerly entitled *The Deep Space Network Progress Report*. Although the practice of reporting progress in the development and operations of the Deep Space Network continues, the report is expanded with this issue to include developments in Earth-based radio technology as applied to other research programs. These programs are:

(1) Geodynamics: For several years, the laboratory has been developing radio interferometry at microwave frequencies for application to geodetic measurements. This branch of telecommunications technology is now being applied to the study of geodynamics.

(2) Astrophysics: The deep space stations, individually and in pairs as an interferometer, have been used by radio astronomers for astrophysics research by direct observations of radio sources.

(3) An activity closely related to radio astronomy's use of the deep space stations is NASA's continuing program of radio search for extraterrestrial intelligence in the microwave region of the electromagnetic spectrum.

Each succeeding issue of this report will present material in some, but not all, of the following categories:

Radio Astronomy
Search for Extraterrestrial Intelligence
Radio Interferometry at Microwave Frequencies

- Geodetic Techniques Development
- Spacecraft Navigation
- Orbiting Very Long Baseline Interferometry

Deep Space Network

- Description
- Program Planning
- Planetary and Interplanetary Mission Support
- Advanced Systems
- Network and Facility Engineering and Implementation
- Operations
- Spacecraft Radio Science
- Planetary Radar
- Energy

In each issue, there will be a report on the current configuration of one of the seven DSN systems (Tracking, Telemetry, Command, Monitor and Control, Test Support, Radio Science, and Very Long Baseline Interferometry).

The work described in this report series is either performed or managed by the Telecommunications and Data Acquisition organization of JPL.

Contents

SEARCH FOR EXTRATERRESTRIAL INTELLIGENCE

RADIO INTERFEROMETRY AT MICROWAVE FREQUENCIES

GEODETIC TECHNIQUES DEVELOPMENT

ORION

THE DEEP SPACE NETWORK

DESCRIPTION OF THE DSN

PLANETARY AND INTERPLANETARY MISSION SUPPORT

Planetary Flight Projects

Interplanetary Flight Projects

ADVANCED SYSTEMS

Communications

Station Control and System Technology

Network Data Processing and Productivity

NETWORK AND FACILITY ENGINEERING AND IMPLEMENTATION

Network

Deep Space Stations

Quality Assurance

OPERATIONS

Deep Space Stations

SPACECRAFT RADIO SCIENCE

PLANETARY RADAR

ENERGY

The Search for Extraterrestrial Intelligence: Telecommunications Technology

R. E. Edelson
Telecommunications Systems Section

G. S. Levy
TDA Technology Development

Efforts to discover evidence of intelligent extraterrestrial life have become not only feasible, but respectable. Fledgling observational projects have begun that will use state-of-the-art hardware to develop sophisticated receiving and data processing systems. The rationale behind the Search for Extraterrestrial Intelligence (SETI), the manner in which the program is taking shape, and the implications for telecommunications are described. We conclude that the breadth of technological development required for the detection of signals from our galactic brethren has particular relevance for the future of telecommunications in earth-oriented uses.

I. Introduction

> *To consider the earth as the only populated world in infinite space is as absurd as to assert that in an entire field sown with millet only one grain will grow.*
>
> —Greek philosopher Metrodoros of Chios, 4th Century B.C.

As described by Brunk (Ref. 1), the past 40 years have witnessed a revolution in thought as to the prevalence of planetary systems. The belief that planetary systems are common phenomena has led to a corollary assigning high probability to the presence of currently existing intelligent life.

Many specialists in the disciplines of biological and cultural evolution believe that intelligent life, molded by the pressures of natural selection, shares a common bond of civilization, curiosity, and the urge for exploration and communication (Ref. 2). The possibility of our communicating with another intelligent species depends on the presence of a large number of intelligent races concurrently possessing the means and will to attempt communication. Taking into account the vast volume of the galaxy, and assuming only that intelligent life is spread uniformly over that volume, scientific opinion suggests that for a reasonable chance for success in detection, the average lifetime of a communicating civilization must exceed 100,000 years (Ref. 3). If intelligent life normally expends its physical and spiritual resources in a few hundred years, as we appear to be in danger of doing, then detection becomes

impossible. If, on the other hand, intelligence really is a survival factor, and sentient life prevails, the galaxy may be seething with communicative species.

Since 1959, when Cocconi and Morrison (Ref. 4) recognized that communication with beings thousands of light years from us had become possible through the tools of the radio astronomer, the major obstacle to attempting the discovery of signals has been the enormous dynamic range of the parameter space in which such signals might be found. Today, however, a good start can be made in examining the total physically reasonable range of the variables involved, using the fast moving technologies of the telecommunications industry.

II. Electromagnetic Communications

Communication can be accomplished through the use of any physical phenomenon that propagates in some manner and can be made to exhibit a detectable change of state when desired. By far the most likely communication medium is that of electromagnetic waves. Such transmissions have the advantage of energy efficiency, propagation at the speed of light, ease of detection, and relative immunity to the interstellar magnetic fields. Generally, the major investigations on SETI (Refs. 2, 5 and 6) agree that reception of electromagnetic waves is the most promising approach to the detection of extraterrestrial intelligence.

III. Search Strategies

A. Description of the Parameter Space

The description of a strategy for searching for artificially generated electromagnetic waves involves the specification of the volume examined in the four dimensional signal space of: source location; source modulation, or the manner in which the signal conveys information; transmitted frequency; and the received power flux density. Plausible ranges for these variables can be determined by physical reasoning alone. Further reduction requires assumptions as to the approach and prowess of the transmitting civilization, an audacious step when considering a society 100,000 or more years our senior. Thus, it is highly desirable to investigate the total reasonable parameter space to levels commensurate with the time, facilities, and resources which can be brought to bear, weighting the effort with extrapolation from our own experience, while not neglecting "unlikely" but physically realizable regimes.

Billingham (Ref. 7) discusses the reasoning behind the range of values that must be examined for a truly comprehensive search. Here, we simply note the rationale behind each of the generally reasonable ranges.

1. Source location. Although particular types of stars (generally nearby stars of spectral classes F, G, and K) have a high *a priori* weight in a search effort, reasonable scenarios asserting adaptability or capability beyond our own suggest a much wider range of target possibilities, including white dwarf systems, the extended regions of interstellar masers and many more. (Simply adding M stars to the target list, for example, multiplies the target opportunities by a factor of 5 to 10.) When these scenarios are included, the number of possible targets expands to where a comprehensive search must examine the entire sky in addition to looking at *a priori* targets.

2. Source modulation. Generally two types of signals may be anticipated from beings attempting to initiate communications with other life: very narrowband continuous signals, or very powerful pulsed transmissions, frequently repeated. The former is a signal compact in frequency, the latter a signal compact in time. Both are logical artifacts of intelligence.

3. Transmitted frequency. A search over the entire electromagnetic spectrum for a weak signal whose bandwidth may be less than a hertz is not a feasible undertaking. Fortunately, as Oliver has shown (Ref. 8), a particular spectral region, the band between approximately 1 and 100 GHz, is uniquely attractive for interstellar transmissions. This region, the microwave "window" (Fig. 1), exhibits the minimum interference from interstellar noise sources. The figure demonstrates that the lower range of the microwave window is of primary interest for Earth-based systems, while the higher end, at which the atmosphere is opaque, or at least murky, is of interest for space-borne systems.

Rationales have been offered to further narrow the plausible spectral region, applying various criteria for determining the behavior of the transmitting society. Regardless of how attractive the reasoning may be, it requires extrapolations based on our own experience and biases. However, these rationales are valuable for selecting *a priori* search preferences for specific bands, notably the "water hole," the band between approximately 1.4 to 1.7 GHz (Ref. 5). Generally, the entire window must be examined, but frequency bands of radio astronomical interest might be emphasized as they provide signposts for all species, and are frequencies at which an initiating society might expect radio astronomers to be listening.

4. Received power flux density. The received power flux density, ϕ, from a source of effective isotropically radiated power, P_r, at range R is proportional to the ratio, P_r/R^2. Thus,

assumptions as to plausible received power flux density are critically dependent on the power of the interstellar transmitter, the range from which it operates, and the directivity of the transmission. Figure 2 shows the joint transmitter-receiver requirements that would permit a signal detection. There is a multidecibel region that might hold the signals we seek.

B. Choosing Search Strategies

Surprisingly, the work of the last two decades has done relatively little to establish the boundaries of the parameter space outside of which there exists no signal. The available technology, particularly in multichannel spectral analysis, has been insufficient to encompass a wideband, sensitive search. In addition, the majority of sky examinations have been conducted for radio astronomical purposes, thus excluding detected narrowband signals from data analysis. The vast majority of such signals are manmade radio frequency interference, but this exclusion also prevents the detection of signals from other beings.

A full-blown examination of the total range of reasonable parameter values is impractical. Thus, the search strategy must seek to simply bound the volume of the four dimensional space, within the constraints of available time and resources, and emphasize regions that have particular *a priori* promise.

One approach to this problem is to implement a two-fold strategy. The first part is to use existing antennas of moderate size to conduct a full-sky survey over a very wide frequency band, varying the achieved flux levels according to the attractiveness of the frequency for SETI and scientific purposes. The second is to limit both frequency and sky coverage to particular interesting frequency bands and targets and extend the boundaries in power flux density by the use of the largest available antennas and long integration times.

These approaches narrow the unknown parameter space in several dimensions while accomplishing realistic programs with realistic resources. Only when the capabilities of existing facilities are exhausted would dedicated SETI antennas be required to further limit the uninvestigated space until a signal is detected, or until we are convinced that we occupy a nearly unique place in the galaxy. It has been estimated that existing facilities, combined with state-of-the-art instrumentation, can achieve 10^7 more coverage of the parameter space than has been achieved in all combined searches to date (Ref. 9).

C. Implications for System Design

Just as a single system cannot be used for both light and electron microscopy, so a SETI requires different system approaches to the investigation of the available signal regimes. Figure 3 displays the essence of a phased program being developed now by the Ames Research Center and JPL that follows a system building block approach to gradually converge on the place where a signal awaits detection. The approach recognizes that the accomplishment of wideband searches with narrowband resolution depends on our ability to replicate millions or billions of spectral bins inexpensively, and to support this data generation by the reduction of immense quantities of input to a quantity suitable for human examination.

Figure 3 shows the flow of the plan from the definition of the search environment, to the generation of the system requirements it engenders, to a detailed technological progression which permits observation with increasing thoroughness as the state-of-the-art advances. In the next section we enumerate the major technological advances required in order to achieve this program approach.

IV. Telecommunications Technology

Current and future telecommunications technology will achieve systems with the high sensitivity and broad bandwidth required for a search for extraterrestrial intelligence. The major developments required for the SETI activity can be conveniently grouped into four categories: receiver systems; data management; supporting technology; and future directions.

A. Receiver Systems and Data Management

There is a substantial difference in the implementation of the hardware and software requirements for the SETI. The receiver system, including the antenna, amplifiers, and spectrum analyzers, is a straightforward application of the state-of-the-art to achieve high sensitivities and very wide bandwidth simultaneously. The system requirements are known, and the design of prototypes is already underway.

The data management approach has substantially different emphasis. The computational devices to construct operational search systems are off-the-shelf items. The algorithms implemented by these devices will be refined and reconstructed to fit this unexplored environment, once observational experience is gained.

1. Receiver systems. Within the context of a very broad spectral search, the major sensitivity improvement for SETI will be achieved through unprecedented spectrum analysis capabilities. The most straightforward approach to the detection of a signal of unknown frequency and phase requires initial processing by a spectrum analyzer. The choice of minimum useful channel bandwidth is based on several phenomena. Useful bandwidths are constrained by the inter-

stellar medium, which probably degrades any signal to a bandwidth of at least 10^{-3} Hz. Uncertainties in relative velocities between stars will provide more severe constraints on the minimum useful bandwidth. The Doppler shift must remain within the bandpass of the individual bins for some time greater than the reciprocal power bandwidth of the bin. Finally, the expectation that some modulation will be present, resulting in a wider minimum bandwidth signal, also affects the choice of minimum bandwidth. Thus, minimum bin widths may be between 10^{-1} to 10 Hz. However, to be compatible with reasonable search times, the total system instantaneous bandwidth should be about 300 MHz. These considerations may ultimately give rise to requirements for about 10^9 bins of spectrum analyzer capacity.

As a first step commensurate with the state-of-the-art, the SETI program is currently funding the development of a 10^5 bin, fast fourier transform spectrum analyzer which is the prototype of one module of a much larger instrument. The assembly and completion is expected within one year. Although the prototype will have a bandwidth of only 64 kHz, the design will be compatible with easy expansion to a 300 MHz bandwidth device with 10^7 channels. This experimental unit uses only a few types of available chips, and the expected cost is about 50¢ per channel.

To accomplish a system design which does not squander the sensitivity potential of the broadband spectrum analyzer, wideband, low-noise amplifiers are required that can be tuned over the entire search bandwidth. The Jet Propulsion Laboratory, working on contract to the National Radio Astronomy Observatory, has built a 19 to 25 GHz tunable maser amplifier with an instantaneous bandwidth of 300 MHz. When used as a postamplifier for a series of parametric up-converters, this device exhibits a noise temperature of 4 to 8 K. A 300 MHz instantaneous bandwidth with perhaps a 2 K amplifier noise temperature can be achieved in a device which covers the entire band from 1 to 25 GHz using approximately nine up-converters and a single maser.

To maintain the amplifier in its operating regime requires a physical temperature of 4 K or less. Currently used closed-cycle cryostats exhibit mean time between failures (MTBFs) on the order of one year. Thus, a basis exists for the design of cryogenic amplifiers that must perform extended, automated search efforts.

2. **Data management.** Any SETI observational program must develop methods to pick the plums from the glut of irrelevant signal. A search system, using a 10^9 channel spectrum analyzer, would produce data enough to fill half-a-million 400-page books for every day of operation were we not to discard uninteresting data. Real-time pattern recognition algorithms must be devised which can discard noise, both natural and manmade, and identify promising data. The preservation of data of scientific and SETI interest will require archival systems similar to those foreseen for Earth applications.

Radio frequency interference (RFI) will be an important limitation on the search. Because of the sensitivity required of a SETI receiver, virtually any radiation picked up in the receiver bandwidth will make the conduct of this search more difficult. Earth-based transmissions reflected into the sidelobes of the antenna by artificial satellites or the moon will cause significant problems. Earth satellites above the horizon will almost preclude operation in their bands. Some bands will probably be unusable, and techniques must be developed so that a search can be conducted in spite of the RFI environment.

Fortunately, the characteristics of RFI are substantially different than those of the desired signal, particularly in Doppler signature. Existing technology in data processing can be successfully applied to remove the RFI-corrupted data from consideration.

B. Supporting Technology

Even the modest program underway will involve observations over several years for a possibly elusive signal. In order to minimize life-cycle cost and ensure reliable detection, this program will require the use of antenna facilities that operate unattended. The implementation for automation will be extensive, and future requirements will be even more stringent.

Partially automated facilities exist today. Wherever possible these facilities will be employed, and the specific requirements for automated pattern recognition will be developed as part of the overall antenna application.

C. Future Directions

A modest search for extraterrestrial intelligence can begin almost immediately with current technology, but research and development offer great promise for future efforts through improvements in data processing and antenna and microwave designs.

Since there exists a minimum useful bandwidth for the spectral bins examined in a search, the primary use of mega- or giga-channel spectrum analyzers is to permit a rapid search over the reasonable spectral region, while retaining the highest possible sensitivity. At some point (see Fig. 2), the capabilities of existing antennas will be exhausted, and facilities with improved quality and quantity of aperture will be required. Because this approach involves great capital expense, it is vital

to make effective use of the aperture achieved. Antenna efficiency can be improved, with 95% a realistic goal. These same efficient antennas can contribute to a reduction in system noise temperature and diminished sidelobes would also alleviate RFI pickup. One challenging approach requires the further development of antenna array technology for very wideband operation.

Orbiting antennas offer particular advantages for high frequency operation (see Fig. 1), and may be competitive with ground facilities for very large aperture operation at the lower frequencies (Ref. 2).

V. Consonance With Technology Trends

Because of the stringent requirements for system sensitivity, bandwidth, automation, and operation in an environment of potentially harmful RFI, the SETI program requirements anticipate many of the trends in telecommunication technology.

The technology involved in the development of spectrum analyzers with 10^9 or more bins has immediate application in processing: (1) radiometer data such as that gathered by Earth applications satellites; (2) RFI in particular bands for interference measurements and trend evaluation; and (3) seismological data for scientific and practical applications.

Data processing will be accomplished with devices capable of recognizing characteristic patterns while handling enormous input. This would also have applications to radiometry, RFI, and seismology. The techniques for reducing the quantities of raw data to manageable proportions and for archival recording will have broad industrial application.

Finally, the fulfillment of the telecommunications and Earth applications requirements for large spaceborne antennas and closed-cycle cryogenic systems will produce direct benefits for the Search for Extraterrestrial Intelligence.

VI. Conclusions

A most imaginative and inspiring project, the Search for Extraterrestrial Intelligence can now be tackled with a broad-based, serious observational program. In its initial stages, this program will be supported by the application of what is now the state-of-the-art in telecommunications and electronics technology. Future developments may make SETI a pioneer in the application of a broad array of technology which can expand our horizons to the stars while solving some very down-to-earth problems. In exploring the cosmos we can given some hard tugs to our own bootstraps.

References

1. W. E. Brunk, "The Planets, the Universe, and Cosmic Evolution," presented at the 1976 National Telecommunications Converence, Dallas, Texas, November 29-December 1, 1976.

2. P. Morrison, J. Billingham, and J. Wolfe, eds., *The Search for Extraterrestrial Intelligence*, NASA SP-419, National Aeronautics and Space Administration, 1977.

3. B. M. Oliver, "Proximity of Galactic Civilizations," *Icarus, 25,* pp. 360-367, 1975.

4. G. Cocconi and P. Morrison, "Searching For Interstellar Communications," *Nature, 184,* pp. 844-846, September 19, 1959.

5. B. M. Oliver and J. Billingham, *Project Cyclops: A Design Study of a System for Detecting Extraterrestrial Intelligent Life,* NASA CR114445, July, 1973.

6. Scientific Council on the Radio-Astronomy Problem Area, Academy of Sciences of the USSR, "The CETI Program," *Soviet Astronomy, 18,* 5, pp. 669-675, March-April 1975.

7. R. E. Edelson, "An Observational Program to Search for Radio Signals from Extraterrestrial Intelligence Through the Use of Existing Facilities," presented at the XXVIIth International Astronautical Congress, Anaheim, California, October 10-16, 1976.

8. B. M. Oliver, Hewlett-Packard Co., "Linear Amplification vs. Photon Detection in the Search for Interstellar Signals," unpublished memorandum, September 12, 1975.

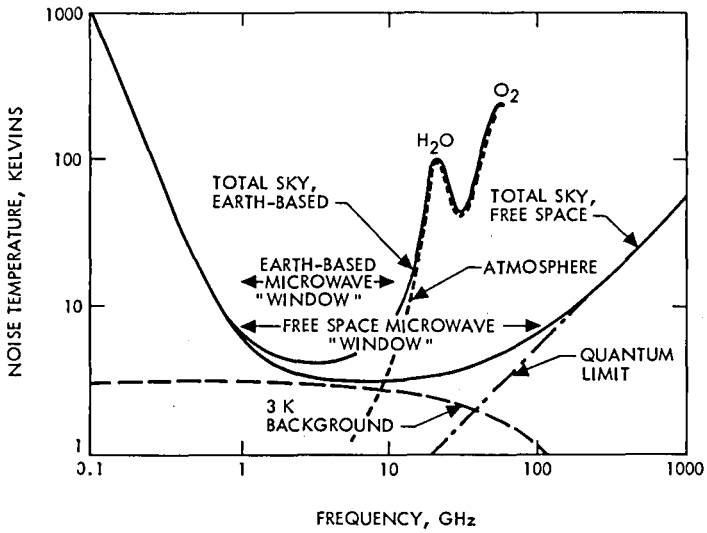

Fig. 1. The Microwave "Window"

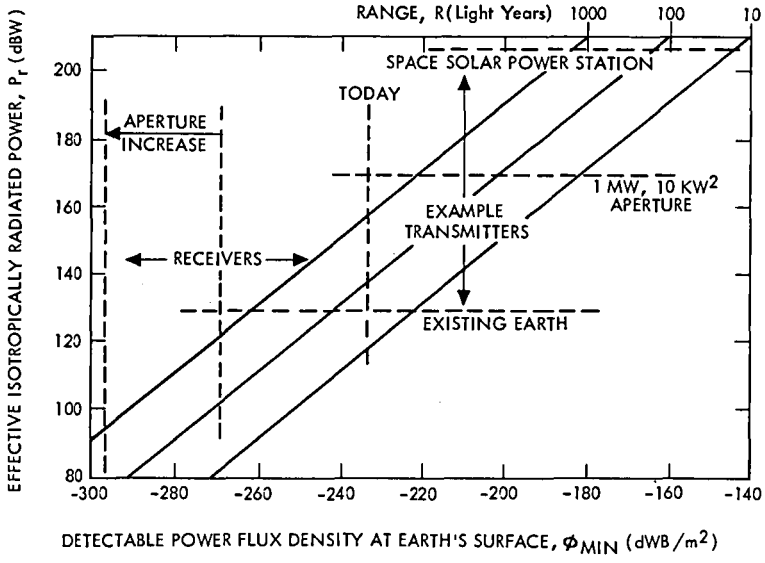

Fig. 2. Joint Transmitter-Receiver Requirements for SETI Detection

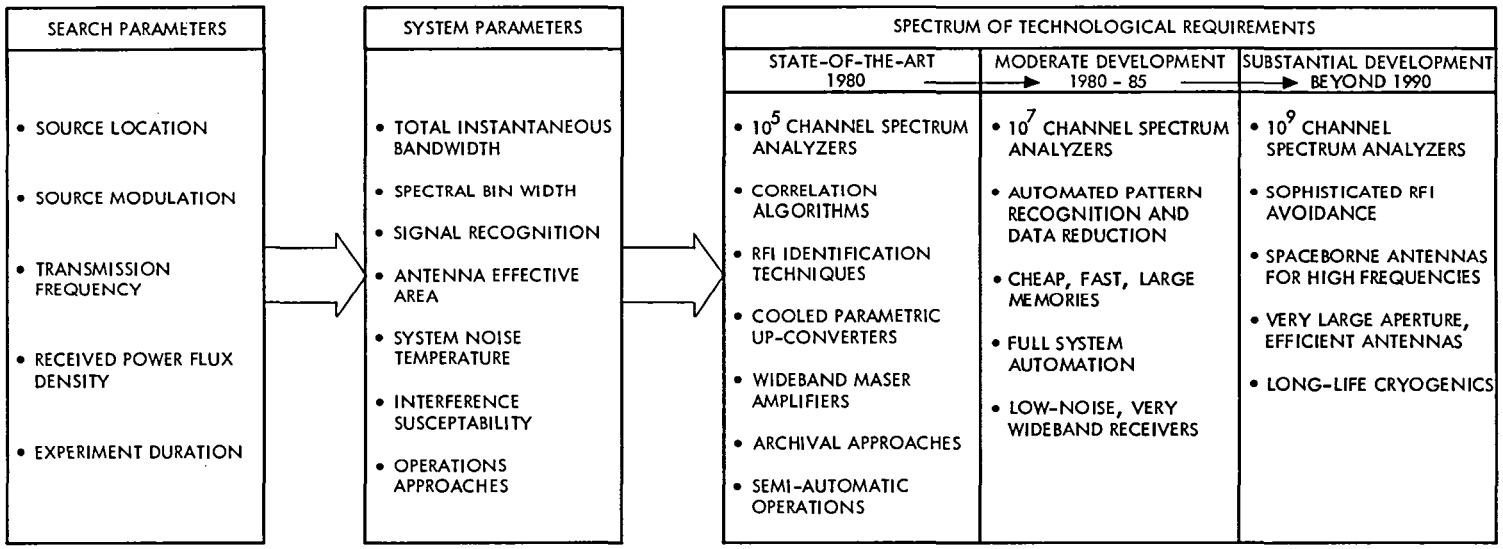

Fig. 3. Implications for Systems Design

The SETI Observational Plan

A. L. Berman
TDA Mission Support

The SETI ("Search for Extraterrestrial Intelligence") Program is a NASA Research and Development Program with primary thrust to search the microwave region of the spectrum for signals of extraterrestrial intelligent origin. The Program will search a well defined volume of "search parameter space" using existing antennae and a new, sophisticated data acquisition and analysis system. The Program includes two major components – the "target survey", which will observe at very high sensitivity all attractive stellar candidates within 75 light years of the sun, and the "sky survey", which will observe the entire celestial sphere at a lower sensitivity.

I. Introduction

Serious scientific concern with detection of extraterrestrial intelligence dates back at least to 1959, with the publication by Cocconi and Morrison (Ref. 1) of a paper entitled "Search for Interstellar Communications." Additional scientific papers on this subject were published during the 1960's. In the 1970's, more intensive and formal studies of the subject were conducted. Notable during this time frame were study efforts which are documented in "Project Cyclops: A Design Study of a System for Detection of Extraterrestrial Life" (Ref. 2) and "The Search for Extraterrestrial Intelligence SETI" (Ref. 3). During the late 1970's, intensive effort was undertaken at the Jet Propulsion Laboratory (JPL) and Ames Research Center (ARC) to obtain the initiation of a formal SETI ("Search for Extraterrestrial Intelligence") Program under NASA sponsorship. Starting in Fiscal (FY) 1980, such a program has come into existence. The NASA SETI Program is a Research and Development effort with primary thrust to search the microwave region of the spectrum for signals of extraterrestrial intelligent origin. The Program is being managed by the Division of Astrophysics in the NASA Headquarters Office of Space Sciences (OSS).

The SETI Program will search a well defined volume of "search parameter space" using existing antennae and a new, sophisticated data acquisition and analysis system. The Program includes two major components – the "target survey," which will observe at very high sensitivity all attractive stellar candidates within 75 light years of the sun, and the "sky survey," which will observe the entire celestial sphere at lower sensitivity. The target survey will require the implementation of a narrowband data acquisition system, which will be used at Arecibo and the DSN 64-m subnet. The sky survey will require implementation of a wideband data acquisition system, which will be used in the DSN 34-m subnet.

II. SETI Search Strategy

In describing the SETI search strategy, one defines a "search parameter space" composed of a relevant set of signal

descriptors. Comprising the search space are both primary signal descriptors:

(1) Signal strength

(2) Direction

(3) Frequency

and secondary signal descriptors:

(1) Bandwidth

(2) Polarization

(3) Modulation

(4) Duration

In constructing a SETI search strategy, the primary descriptors provide the basic structure, while the secondary descriptors influence the detailed strategy design.

At this point, the central SETI problem is seen to be in evidence. Obviously, it is not physically possible to search the entire multidimensional SETI search parameter space; hence one must devise a logical methodology in bounding the search parameter space to that parameter subset which is both desirable and practical. In devising bounds, there are three basic categories:

(1) Bounds dictated by physical factors

(2) Bounds dictated by resource limitations

(3) Bounds dictated by a priori assumptions

The very selection of the microwave region for the SETI Program is an example of bounds dictated by physical factors. Figure 1 (from Ref. 3) shows total noise versus frequency. There is immediately apparent in Fig. 1 a "terrestrial microwave window" from about 1 to 10 GHz. Below 1 GHz, galactic noise increases rapidly, while above 10 GHz tropospheric and spontaneous emission noise become quite severe.

As an example of bounds dictated by resource limitations, the program may well choose to first search portions of the frequency spectrum within the microwave window for which we already possess the requisite radio frequency (RF) hardware, i.e., S-band and X-band.

Finally, as an example of bounds dictated by a priori assumptions, one has the "waterhole" and "good suns" concepts. The "waterhole" is defined as the frequency band encompassing the hydrogen line (1.42 GHz) at the lower extent and the hydroxyl lines (1.61 to 1.72 GHz) at the upper extent. Obviously, since these physical constituents are so fundamental to terrestrial life and so well represented throughout the universe, one must consider the possibility of the usage of their spectral line frequencies for communication by extraterrestrial intelligent life; hence, in any SETI search scheme, the waterhole becomes an a priori "preferred" region for observation. Similarly, one may assume that stars like our own sun ("good suns") may be good locations for the presence of intelligent life.

Using such logic, a two-pronged search strategy for the microwave window has gradually evolved; the two elements of this strategy, termed the "target" and "sky" surveys, are described below.

A. The Target Survey

In this *a priori* survey, all attractive stellar candidates within 75 light years of the sun will be subjected to high sensitivity observation. The basic goal here is to achieve a search sensitivity of approximately 10^{-26} W/m^2 in the region of 1.0 to 3.0 GHz.

B. The Sky Survey

The goal of this *non a priori* survey is to systematically search the entire celestial sphere, albeit at a substantially lower sensitivity than the target survey. The sky survey sensitivity goal is approximately 10^{-23} W/m^2 in the region of 1.0 to 10.0 GHz.

A more detailed parametric description of the two search modes is provided in the following sections.

III. The SETI Instrument System

The SETI narrowband and wideband instrument systems will basically consist of:

(1) New Radio Frequency (RF) Equipment

(2) Multi-channel Spectrum Analyzer (MCSA)

(3) Computer-based signal detection unit

The central element of the SETI instrument is the MCSA. The multi-million (8×10^6) channel capability of the MCSA is that which makes the planned SETI search practical, and it is the MCSA which will require the bulk of SETI program new technology development and resources.

High level SETI Instrument functional requirements have been established as follows:

(1) Radio Frequency Range

(a) 1-3 GHz; with "spot bands" between 3 and 10 GHz (target survey)

(b) 1-10 GHz; with "spot bands" between 10 and 25 GHz (sky survey)

(2) Radio Frequency Instantaneous Bandwidth

(a) 8 MHz (target survey)

(b) 256 MHz (sky survey)

(3) Polarization

Right Circular Polarization (RCP) and Left Circular Polarization (LCP) simultaneously

(4) Gain (G) Stability

$\Delta G/G = 10^{-3}$

(5) Frequency (F) Stability

$\Delta F/F = 10^{-13}$ over a 1000 second averaging period

(6) System Noise Temperature (T_s)

$T_s = 20°K$

(7) Required Computerized Control

(a) Antenna drive

(b) Receiver local oscillator

(c) Gain

(d) Polarization

(e) Integration time

(f) Bandwidth

(g) Resolution

(8) Spectrum Analyzer Channels

8×10^6

(9) Minimum Channel Resolution

(a) 1 Hz (target survey)

(b) 32 Hz (sky survey)

Figure 2 presents a functional block diagram of the SETI Instrument System. Starting at the dual polarization antenna feed, signals are separated into RCP and LCP components. These are upconverted prior to low noise amplification by a tunable, cryogenic maser. The maser is expected to operate in the region of 19 to 25 GHz with an instantaneous bandwidth of better than 300 MHz. To achieve the required RF range of 1 to 25 GHz, nine cryogenically cooled parametric upconverters will be required, in the following ranges: 1.1 to 2.0 GHz, 2.0 to 2.8 GHz, 2.8 to 4.0 GHz, 4.0 to 5.6 GHz, 5.6 to 8.0 GHz, 8.0 to 11.0 GHz, 11.0 to 16.0 GHz, and 16.0 to 22.0 GHz. Following low noise amplification, open-loop receivers heterodyne down and filter the signals to instantaneous bandwidths of either 8 or 256 MHz. These signals are digitized by A/D converters, and provided to the MCSA. The MCSA utilizes finite impulse response filters to convert an 8.4 MHz input into 8192 channels of 1024 Hz width each. The transition from 1024 Hz channels to 32 Hz and 1 Hz channels is accomplished through usage of microprocessor-controlled digital fourier transform (DFT) algorithms. The MCSA is modular in construction. One basic channel comprises the narrowband MCSA (8.0 MHz); to achieve the required 256 MHz of the wideband MCSA, 32 8 MHz channels are tied together. Within the MCSA, the data are accumulated for the appropriate time and then passed to the signal detection unit. The signal detection unit is composed of a 32 bit minicomputer and software containing the necessary algorithms for signal detection. The signal detection unit will provide real-time messages and initiate the recording of raw data when possible signals are detected. In addition, data of interest to the Radio Astronomy community will be recorded and archived.

IV. SETI Observational Strategy

As might have been anticipated, the differing requirements and goals of the sky and target surveys lead to substantially different telescope requirements and observational strategies. In the case of the target survey, aperture is by far the overriding concern; for the sky survey, on the other hand, aperture is not nearly so important as the availability of the antenna on nearly a continuous basis for long periods of time (i.e., ~ 12 months).

A. The Target Survey

For the target survey, the minimum detectable flux (in W/m^2) is given by (Ref. 4):

$$\phi = (4\alpha k T_s/\pi\eta D^2)\ \sqrt{b/t}$$

where:

ϕ = flux, W/m^2

α = signal-to-noise ratio

k = Boltzman's constant

T_s = system noise temperature, °K

η = aperture efficiency

D = diameter, m

b = bandwidth, Hz

t = integration time, sec

the integration time required to achieve a given flux level thus scales as:

$$t \propto T_s^2 D^{-4}$$

In considering the target survey, Arecibo, located in Puerto Rico with an antenna diameter of 213 m, is clearly the preferred telescope, and can achieve a sensitivity of 3×10^{-27} W/m^2 for 60 second integration times. For star targets not visible to Arecibo, the next largest class of telescopes are 64-m diameter (DSN and Parkes). Since it would not be practical to increase the integration time to achieve 3×10^{-27} W/m^2 (t = 7400 sec), the integration time at 64-m class telescopes will be kept the same as for Arecibo and a sensitivity penalty of a factor of ~ 10 will be accepted.

B. The Sky Survey

For the sky survey, the antenna will be swept at a constant angular tracking rate (ω, in deg/sec). The minimum detectable flux for this case is (Ref. 4):

$$\phi = (4\alpha k T_s/\pi\eta)\ \sqrt{\omega b \nu / 70 c D^3}$$

where:

ϕ = flux, W/m^2

α = signal-to-noise ratio

k = Boltzman's constant

T_s = system noise temperature, °K

η = aperture efficiency

ω = angular tracking rate, deg/sec

b = bandwidth, Hz

ν = frequency, Hz

c = speed of light, m/sec

D = diameter, m

for a given total survey time (t, where $t \propto D\omega^{-1}$), sensitivity scales directly with system noise temperature and inversely with diameter:

$$\phi \propto T_s D^{-1}$$

Therefore, the sensitivity penalty in going from a 64-m antenna to a 34-m antenna is less than a factor of 2. Given the far greater likelihood of gaining access, on a nearly continuous basis, of a 34-m telescope versus a 64-m telescope, it is nearly axiomatic that the sky survey will accept the sensitivity penalty and be conducted on the smaller telescope.

C. Observatory Coverage Requirements

Taking into account the SETI Program requirements and the observational considerations as described above for the target and sky surveys, functional requirements for observatory coverage have been developed as follows:

(1) Target Survey Requirements

(a) Acceptable aperture (diameter) is ≥64 m

(b) Average telescope time required is 3 hours/day (average) during the period FY 1985.0 to FY 1990.0.

(c) Observatory time shall be approximately equally divided between northern and southern latitudes.

(2) Sky Survey Requirements

(a) Acceptable aperture (diameter) is ≥34 m

(b) Average telescope time required is 16 hours/day (average) during the period FY 1985.0 to FY 1990.0.

(c) A minimum of 1/3 of the total observatory time shall be spent at a northern latitude complex and a minimum of 1/3 of the total observatory time at a southern latitude complex.

(d) The SETI wideband instrument will initially be installed at the Goldstone complex.

(3) General Requirements

(a) The SETI instrument systems will be transferred between antennae at intervals of no less than 12 months. SETI instrument system downtime will not exceed two weeks for intracomplex transfers and six weeks for intercomplex transfers.

(b) Non-SETI telescope operations will be on a non-interference basis with the SETI system configuration.

Acknowledgment

The author would like to thank E. T. Olsen, who reviewed this article and provided many excellent comments and suggestions.

References

1. Cocconi, G., and Morrison, P., "Searching for Interstellar Communications," *Nature*, Vol. 184, pp. 844, 1959.
2. Oliver, B. M., and Billingham, J., *Project Cyclops*, NASA Document CR114445, 1973.
3. Morrison, P., Billingham, J., and Wolfe, J., *The Search for Extraterrestrial Intelligence SETI*, NASA Publication SP-419, 1977.
4. Billingham, J., Edelson, R. E., Wolfe, J. H., and Gulkis, S., "A Program Plan For a Search for Extraterrestrial Intelligence (SETI)," Ames Research Center/Jet Propulsion Laboratory (in preparation).

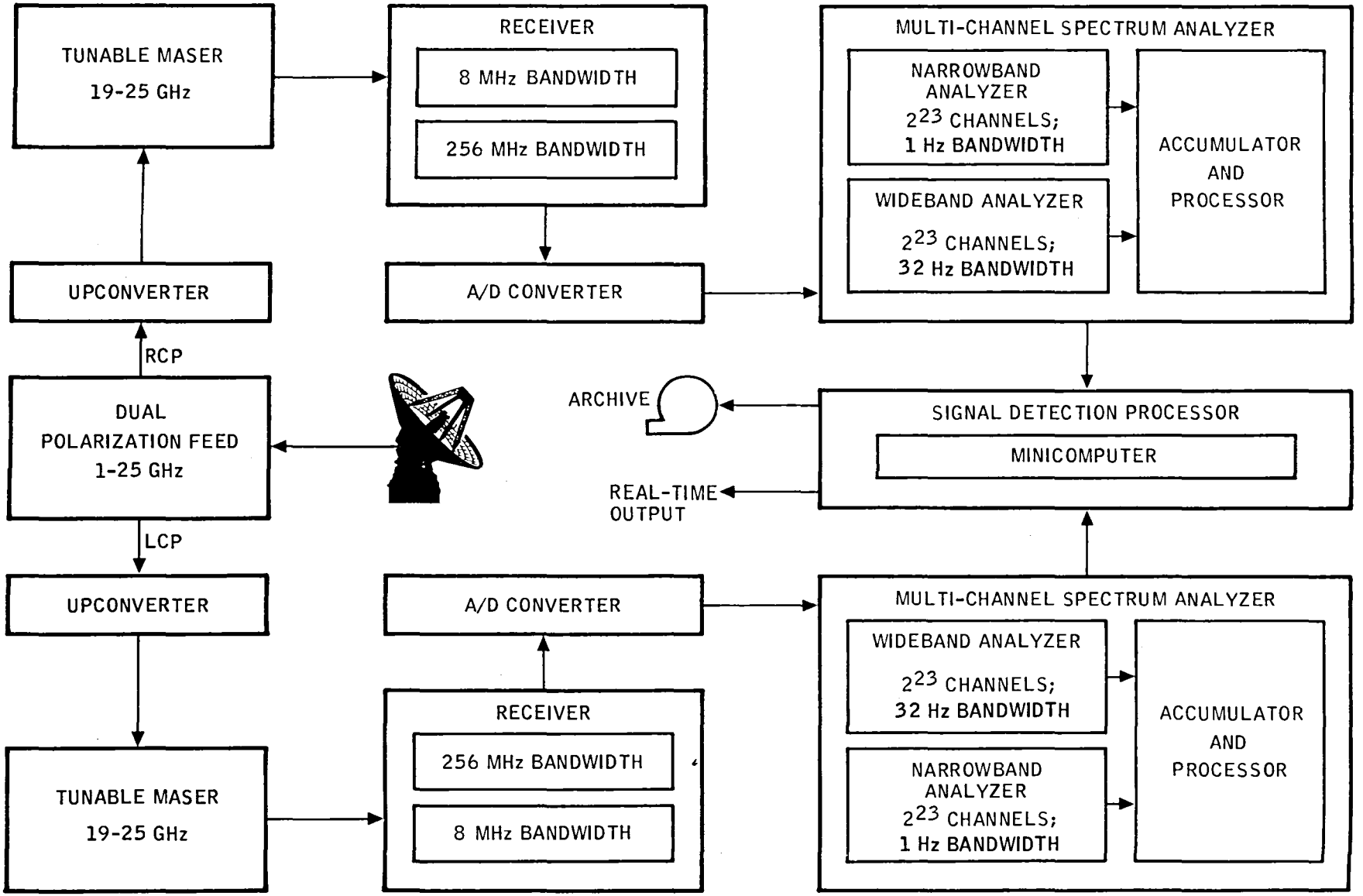

Fig. 1. Terrestrial microwave window

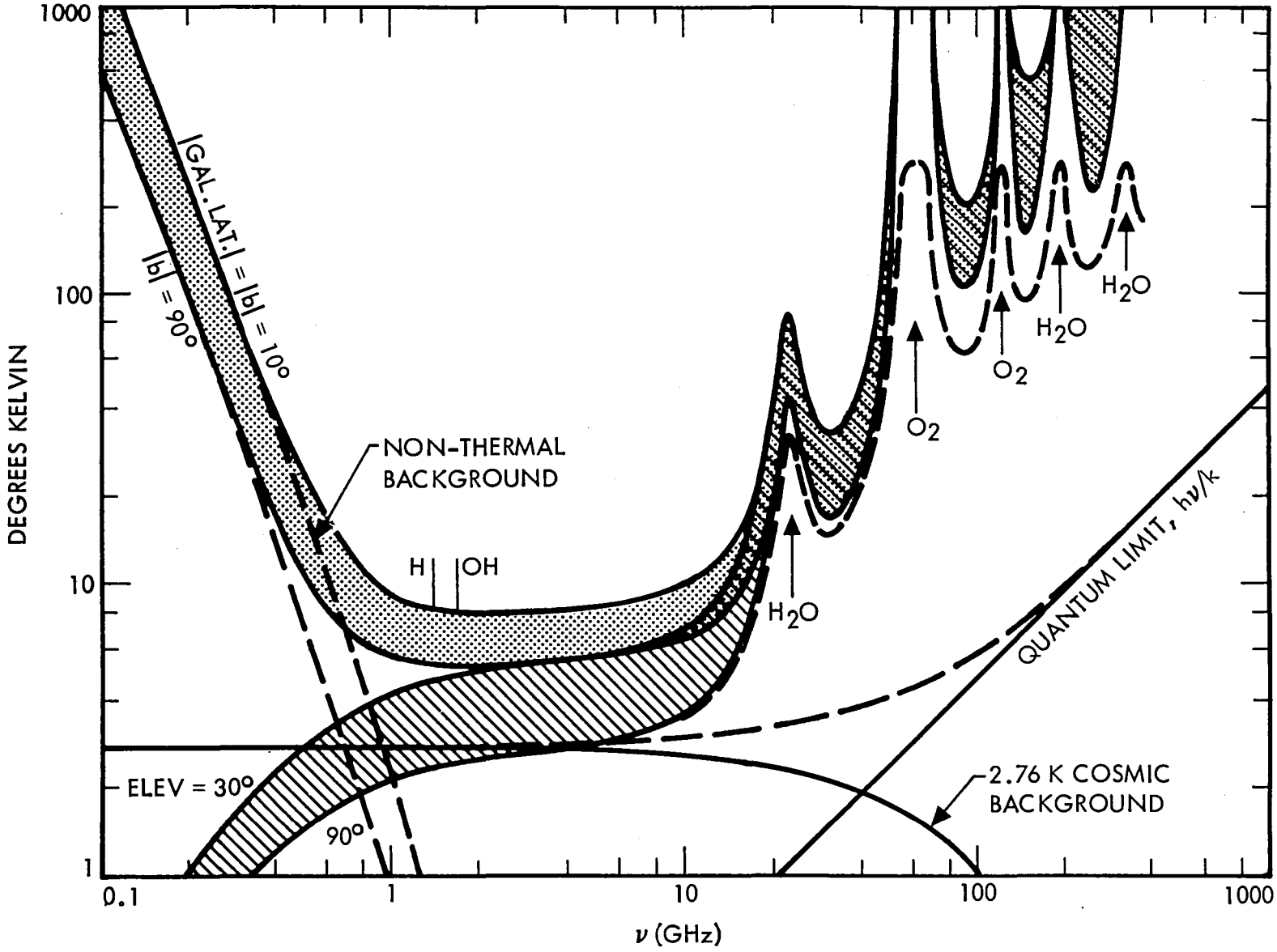

Fig. 2. SETI instrument system functional block diagram

Error Estimation for ORION Baseline Vector Determination

S. C. Wu
Tracking Systems and Applications Section

Effects of error sources on ORION baseline vector determination are studied. Partial derivatives of delay observations with respect to each error source are formulated. Covariance analysis is then performed to estimate the contribution of each error source to baseline vector error. System design parameters such as antenna sizes, system temperatures and provision for dual-frequency (S- and X-band) operation are discussed.

I. Introduction

System design of an Operational Radio Interferometry Observing Network (ORION) is underway. The basic network will consist of a base station having a relatively large antenna and a mobile station having a smaller antenna. Nominal operating frequencies will be at X-band with a span bandwidth of up to 400 MHz. Among the cost-effective parameters to be designed are the antenna sizes, system temperatures and the provision for S- and X-band operation for possible need of charged media calibration. To understand how these parameters will affect the ultimate baseline measurement accuracy, the effects not only of these parameters but of all other possible error sources need to be studied. This article provides a covariance analysis to give an estimate of the effects of each individual error source. The ultimate baseline determination accuracy is estimated by taking the root-sum-square (rss) of the effects from all error sources. Baseline lengths of from 300 km to 5000 km are to be considered. Both 3-D baseline vector accuracy and baseline length accuracy are to be estimated.

II. Delay Observation

The information for the solution of baseline vector is derived from delay observations, over the baseline, of extragalactic radio sources (EGRS). The error-free information content of a single observation can be written as

$$\tau = -B_x \cos\delta \sin HA - B_y \cos\delta \cos HA + B_z \sin\delta \quad (1)$$

where δ = EGRS declination angle, HA = EGRS hour-angle at baseline center, B_x, B_y, B_z = baseline components with B_z parallel to the Earth's spin axis, B_x perpendicular to the meridian plane at baseline center and B_y completing a right-hand Cartesian coordinate system as shown in Fig. 1, and τ is delay over the baseline in km.

To determine the three baseline components at least three observations with non-coplanar lines-of-sight are needed, with orthogonal observations (perpendicular lines-of-sight) being optimum (in the sense of decoupling the three baseline components from one another).

In general, observations are sensitive to such systematic parameters as epoch offset, frequency drift, etc. Such sensitivity can be alleviated by including these parameters as additional estimated parameters (Ref. 1). Furthermore, it is well known that the sensitivity of a solution vector to observation error decreases as the number of independent observations increases. On the other hand, increasing the number of independent observations increases the total observation time and the data volume to be processed. Hence a compromise needs to be made.

When the number of observations is greater than three, the optimum combination is such that the direction vectors of the EGRS being observed have equal spreads in all three orthogonal directions. On the other hand, the availability of EGRS within a viewing window is limited. Specifically, the 14 sources listed

in Table 1 have been found to have correlated flux densities higher than 4 Janskys at X-band over a 300-km baseline. Hence an optimum observation sequence is not always attainable. A near optimum sequence, however, may be approached by proper scheduling. Table 2 is an observation sequence out of the 14 sources over a 24-hour period. Any 6-hour subset of this sequence provides a reasonable coverage of source position vectors in any three orthogonal directions. The sequence is in terms of the mean right ascension (RA) of the baseline center. The nominal observation time is 12 minutes except for the two sources having flux densities higher than 20 Janskys for which 4-minute observation time is allotted. A 1°/sec antenna slew rate has been assumed without considering cable wrapup allowances.

III. Covariance Analysis

The sensitivities of a delay observation to a perturbation of the baseline vector components are the partial derivatives of Eq. (1) with respect to these components:

$$\left\{\frac{d\tau}{dB_{x,y,z}}\right\} = \begin{bmatrix} \frac{\partial\tau}{\partial B_x} \\ \frac{\partial\tau}{\partial B_y} \\ \frac{\partial\tau}{\partial B_z} \end{bmatrix} = \begin{bmatrix} -\cos\delta \sin HA \\ -\cos\delta \cos HA \\ \sin\delta \end{bmatrix} \tag{2}$$

It is felt that perturbations in the length L and in the lateral LT and vertical VT directions of a baseline would provide better physical meaning than those in B_x, B_y and B_z. The partial derivatives of a delay observation with respect to these three physically meaningful components of a baseline can be derived from Eq. (2) with the aid of the following transformation matrix, which is straightforward in view of Fig. 2:

$$\left[\frac{\partial B_{x,y,z}}{\partial B_{L,LT,VT}}\right] = \begin{bmatrix} \frac{\partial B_x}{\partial B_L} & \frac{\partial B_x}{\partial B_{LT}} & \frac{\partial B_x}{\partial B_{VT}} \\ \frac{\partial B_y}{\partial B_L} & \frac{\partial B_y}{\partial B_{LT}} & \frac{\partial B_y}{\partial B_{VT}} \\ \frac{\partial B_z}{\partial B_L} & \frac{\partial B_z}{\partial B_{LT}} & \frac{\partial B_z}{\partial B_{VT}} \end{bmatrix}$$

$$= \begin{bmatrix} \cos\Omega & -\sin\Omega & 0 \\ \sin\Omega\sin\phi & \cos\Omega\sin\phi & -\cos\phi \\ \sin\Omega\cos\phi & \cos\Omega\cos\phi & \sin\phi \end{bmatrix} \tag{3}$$

where ϕ is the latitude of the baseline center and Ω is the lateral orientation angle of the baseline from due east. Hence

$$\left\{\frac{d\tau}{dB_{L,LT,VT}}\right\} = \left[\frac{\partial B_{x,y,z}}{\partial B_{L,LT,VT}}\right]^T \left\{\frac{d\tau}{dB_{x,y,z}}\right\}$$

$$= \begin{bmatrix} -\cos\delta\,(\sin HA\cos\Omega + \cos HA\sin\Omega\sin\phi) \\ \qquad + \sin\delta\sin\Omega\cos\phi \\ \cos\delta\,(\sin HA\sin\Omega - \cos HA\cos\Omega\sin\phi) \\ \qquad + \sin\delta\cos\Omega\cos\phi \\ \cos\delta\cos HA\cos\phi + \sin\delta\sin\phi \end{bmatrix} \tag{4}$$

As mentioned in Section II, effects of clock parameters can be alleviated by estimating these parameters. These include the epoch offset T_o and as many as 12 segments of clock rate offsets, $f_1, f_2, \ldots f_{12}$. The sensitivities of a delay observation to these parameters can easily be formulated: Let f_n applies to observations within the time segment $t_{n-1} < t < t_n$; then the sensitivities of a delay observation to these additional parameters within this time segment are

$$\frac{\partial\tau}{\partial T_o} = c \tag{5}$$

and

$$\frac{\partial\tau}{\partial f_i} = \begin{cases} c(t_i - t_{i-1}) & , \; i < n \\ c(t - t_{n-1}) & , \; i = n \\ 0 & , \; i > n \end{cases} \tag{6}$$

where c is the velocity of light.

For the solutions of N_e estimated parameters from M independent delay observations, an $N_e \times N_e$ information

matrix $J = A^T WA$ can be constructed the inverse of which is the computed covariance matrix

$$P_x = J^{-1} = (A^T WA)^{-1} \tag{7}$$

Here, A is an $M \times N_e$ sensitivity matrix with elements calculated according to Eqs. (4) – (6) for the M observations; W is an $M \times M$ diagonal weighting matrix with $W_{mm} = \sigma^{-2}_{\tau,m}$, the inverse of the error variance of the m^{th} delay observation. The diagonal elements of the computed covariance matrix (7) are the variances of the estimated parameters due to random errors in delay observations. Such errors include the effects of system noise and *random* tropospheric and ionospheric delay errors. Effects of *systematic* errors, such as atmospheric delay model errors, clock instability and source position errors, can be accounted for by including these parameters as "consider" parameters. The covariance matrix due to such systematic errors is given (Ref. 2) by

$$P'_x = P_x A^T W C P_c C^T W A P_x \tag{8}$$

where P_c is the covariance matrix of the N_c consider parameters and C is the sensitivity matrix to these parameters of the M delay observations.

Platform parameter errors (polar motion, UT1) and antenna location error are directly related to baseline vector error independent of observation sequence. Hence no covariance analysis of such errors is necessary.

Note that the effects of each *individual* error source on baseline vector components are of interest. These are calculated one at a time by setting all other error sources to be zero.

IV. Error Sources

This section calculates the variances σ_τ^2 of a delay observation due to random error sources and the sensitivities of the observation to systematic error sources. The variances σ_τ^2 will be used to construct the weighting matrix W in Eq. (7) and the sensitivities will be used in the construction of sensitivity matrix C in Eq. (8). Covariance matrices can then be calculated. The errors in the three baseline components are, respectively, given by the square roots of the first three diagonal elements of the corresponding covariance matrix. The following paragraphs study the effects of each error source.

A. System Noise

Delay observation error due to the system noise in the receiver front ends at the two sites of a baseline can be derived from Ref. 3 as[1]

$$\sigma_\tau = \frac{\sqrt{2}\,c}{2\pi f_{span}} \frac{1}{2.05 \times 10^{-4} S D_1 D_2} \left(\frac{T_{s,1} T_{s,2}}{e_1 e_2 BT} \right)^{1/2} \tag{9}$$

where

c = speed of light

f_{span} = span bandwidth, Hz

D_i = antenna diameter at site i, m

$T_{s,i}$ = system noise temperature at site i, K

B = channel bandwidth, Hz

e_i = antenna efficiency at site i

S = correlated flux density of EGRS, Janskys

T = observation (integration) time, sec

This is a random error and its effects on baseline vector components are calculated from the computed covariance matrix of Eq. (7).

B. Ionosphere

Ionospheric error can be divided into two types, systematic and random. Systematic error is a mismodeling error which can be expressed as

$$\sigma_\tau = [f(X_1) g(\gamma_1) - f(X_2) g(\gamma_2)]\ \epsilon_{peak} \tag{10}$$

where $f(X_i)$ and $g(\gamma_i)$ are the solar-zenith-angle factor and elevation-angle factor of site i, and ϵ_{peak} is the modeling error of the ionospheric peak at zenith. The solar-zenith-angle factor can be represented by the empirical function

$$f(X) = 0.2 + 0.8 \cos^{2/3} X \tag{11}$$

and the elevation-angle factor is given by (Ref. 4)

$$g(\gamma) = \{[(R_e + h_2)^2 - R_e^2 \cos^2 \gamma]^{1/2} - [(R_e + h_1)^2 - R_e^2 \cos^2 \gamma]^{1/2}\}/(h_2 - h_1) \tag{12}$$

[1] A "fudge factor" of 0.8 has been included to account for possible imperfect bandpass overlap and data processing loss.

where R_e = 6370 km, h_1 = 215 km and h_2 = 454 km.

Random ionospheric error is the result of fluctuations from the nominal values which can be represented by

$$\sigma_\tau = \frac{1}{2}\,[f(X_1)\,g(\gamma_1) + f(X_2)\,g(\gamma_2)]\;\epsilon'_{peak} \qquad (13)$$

where ϵ'_{peak} is the standard deviation of the peak zenith fluctuation difference between the two sites.

C. Troposphere

Both dry and wet components of tropospheric error can be divided into systematic and random parts. Systematic error can be written as

$$\sigma_\tau = \left(\frac{\epsilon^2_{z,1}}{\sin^2\gamma_1} + \frac{\epsilon^2_{z,2}}{\sin^2\gamma_2}\right)^{1/2} \qquad (14)$$

where $\epsilon_{z,i}$ is the zenith tropospheric calibration error at site i.

Random tropospheric error due to inhomogeneity can be written as

$$\sigma_\tau = \left(\frac{1}{\sin^2\gamma_1} + \frac{1}{\sin^2\gamma_2}\right)^{1/2} \epsilon'_z \qquad (15)$$

where ϵ'_z is the 1-σ standard deviation of the zenith fluctuation on each site.

D. Clock Instability

The effect of imperfect clocks on a delay observation is directly related to the difference between the drifts of the two clocks. It consists of an epoch offset and a relative drift. Epoch offset is an estimated parameter which is well isolated from baseline vector components and needs no further discussion. Clock drift effect is of a flicker random noise (as integrated over an observation time of ~12 minutes). It differs from a white random noise in that its Allan variance remains constant over all integration time instead of a linear decrease with integration time as for white random noise. Hence its effects cannot be treated as random effects. Instead, it is to be considered as systematic. The sensitivities of delay observations to such error can be simulated by a simple flicker noise model:

$$\sigma_{\tau,m} = f(N_m)\left[\left(\frac{\Delta f}{f}\right)^2_1 + \left(\frac{\Delta f}{f}\right)^2_2\right]^{1/2} c(\Delta t) \qquad (16)$$

where $(\Delta f/f)^2_i$ is the Allan variance of the clock at site i and $f(N_m)$ is a discrete function, at sampling time Δt, simulating a flicker noise of unity Allan variance given by the following recurrence formula:

$$f(j) = 1.95\,f(j-1) - 0.95\,f(j-2) + \frac{1}{0.74}\left[\sum_{m=1}^{100} m^{0.6}\,g_{j+1-m} - 1.95\sum_{m=1}^{99} m^{0.6}\,g_{j-m} + 0.95\sum_{m=1}^{98} m^{0.6}\,g_{j-1-m}\right] \qquad (17)$$

with g_j being the j^{th} sample of a Gaussian random number of unity standard deviation and $g_j = 0$ for $j < 1$. For a 60-sec sampling time N_m becomes the time of observation in minutes rounded to the nearest integer.

E. Source Positions

The angular position error of any single EGRS can be considered to be fixed. The right ascension and declination components of this error are assumed to be uncorrelated to and independent of each other and of any other sources. Hence the effects of each component of a source should be treated as an independent consider parameter and yet the effects of all sources can be included in a single estimation.

The sensitivities of a delay observation to the right-ascension and declination errors of an EGRS can be formulated from Eq. (1):

$$\frac{\partial\tau}{\partial\alpha} = B_x\cos\delta\cos HA - B_y\cos\delta\sin HA$$

$$\frac{\partial\tau}{\partial\delta} = B_x\sin\delta\sin HA + B_y\sin\delta\cos HA + B_z\cos\delta \qquad (18)$$

F. Polar Motion and UT1

The effects of polar motion error and of UT1 error on a baseline are independent of observation sequence and need no covariance analysis for their determination. It has been readily shown (Ref. 5) that x- and y-components of polar motion

error can be translated into the following baseline component errors:

$$\epsilon_{B_x} = \frac{-B_z}{a}\epsilon_x$$

$$\epsilon_{B_y} = \frac{B_z}{a}\epsilon_y \qquad (19)$$

$$\epsilon_{B_z} = \frac{B_x}{a}\epsilon_x - \frac{B_y}{a}\epsilon_y$$

where a is the Earth's radius at the pole.

These can be translated, with the aid of Fig. 2, into errors in baseline length and in lateral and vertical directions:

$$\epsilon_{B_L} = 0$$

$$\epsilon_{B_{LT}} = \frac{B}{a}\cos\phi\ \epsilon_x \qquad (20)$$

$$\epsilon_{B_{VT}} = \frac{B}{a}[(\cos\Omega\sin\phi)\epsilon_x - (\sin\Omega)\epsilon_y]$$

Therefore, the effects of polar motion error will be on baseline orientation only; baseline length will not be affected.

The effects of UT1 error on baseline vector can be derived from Eq. (1). Let $B_x = B_e \cos\lambda$ and $B_y = B_e \sin\lambda$; then (1) can be rewritten as

$$\tau = -B_e \cos\delta \sin(HA + \lambda) + B_z \sin\delta\ . \qquad (21)$$

A perturbation in UT1 of ϵ_{UT1} corresponds to a perturbation in HA of $\omega_e\ \epsilon_{UT1}$ where ω_e is the Earth's spinning speed. Such error will result in an error in λ of equal magnitude but of opposite sign. In turn, an error in λ of $\epsilon_\lambda = -\omega_e \epsilon_{UT1}$ will result in errors in B_x and B_y of

$$\epsilon_{B_x} = \frac{\partial B_x}{\partial\lambda}\epsilon_\lambda \qquad (22a)$$

$$= \omega_e B_y \epsilon_{UT1}$$

and

$$\epsilon_{B_y} = \frac{\partial B_y}{\partial\lambda}\epsilon_\lambda \qquad (22b)$$

$$= -\omega_e B_x \epsilon_{UT1}.$$

As before, these can be translated into errors in baseline length and in lateral and vertical directions:

$$\epsilon_{B_L} = 0$$

$$\epsilon_{B_{LT}} = -\omega_e B \sin\phi\ \epsilon_{UT1} \qquad (23)$$

$$\epsilon_{B_{VT}} = \omega_e B \cos\Omega \cos\phi\ \epsilon_{UT1}$$

Therefore, UT1 error will affect only baseline orientation but not baseline length.

G. Antenna Location

Antenna location may vary from one visit to another. Such error in repeatability translates directly into baseline error.

H. Phase Accountability

This is a random phase variation in the receiver bandpass. Its effects on baseline are estimated in the same way as system noise effects.

V. Results

In this section, covariance analysis will be performed for the determination of a 300-km baseline at mid-latitude ($\phi = 35°$) with a sequence of 32 delay observations. Such 32-observation (~6-hr) sequence is picked out of Table 2. To examine the dependence on the observation sequence, the first of the 32 consecutive observations runs through Table 2. Baseline error due to each error source will then be shown as a function of the starting RA of the baseline center. The following assumptions are to be made:

Baseline: 300 km at $\phi = 35°$

Antenna diameters: 26 m (base)
3 m (mobile)

Antenna efficiencies: 50%

System temperatures: 40 K (base)
130 K (mobile)

Channel bandwidth: 2 MHz

Span bandwidth: 400 MHz

EGRS flux densities: As in Table 1

Observation times: As in Table 2

Phase accountability: 0.2 cm each site (phase calibration assumed)

Clock instability: $\Delta f/f = 10^{-14}$ (hydrogen maser)

Zenith dry tropospheric error: 0.5 cm each site (systematic)

Zenith wet tropospheric error[2]: $0.5/\sqrt{2}$ cm each site (systematic)
$0.5/\sqrt{2}$ cm each site (random)

Zenith ionospheric error: 10 cm peak (systematic)
2 cm difference per 1000 km (random)

Polar motion error: 30 cm

UT1 error: 0.6 msec

EGRS angular position error: $0.01''/\sqrt{2}$ in RA and dec

Antenna location error: 0.5 cm (mobile site only)

Figures 3–11 display the results of covariance analysis. Here only the resultants of 3-D baseline errors are shown. Their mean values are summarized in Fig. 12 together with the effects due to platform parameter errors and antenna location error. Also shown in Fig. 12 are the corresponding errors in baseline length. It is observed that baseline length error accounts for only 30% of the total (3-D) baseline error. When baselines of different length are considered, it is found that errors due to ionosphere, source positions, polar motion and UT1 increase nearly linearly with baseline length. Such errors are drawn cross-hatched in Fig. 12. Errors due to other error sources essentially remain the same for all baseline lengths. (Tropospheric errors may increase slightly due to lower elevation angles for longer baselines.)

VI. Discussions

The above analysis provides an estimate of the effects of each possible error source on baseline vector determination. However, such information may not be of direct benefit to system design. In particular, one would need to look into the requirements on front-end system temperatures and antenna sizes to meet a given overall precision. These two parameters are among a few that are cost effective and controllable in the ORION System design. Other error sources are limited by state-of-the-art capabilities: for instance, clock stability, media and platform parameter calibrations and the knowledge of EGRS angular positions. Both antenna sizes and system temperatures affect baseline vector determination through Eq. (9), the equation for system noise effect. The variation of such effect with antenna sizes and system temperatures will be studied, keeping all other effects unchanged. To account for reduced correlated flux densities over longer baselines and for full capability of 14 pairs of 2-MHz channels of the Mark III VLBI System, the following changes of parameters are assumed:

EGRS correlated flux densities: 2 Janskys for all sources.

Total channel bandwidth: 14 X 2 MHz per sideband.

Observation times: 10 min.

Figure 13 displays the effects of system noise as functions of antenna sizes. Three combinations of system temperatures are considered: 130 K/130 K, 40 K/130 K, and 40 K/40 K. The higher temperature refers to an uncooled receiver front end and the lower temperature to a cooled front end. The tick marks along the abscissa indicate typical combinations of antenna diameters in meters. The absolute maximum of the system noise effect is limited by the minimum fringe phase signal-to-noise ratio (SNR) below which phase tracking may fail. This corresponds to a baseline vector error of ~3.1 cm and a baseline length error of ~1.2 cm. This threshold is shown as a dashed line in Fig. 13.

For a base station with $D = 26$ meters and $T_S = 40$ K and a mobile station with $D = 3$ meters and $T_S = 130$ K, the system noise effects are found to be ~0.8 cm on baseline vector and ~0.3 cm on baseline length. These are comparable with the results shown in Fig. 12 for a 300-km baseline. It is observed that for such, and shorter, baseline lengths the effects of system noise are comparable with other error sources and consideration of antenna sizes and system temperatures may play an important role in overall baseline determination accuracy. For baselines longer than 300 km, those errors which are cross-hatched in Fig. 12 are to be scaled directly by baseline length[3]. Hence, for baselines 1000 km or longer, effects from ionosphere, source positions, polar motion and UT1 will dominate. It becomes relatively immaterial as to what combination of antenna sizes and system temperatures are used. This is illustrated in Figs. 14 and 15 for baseline vector error and baseline length error respectively. For a 5000-km baseline, the overall errors are effectively constant regardless of antenna sizes and system temperatures. Unless the knowledge of source positions, polar motion and UT1 can

[2] Assuming water vapor radiometers are used. Bias errors will appear as clock epoch error which is to be estimated.

[3] Error from troposphere will also increase slightly due to lower elevation angles for longer baselines.

be improved by a factor of ~3, consideration of antenna sizes and system temperatures is insignificant for baselines longer than 2000 km, as long as the signals are sufficiently strong to maintain a fringe phase SNR exceeding the minimum threshold.

The above study has been based on observations over an integration time of 600 sec. Of course, tradeoffs can be made between antenna sizes and observation time and between system temperatures and observation time: A decrease in observation time by a factor of 2 corresponds to a decrease in the product of antenna diameters by a factor of $\sqrt{2}$ or an increase in one of the system temperatures by a factor of 2. Therefore, antenna sizes greater than or system temperatures smaller than are needed to attain a specified precision allow a shorter integration time (and hence smaller data volume) per observation. Figures 13–15 can be used for integration times T other than 600 sec by simply moving the scale on the abscissa to the left by a factor $(600/T)^{1/2}$

In regard to Fig. 12, the S/X calibration of ionospheric error needs to be mentioned. With the projected capabilities of source-position, polar-motion and UT1 calibrations assumed, the effects on baseline *vector* determination of these errors are much higher than that of ionospheric error (with Faraday rotation calibration). The dominance of these errors over ionospheric error will remain for all baseline lengths since they all increase with baseline length. Hence the need of S/X calibration does not seem justified unless the knowledge of source positions, polar motion and UT1 can be improved. This statement is not true in the case of baseline *length* determination since polar motion and UT1 do not affect its accuracy as shown in the lower part of Fig. 12. Ionospheric error without S/X calibration becomes a major error souce in the determination of baseline *length* 1000 km or longer.

References

1. MacDoran, P. F., et al., "Radio Interferometric Geodesy Using a Rubidium Frequency System," Proc. of the 7th Annual Precision Time and Time Interval (PTTI) Applications and Planning Meeting, Goddard Space Flight Center, Greenbelt, Maryland, December 2-4, 1975, pp. 439-454.
2. Bierman, G. J., *Factorization Methods for Discrete Sequential Estimation*, Academic Press, 1977, Chapter 8.
3. Thomas, J. B., *An Analysis of Long Baseline Radio Interferometry, Part II*, Technical Report 32-1526 Vol. VIII, Jet Propulsion Laboratory, Pasadena, Calif., April 1972, pp. 29-38.
4. Liu, A., and Cain, D., *Ionospheric Range and Angular Corrections*, Technical Memorandum, 312-694, Jet Propulsion Laboratory, Pasadena, Calif., March 1966.
5. Williams, J. G., "Very Long Baseline Interferometry and Its Sensitivity to Geophysical and Astronomical Effects," *Space Program Summary 37-62, Vol. II*, Jet Propulsion Laboratory, Pasadena, Calif., March 1970, pp. 49-54.

Table 1. X-band VLBI extragalactic radio sources

Source	Right-ascension	Declination	Correlated flux density over 300-km baseline,[a] Janskys
3C 84	49.12°	41.33°	44.6
DA 193	88.01	39.81	5.2
P 0605-08	91.40	−8.57	4.5
OJ 287	132.99	20.30	4.7
4C 39.25	140.98	39.26	7.8
3C 273	186.64	2.33	32.5
3C 279	193.40	−5.52	12.2
3C 345	250.32	39.90	6.8
NRAO 530	262.56	−13.05	5.1
P 1741-038	265.34	−3.81	5.6
OV −236	290.87	−29.28	6.8
3C 418	309.28	51.14	5.6
P 2134+004	323.72	.47	8.0
3C 454.3	342.87	15.88	6.3

[a]Correlated flux density may vary with time; for the current analysis, however, these crude estimates can be used without introducing unrealistic error.

Table 2. ORION 24-hour observation sequence

Source	T_{obs}	Right-ascension of baseline center hr	min	sec
DA 193	12	0	0	0
3C 84	4	0	8	29
3C 454.3	12	0	17	31
P 2134+004	12	0	29	55
3C 418	12	0	42	47
3C 84	4	0	51	51
DA 193	12	1	0	20
P 2134+004	12	1	14	15
3C 454.3	12	1	26	39
3C 418	12	1	39	23
3C 84	4	1	48	27
DA 193	12	1	56	56
P 0605-008	12	2	9	44
3C 84	4	2	18	47
3C 454.3	12	2	27	49
P 0605-08	12	2	41	39
3C 418	12	2	55	46
3C 84	4	3	4	50
P 0605-08	12	3	13	53
4C 39.25	12	3	26	59
3C 84	4	3	36	5
DA 193	12	3	44	34
OJ 287	12	3	57	17
P 0605-08	12	4	10	7
3C 84	4	4	19	10
DA 193	12	4	27	39
OJ 287	12	4	40	22
4C 39.25	12	4	52	42
P 0605-08	12	5	5	48
3C 84	4	5	14	51
P 0605-08	12	5	23	54
DA 193	12	5	36	42
OJ 287	12	5	49	25
P 0605-08	12	6	2	15
3C 84	4	6	11	18
DA 193	12	6	19	47
P 0605-08	12	6	32	35
4C 39.25	12	6	45	41
OJ 287	12	6	55	1
DA 193	12	7	10	44
P 0605-08	12	7	23	32
3C 84	4	7	32	35
OJ 287	12	7	41	47
4C 39.25	12	7	54	7
P 0605-08	12	8	7	13
3C 273	4	8	16	49
3C 84	4	8	22	51
OJ 287	12	8	32	3
3C 84	4	8	41	15
3C 279	12	8	51	27
3C 273	4	8	59	37
P 0605-08	12	9	9	13
DA 193	12	9	22	1
OJ 287	12	9	34	44
4C 39.25	12	9	47	4
3C 273	4	9	55	59
3C 279	12	10	4	9
4C 39.25	12	10	17	15
3C 345	12	10	30	33
3C 273	4	10	39	42
OJ 287	12	10	48	37
3C 279	12	11	1	42
DA 193	12	11	15	27

Source	T_{obs}	Right-ascension of baseline center hr	min	sec
4C 39.25	12	11	28	7
3C 273	4	11	37	2
DA 193	12	11	46	37
3C 345	12	12	0	16
3C 279	12	12	13	25
3C 273	4	12	21	35
OJ 287	12	12	30	30
3C 279	12	12	43	35
4C 39.25	12	12	56	41
3C 279	12	13	9	47
3C 345	12	13	22	56
3C 273	4	13	32	5
P 1741-038	12	13	41	24
3C 418	12	13	54	30
3C 345	12	14	7	12
3C 279	12	14	20	21
NRAO 530	12	14	33	29
3C 279	12	14	46	37
3C 418	12	15	0	27
3C 345	12	15	13	9
3C 273	4	15	22	18
4C 39.25	12	15	31	13
NRAO 530	12	15	45	16
3C 345	12	15	58	10
P 1741-038	12	16	10	56
NRAO 530	12	16	23	6
3C 273	4	16	32	23
3C 418	12	16	42	11
P 1741-038	12	16	55	17
3C 345	12	17	8	3
NRAO 530	12	17	20	57
P 2134+004	12	17	33	59
OV -236	12	17	46	42
3C 454.3	12	17	59	49
OV - 236	12	18	12	56
3C 418	12	18	26	18
NRAO 530	12	18	39	34
3C 345	12	18	52	28
P 1741-038	12	19	5	14
3C 418	12	19	18	20
OV -236	12	19	31	42
P 2134+004	12	19	44	25
NRAO 530	12	19	57	27
3C 345	12	20	10	21
OV -236	12	20	23	40
3C 418	12	20	37	2
3C 454.3	12	20	49	46
OV -236	12	21	2	53
3C 418	12	21	16	15
3C 84	4	21	28	15
P 2134+004	12	21	41	7
3C 84	4	21	50	33
P 2134+004	12	21	59	59
3C 454.3	12	22	12	23
3C 345	12	22	25	45
3C 84	4	22	35	22
P 2134+004	12	22	44	48
3C 418	12	22	57	40
3C 454.3	12	23	10	24
P 2134+004	12	23	22	48
3C 418	12	23	35	40
P 2134+004	12	23	48	32

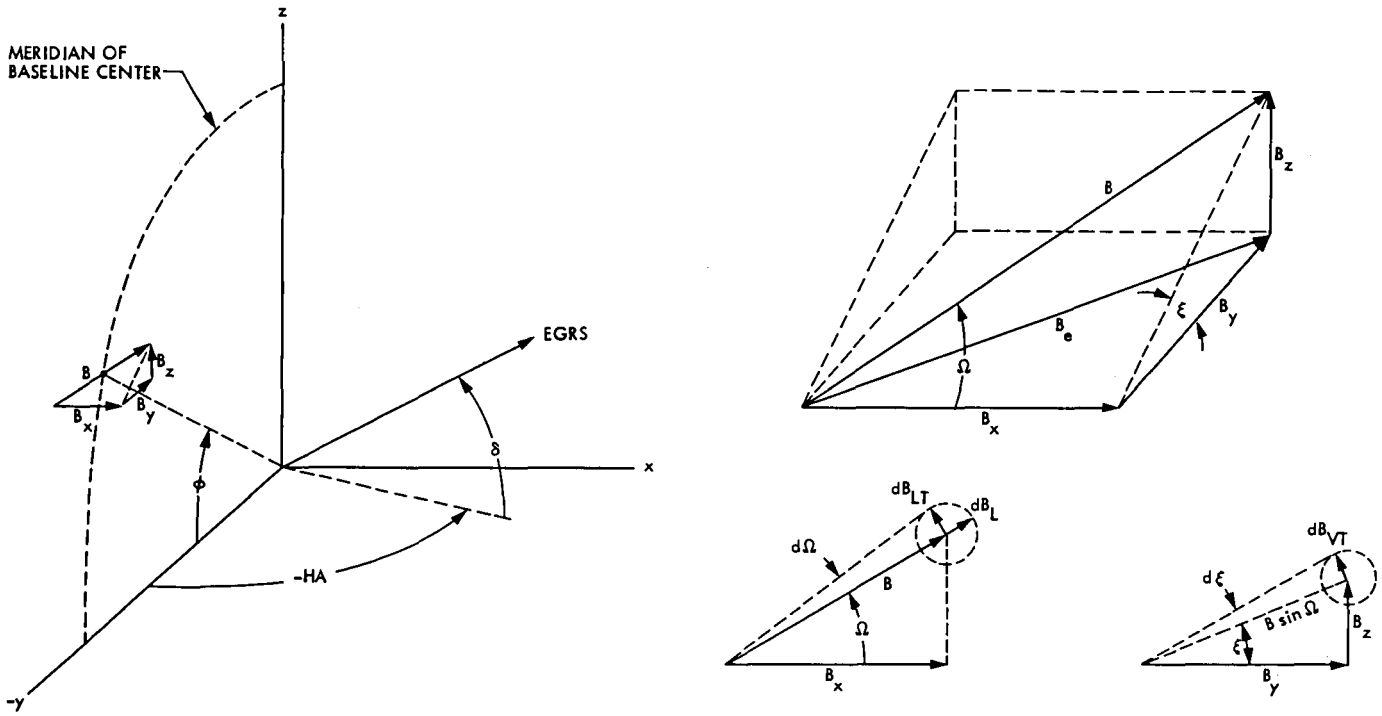

Fig. 1. Geometry of baseline and EGRS

$B_x = B \cos \Omega$ $\quad dB_L = dB$ (LENGTH)

$B_y = B \sin \Omega \cos \xi$ $\quad dB_{LT} = B\, d\Omega$ (LATERAL)

$B_z = B \sin \Omega \sin \xi$ $\quad dB_{VT} = B \sin \Omega\, d\xi$ (VERTICAL)

$\pi/2 - \xi = \phi$ = BASELINE CENTER LATITUDE

Fig. 2. Transformation of baseline component differentials

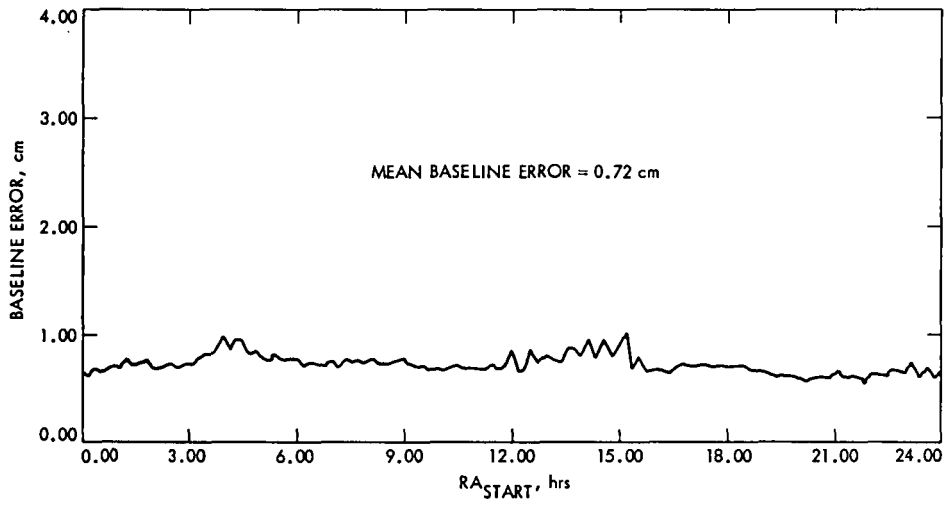

Fig. 3. System noise effects on baseline vector determination

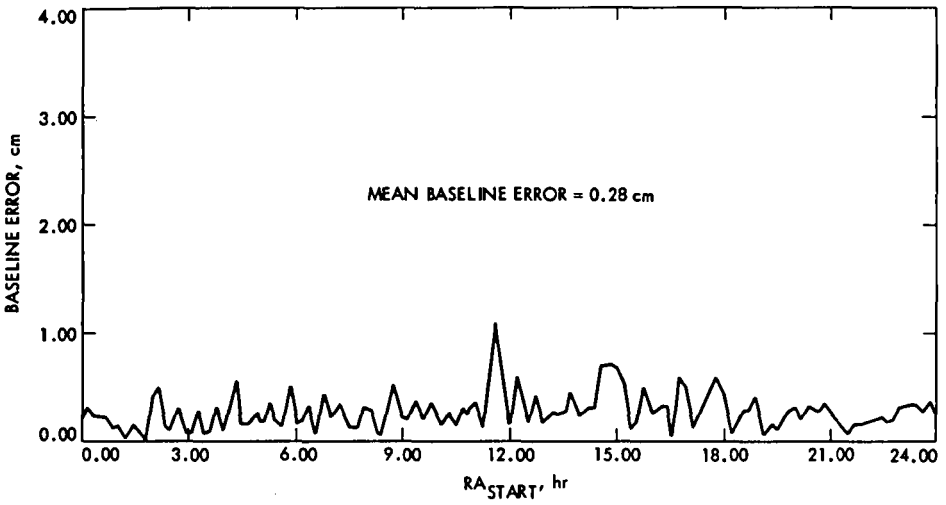

Fig. 4. Clock instability effects on baseline vector determination

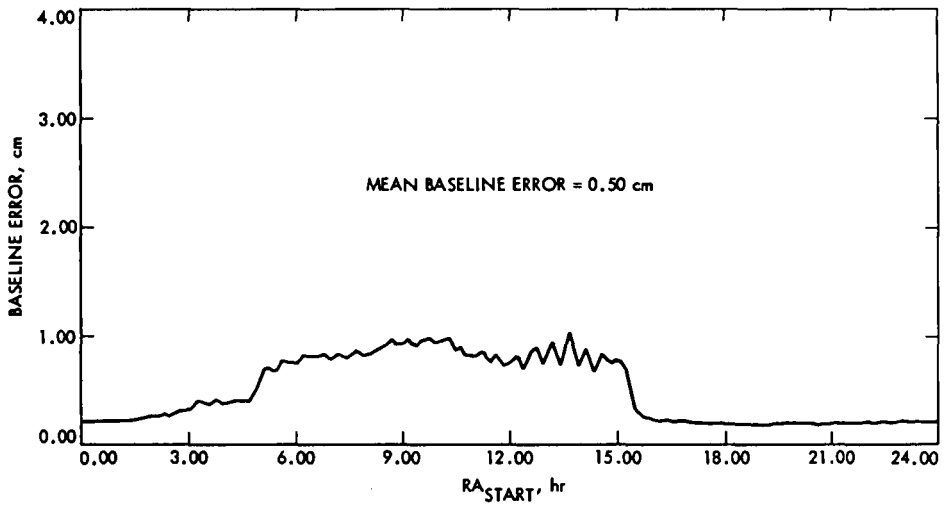

Fig. 5. Effects of systematic ionospheric error on baseline vector determination

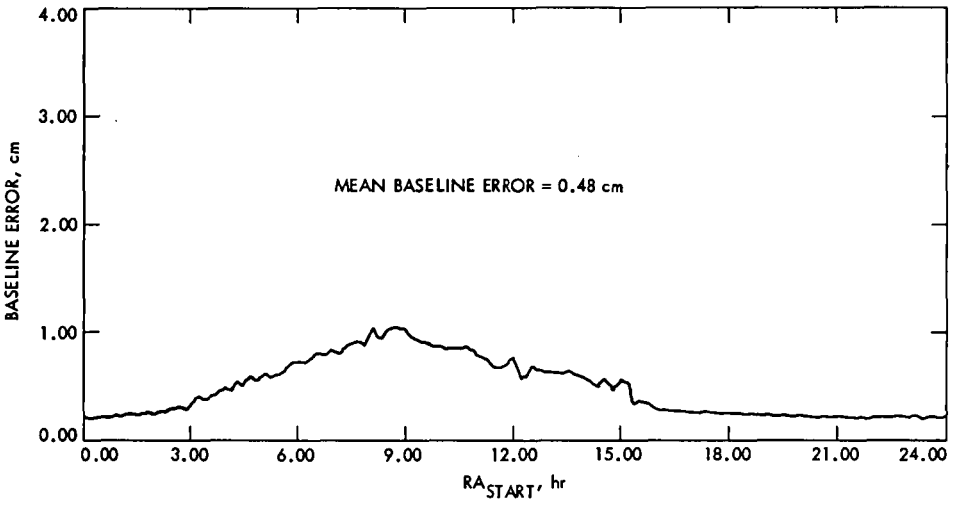

Fig. 6. Effects of random ionospheric error on baseline vector determination

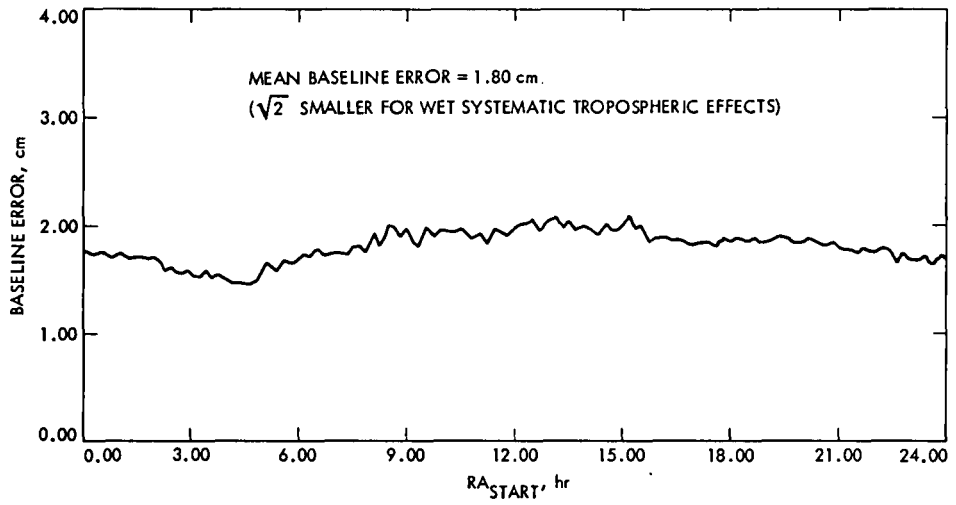

Fig. 7. Effects of dry tropospheric error on baseline vector determination

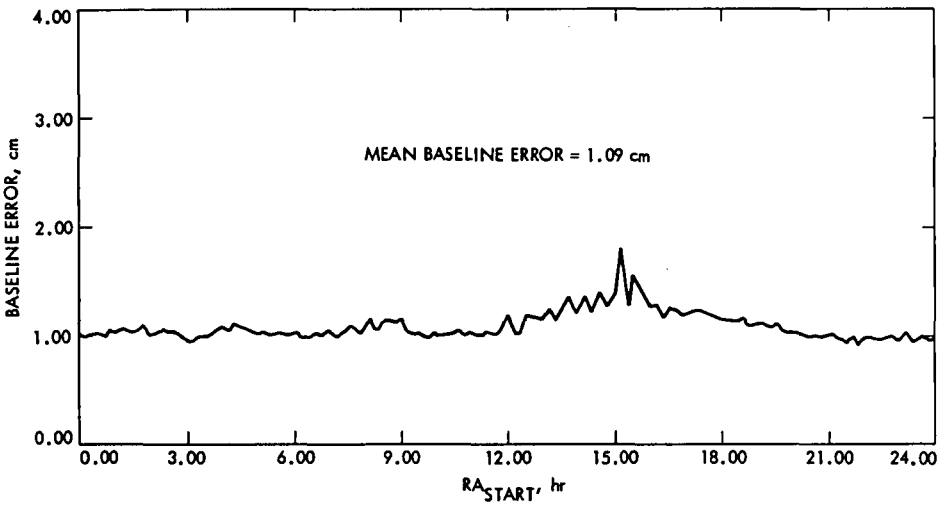

Fig. 8. Effects of random wet tropospheric error on baseline vector determination

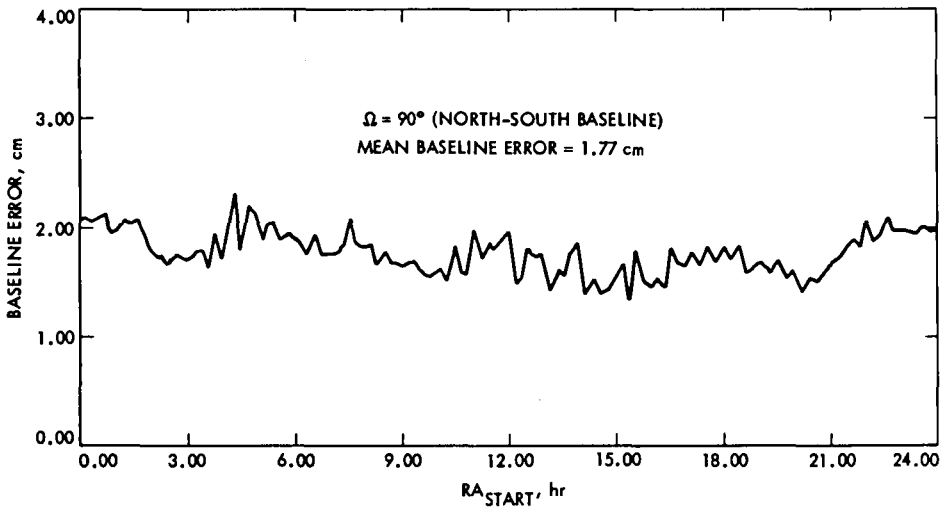

Fig. 9. Effects of EGRS position errors on baseline vector determination

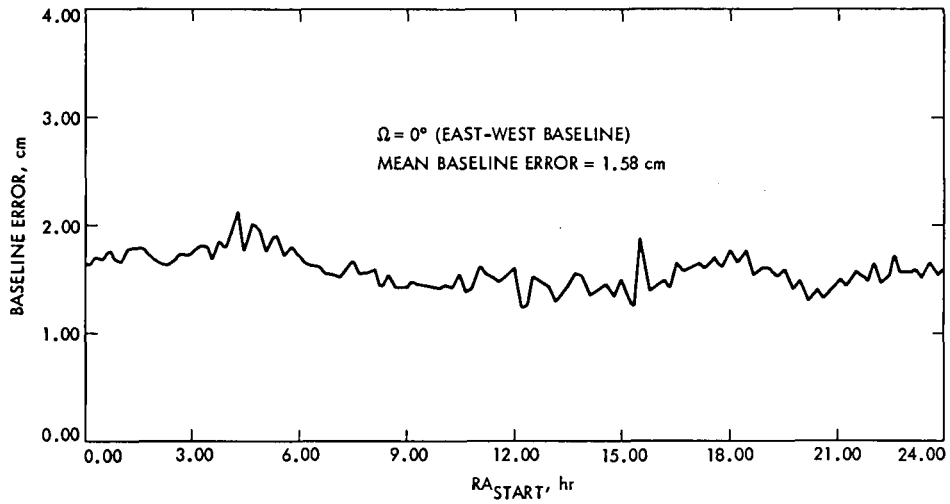

Fig. 10. Effects of EGRS position errors on baseline vector determination

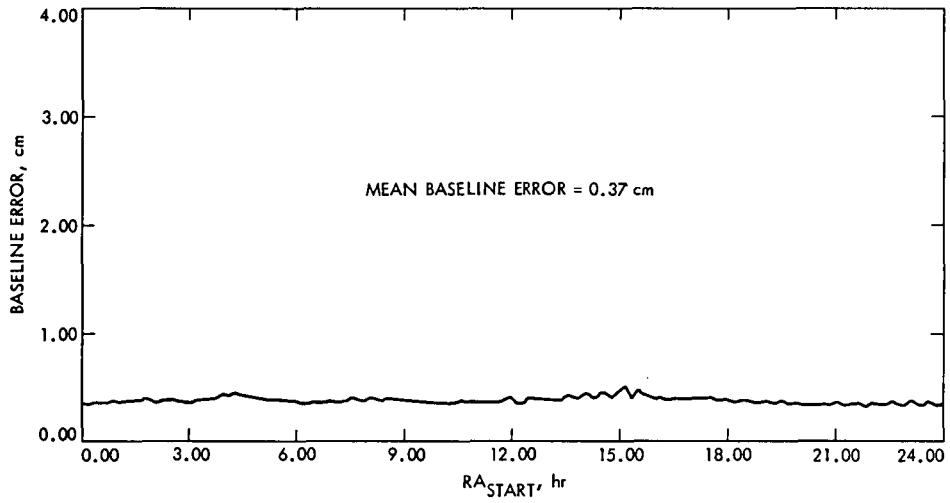

Fig. 11. Effects of system phase accountability error on baseline vector determination

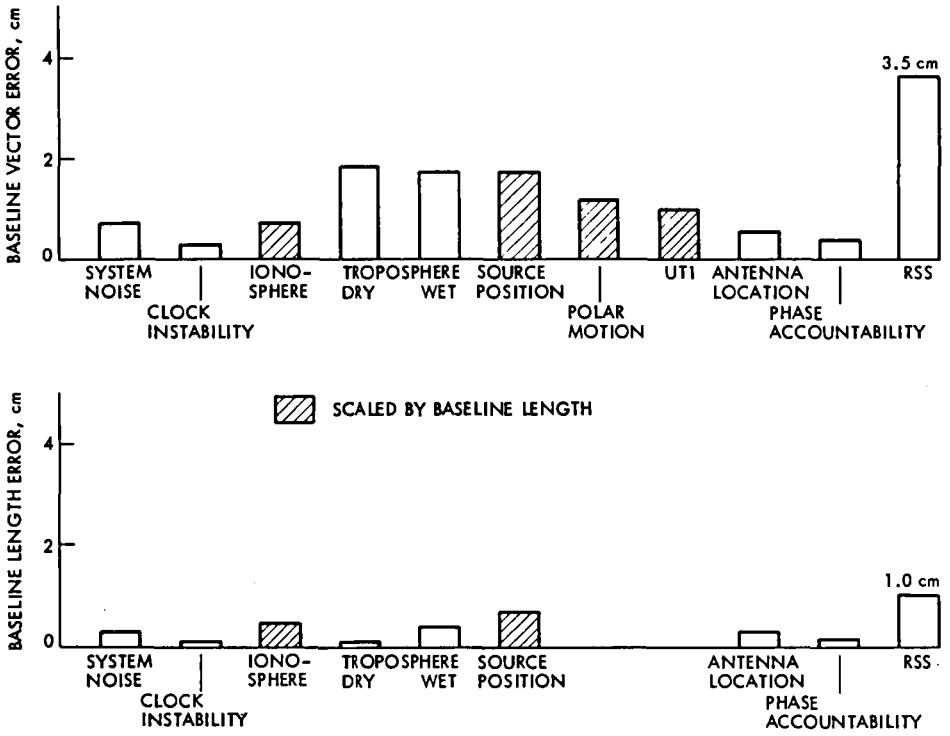

Fig. 12. Baseline vector and length determination errors

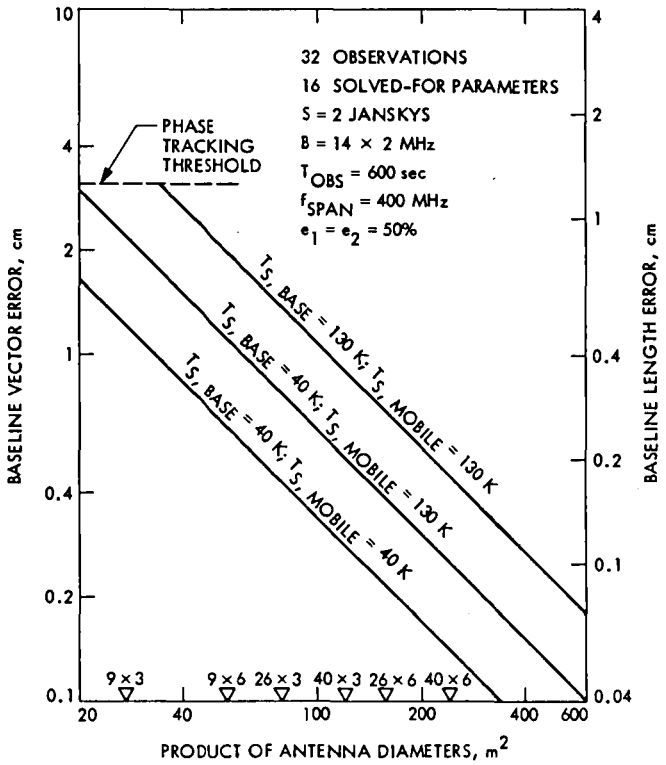

Fig. 13. Contribution of system noise to baseline determination error

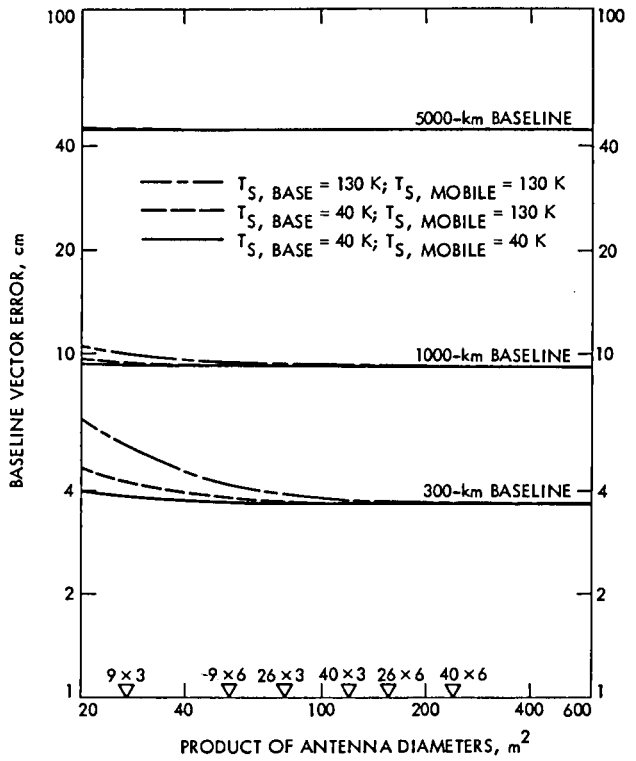

Fig. 14. Total baseline vector determination error

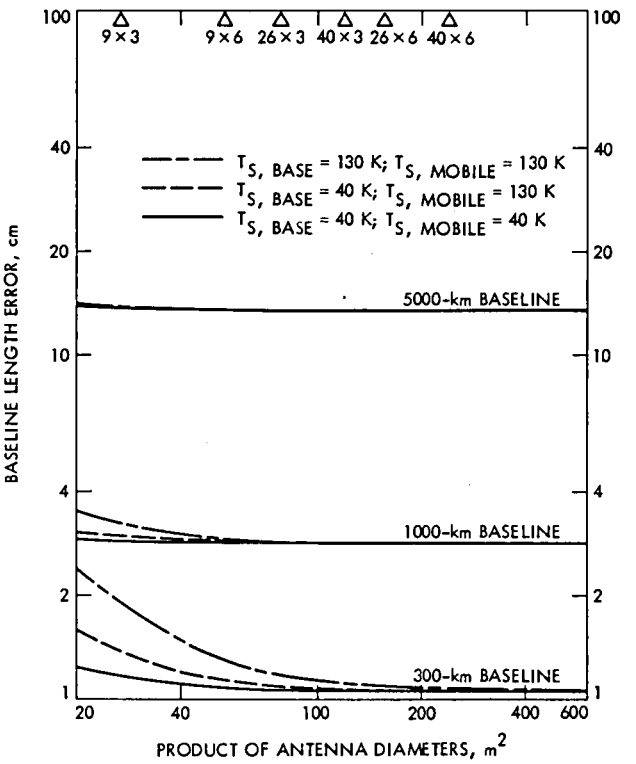

Fig. 15. Total baseline length determination error

Network Functions and Facilities

N. A. Renzetti
Office of Tracking and Data Acquisition

The objectives, functions, and organization of the Deep Space Network are summarized; deep space station, ground communication, and network operations control capabilities are described.

The Deep Space Network was established by the National Aeronautics and Space Administration (NASA) Office of Space Tracking and Data Systems and is under the system management and technical direction of the Jet Propulsion Laboratory (JPL). The network is designed for two-way communications with unmanned spacecraft traveling approximately 16,000 km (10,000 miles) from Earth to the farthest planets and to the edge of our solar system. It has provided tracking and data acquisition support for the following NASA deep space exploration projects: Ranger, Surveyor, Mariner Venus 1962, Mariner Mars 1964, Mariner Venus 1967, Mariner Mars 1969, Mariner Mars 1971, and Mariner Venus-Mercury 1973, for which JPL has been responsible for the project management, the development of the spacecraft, and the conduct of mission operations; Lunar Orbiter, for which the Langley Research Center carried out the project management, spacecraft development, and conduct of mission operations; Pioneer, for which Ames Research Center carried out the project management, spacecraft development, and conduct of mission operations; and Apollo, for which the Lyndon B. Johnson Space Center was the project center and the Deep Space Network supplemented the Manned Space Flight Network, which was managed by the Goddard Space Flight Center. The network is currently providing tracking and data acquisition support for Helios, a joint U.S./West German project; Viking, for which Langley Research Center provided the Lander spacecraft and project management until May, 1978, at which time project management and mission operations were transferred to JPL, and for which JPL provided the Orbiter spacecraft; Voyager, for which JPL provides project management, spacecraft development, and is conducting mission operations; and Pioneers, for which the Ames Research Center provides project management, spacecraft development, and conduct of mission operations. The network is adding new capability to meet the requirements of the Galileo mission to Jupiter, for which JPL is providing the Orbiter spacecraft, and

the Ames Research Center the probe. In addition, JPL will carry out the project management and the conduct of mission operations.

The Deep Space Network (DSN) is one of two NASA networks. The other, the Spaceflight Tracking and Data Network (STDN), is under the system management and technical direction of the Goddard Space Flight Center (GSFC). Its function is to support manned and unmanned Earth-orbiting satellites. The Deep Space Network supports lunar, planetary, and interplanetary flight projects.

From its inception, NASA has had the objective of conducting scientific investigations throughout the solar system. It was recognized that in order to meet this objective, significant supporting research and advanced technology development must be conducted in order to provide deep space telecommunications for science data return in a cost effective manner. Therefore, the Network is continually evolved to keep pace with the state of the art of telecommunications and data handling. It was also recognized early that close coordination would be needed between the requirements of the flight projects for data return and the capabilities needed in the Network. This close collaboration was effected by the appointment of a Tracking and Data Systems Manager as part of the flight project team from the initiation of the project to the end of the mission. By this process, requirements were identified early enough to provide funding and implementation in time for use by the flight project in its flight phase.

As of July 1972, NASA undertook a change in the interface between the Network and the flight projects. Prior to that time, since 1 January 1964, in addition to consisting of the Deep Space Stations and the Ground Communications Facility, the Network had also included the mission control and computing facilities and provided the equipment in the mission support areas for the conduct of mission operations. The latter facilities were housed in a building at JPL known as the Space Flight Operations Facility (SFOF). The interface change was to accommodate a hardware interface between the support of the network operations control functions and those of the mission control and computing functions. This resulted in the flight projects assuming the cognizance of the large general-purpose digital computers which were used for both network processing and mission data processing. They also assumed cognizance of all of the equipment in the flight operations facility for display and communications necessary for the conduct of mission operations. The Network then undertook the development of hardware and computer software necessary to do its network operations control and monitor functions in separate computers. A characteristic of the new interface is that the Network provides direct data flow to and from the stations; namely, metric data, science and engineering telemetry, and such network monitor data as are useful to the flight project. This is done via appropriate ground communication equipment to mission operations centers, wherever they may be.

The principal deliveries to the users of the Network are carried out by data system configurations as follows:

(1) The DSN Tracking System generates radio metric data, i.e., angles, one- and two-way doppler and range, and transmits raw data to Mission Control.

(2) The DSN Telemetry System receives, decodes, records, and retransmits engineering and scientific data generated in the spacecraft to Mission Control.

(3) The DSN Command System accepts spacecraft commands from Mission Control and transmits the commands via the Ground Communications Facility to a Deep Space Station. The commands are then radiated to the spacecraft in order to initiate spacecraft functions in flight.

(4) The DSN Radio Science System generates radio science data, i.e., the frequency and amplitude of spacecraft transmitted signals affected by passage through media such as the solar corona, planetary atmospheres, and planetary rings, and transmits these data to Mission Control.

(5) The DSN Very Long Baseline Interferometry System generates time and frequency data to synchronize the clocks among the three Deep Space Communications complexes. It will generate universal time and polar motion and relative Deep Space Station locations as by-products of the primary data delivery function.

The data system configurations supporting testing, training, and network operations control functions are as follows:

(1) The DSN Monitor and Control System instruments, transmits, records, and displays those parameters of the DSN necessary to verify configuration and validate the Network. It provides the tools necessary for Network Operations personnel to control and monitor the Network and interface with flight project mission control personnel.

(2) The DSN Test and Training System generates and controls simulated data to support development, test, training and fault isolation within the DSN. It participates in mission simulation with flight projects.

The capabilities needed to carry out the above functions have evolved in the following technical areas:

(1) The Deep Space Stations, which are distributed around Earth and which, prior to 1964, formed part of the Deep Space Instrumentation Facility. The technology involved in equipping these stations is strongly related to the state of the art of telecommunications and flight-ground design considerations, and is almost completely multimission in character.

(2) The Ground Communications Facility provides the capability required for the transmission, reception, and monitoring of Earth-based, point-to-point communications between the stations and the Network Operations Control Center at JPL, Pasadena, and to the JPL Mission Operations Centers. Four communications disciplines are provided: teletype, voice, high-speed, and wideband. The Ground Communications Facility uses the capabilities provided by common carriers throughout the world, engineered into an integrated system by Goddard Space Flight Center, and controlled from the communications Center located in the Space Flight Operations Facility (Building 230) at JPL.

The Network Operations Control Center is the functional entity for centralized operational control of the Network and interfaces with the users. It has two separable functional elements; namely, Network Operations Control and Network Data Processing. The functions of the Network Operations Control are:

(1) Control and coordination of Network support to meet commitments to Network users.

(2) Utilization of the Network data processing computing capability to generate all standards and limits required for Network operations.

(3) Utilization of Network data processing computing capability to analyze and validate the performance of all Network systems.

The personnel who carry out the above functions are located in the Space Flight Operations Facility, where mission operations functions are carried out by certain flight projects. Network personnel are directed by an Operations Control Chief. The functions of the Network Data Processing are:

(1) Processing of data used by Network Operations Control for control and analysis of the Network.

(2) Display in the Network Operations Control Area of data processed in the Network Data Processing Area.

(3) Interface with communications circuits for input to and output from the Network Data Processing Area.

(4) Data logging and production of the intermediate data records.

The personnel who carry out these functions are located approximately 200 meters from the Space Flight Operations Facility. The equipment consists of minicomputers for real-time data system monitoring, two XDS Sigma 5s, display, magnetic tape recorders, and appropriate interface equipment with the ground data communications.

DSN Command System Mark III-80

H. C. Thorman
TDA Engineering Office

DSN Command System configuration and functional operation are described. Voyager and Helios command operations are supported with DSS store-and-forward data handling; Viking and Pioneer are supported with the older, near-real-time data handling method.

I. System Functional Description

End-to-end command system operations are represented functionally in Fig. 1. Command sequences for one or more spacecraft are generated and stored at a Mission Operations Center (MOC). Commands for a particular spacecraft are selected from the command files, formatted into messages, and stored for transmittal to a specified Deep Space Station (DSS). Command data are extracted from the messages received at the DSS and stored until radiated. Finally, the commands arrive at the spacecraft and are either executed immediately, or stored onboard for later execution.

The functions of the DSN Command System in this process include the following:

(1) Establishing the DSS configuration for the specified spacecraft.

(2) Receiving and storing command data at the DSS.

(3) Queuing command data to be radiated to the spacecraft.

(4) Radiating the command data to the spacecraft.

(5) Monitoring and reporting system status and events.

The Network Operations Control Center (NOCC) provides control and monitoring of the DSN Command System. Instructions from NOCC and command data from MOC are communicated to the DSS via the Ground Communication Facility (GCF) High-Speed Data Subsystem (GHS), as shown in Fig. 2.

II. System Configuration

A detailed diagram of the DSN Command System Mark III-80 is presented in Fig. 3. The Mark III-80 system configuration includes provision for uplink frequency control, as described in Ref. 1, via the DSN Tracking System. The Digitally-Controlled Oscillator (DCO) on the exciter assembly receives tuning parameters from the Metric Data Assembly (MDA). Manual operation of the DCO is also provided, for emergency backup. All other features of the Mark III-80 configuration are the same as in the Mark III-78 configuration described in Ref. 2.

During 1978, the DSS Command Processor Assembly (CPA) software program was upgraded to include the "store-and-forward" data-handling method and increased command storage capacity. The JPL Mission Control and Computing Center (MCCC) was reconfigured to provide the required processing functions to utilize the store-and-forward technique for Voyager and Helios spacecraft command operations. The Pioneer and Viking mission operations organizations chose to

continue to use the older, near-real-time method of command data handling.

The CPA program (DMC-5084-OP-F; Rev. A) was transferred to operations in November 1978 with several anomalies in the status reporting functions of the store-and-forward portion of the software. A new version of the program (DMC-5084-OP-G) was developed during 1979 and was transferred to operations in April 1980, after extensive acceptance tests showed that the major anomalies were corrected. This program version is to become operational in early May after the Voyager Project Ground Data System (GDS) organization completes MCCC interface tests with the various Deep Space Stations.

Some minor anomalies, related to local DSS displays, were identified in testing of the OP-G version of CPA software. Correction of those anomalies is planned in a program upgrade to be implemented in early 1981. The upgrade is also intended to expand the store-and-forward capability to multimission applicability for support of future missions.

III. Pretrack System Preparation

DSS pretrack operations performed by station personnel include initializing the CPA software for "phase 1" for "phase 2" operation so that the CPA will be prepared to recognize the content of the high-speed data blocks to be received from NOCC and the flight project command center. Phase 1 initialization is required for the older type (Mark III-74) command data messages; phase 2 initialization is required for the new (Mark III-78, store-and-forward) type. Additional on-site initialization inputs to the CPA specify the flight project name and the spacecraft identification number. These inputs cause the software to transfer a specific configuration and standards and limits table from disk storage to memory, and to configure the Command Modulator Assembly (CMA) and CPA according to the table. Changes may later be made by high-speed data messages from NOCC or by keyboard entries at the Data System Terminal (DST) in the station.

Upon initialization, the CPA sends DSS Command Subsystem (DCD) configuration and status information across the star switch controller (SSC) to the DSS Monitor and Control Subsystem (Fig. 4) for inclusion in the monitor data blocks that are periodically transmitted to the NOCC to provide station status displays in the Network Operations Control Area (NOCA). The subsystem configuration and status information are also sent from the CPA to the DST for station display.

Prior to the beginning of the scheduled spacecraft track, the control of the station command functions is transferred to the NOCC. Configuration and standards and limits are updated by transmission of high-speed data messages from the NOCC Command Subsystem (NCD) real-time monitor (RTM) processor. The configuration and standards and limits are derived from files maintained in the Network Support Computer (NSC). Spacecraft-dependent parameters, such as symbol period, subcarrier frequency, alarm limits, and abort limits, are established via these messages. After the proper configuration and standards and limits have been established, test commands are transmitted through the system to ensure that the system can accept spacecraft commands via high-speed data messages, temporarily store the commands, and confirm radiation. After NOCC operations personnel have established that the system is operating properly, the system control is transferred to the flight project's MOC for transmission of actual spacecraft command sequences during the spacecraft track period.

At the time for radiation of each command element, the CPA establishes the proper mode (see Fig. 5 for description of the various modes) and configuration of the CMA; then the command is transferred to the CMA for immediate radiation via the Receiver-Exciter, Transmitter, Microwave, and Antenna Subsystems.

IV. Command Data Handling

A. Phase 1 Method: Near-Real-Time

With the CPA initialized for phase 1 operation, the data handling method is functionally the same as has been used since 1973. A command stack provides storage of up to four high-speed data blocks (stack modules) of command data. Each block may contain up to six command elements. Each command element consists of up to 71 bits of command data and, at project option, can be either timed or nontimed. Since the phase 1 storage is small, the MOC may need to update the CPA command stack frequently during a DSS spacecraft track.

The top command element in the first stack module is eligible for radiation to the spacecraft. Nontimed commands are radiated immediately after eligibility. Timed commands are radiated after becoming eligible at the time specified in the high-speed data block.

During command operations, events may occur in which high-speed data message transmission to the NOCC and MOC becomes necessary. The following events initiate message transmission:

(1) Acknowledged receipt of a high-speed data block.

(2) High-speed data block rejected by the CPA.

(3) DSS alarm or alarm clear.

(4) Response to a recall request.

(5) Confirmed command element.

(6) Aborted command element.

B. Phase 2 Method: Store-and-Forward

The store-and-forward data-handling method associated with phase 2 initialization of the CPA utilizes the CPA disk to provide expanded storage of command data. This method is designed to allow mission operations to prepare large files of spacecraft commands in advance and then to forward several files to the DSS at the beginning of a DSS spacecraft track.

1. Command files. Each file may consist of 2 to 256 high-speed data blocks. The content of each data block is a file *element*. The first block in a file contains the *header element* and each remaining block contains a *command element*. Each command element may consist of up to 800 bits of spacecraft command data. Up to 8 files for a given mission can be stored by the CPA. Thus, the available storage is over 1.6 million command bits.

The header element contains file identification information, file processing instructions, and a file checksum for error protection. Once generated (normally by project command generation software), the information is unchanged throughout the ground system. The file processing instructions include optional file radiation open and close window times, and an optional file bit 1 radiation time. File open and close window times specify the time interval during which command elements in the file may begin radiation (i.e., a mission sequence may demand that specific commands *not* be sent before or after a certain time). The bit 1 radiation time allows the project to specify the exact time at which the file is to begin radiation to the spacecraft. The file checksum is intended to provide error protection for the end-to-end ground command system. It is created at the time of file generation and is passed intact to the DSS. It adds reliability to insure that no data were dropped or altered in the transfer from one facility to another.

The command elements each contain command bits, file identification information, element number, element size, and an optional "delay time" (interval from start of previous element). If delay time is not specified, the element will start radiating immediately after the end of the previous element.

2. Receiving and storing command data at a DSS. Normally, the files of commands to be radiated to the spacecraft are sent to a DSS at the beginning of a spacecraft track period. The first step in receiving and storing command data at a DSS is the process of opening a file area on the CPA disk at a DSS. The MOC accomplishes this by sending a header element, which serves as a *file-open* directive. After the CPA acknowledges receipt of the header element, the MOC sends the remainder of the file (up to 255 command elements) and follows it with a *file-close* directive. The CPA acknowledges the file-close instruction and indicates whether the file loading was successful or unsuccessful. If the file loading was unsuccessful, the acknowledge message contains the reason for the failure, and from what point in the file the command elements are to be retransmitted. When the file is successfully closed, the MOC may proceed to send additional files, up to a total of eight.

3. Queuing the command data for radiation. After the files are stored at the CPA, the MOC sends one or more file-attach directives to place up to five file names in the radiation *queue*. The Mission Control Team determines in which order the files are to be attached. The order in which they are attached determines the sequence in which they will be radiated: that is, first attached, first to radiate to the spacecraft.

4. Command radiation to the spacecraft. The first command element in the top (prime) file in the queue begins radiation to the spacecraft immediately after attachment or as soon as all optional file instructions are satisfied. The prime file status is defined to be active when the first command element begins radiation. Upon completion of radiation of the first command element, the second command element begins radiation either immediately or when the optional delay time has been satisfied. The process continues until all command elements in the file have been radiated. After the first file completes radiation, the second file in the queue automatically becomes the prime file and the command radiation process is repeated. After the second file completes radiation, the third file becomes prime, etc. This process is repeated until all files in the queue are exhausted. The MOC can attach new files to the queue whenever space is available.

Confirmations of command element radiation are reported in *event messages* to the MOC and NOCC once per minute, or after five elements have been radiated, whichever occurs first. If a command element is aborted, an event message is sent immediately.

5. Additional data processing. The foregoing descriptions of the functions of storing the command files at a DSS, attaching the files to the queue, and radiating the commands to the spacecraft assume nominal-standard operation. Additional data processing functions are provided for worst-case conditions, nonnominal operations, and failure recovery.

a. File erase. The capability exists to delete a file from storage at the CPA. This *erase* function can be accomplished

either locally at a DSS or via a high-speed data message from the MOC.

b. Clearing the queue. As previously stated, the order of file radiation to the spacecraft is dependent on the order of files in the queue. To rearrange the order, the MOC must send a *clear-queue* directive, followed by file-attach directives in the desired order.

c. Suspend radiation. If the Mission Control Team desires to stop command radiation, a *suspend* message can be sent from the MOC. This message stops command radiation to the spacecraft upon completion of the current element. The file status then changes from active to suspended.

d. Resume command radiation. To restart radiation of a suspended file (either suspended intentionally or from an abort), a message can be sent from MOC to *resume* radiation *at* a specific element in the file.

e. Command abort. As each command bit is radiated to the spacecraft, numerous checks are made to insure validity of the command data. If a failure is detected during radiation, the command element is *aborted*, and the prime file status is changed from active to suspended. Optional methods of treating an abort are provided. If one or more automatic recovery attempts have been specified in the standards and limits, the CPA will try to resend the command element, or else radiation will be terminated until operator intervention occurs.

f. Close window time override. The close window time (previously discussed) can cause an actively radiating file to become suspended. If this occurs, the MOC can send an *override* message that directs the CPA to ignore the close window time and proceed to radiate the complete file.

V. Data Records

All high-speed data blocks received by the CPA and all high-speed data blocks sent from the CPA are logged at the DSS on the Original Data Record (ODR) by the Communications Monitor and Formatter (CMF). The CPA has the capability to record a temporary ODR on disk, if the CMF ODR is disabled.

High-speed data blocks from all DSS are recorded at the GCF central communications terminal (CCT). Command system high-speed data blocks from a Mission Operations Center to the DSS are also recorded at the CCT.

The DSS original data records and the CCT recordings provide information for fault isolation in case problems occur in the command system operation.

References

1. Spradlin, G. L., "DSN Tracking System Uplink Frequency Control," in *The Deep Space Network Progress Report 42-53*, pp. 108–112, Jet Propulsion Laboratory, Pasadena, California, October 15, 1979.
2. Thorman, H. C., "DSN Command System Mark III-78," in *The Deep Space Network Progress Report 42-49*, pp. 11–18, Jet Propulsion Laboratory, Pasadena, California, February 15, 1979.

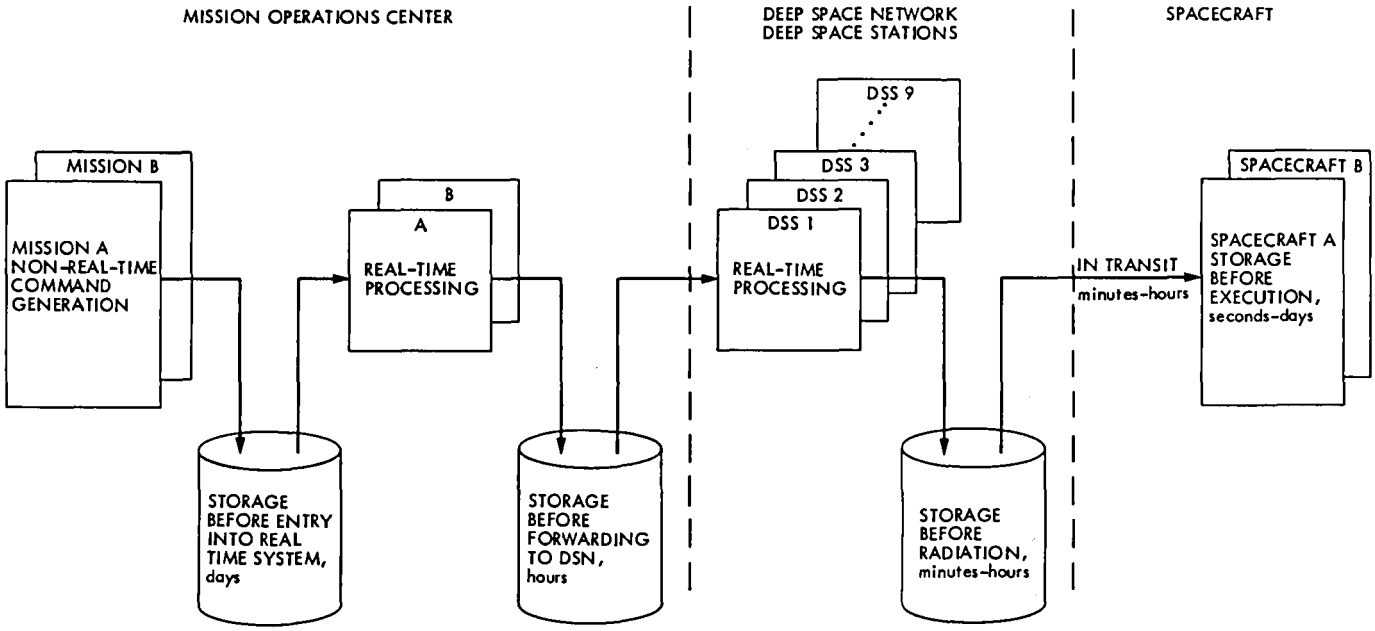

Fig. 1. End-to-end command data flow—typical storage times

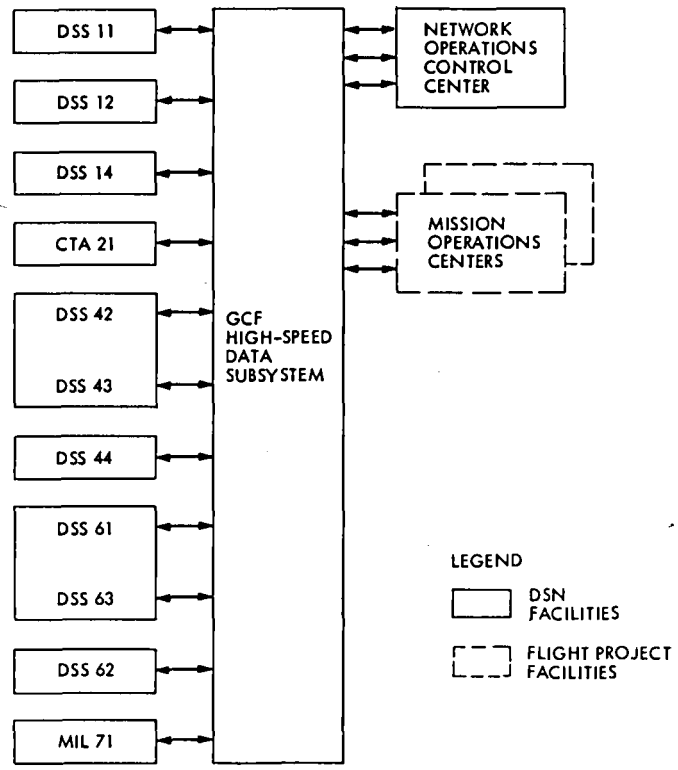

Fig. 2. Facilities that participate in command operations

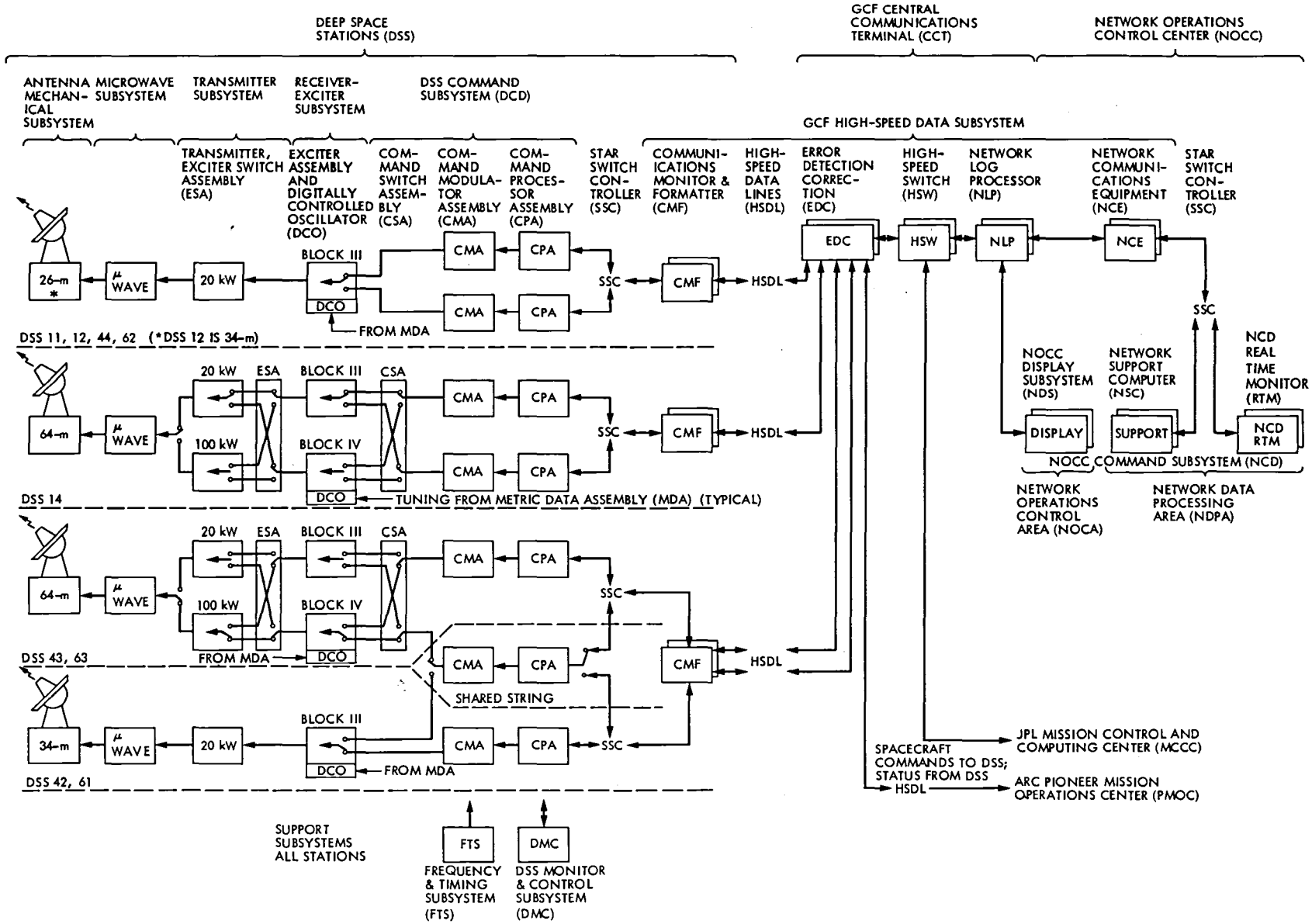

Fig. 3. DSN Command System Mark III-80

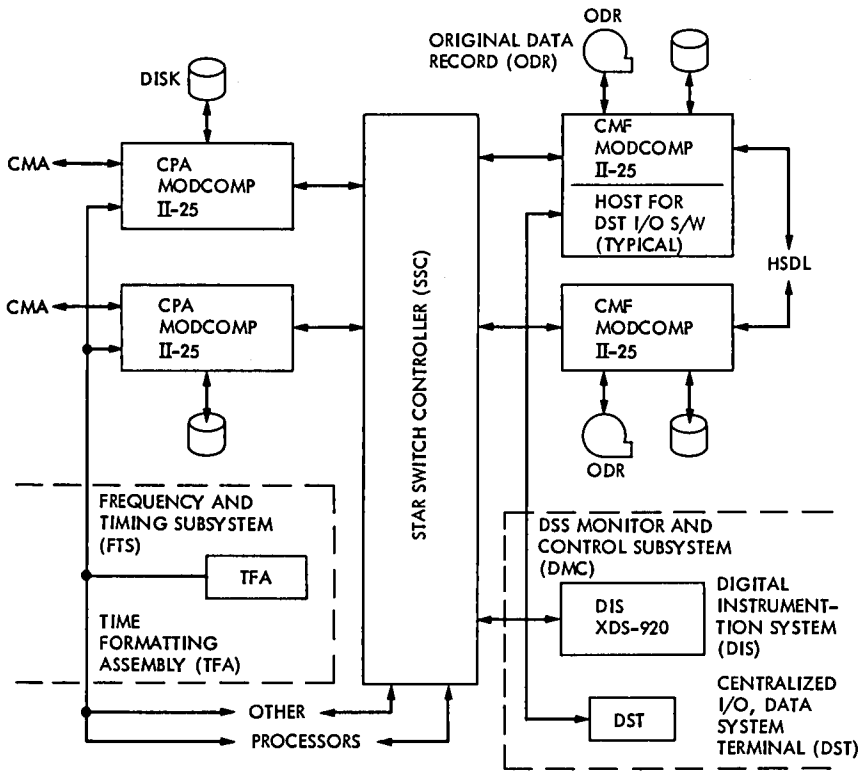

Fig. 4. Deep Space Station interface details

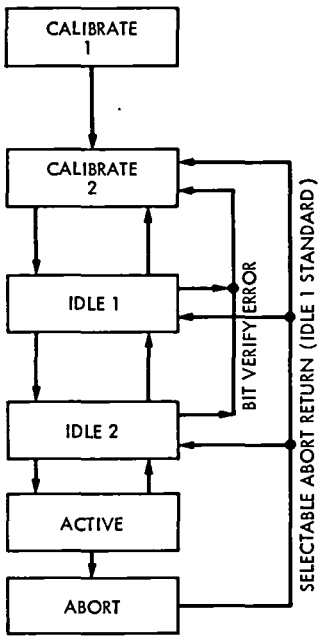

SUBSYSTEM MODE	PRIME PURPOSE	DATA ACCEPTED VIA HIGH SPEED	COMMENTS
CALIBRATE 1	ALLOWS DSS OPS PERSONNEL TO PERFORM INITIALIZATION TASKS	CONFIGURATION, STANDARDS AND LIMITS, MODE CONTROL, RECALL	UPON RECEIPT OF A STANDARDS AND LIMITS AND CONFIGURATION HSD BLOCK, THE CALIBRATE 2 MODE WILL BE ENTERED
CALIBRATE 2	STANDARD MODE FOR UPDATING STANDARDS AND LIMITS AND CONFIGURATION DATA VIA HIGH SPEED PRIOR TO SPACECRAFT ACQUISITION	CONFIGURATION, STANDARDS AND LIMITS, MODE CONTROL, RECALL	MULTIMISSION STANDARD PROCEDURES SHOULD STATE THAT THIS MODE IS TO BE ENTERED FOR CHANGING SUBCARRIER FREQUENCY, BIT RATE
IDLE 1	SAFE MODE - CANNOT COMMAND. PROVISION FOR IDLE/ACQUISITION SEQUENCE. ALLOWS CONFIGURATION AND STANDARDS AND LIMITS TO BE CHANGED	CONFIGURATION, STANDARDS AND LIMITS, MODE CONTROL, RECALL	ALL STANDARDS AND LIMITS AND CONFIGURATION DATA PARAMETERS WILL TAKE IMMEDIATE EFFECT IN THIS MODE
IDLE 2	ALLOWS ENTRY INTO ACTIVE MODE. PROVIDES IDLE/ACQUISITION SEQUENCE DURING COMMAND PERIODS	RECALL AND MODE CONTROL DATA ONLY	MODE CONTROL DATA CONTAINED IN THE COMMAND ELEMENT BLOCK
ACTIVE	COMMAND TRANSMISSION	RECALL AND MODE CONTROL DATA ONLY	
ABORT	PROVIDES ABORT INSTRUCTION TO CMA	RECALL AND MODE CONTROL DATA ONLY	

NOTES: 1. COMMAND DATA MESSAGES WILL BE ACCEPTED IN ALL MODES
2. ALARM MESSAGES/ALARM DATA WILL BE TRANSMITTED TO THE MOC IN ALL MODES EXCEPT ABORT

Fig. 5. DSS Command Subsystem modes

Pioneer Venus Multiprobe Entry Telemetry Recovery

R. B. Miller
TDA Mission Support
and
R. Ramos
Ames Research Center

The Entry Phase of the Pioneer Venus Multiprobe Mission involved data transmission over only a two-hour span. The criticality of recovery of those two hours of data, coupled with the fact that there were no radio signals from the Probes until their arrival at Venus, dictated unique telemetry recovery approaches on the ground. The result was double redundancy, use of spectrum analyzers to aid in rapid acquisition of the signals, and development of a technique for recovery of telemetry data without the use of real-time coherent detection, which is normally employed by all other NASA planetary missions.

I. Introduction

Two aspects of the Pioneer Venus Multiprobe Mission dictated unique approaches to the telemetry recovery compared to other NASA planetary missions: the number of spacecraft that simultaneously transmitted data and the two-hour duration of one-chance prime data transmission. Since the four Probes entered the Venusian atmosphere essentially simultaneously, each of two large antenna ground stations that could view the entry had to be able to acquire the signal and recover the information content from four separate spacecraft simultaneously. Each Probe transmitted the data directly to Earth during the mission, which meant that only the data captured in "real-time" (i.e., as it actually happened) on Earth would ever be recovered.

The multiplicity of signals, although challenging operationally, was not a unique technological challenge since it merely required replicating the equipment ordinarily used for recovering telemetry data for deep space missions. See Refs. 1 and 2 for descriptions of the general problem of communications at interplanetary distances and the techniques used for NASA planetary missions. The ground equipment ordinarily used for telemetry recovery in a deep-space mission will be briefly described for completeness and to develop the framework to understand why a second method of telemetry recovery was felt to be necessary.

Fundamental to all deep space communications to date has been the process of coherent detection: first for the carrier, then the subcarrier, and finally bit synchronization. For the Pioneer Venus Multiprobe entry, a means was developed of producing a permanent record of the Probe signals as they reached the Earth without utilizing a coherent detection process. These recordings could be played after the fact many times (even backwards) into the equipment ordinarily used for telemetry recovery. In effect, the precious two hours of

Multiprobe entry data could be repeated over and over again until all useable data had been extracted from the signals that reached the Earth.

II. The Probes' Telecommunications Link

The telecommunications hardware on board the Probes consisted of the formatters, multiplexers, encoders, and modulators in the Data Handling Subsystem, and the oscillators, exciters, power amplifiers, and antennas in the Communications Subsystem necessary to format and transmit the telemetry on the downlink. In addition, the Large Probe had a receiver to receive a signal from the Earth for coherency reference.

The Data Handling Subsystem received analog and digital signals from the scientific experiments and from the rest of the spacecraft. It converted the analog signals to digital data, reformatted the digital signals, and multiplexed all these data into a nonreturn-to-zero-level (NRZ-L) data stream. The data were then convolutionally encoded, and were used to phase modulate a square wave subcarrier, which was then sent to the exciter in the Communications Subsystem. The frequency of the Large Probe subcarrier was 8192 Hz and that of the Small Probe subcarrier was 4096 Hz.

A block diagram of the Small Probe Communications Subsystem is shown in Fig. 1. The stable oscillator generated a signal whose frequency was approximately 19 MHz. The value was slightly different for each one of the Probes. This frequency was then multiplied by 110.5 times in the exciter to provide a carrier signal at *S*-band. The assigned frequencies of the transmitted signals are shown in Table 1.

The exciter used the subcarrier from the Data Handling Subsystem to modulate the *S*-band carrier at either 0.78 or 1.02 rad. This signal was then amplified by the driver amplifier/power amplifier to a value of 10 W and transmitted by a crossed dipole antenna. The antenna provided hemispherical coverage with a gain of 0 to 2 dB at the expected communications angles.

There was a requirement for the *S*-band signal to maintain its frequency stability to within $\pm 1 \times 10^{-9}$ from a calibration curve to provide a stable frequency standard for the Differential Long Baseline Interferometry (DLBI) Experiment.

A block diagram of the Large Probe Communications Subsystem is shown in Fig. 2. The only difference in the transmitting function between the Large Probe and the Small Probe is that the Large Probe generated 40 W of power by the combination of power amplifiers shown in the block diagram.

The difference in the carrier frequency generation is that the Large Probe, in addition to having the capability of generating the reference frequency by its internal auxiliary oscillator, also had the capability of receiving a signal from the ground (uplink signal) and using that signal as the reference for the downlink signal. This mode of operation is known as the coherent mode. The switch to the coherent mode was automatic anytime that the receiver was locked on the uplink signal. The modulation index used in the Large Probe was 1.18 rad.

Because the electrical power was supplied by batteries, and was therefore limited, the Probes were not turned on until 22 min before their entry into the Venus atmosphere. The Deep Space Network (DSN) stations were faced with the requirement to receive these four extremely weak signals plus the signal from the Multiprobe Bus simultaneously and extract telemetry from them during the 1.5 to 2 h of operation.

The total power received at the input of the low noise amplifier at the DSN stations was approximately 5×10^{-19} to 1.6×10^{-18} W.

III. Real-Time Coherent Detection Telemetry Recovery

The telemetry recovery portion of the configurations used at the deep space stations is shown at a gross level in Fig. 3. An additional receiver and recording that formed a part of the DLBI wind measurement experiment is also shown. The first step in recovery is to capture as much of the energy reaching the Earth as practical, and this is accomplished with 64-m diameter parabolic antennas. Two of the three tracking sites of NASA's DSN had Venus in view during the entry: Goldstone, CA, and Tidbinbilla, near Canberra, Australia. The first level of redundancy in data recovery was achieved by timing the entry event in the mutual view and equipping these two 64-m sites identically for the entry event. The moving portion of the 64-m antennas weigh 2.7×10^6 kg and are figured to an accuracy of 1 mm (rms of surface area). This 0.85-acre surface provides an effective gain at *S*-band of 61.7 dB, which is a factor of 1.5×10^6. The feed system is Cassegrainian and focuses the captured power into a low noise amplifier system located above the antenna surface. It is the signal-to-noise ratio rather than absolute signal strength that matters in communications systems. It is not possible to do anything about the external sources of noise (e.g., intergalactic, tropospheric, natural radio sources, etc.) which reach the ground antenna and undergo the same gain as the wanted signal. The critical element in achieving a useable signal-to-noise ratio is the first amplification after the antenna system. Noise is usually expressed in

terms of the noise temperature in kelvin, and the total system noise temperature of the antenna and first amplifier system is the key figure of merit. The first amplifier used by the DSN at *S*-band is a cryogenically cooled ruby maser which adds less than 3 K to the noise temperature. The resulting total system noise temperature figure is only 22 K. The maser is a broad-band device which passes all *S*-band frequencies of interest and does not have to be tuned for any particular mission.

The next step in real-time telemetry recovery is coherent phase detection and tracking of the carrier of a particular Probe. Such a phase coherent or "closed-loop" receiver must be tuned until the tuned frequency matches the received signal, then "lock" is achieved, and the closed-loop receiver will track, i.e., automatically follow, the detected carrier as the relative motion between the Probe and the Earth Doppler shifts the frequency of the signal. The locking process takes some amount of time and a skilled operator. After carrier lock is achieved, the rest of the ground system can operate at a fixed frequency (10 MHz) and fixed signal levels because of automatic gain control in the closed-loop receiver.

The next process is subcarrier detection, another closed-loop process, which takes a finite amount of time to acquire "lock." Subcarrier acquisition and tracking takes place without operator intervention because the subcarrier frequency is fully known *a priori* and has an essentially fixed relationship to the carrier frequency. The output of the subcarrier detection process is an integrated symbol stream. To estimate the value of individual symbols, first the bit timing has to be estimated, acquired, and then tracked. This is another closed-loop tracking process that has a finite acquisition time. Quantized symbol estimates are then passed to a telemetry processing minicomputer, which must first synchronize with the telemetry frames and then decode (in the Pioneer case, using the Fano algorithm) the data. The detected and decoded (essentially error-free) data are then formatted and recorded on a magnetic tape at the tracking station. The data are also transmitted in real-time over NASA ground communications circuits to Ames Research Center. In the case of the Probes, since the entire Probe sequence took place automatically, there was no real-time control role necessary at Ames, and the flow of data to Ames was, unlike the Pioneer Venus Orbiter mission, not critical to mission success.

IV. Special Equipment to Support Real-Time Telemetry Recovery

The above equipment was replicated four times, once for each Probe. The critical step of locking the receivers to the signals when they first appeared, and again after the large Doppler shift of atmospheric entry, was highly dependent on operator skill. Also, *a priori* uncertainties in the frequencies were very large. For all previous deep space missions, the spacecraft are tracked every day prior to arriving at the planet, and the stations become very familiar with each spacecraft's characteristics. For this mission, the radio transmissions turned on just 22 min before hitting the atmosphere of Venus. It was not until that time that the stations and the receiver operators saw the actual probe signals. To help this situation, a means of dynamically simulating all four probe signals simultaneously, realistic both in frequency and signal level, was designed and built in-house at JPL and provided to both stations. Test and training activities took place over the 10 months preceding the entry event. In addition, to help the acquisition process, three commercial FFT spectrum analyzers were provided to each station with a switching matrix to enable each operator at each analyzer to switch to monitor any of the output of the "open-loop" receivers described below. A microprocessor was added by JPL to the commercial spectrum analyzers to allow automatic calculation of frequencies at the proper levels to pass on to the closed-loop receiver operators. The microprocessors also provide an automatic search mode for the analyzers for the eventuality of a Probe signal not appearing where expected. A 50-kHz bandwidth was used on the spectrum analyzers in order to have enough signal-to-noise ratio per analyzer cell width to have a detectable signal. The search mode moved the 50-kHz bandwidth automatically across the 300-kHz bandwidth of the "open-loop" receiver.

V. Telemetry Recovery Without Coherent Detection

The real-time telemetry recovery equipment described above had well-understood performance that could be used in the Probe telecommunications design. However, real-time telemetry recovery would require a large amount of equipment to operate properly and would be highly dependent on operator skill to assure rapid lockup of the closed-loop receivers. It was recognized, when the Multiprobe mission was in the conceptual design stage, that dependence of the mission data recovery solely on the above real-time telemetry recovery process would represent a very high risk to the mission. Based on discussions that took place in 1972, the Pioneer Venus Study Team asked DSN Engineering personnel if it might not be feasible to record the output of an open-loop receiver (a receiver set to a fixed frequency that passes everything present in a certain bandwidth), which would later be played back for telemetry recovery. In May 1973, the Study Team was informed that a precarrier detection recording did look like a feasible technology. By November 1973, based on breadboard testing, the DSN was confident enough in the approach to

commit a performance level not to exceed 1.5-dB loss compared to the real-time telemetry recovery system. This additional loss then became a part of the mission's telecommunications design. The basic plan was then settled: enough equipment would be implemented to attempt real-time recovery for all four probes, and work would continue to engineer a means of recording the Probe signals without coherent carrier detection. The open-loop telemetry recovery configuration is also shown in Fig. 1 and involved four open-loop receivers, one per Probe. The 300-kHz bandpass of each of these receivers encompassed all uncertainties, doppler, and useable harmonics of an individual Probe. The 300-kHz bandpass could be set a fixed frequency for each Probe in advance of the encounter, and the only operator action required in real time was starting the recorder and changing the tape. Each 300-kHz band was recorded on separate tracks of redundant recorders with staggered tape changes. The entry involved a total of ten receivers at each station, including the 2-MHz bandpass DLBI receiver and a contingency closed-loop receiver.

The first approach for precarrier detection recording used by DSN Engineering at JPL was to construct in-house a digital time jitter compensator to work on the output of rather antiquated analog recorders that were already in the DSN inventory. This involved recording a reference signal on one track of the analog recorder along with the spacecraft signals on separate tracks. The tape would be played back through the time jitter compensator which analog-to-digital converted a Probe signal track and the reference track, digitally servoed the Probe channel to the reference signal, and then digital-to-analog converted. This technique reduced playback phase jitter from the region of 50 to 100-deg rms to less than 1-deg rms. The output analog signal was then upconverted back to *S*-band and inserted in front of the coherent closed-loop telemetry recovery equipment. The in-house time jitter compensator and up converter were used for the early feasibility demonstration and performance determination. With time, it became apparent that the commercial analog recording technology (involving the same kind of compensation internally) was maturing. Tests of new commercial recorders were performed that proved equal to or better than the in-house compensator used with an older commercial recorder. By March 1977, a particular commercial recorder without external compensation was selected as the final approach in concert with a JPL upconverter. Performance tests of the precarrier detection recording were now consistently getting results with less than 1-dB degradation. Although the probe entry tracking stations were provided with the necessary upconverters and interface equipment to playback the recordings for test purposes, the actual playback for the mission data would take place on DSN equipment located at JPL in Pasadena, California.

VI. Reverse Playback

The precarrier detection recording committed to the Pioneer Venus Multiprobe mission had now assured that the entry event could be "replayed" after the fact to recover any data lost in real time due to equipment failure, operator error, or frequency uncertainties. Since the playback still involved the sequential acquisition of carrier, subcarrier, symbol stream, and decoder, there would still be a data loss, even with all time and frequency uncertainties removed *a posteriori*, every time the Probe signal became too weak (entry blackout, atmospheric fading, or turbulence) and during planned bit rate changes. As the precarrier detection work unfolded, the Project inquired of the DSN whether the analog recording could be played in the reverse direction. This would enable going beyond any out-of-lock condition and proceeding in the reverse direction so that the serial lockup time of the ground equipment would occur where data had already been recovered in the forward direction. The telemetry could then be recovered in the reverse direction, right up to the time of the event that forced the out-of-lock condition. After cursory study of feasibility by DSN Engineering, reverse-playback tests were performed at JPL, and negligible additional loss was measured. In 1977, the reverse-playback became part of the mission recovery plan with the DSN producing special software to digitally record the reverse symbol estimates out of the DSN equipment, and the Project taking the responsibility for decoding the reverse-playback tapes. The reverse-playback symbol decoding was performed at Ames Research Center. The technique employed was to buffer the backward frames and use the conventional forward decoding algorithm once a whole frame was collected. The software also allowed for recovery of the raw, uncorrected data for frames that could not be successfully decoded.

VII. Results

On December 9, 1979, the sum of the Australian and Goldstone tracking stations' efforts recovered in real time an average of over 85 percent of all the data transmitted by the four probes. The combination of forward and backward playback of the precarrier detection recordings raised the recovery to essentially 100 percent of all useable data.

Note

This article originally appeared in a special Pioneer Venus Spacecraft Instrumentation issue of the *IEEE Transactions on Geoscience and Remote Sensing*, Vol. GE-18, No. 1, January 1980.

Acknowledgment

A large number of DSN personnel were involved in the work described here and in the companion DLBI work described in J. Smith's article in this issue. The caliber of their work and its importance to the Mission were recognized in two NASA group achievement awards: a Pioneer Venus Multiple Data Acquisition Implementation Team award, which recognized the key personnel involved in the engineering, construction, installation, and performance verification of the systems involved, and a Pioneer Venus Ground Data System Team award, which recognized the key personnel of the DSN Operations and the deep space tracking stations, as well as the support of the DLBI experiment by Goddard Space Flight Center personnel and stations.

References

1. M. F. Easterline, "From 8-1/3 bits/s to 100,000 bits/s in ten years," *IEEE Commun. Soc. Magazine*, Nov. 1977. (Also see related companion articles in the same issue.)
2. R. E. Edelson, *et al.*, "Voyager telecommunications: The broadcasts from Jupiter," *Science*, June 1, 1979.

Table 1. Probe frequency assignments

Spacecraft	Uplink, MHz	Downlink, MHz
Large Probe	2110.317247	2291.747237
SP1	–	2292.281357
SP2	–	2292.437317
SP3	–	2291.394837

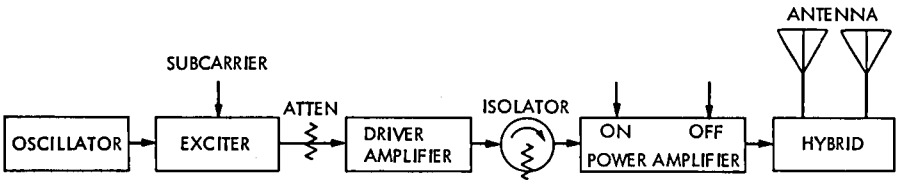

Fig. 1. Small Probe Communications Subsystem

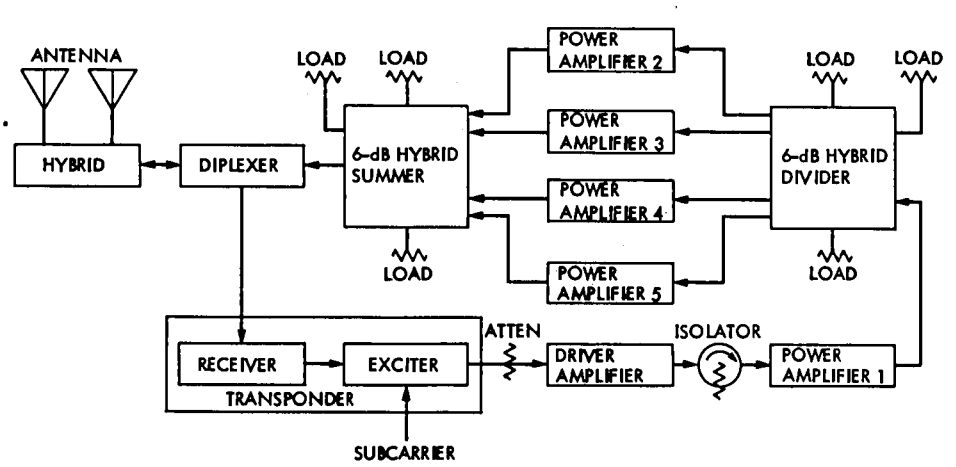

Fig. 2. Large Probe Communications Subsystem

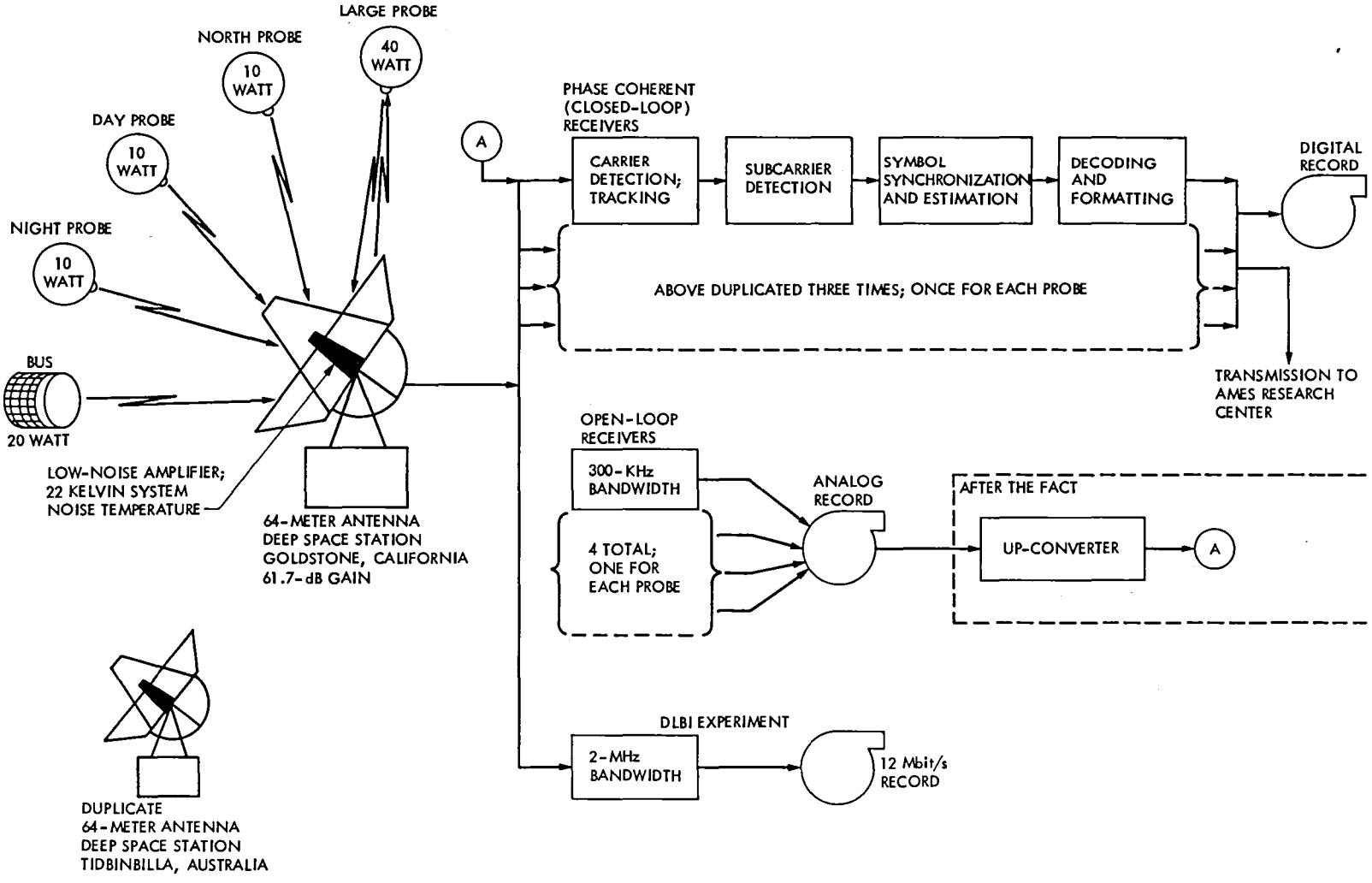

Fig. 3. Pioneer Venus Multiprobe entry data recovery configuration at the Deep Space Stations

Voyager Mission Support

N. Fanelli and H. Nance
Deep Space Network Operations Section

This is a continuation of the Deep Space Network report on Tracking and Data Acquisition for Project Voyager. This article covers the period for February through April 1980.

I. Introduction

Both Voyager 1 and 2 have continued on the Jupiter-Saturn cruise phase of the mission. In addition to the normal cruise activities, Voyager 1 has performed some preliminary maneuver and imaging activities in preparation for the Saturn encounter.

II. DSN Support

The engineering and science activities continued with both Voyager spacecraft on the predetermined requirement sequence. Some representative tests and the number of times each was supported by the DSSs during the reporting period are given in Table 1.

In addition to the routine test/calibration activities, some special events were participated in by the stations.

(1) On 20 and 21 February, a cruise science maneuver was performed by Voyager 1. The maneuver went well and the spacecraft reacquired after the antenna came back to Earth point.

(2) The scan platform was calibrated and on 20 March and 22 April, Saturn exposures were made and received.

(3) On 31 March, a stellar reference activity was performed. On 2 April, the Canopus star tracker sensitivity was checked and on 3 April, a Titan Moveable Block Capability Demonstration Test was conducted.

(4) During the period, there were six navigation cycles completed with Delta differential one-way ranging (Delta DOR) activities occurring twice during each navigation cycle. The Delta DOR activity was conducted by the 64-meter stations during mutual view periods. During the time DSS 14 was down, DSS 13 provided the Delta DOR support.

(5) During the period 4-11 March, real-time combiner (RTC) and arraying training and operations indoctrination were conducted at Goldstone. Representatives from DSS 43 and 63 attended and returned to their stations to prepare for the training and support at the conjoint facilities. The training period included classroom training, hands-on training, and actual support of three scheduled array passes. Applicable operations procedures were evaluated and updated as required.

(6) During the month of March, the X-band drivers were turned off on Voyager 1 three different times for a total of 148 hours, 42 minutes. During these times, only S-band telemetry was received and processed by the stations.

III. DSS Status

A. DSS 61

The implementation of the S/X-band capability and upgrade of DSS 61 from a 26-meter-diameter antenna to a 34-meter-diameter antenna was completed on 1 March 1980. The subsystem testing was completed at the same time and System Performance Tests (SPTs) started the following day. The SPTs were essentially completed on 12 March. These tests were divided into two phases, one with antenna operation and one without antenna operation. This was necessary because previous inspection had determined that repair was required on the antenna gear boxes prior to returning the station to an operational status. This gear box repair work was accomplished during the SPT time frame, restricting antenna operation during that repair function.

The Network Operation Project Engineer (NOPE) for Voyager conducted Operational Verification Tests (OVTs) following the SPTs as the final testing step in returning the station to an operational status. The OVTs were structured so as to meet the verification requirements for all projects. These tests were conducted long-loop with telemetry data being generated by NOCA SIM and/or MCCC SIM and transmitted to the station for standard processing. This mode of testing not only verified the normal station processing equipment, but the Simulation Conversion Assembly (SCA) in preparation for future encounter Ground Data System (GDS) testing. Each station operational crew supported two OVTs so that a training requirement was likewise completed.

At the conclusion of the OVT testing, demonstration tracking passes were scheduled for all projects to validate actual spacecraft data processing. The demonstration passes were completed on 1 April 1980 and the station declared operational for Project support on 2 April 1980.

B. DSS 42

The implementation of the S/X-band capability and upgrade of DSS 42 from a 26-meter-diameter antenna to a 34-meter-diameter antenna was completed on 28 March 1980. The subsystem testing was completed at the same time and the SPTs started the following day. The SPTs progressed on schedule and were completed on 15 April. The OVTs were started on 16 April and completed on 24 April. Demonstration tracks followed the OVTs.

The same philosophy was followed at DSS 42 for verification of operations as was followed for DSS 61. Under this testing and training philosophy the maximum return is realized from the utilization of the station resources and results in the highest degree of confidence as to the station's operational capability.

C. DSS 14

DSS 14 was removed from operational status on 14 March 1980 for an estimated 60-day period. During this time period the antenna subreflector was to be replaced, the antenna panels realigned and a controller installed. It has been found that the time necessary for panel realignment was overestimated and that the station will become operational on 9 May. The work was completed on 30 April. During the period 4-8 May, SPTs will be conducted at the station and an OVT will be performed on 8 May 1980. The first scheduled tracking passes after the OVT will be considered demonstration tracks for final station validation.

D. DSS 62

DSS 62 was removed from operational status on 17 April for an estimated 25-day period. During this time period the antenna gear boxes will be inspected and repaired as required. This work is the same as was acomplished at DSS 61 during the 34-meter upgrade activity. The station will be returned to operational status on 12 May 1980.

During the time that DSS 61 was undergoing conversion, the Programmed Oscillator Control Assembly (POCA) was removed from DSS 61 and installed at DSS 62. This gave DSS 62 the capability of uplinking with Voyager 2. The POCA was removed from DSS 62 and reinstalled at DSS 61 on 21 March as part of the 34-meter capability.

E. DSS 44

During the DSS 42 conversion, the POCA was likewise removed from the station and installed at DSS 44. This provided the 26-meter station uplink capability for Voyager 2 and, like the DSS 62 operation, relieved some of the load on the 64-meter net. The POCA was reinstalled at DSS 42 on 9 April 1980.

IV. Software

During this reporting period several new software packages providing the required capabilities for the Saturn encounters were tested and accepted for operation at the Deep Space Stations. Companion packages for the Network Data Processing Terminals were also tested and accepted for operation at JPL in Pasadena.

(1) Antenna Pointing Subsystem (APS). New software has completed probationary testing and is awaiting anomaly resolution.

(2) Communication Monitor and Formatter (CMF). Major upgrade completed and now in operational use.

(3) Command (CMD). Completed probationary and Ground Data System testing and now scheduled for operational use.

(4) Metric Data Assembly (MDA). Major anomalies encountered and software package returned for correction and incorporation with capabilities of the next version. New release date established.

(5) Meteorological Monitor Assembly (MMA). Tested and in operational use. Provides interface with MDA for Very Long Baseline Interferometer (VLBI) support.

(6) Occultation Data Assembly (ODA). Tested and in operational use for VLBI and other baseline data recording.

(7) Planetary Ranging Assembly (PRA). Tested and in operational certification cycle.

Table 1. Type and number of activities support for both Voyager spacecraft, February–April 1980

Test/Calibration	Number supported
Ultrastable oscillator	16
Tracking loop capacitor	11
Ultraviolet spectrometer sun col	2
Ultraviolet spectrometer star col	7
Imaging science subsystem calibration lamps	1
Plasma subsystem/magnetometer	7
Command detector unit/signal-to-noise ratio	10
Scan hysteresis	2
Scan platform cal	1
Periodic engineering and science cal	10
Plasma wave subsystem	2
Radio frequency subsystem/auto gain control	5
High gain antenna and sensor cal	5
Magnetometer boom alignment	1
Infrared interferometer spectrometer flash off heater sequence	9
Flash off heater sequence	7
Canopus star tracker sensitivity	1

International Solar Polar Mission Support

R. B. Miller
TDA Mission Support Office

This article provides an introduction to the International Solar Polar Mission, which is now scheduled for a late March to early May 1985 launch.

I. Introduction

The International Solar Polar Mission (ISPM) is a joint project between the European Space Agency (ESA) and the National Aeronautics and Space Administration (NASA). The primary objective of the mission is to investigate solar and interplanetary phenomena as a function of the solar latitude. The mission is to be accomplished by using a gravity assist at the planet Jupiter to send two spacecraft out of the ecliptic plane. One spacecraft will be built by ESA and the other will be NASA's responsibility. Both spacecraft will carry complementary science and include experiments from both the United States and Europe. NASA is also responsible for providing the launch vehicle in addition to the tracking and data acquisition support for the mission.

ISPM will be only the second interplanetary mission since Pioneer Venus in 1978 and will follow the launch of the Galileo spacecraft by one year. Current plans call for two shuttle launches using a three-stage inertial upper stage (IUS) separated by at least 20 days between March 27 and May 5 of 1985.

II. Trajectory

Trajectory information at the time of writing was very preliminary because of the recent two-year delay in the mission. The actual spread of launch dates, Jupiter encounter, and high heliographic latitude phases were not known at the time of writing.

The mission trajectory is portrayed schematically in Fig. 1 which is an oblique view of the ecliptic plane. Following the launch and early midcourses, both spacecraft would enter the Earth-to-Jupiter cruise phase of the mission. It is a secondary mission objective to gather continuous fields and particles and daily coronagraph data while in transit to Jupiter. The Jupiter encounter will be in June or July of 1986 depending upon the launch date and available energy. One spacecraft will be targeted over the north pole of Jupiter to throw it out of the ecliptic plane in the southern direction, while the other spacecraft will be targeted over the south pole of Jupiter to be thrown into the northern hemisphere. Fields and particle measurements within the Jupiter environment are also a secondary mission objective. Targeting constraints in the basic mission plan call for the perihelion distance to be equal to or greater than one astronomical unit and for the time above heliographic latitudes greater than $|70|^\circ$ (absolute value) to be maximized. It is also required that during the high heliographic latitude phase of the mission, the heliocentric distance be equal to or less than two astronomical units. The first high heliographic latitude phase of the mission will extend over the last half of calendar 1988. The two spacecraft will then cross the ecliptic plane and reverse positions in a second high heliographic latitude phase of the mission, where the time above $|70|^\circ$ heliographic latitude will occur in the second and third quarters of calendar 1989. The end of the prime mission is defined as when both spacecraft have crossed to a latitude below $|70|^\circ$ for the second time which will occur in or near August of 1989.

The nature of the ISPM trajectories will place unique requirements on the Deep Space Network coverage. During the

high latitude phases of the mission, one of the spacecraft will be visible only in the southern hemisphere of the earth, while the other spacecraft will be visible only in the northern hemisphere. During brief periods of the missions at the highest latitude phases, the spacecraft will become circumpolar as viewed from the Deep Space Stations. (For example, the spacecraft in the southern hemisphere will reach a point where it never falls below the horizon in Australia.) The hour angle declination construction of the typical DSN 34-meter-diameter antenna will restrict antenna view periods to periods on the order of 12 hours; however, the azimuth-elevation 64-meter-diameter antennas could, in principle, track the spacecraft continuously except for periodically unwrapping its cables.

During the Earth-to-Jupiter phase of the mission, both spacecraft will have a southern declination which unfortunately results in very short view periods from Madrid and Goldstone.

III. Science Objectives

As previously mentioned, both spacecraft will carry a complement of European and U.S. experiments. NASA funds the U.S. experiments on the ESA spacecraft, and ESA funds the European experimenters on the NASA spacecraft. A list of the experiments on both spacecraft, the principal investigators and their affiliations follows:

ESA Spacecraft

ESA spacecraft	Principal investigator	Affiliation	Code
Magnetic Field	P. C. Hedgecock	Imperial College, London	HED
Solar Wind Plasma	S. J. Bame	LASL, Los Alamos	BAM
Solar Wind Ion Composition	G. Gloeckler	Univ. of Maryland	GLG
	G. Geiss	Univ. of Berne	
Low Energy Charged Particles	L. Lanzerotti	Bell Lab Murray Hill	LAN
Low Energy Ion Composition	E. Keppler	MPI, Lindau	KEP
Cosmic Ray and Solar Charged Particles	J. A. Simpson	Univ. of Chicago	SIM
Solar Flare X-Ray and Cosmic Gamma Bursts	K. Hurley M. Sommer	CESR, Toulouse MPI, Garching	HUS
Radio and Plasma Waves	R. G. Stone	NASA/GSFC	STO
Cosmic Dust	E. Gruen	MPI, Heidelberg	GRU

NASA Spacecraft

NASA spacecraft	Principal investigator	Affiliation	Code
White Light Coronagraph X-Ray XUV	R. M. MacQueen	High altitude	CXX
Solar Flare X-Ray and Cosmic Gamma-Ray	T. L. Cline	GSFC	SXR
Comprehensive Particle Analysis	E. C. Stone	Cal Tech	CPA
Solar Wind Experiment	H. Rosenbauer	Max Planck Institute, Germany	SWE
Magnetic Field Experiment	M. H. Acuna	GSFC	MAG
Radio Astronomy Experiment	R. G. Stone	GSFC	RAP
Neutral Gas Measurement	H. Rosenbauer	Max Planck Institute, Germany	GAS
Zodiacal Light Experiment	R. H. Giese	Ruhr-Univ., Bochum, Germany	ZLE
Radio Science	P. Esposito	JPL	RSI

An additional experiment under consideration is a gravity wave experiment. The acceptance of this experiment on the NASA mission is tied to the addition of an experimental X-band receive capability on the spacecraft and X-band transmission capability in the DSN. If this experiment is accepted, the principal investigator will be H. Wahlquist, of the Jet Propulsion Laboratory. An S-band experiment on the ESA portion of the mission has been proposed by Professor B. Bertotti of the Instituto di Fisica Teorica of the University of Pavia in Italy.

Descriptions of some of these experiments and, in particular, the radio science and gravity wave experiments will be provided in future articles on the ISPM mission.

IV. Key Spacecraft Characteristics

The individual ESA and NASA spacecraft will be described in more detail in future articles. The following will serve as a basic introduction to their key characteristics. Both spacecraft will be spin-stabilized and powered by a single radio isotope thermal electric generator (RTG). The NASA spacecraft will be on the order of 450 kilograms, while the ESA spacecraft will be on the order of 350 kilograms. Each spacecraft's principal communication link to the ground will be via a parabolic high-gain antenna which is rigidly mounted parallel to the spin axis of the spacecraft. Therefore, Earth pointing

will have to be maintained by periodic positioning of the spacecraft's spin axis as the apparent position of the Earth moves. The ESA high-gain antenna will be about 1.6 meters in diameter and located essentially on the spin axis. The NASA high-gain antenna will be 1.98 meters in diameter, located significantly offset from the spin axis in order to accommodate a coronagraph instrument. The coronagraph will be despun in order to maintain Sun pointing and will be located on the spin axis. S-band uplink for commanding and X-band downlink with telemetry will be the primary communication channels for both spacecraft. An S-band downlink will be provided on both spacecraft in order to provide for Tracking Data Relay Satellite System compatibility in the near-Earth phase. The S-band downlink will also be used to provide wider beam width antenna coverage during certain maneuvers and to support certain navigation and radio science requirements. The most common mode expected during the flight will be a "split coherency" mode where the downlink S-band is derived in the spacecraft phase coherent with the received uplink S-band signal while the X-band is noncoherently derived from an onboard oscillator. This split mode is in order to enable collection of extensive amounts of doppler data while not suffering the turnaround loss for the X-band telemetry performance. Both spacecraft will include ranging capability using S- and/or X-band downlink(s). Note that in DSN jargon, uplink refers to the radio transmission from the ground to the spacecraft while downlink indicates the spacecraft to ground.

As currently understood, the command, telemetry, and general telecommunications design of both spacecraft is compatible with the multimission capabilities of the Deep Space Network. Although at the detailed level, certain aspects of the ESA telemetry and command design violate the NASA Planetary Standards, the spacecraft is expected to be fully compatible with the Deep Space Network. This means that the only implementation required to support the ISPM will be a minor amount of software in order to initialize the DSN systems for the specific spacecraft identification numbers and telemetry formats. The only exception currently under study is the addition of an experimental X-band uplink capability as an engineering development exercise and in order to support the gravity wave experiment on the NASA spacecraft. The current plan would result in a Supporting Research and Technology X-band uplink capability from DSS 13 (the Goldstone R & D site) and an operational X-band uplink from DSS 42 (Australian 34-meter site).

The principal data rates for the life of the ESA mission will be 4,096 and 8,192 bits per second although a lower rate may be required for a few months around the maximum range portion of the mission. The data rates for the NASA mission are not yet determined, but they may extend from 2 to as high as 48 kilobits per second principally due to the higher rates required to support the images from the coronagraph. Continuous return of instrument measurements for the life of the mission is a requirement for both spacecraft. To meet this objective, the basic coverage requirement for the ISPM is an eight-hour 34-meter track per day per spacecraft. Each spacecraft will have a tape recorder in order to record the 16 hours of data during the nontracking period. It is clear that this coverage requirement cannot always be met because the ISPM lifetime extends through the Galileo Mars flyby, the Uranus encounter of Voyager, and the Jupiter orbital operational phase and probe entry of the Galileo Mission. In addition, eight other extended mission spacecraft are expected to still be alive during the mission and require coverage. The basic coverage problem and interaction with other mission support will also be a topic of future Progress Report articles.

V. The Two-Year Launch Delay

A short time before this article was written, the ISPM was officially delayed from a February 1983 launch to the 1985 Jupiter window. The reason for the delay was a major budget cut that NASA had to accommodate to help the President achieve the objective of a balanced FY81 U.S. budget. The 1985 opportunity is less favorable than 1983 from a trajectory performance standpoint, with an effect of about 40 kg less payload capability. For this reason, the basic plan for 1985 is a split (two-shuttle) launch whereas the basic 1983 plan was to launch both the ESA and NASA in a tandem single shuttle launch. To accommodate the two-year stretch out, the NASA strategy is to slow down the program and serialize some activities that would have been in parallel. The ESA side of the mission plans to stretch work out only one year and to store the completed spacecraft and instruments for one year.

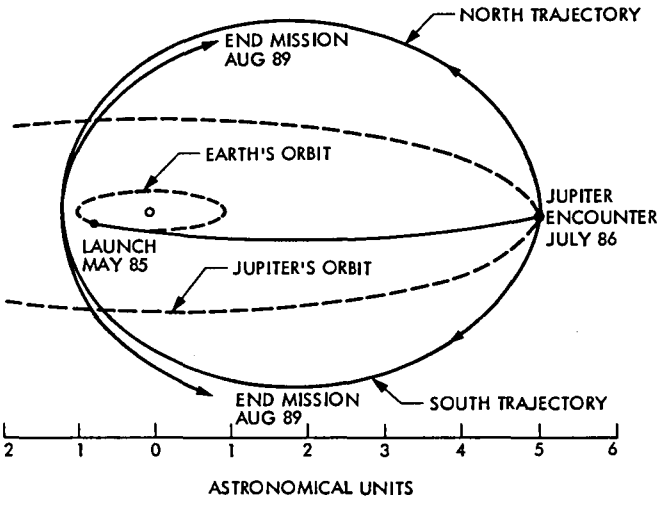

Fig. 1. Trajectory overview

Viking Orbiter Completion Mission and Viking Lander Monitor Mission

R. L. Gillette
Deep Space Network Operations Section

This report covers the period from 1 February 1980 through 31 March 1980 and continues reporting on DSN Viking Tracking Support for the same period.

I. Viking Operations

A. Mission Overview

The primary Viking Mission was terminated on 15 November 1976, at the time of solar conjunction, due to the loss of the communications link between Mars and Earth. At the end of the solar conjunction period the communications link was reestablished, and the Viking Extended Mission (VEM) commenced on 15 December 1976.

The objective of the Viking Extended Mission was to make use of the functioning spacecraft to observe seasonal variations on Mars, to provide long-duration sampling for experiments that require it, and to obtain data not possible during the primary mission because of time constraints and observational limitations. The VEM was terminated on 31 May 1978.

Since both Orbiters and Landers were still operational at the termination of the VEM, funding was approved for a Viking Continuation Mission (VCM). The objectives of the VCM were essentially the same as those of the extended mission, but with a shift of emphasis more towards the Orbiters than the Landers. The major goal was to complete one full Mars year of observation of the planet, including filling in the season that was obscured by solar occultation at the end of the primary mission, and also to make a start on determining the extent to which weather conditions repeat in succeeding years.

During the VCM both Landers were in the automatic mission mode, performing repetitive observations on 37 day cycles, so that no more than one command load was required for each Lander during the entire period. Data was acquired from Imaging, Meteorology and Seismology experiments. The Inorganic analysis experiment continued to provide data on its final surface samples, but no new samples were acquired.

Radio Science investigations, including the occultation experiment, the local gravity anomaly experiment and Lander ranging, continued; and in December 1978, and January and February 1979 (solar conjunction), the Solar Corona and Relativity experiments were repeated.

All three Viking Orbiter 1 (VO-1) science experiments continued during the VCM, but their observational sequences were simpler and more repetitious than previously.

From late March until July, 1978, the Viking Orbiter 2 (VO-2) mission was seriously hampered by gas leaks in both halves of the Attitude Control Reaction System. Except for a brief science sequence in June and a final one in July, VO-2 was confined to a gas-conserving housekeeping mode. The efforts to extend the VO-2 mission through the June/July sequences were dictated by the strong desire of the Viking Science Team to acquire specific visual imaging subsystem and infrared coverage at those times. The efforts were rewarded in that adequate coverage was obtained in the June/July sequences to satisfy the data closure needs of the scientists. On 25 July 1978, approximately four days into the final VO-2 science sequence, the attitude control gas was depleted and VO-2 began to drift off sun line. After a short sequence to establish the final engineering status of the vehicle, the ground command was issued to turn the VO-2 transmitters off, ending the VO-2 mission.

Lander automatic sequences for the VCM were designed to consign all science data playbacks to relay links because of the higher data rates achievable and, therefore, the more efficient utilization of station playback time. The initial sequences included periodic playbacks to both VO-1 and VO-2 for both landers. Owing to the onset of VO-2 gas leakage problems and the consequent uncertainty as to the future status of VO-2, the sequences were redesigned to purge them of all VO-2 relays. With only VO-1 as a relay, playbacks were limited to 25 to 30 day centers for each lander, with a consequent reduction in the total amount of science data which could be returned from each lander.

Finally, an earlier-than-planned termination of the Viking Lander 2 (VL-2) seismology experiment was necessitated by the failure of the VL-2 data storage memory (DSM), required for the effective accumulation and storage of the seismology data.

Even with operational deficiencies of the sort cited, the VCM was an active and productive period for the several orbiter and lander science experiments carried into the VCM. The Viking Continuation Mission concluded on 25 March 1979.

The fourth phase of the Viking Mission, known as the Viking Survey Mission (VSM), began on 25 March 1979. The objectives of the VSM were to acquire high-resolution contiguous coverage with the Visual Imaging Subsystem of a region on the planet that is likely to contain the landing sites for the next Mars mission. The Lander Mission objectives were to take advantage of the unique capability of a transponder on a planetary surface to make frequent radio ranging measurements and to conduct a long-duration monitoring of weather conditions and surface changes at the Lander 1 site. The Viking Survey Mission terminated on 31 October 1979.

At the end of the VSM there was still approximately 0.454 kilograms of attitude control gas remaining in the orbiter. In response to urgent requests by some of the Viking scientists, NASA Headquarters allocated some FY-80 funds to extend Orbiter operations through June 1980. This final phase of Viking Orbiter operations has been designated the Viking Orbiter Completion Mission (VOCM).

Because of the capability of the Viking Lander 1 to continue operating long after the termination of the Orbiter, the Lander Mission has been separated from the Orbiter Mission and as of 1 November 1979, has been designated the Lander Monitor Mission (LMM). The Viking Lander 1 spacecraft should be capable of returning Mars data through 1990.

Due to the failure of the direct link transmitters on Lander 2, data collection from Lander 2 will cease after the termination of the Orbiter Mission.

B. Spacecraft Status

1. **Orbiter.** During this reporting period, the Orbiter 1 spacecraft continued to operate normally, collecting and returning weather data and moderate resolution Mars surface photos to Earth, as well as relaying data from the Lander-2 (VL-2) spacecraft.

As of 3 March, the remaining attitude control gas has been estimated at approximately 0.272 kilograms plus or minus 0.09 kilograms. With a daily usage of 0.0027 kg and with the uncertainties of the gas supply, the orbiter termination could occur anywhere from May to September 1980.

2. **Landers.** The Viking Landers continued to operate as expected during this reporting period. All Lander-1 essential subsystems are healthy as the spacecraft collects imaging and meteorology data for weekly transmission to Earth, whenever a Deep Space Station (DSS) is available. All Lander 2 essential subsystems are healthy, except for the transmitter. This transmitter, which supports transmission of telemetry data directly to Earth and the Data Storage Memory (DSM) unit, intermittently causes loss of data.

The DSM problem is believed to be a thermal problem related to the high temperatures during the Martian summer.

All data from Lander-2 are transmitted to Orbiter-1 and then relayed to Earth using the Orbiter transmitter.

II. Radio Science

Radio Science activity increased in March as the Project continued with the occultation experiments. These experiments were reimplemented in November and December 1979, after the start of the Viking Orbiter Completion Mission. Geometrically, the spacecraft (as viewed from Earth) is occulted by Mars every 24 hours for about 23 minutes. Acquisition of data from occultations will provide new information on seasonal atmospheric fluctuations at the 5 km level, the correlation of ionosphere plasma temperature with solar activity and improved characterization of several Martian topographic features.

III. Network Support

Table 1 shows the DSN tracking support from August 1979 through March 1980.

In January the Orbiter science instruments were shut down and the spacecraft configured to the low-gain antenna due to the lack of a sufficiently bright star to maintain high-gain antenna pointing. DSN tracking support returned to normal in February and March after the spacecraft was configured back to the high-gain antenna.

Table 1. DSN Viking Mission tracking support

DSS	1979 – 1980							
	Aug	Sept	Oct	Nov	Dec	Jan	Feb	Mar
11	*a* – *b*	1 6	1 3	2 11	–	2 15	3 15	3 21
12	–	–	–	–	–	–	–	3 15
14	22 91	15 65	12 62	8 64	6 52	2	7 49	–
42	1 5	2 10	–	–	–	–	–	–
43	1 5	1 1	1 6	–	2 13	2 8	1 8	2 17
44	4 18	–	3 12	–	–	–	–	1 5
61	–	–	–	–	–	–	–	1 11
62	2 2	1 4	–	–	–	6 41	3 20	2 10
63	29 131	27 105	19 104	15 119	16 142	2 14	11 101	17 158
Total	59 252	47 191	36 187	25 194	24 207	14 78	25 193	29 237

[a]Total number of Viking tracks.

[b]Total Viking station support in hours.

A Theoretical Model of Phase Changes of a Klystron Due to Variation of Operating Parameters

A. Kupiszewski
Radio Frequency and Microwave Subsystems Section

A mathematical model for phase changes of the VA-876 CW klystron amplifier output is presented and variations of several operating parameters are considered. The theoretical approach to the problem is based upon a "gridded-gap" modeling with inclusion of a second-order correction term so that actual gap geometry is reflected in the formulation. Physical measurements are contrasted to theoretical calculations.

I. Introduction

Phase stability of klystron amplifier output in the regime of 10^{-14} to 10^{-16} $\sigma\Delta f/f$ in one hour is currently a growing concern. Interest in the subject is sparked by recent proposals to use uplink signals for the detection of gravity waves. Changes in amplifier operating parameters are strongly reflected in changes in electrical path length in microwave tubes and consequently in output phase changes. A much greater understanding of the physical processes causing phase changes is necessary if phase stability requirements for detecting gravity waves are to be met.

As a result of such interest, an experimental study program on a VA-876 X-band five-cavity CW klystron amplifier was carried out at Goldstone (Ref. 1). Operating parameter changes were initiated and output phase difference measurements obtained. Included in the program were the pushing factor, heater current changes, drive level variation near saturation, changes in magnet current, and variation in inlet coolant temperature. Theoretical modeling for certain of the aforementioned factors was also initiated so that a comparison between calculation and measurement could be made.

A "gridded-gap" approach was employed to calculate the total drift length including both the gaps and the drift spaces where most of the bunching takes place. Higher-order terms were considered and a second-order time averaged correction was included. Actual physical gap geometry is taken into account in this higher-order term through the beam coupling factor, μ. For the sake of simplicity, one may consider at first the formalism for a two-cavity tube, but subsequent summation yields results for multicavity amplifiers and hence results for more than two cavities will be presented.

II. Theoretical Analysis

Starting with conservation of energy and taking the limit of a small ratio of acceleration caused by RF modulation in the

klystron gaps to the initial electrostatic acceleration (Ref. 2), one obtains the following after-time averaging:

$$\Delta\phi = \sum_{i=1}^{\kappa}\left(\frac{\omega l_i}{V_0}\sqrt{1-(V_0/c)^2} + \frac{3}{16}\sum_{j=1}^{i}\frac{\mu_j^2 V_j^2}{(V_0')^2}\right) \quad (1)$$

where:

- ω is the frequency in radians
- $\Delta\phi$ is the phase difference between output and input
- l_i is the length of the i^{th} driftspace
- c is the velocity of light in free space
- V_0 is the initial velocity due to electrostatic acceleration
- κ is the number of gaps
- V_0' is the initial accelerating voltage
- V_j is the voltage of the RF field in the j^{th} gap
- μ_j is the beam coupling coefficient in the j^{th} gap

The parameter μ_j is given by (Refs. 3 and 4)

$$\mu_j = \frac{2 I_1(\gamma_e b)\left|\int_{-\infty}^{\infty} f_j(z)\exp(i\beta_e z)\,dz\right|}{\gamma_e b\, I_0(\gamma_e a)\, d_j\sqrt{1-\frac{V_0^2}{c^2}}} \quad (2)$$

where:

- d_j is the length of the j^{th} gap
- b is the electron beam radius
- a is the guiding tunnel radius
- I_1, I_0 are modified Bessel functions

$$\gamma_e^2 = \beta_e^2 - \beta_0^2 \quad (3)$$

$$\beta_e = \omega/V_0 \quad (4)$$

- β_0 is the wavenumber

The electric field envelope function, $f_j(z)$, in the j^{th} gap, is defined as

$$f_j(Z) = \begin{cases} 1 \\ \left(1-\left(\frac{2Z}{d_j}\right)^2\right)^{-1/2} \\ \cosh m_j z \\ 0, \text{ outside the gap} \end{cases} \quad (5)$$

where $f_j(z) = 1$ is chosen if the tunnel mouth ends that open onto the j^{th} gap are blunt or rounded as in the VA-876 klystron;

$$f(Z) = \left(1-\left(\frac{2z}{d_j}\right)^2\right)^{-1/2}$$

is chosen if the ends are knifelike in profile; $f(z) = \cosh m_j z$ is chosen if the tunnel mouth ends conform to neither of the previous two extremes. The field parameter m_j is somewhat arbitrarily picked to best approximate the fields in the j^{th} gap.

To calculate phase changes due to variations in operating parameters, $\Delta\phi$ may be computed under normal circumstances and then again for the parameter change under investigation. Subtraction yields the desired result, i.e.,

$$\langle\Delta\phi\rangle_{\Delta\text{ parameter}} = \langle\Delta\phi\rangle_{\text{change}} - \langle\Delta\phi\rangle_{\text{normal}} \quad (6)$$

Accelerating voltage changes result in a different initial beam velocity. Magnet current drifts cause variation in both beam diameter and effective initial beam velocity (adiabatic invariants are responsible). A difference in the coolant inlet temperature changes the drift lengths and gap geometry dimensions due to thermal expansion and contraction. All of these effects can be reflected as corrections to formulae (1) through (5), and the results for the VA-876 klystron are compared with experimental results (Ref. 1) in Table 1. In the magnet current case, it was assumed that a little more than 99 percent of the beam energy was initially parallel to the axial Brillouin field. The expansion coefficient used was 0.07 percent/°C (Ref. 5).

III. Conclusion

The agreement between theory and experiment is fairly good, especially considering the number of approximations made in obtaining the hybrid gridded-gap-tunnel-geometry model. Further work on the phase lag effects of drive level changes near saturation is in progress and will be reported at a later time.

References

1. Kolbly, R. B., "Evaluation of the VA-876P Klystron for the 20-KW X-band Transmitter," *Deep Space Network Progress Report 42-54*, pp. 41-50, Jet Propulsion Laboratory, Pasadena, Calif., Dec. 1979.

2. Hamilton, D., Knipp, J., Kuper, J., *Klystrons & Microwave Triodes*, Dover, 1966, p. 201.

3. Branch, G. M., "Electron Beam Coupling in Interaction Gaps of Cylindrical Symmetry," *IRE Trans-ED-8*, May 1961.

4. Kosmahl, H. G., and Branch, G. M., "Generalized Representation of Electric Field in Interaction Gaps of Klystrons and Traveling Wave Tubes," *IEEE ED-20*, June 1973, p. 621.

5. Goldsmith, A., Waterman, T. E., Hirschhorn, H. J., *Handbook of Thermophysical Properties of Solid Materials*, Vol I Elements, Macmillan Co., N.Y., 1961.

Table I. Phase factor magnitudes

Parameter	Calculated factor	Measured factor
Accelerating voltage, deg/V	+0.048[a]	+0.04
Magnet current, deg/A	−1.04[b]	−1.0
Inlet coolant temperature, deg/°C	−1.19	−1.3

[a] + Sign implies a reduction in phase lag
[b] − Sign implies an increase in phase lag

64-Meter Antenna Operation at K_A-Band

P. D. Potter
Radio Frequency and Microwave Subsystems Section

As a part of a FY-80 study of the future potential of the 32-GHz K_A-band frequency region to planetary exploration, this article addresses the expected performance of the 64-m antenna network at 32 GHz. A modest level of noninterference upgrade work is assumed to achieve reasonable antenna aperture efficiency and alleviate antenna pointing difficulties. As a final item, electronic compensation of antenna aperture phasing errors is briefly considered as an alternative to the physical upgrade.

I. Introduction

Communications is clearly a vital factor in the planetary exploration program. As a dramatic example of improvements made during the last 20 years, the 1959 Pioneer IV Lunar probe with its 0.27-W transmitter could have transmitted from a distance of one AU at a data rate of only 0.00025 bit/s to the then existing 26-m ground antenna; whereas on March 5, 1979, Voyager I transmitted from a distance of 4.5 AU (Jupiter) at a rate of 115,200 bit/s to a 64-m ground antenna. This spectacular improvement of 100 dB represents an overall average of 5 dB per year. In addition to the larger ground antenna aperture (7.9 dB), a higher frequency (8.5 GHz as opposed to 0.96 GHz) and a larger spacecraft antenna combined to provide a spacecraft antenna gain improvement of 45.6 dB. Other major improvements were made in transmitted power, receiving system effective noise temperature, and information coding efficiency. Major future improvements in these last three areas are unlikely, since rather basic limitations have been approached.

Looking to the future, it appears that the most fruitful areas for link capability improvement lie in the increase of ground antenna aperture and spacecraft antenna gain. Present plans call for enhancement of ground aperture by the arraying of existing antenna equipments. Further ground improvement by construction of additional aperture area, however, is expensive and does not presently appear probable. Enhancement of the spacecraft antenna gain by use of large unfurlable antennas is technically feasible; however, this approach is associated with severe spacecraft configuration constraints, weight penalty, and mission reliability questions. A more practical approach is to increase spacecraft antenna gain by use of a higher frequency.

In 1969, JPL performed a general study of possible frequency bands for future deep-space-to-Earth data links (Ref. 1). Four frequency bands were studied in detail: 8.5 GHz (3.5-cm wavelength), 90 GHz (3.3-mm wavelength), 10 μm (coherent carbon dioxide laser system), and a 0.87-μm gallium arsenide "photon bucket" laser system. This study was unique in that, by definition, all four systems had exactly equal link performances; with this technique, the relative attractiveness of each system was clearly displayed. A highly-visible output of the JPL study was that, compared with the

microwave region, the infrared and optical (laser) frequency region is not attractive for a deep-space-to-Earth communications link. This conclusion, still valid in 1980, derives from basic considerations of high noise level, poor daytime performance, severe logistics problems (site selection), total weather dependency, severe spacecraft pointing problems, and poor hardware component technology.

The K_A-band and (32-GHz) frequency region has become increasingly attractive recently by virtue of a number of technical advances: the proven reliability and high efficiency of the 64-m antenna network at 8.5 GHz, demonstration of K-band low noise maser receiver designs (Ref. 2), demonstration of the low surface error Voyager spacecraft antenna, and availability of suitable K_A-band travelling wave tube spacecraft transmitter devices. Finally, this frequency band is attractive from a microwave components standpoint: the 1-cm wavelength is compatible with normal manufacturing tolerances and quality control considerations. From a system standpoint, the K_A-band represents a 4:1 step from the existing X-band system, large enough for a substantial link performance enhancement, but not large enough to require new or radically different technology. The associated reduced spacecraft antenna beamwidth, however, does impact the spacecraft design in terms of a more stringent antenna pointing requirement. This problem is being studied as a part of this task.

II. The Effect of Atmospheric Turbulence at K_A-Band

The ground antenna effective aperture would remain essentially constant with increasing frequency were it not for the effect of aperture phase distortions, the so-called "Ruze" effect (Refs. 3 and 4), which becomes serious (4-dB loss) as the standard deviation of these phase distortions approaches 1/12 wavelength. Mechanical deflections, manufacturing tolerances, and small-scale tropospheric turbulence all result in more or less random phase errors whose associated aperture efficiency loss factor, η_s, is given by (Ref. 4):

$$\eta_s = e^{-\left(\frac{4\pi\sigma}{\lambda}\right)^2} \tag{1}$$

where

σ = standard deviation of the one-half path-length error

λ = wavelength

It should be noted that, because of the exponential form of Eq. (1), if several statistically independent aperture phase errors exist, then the total loss in dB is simply the sum of the individual losses in dB.

The effect of tropospheric inhomogeneities in perturbing the incoming wavefront is depicted in Fig. 1. Curiously, it can be seen that the aperture precision quantity, σ/D, decreases with larger aperture sizes, whereas this quantity generally *increases* as a function of antenna size for physical distortions. For the small scale case, Ruina and Angula (Ref. 5) derived a simple expression for the associated standard deviation of the 1/2 pathlength variation, σ_{ss}:

$$\sigma_{ss} = 0.5\,(R\ell_0)^{1/2}\,\delta \tag{2}$$

where

R = effective path length through the turbulent region

ℓ_0 = inhomogeneity scale size

δ = rms fractional index of refraction variation of the inhomogeneities

For the large scale case, they derived a simple expression for rms wavefront tilt, β:

$$\beta = \left(\frac{2R}{\ell_0}\right)^{1/2}\delta, \text{ rad} \tag{3}$$

The antenna power gain function, $G(\beta)$ may be conveniently expressed in a Gaussian form:

$$G(\beta) \equiv e^{-\alpha\left(\frac{\beta}{B}\right)^2} = e^{-\alpha\left(\frac{D\beta}{\lambda}\right)^2} \tag{4}$$

where

B = antenna beamwidth, rad

α = $\ln(2)/0.25 = 2.77$

D = antenna diameter

λ = wavelength

For large-scale inhomogeneities, an equivalent "Ruze Loss" standard deviation σ_{1s} may be defined such that the $G(\beta)$ loss given by Eq. (4) equals the loss predicted by Eq. (1) for σ_{1s}. When this is done, and the result combined with Eq. (3), the following result is obtained:

$$\sigma_{1s} = \frac{(2\alpha)^{1/2}}{4\pi}\left(\frac{R}{\ell_0}\right)^{1/2} D\delta = 0.187\left(\frac{R}{\ell_0}\right)^{1/2} D\delta \tag{5}$$

If the turbulence scale size, ℓ_0, is small compared to the aperture size, D, then Eq. (2) is the appropriate relationship to use; if ℓ_0 is large compared to D, then Eq. (5) is appropriate. Typically (Ref. 6), $R = 1.8 \times 10^4$ m (10-deg elevation), $\ell_0 =$ 40 m, and $\delta = 0.4 \times 10^{-6}$. Figure 2 shows the resulting σ/D value as a function of antenna diameter for 10- and 30-deg elevation angles. These calculations are semiquantitatively confirmed by 1969 National Radio Astronomy Observatory (NRAO) tropospheric phase stability tests (Ref. 7), which showed a σ of 0.3 to 0.45 mm for baselines up to 300 m. The troposphere thus behaves in a well understood way in its distortion of a signal wavefront, and, as shown in Table 1, does not seriously degrade a K_A-band 64-m antenna system.

III. 64-m Antenna Aperture Efficiency at K_A-Band

Three modifications to the 64-m antennas are assumed to provide K_A-band usability: (1) a new precision subreflector, (2) new precision surface panels, and (3) reduction of the gravity-induced surface errors over the elevation wheel assembly. A practical technique for reduction of the gravity errors was studied by Katow (Ref. 8). Katow presented zenith look and horizon look gravity off-on distortions of 0.43 mm and 0.46 mm, respectively. The resulting gravity distortions are elevation-angle dependent, and are given to good approximation by:

$$\sigma_G^2 = \sigma_H^2 (\cos\theta - \cos\theta_s)^2 + \sigma_Z^2 (\sin\theta - \sin\theta_s)^2 \qquad (6)$$

where

σ_G = rms surface error due to gravity

σ_H = rms gravity off-on horizon distortion

σ_Z = rms gravity off-on zenith distortion

θ = antenna elevation angle

θ_s = elevation angle at which the panels are set

Table 1 collects the various estimates of surface distortion, the troposphere turbulence effect, and the effect of a 0.001-deg rms pointing error (Ref. 9). By combining Eqs. (1) and (4), the σ equivalent in mm of a 64-m antenna pointing error is found to be 150 times the rms pointing error in degrees. Figure 3 shows the aperture efficiency as a function of frequency for the σ's in Table 1, as predicted by Eq. (1).

IV. Electronic Surface Error Compensation

In principle, aperture phasing errors may be compensated electronically by use of an extended adaptive feed. Such an approach provides an alternative to the structural upgrade described in the previous section. A multielement feed is not necessarily incompatible with low receiving system effective noise temperature. Refrigeration techniques (Ref. 10) may be used to reduce dissipative losses and their effect.

In 1970, Rudge and Davies (Ref. 11) published a detailed analysis of electronic surface error compensation and reported promising experimental results. The novel feature of the Rudge-Davies feed is that a Fourier transform of the focal plane array feed outputs is performed, thereby reconstructing the aperture distribution. Since the receive aperture distribution is constant in amplitude (but not in phase), it can be readily corrected to the ideal uniform phase distribution by a set of phase shifters and then inverse Fourier transformed to thus reconstruct the output that would result with no surface errors. The Rudge-Davies implementation was nonadaptive and used Butler Matrices (Ref. 12) to perform analog Fourier transforms.

An alternative adaptive mechanization would involve a microwave Butler Matrix to provide the first Fourier transformation and a multichannel phase-sensitive receiver to correct phase errors (see Ref. 13 for receiver details). Because of its versatility and apparent compatibility with existing 64-m antenna surface errors, an electronically compensated feed system is attractive; its technical feasibility remains to be demonstrated, however.

V. Electronic Beam Pointing

The electronic system described in the previous section can compensate for pointing errors. If such a system is not used, i.e., the physical upgrade approach is selected, then an electronic pointing system can be used to achieve reliable pointing accuracies of less than 0.001 deg. This system, described in a previous article (Ref. 14) uses higher-order corrugated waveguide modes to achieve the desired antenna beam squint to compensate for physically induced pointing errors. The required mode amplitudes and phases are established by a system of semiconductor waveguide probes or couplers. Such a system may be implemented either as a conscan or as a monopulse system, or perhaps an operator-selectable system.

VI. Conclusion

There does not appear to be any serious difficulty in upgrading the DSN 64-m antenna network to operate efficiently at K_A-band (32 GHz). This may be achieved either by conventional physical upgrade, or by use of advanced electronic techniques.

References

1. Potter, P. D., Shumate, M. S., Stelzried, C. T., and Wells, W. H., *A Study of Weather-Dependent Data Links for Deep Space Applications*, Technical Report No. 32-1392, Jet Propulsion Laboratory, Pasadena, Calif., October 15, 1969.

2. Moore, C. R., and Clauss, R. C., "A Reflected – Wave Ruby Maser with K-Band Tuning Range and Large Instantaneous Bandwidth," *IEEE Transactions on Microwave Theory and Techniques*, Vol. MTT-27, No. 3, pp. 249-256, March, 1979.

3. Ruze, J., *Physical Limitations on Antennas*, Technical Report No. 248, Research Laboratory of Electronics, MIT, Astia Document 62351, October, 1952.

4. Ruze, J., "Antenna Tolerance Theory–A Review," *Proceedings of the IEEE*, Vol. 54, No. 4, pp. 633-640, April, 1966.

5. Ruina, J. P., and Angulo, C. M., "Antenna Resolution as Limited by Atmospheric Turbulence," *IEEE Transactions on Antennas and Propagation*, Vol. AP-11, No. 2, pp. 153-161, March, 1963.

6. Crain, C. M., Straiton, A. W., and Von Rosenberg, C. E., "A Statistical Survey of Atmospheric Index-of-Refraction Variation," *IRE Transactions on Antennas and Propagation*, Vol. AP-1, No. 2, pp. 43-46, October, 1953.

7. Basart, J. P., Miley, G. K., and Clark, B. G., "Phase Measurements with Interferometer Baselines of up to 35 km," *National Radio Astronomy Observatory*, VLA Scientific Memorandum No. 12, June 4, 1969.

8. Katow, M. S., "A Proposed Method of Reducing the Gravity Distortions of the 64-Meter Antenna Main Reflector," *JPL Deep Space Network Progress Report No. 42-23*, July – August, 1974, pp. 92-97.

9. Ohlson, J. E., and Reid, M. S., *Conical-Scan Tracking with the 64 m-Diameter Antenna at Goldstone*, Jet Propulsion Laboratory Technical Report No. 32-1605, October 1, 1976.

10. *Final Report, Refrigerated Transmission Line Study, Volumes I and II*, Rantec No. 66327-FR, The Rantec Corporation, Calabasas, California.

11. Rudge, A. W., and Davies, D. E. N., "Electronically Controllable Primary Feed For Profile-Error Compensation of Large Parabolic Reflectors," *Proceedings of the IEE (British)*, Vol. 117, No. 2, February, 1970, pp. 351-358.

12. Butler, J., and Lowe, R., "Beam Forming Matrix Simplifies Design of Electronically Scanned Antennas," *Electronic Design*, Vol. 9, pp. 170-173.

13. Brockman, M. H., "Radio-Frequency Carrier Arraying for High-Rate Telemetry Reception," *JPL Deep Space Network Progress Report No. 42-45*, March and April 1978, pp. 209-223.

14. Potter, P. D., "Feasibility of Inertialess Conscan Utilizing Modified DSN Feed Systems," *JPL Deep Space Network Progress Report 42-51*, June, 1979, pp. 85-93.

Table 1. Upgraded 64-m antenna 1/2 pathlength errors and associated 32-GHz gain losses

Error mechanism	Elevation angle: Zenith σ, mm	Zenith Loss, dB	30 deg σ, mm	30 deg Loss, dB	10 deg σ, mm	10 deg Loss, dB
Gravity (structure)	0.42	−1.38	0.038	−0.01	0.19	−0.28
Wind (32 km/hr)[a]	0.28	−0.61	0.28	−0.61	0.28	−0.61
Surbreflector[a] manufacturing	0.25	−0.49	0.25	−0.49	0.25	−0.49
Panel[a] manufacturing	0.25	−0.49	0.25	−0.49	0.25	−0.49
Panel[a] setting	0.25	−0.49	0.25	−0.49	0.25	−0.49
Tropospheric turbulence	0.12	−0.11	0.18	−0.25	0.30	−0.70
Antenna pointing	0.15	−0.17	0.15	−0.17	0.15	−0.17
TOTALS	0.69 (RSS)	−3.74	0.57 (RSS)	−2.51	0.64 (RSS)	−3.23

[a]Estimates provided by M. S. Katow of the JPL DSN Engineering Section.

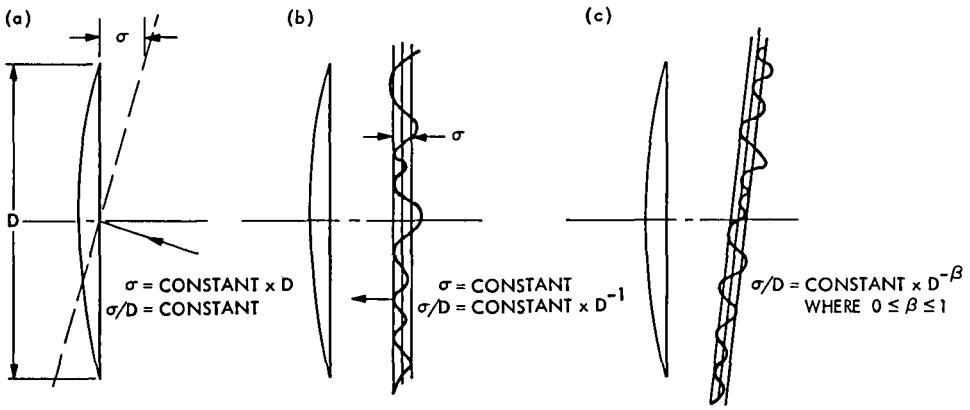

Fig. 1. Effect of scale size on tropospheric distortion effect: (a) model of large-scale wavefront distortion; (b) model of small-scale wavefront distortion; (c) model of the general case

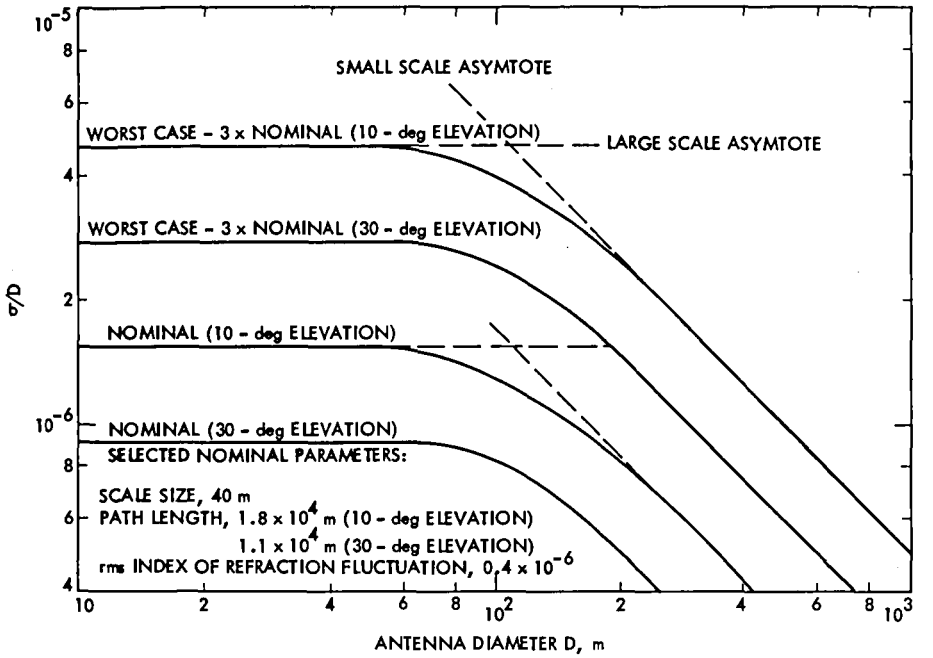

Fig. 2. σ/D equivalent of the troposphere

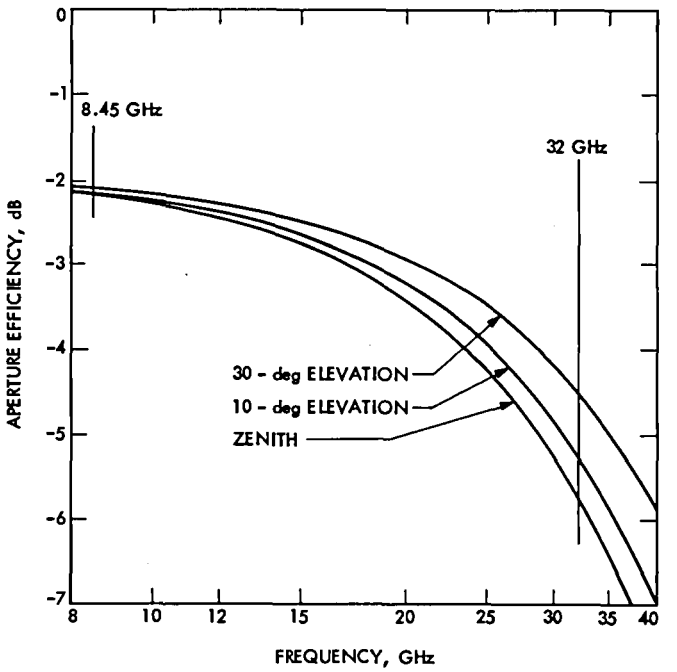

Fig. 3. Upgraded 64-m antenna aperture efficiency vs frequency

High-Power Transmitter Automation

R. Gosline
Radio Frequency and Microwave Subsystems Section

This report describes the current status of the transmitter automation development. The work being done is applicable to all transmitters in the DSN. New interface and software designs are described that improve reliability and reduce the time required for subsystem turn-on and klystron saturation to less than 10 minutes.

I. Introduction

The benefits of transmitter automation are the reduction of life-cycle costs and increased availability. Life-cycle costs will be reduced not only by the requirement for fewer operators, but also by more effective preventive maintenance through increased and more accurate reporting of critical subsystem parameters. Increased availability will be provided by eliminating the need for operations personnel on evening and weekend shifts. Automatic fault diagnosis and programmed recovery procedures will also increase availability.

The development work currently being done for the DSS 13 high-power S-band transmitter is applicable to all other known or planned transmitters in the Deep Space Network including the X-band uplink development at DSS 13. The difference in operational parameters of the various transmitters is provided for by including a configuration table (see Fig. 1 for a typical set) for each transmitter in the program. Each klystron has its own table. The upper block contains the klystron serial numbers for which the program contains a configuration data block. The middle block contains maximum and minimum operating values. The lower block contains the analog channels full-scale meter values. Instrumentation amplifiers convert all analog channel inputs to 5 volts full scale. The target values are used as adjustment goals and are changed as required during operation of the transmitter. Each channel has a delta value used as an out-of-adjustment tolerance. It should be noted that the data are easily understood even though it is actually part of the program code. Provision for operating in an unsaturated mode has been included. All commands, analogs, interlocks, and indicators (from the program listing) are shown in Figs. 2 through 5.

II. History

Prior automation efforts for the transmitter subsystem met with limited success. The first attempt used a PDP-11 minicomputer for the controller. Poor hardware reliability was encountered and the only high-level language available (Basic) was unsuitable for real-time control. Memory requirements and computing time limited the degree of automation that could be performed. With the development of microprocessors and the availability of a high-level language suitable for control applications (*PL/M*), the next effort used a JPL packaged microprocessor and provided a controller that has proved satisfactory although improvements in some areas are desirable. About 30 percent of the software was written in assembly language and a floating point math package was used

that slowed the execution time considerably. The time required to turn on and calibrate the transmitter was about 35 minutes. In addition, special interface logic was built that would be too difficult and expensive to maintain in the field. Thus, it was decided to rewrite the software entirely in *PL/M* and use integer arithmetic for all computing. All analog quantities are represented internally by an eight-bit binary fraction of the full-scale value. In addition, it was decided to eliminate all custom designed circuitry and use only commercially available off-the-shelf items of proven performance, reliability, and availability.

III. New Hardware

The new controller is based on the Intel industrial control series using an 8080 microprocessor and standard CCM approved modules. These include the 80/20-4 CPU with 8 kbytes of RAM and provision for 24 digital output lines and a PROM card for program storage. Communication is provided by an SBC-534 module with four RS-232C ports. An SBC-519 input-output card provides for 72 digital input signals. A 32-channel differential input multiplexer and analog-to-digital converter is used for analog inputs (only 16 channels are used). A block diagram of the transmitter controller appears in Fig. 6. This controller is located in the High Power Test Facility at DSS 13 near the Local Control Console. A second controller (without the signal interfaces) is in the control room near the Remote Control Console. This controller acts solely as a communications buffer for the 15-line standard interface to the station controller. The interface between the transmitter controllers is a serial interface (RS-232C) through short-haul modems. The interface modules are also part of Intel's industrial control line, and provide for filtering and level shifting with optoisolators. Most of the transmitter control and indicator circuitry is 28 volts. A photograph of the transmitter controller showing the vertically mounted interface modules is shown in Fig. 7.

A transmitter simulator was constructed using TTL logic and operational amplifiers to facilitate checkout of the new controller. The device simulates all major functions of the transmitter including interlock logic and realistic klystron characteristics, and has been invaluable in the checkout of the controller and evaluation of new algorithms. A photograph of the transmitter simulator appears in Fig. 8.

IV. Software

The software conforms to top-down structured methodology and is 100 percent *PL/M*. The programs (both controllers) require about 6000 lines of code that produce 40 kbytes when assembled. A composite top-level flowchart is shown in Fig. 9. The time between successive passes through the monitor is about 600 ms. The time required for turn on and calibration is now about 10 minutes (using the simulator). A photograph of the maintenance display is shown in Fig. 10.

V. Present Status

Testing of the controller with the simulator has been completed and currently the controller is being installed at DSS 13 for further evaluation and support of unattended operation demonstrations.

```
/**** CONFIGURATION DATA STRUCTURE  04/09/80 ********/
CONFIG$DAT: DO;
DECLARE SERIAL$NO$DAT(8) STRUCTURE(DAT(14) BYTE) PUBLIC DATA (
  /*  0  */  'SIMULATOR     '  ,
  /*  1  */  'L5- 3-R1 DSS63'  ,
  /*  2  */  'L5-34-R1 DSS63'  ,
  /*  3  */  'K5-24-R1 DSS43'  ,
  /*  4  */  'A6-17-R2 DSS13'  ,
  /*  5  */  'J5-24-R2 DSS14'  ,
  /*  6  */  'H5-30-R2 DSS43'  ,
  /*  7  */  'B8- 1-R1 DSS14'  );

DECLARE CFG1(64) STRUCTURE (DAT(4) BYTE ) PUBLIC DATA (   /**  DSS-13  **/

  /*         NAME                    LIMIT       */

  /* SERIAL NUMBER REF          */  '   4'  ,
  /* TBEMCB - CB TEST V         */  '  20'  ,
  /* TBEMLO - MIN PWR BM V      */  '  20'  ,
  /* TBEMMI - MAX BM I          */  ' 4.4'  ,
  /* TBEMMV - MAX BM V          */  '  25'  ,
  /* TDRIVL - MIN DRIVE         */  ' 300'  ,
  /* TDRVMX - MAX DRIVE         */  ' 996'  ,
  /* TFILMX - MAX FIL V         */  '  11'  ,
  /* TMAGMX - MAX MAG I         */  '  18'  ,
  /* TPERVI - PERVEANCE BM I    */  ' 4.4'  ,
  /* TPWRMN - MIN PWR OUT       */  '  10'  ,
  /* TPWRMX - MAX PWR OUT       */  '  30'  ,
  /* TBM10                      */  '19.9'  ,
  /* TBM20                      */  '22.1'  ,
  /* TBM30                      */  '23.4'  ,
  /* NULL                       */  '   0'  ,

  /*  NAME      FULLSCALE     TARGET      DELTA    */

  /*  OUTPW  */  ' 100'  ,  '  10'  ,  '   1'  ,
  /*  BEAMV  */  ' 100'  ,  '   0'  ,  ' 0.5'  ,
  /*  BEAMI  */  '  25'  ,  '   0'  ,  ' 0.5'  ,
  /*  DRIVP  */  '1000'  ,  '   0'  ,  ' 100'  ,
  /*  REFLC  */  '1000'  ,  ' 500'  ,  ' 100'  ,
  /*  BODYI  */  '1000'  ,  ' 600'  ,  ' 300'  ,
  /*  COLEC  */  '  25'  ,  '   0'  ,  ' 0.3'  ,
  /*  FILAV  */  '  25'  ,  ' 9.0'  ,  ' 0.3'  ,
  /*  FILAI  */  '  25'  ,  '10.5'  ,  ' 0.3'  ,
  /*  MAGNT  */  '  25'  ,  '17.4'  ,  ' 0.2'  ,
  /*  VACUM  */  '  50'  ,  ' 1.5'  ,  ' 1.5'  ,
  /*  CRWBR  */  '  50'  ,  '  10'  ,  '   5'  ,
  /*  NULL   */  '   0'  ,  '   0'  ,  '   0'  ,
  /*  NULL   */  '   0'  ,  '   0'  ,  '   0'  ,
  /*  NULL   */  '   0'  ,  '   0'  ,  '   0'  ,
  /*  NULL   */  '   0'  ,  '   0'  ,  '   0'  );
```

Fig. 1. Typical configuration table

```
PL/M-80 COMPILER


ISIS-II PL/M-80 V3.1 COMPILATION OF MODULE COMMANDDAT
OBJECT MODULE PLACED IN :F1:CMDEFT.OBJ
COMPILER INVOKED BY:  PLM80 :F1:CMDEFT.PLM DEBUG XREF IXREF SYMBOLS



                /******** COMMAND DATA DEFINITION   03/25/80 *******/

   1            COMMAND$DAT: DO;

   2    1       DECLARE CMND$BUF(3) BYTE EXTERNAL;
   3    1       DECLARE CMND$DAT(21) STRUCTURE (
                  BYTE$NUM BYTE, BIT$NUM BYTE,
                  COL BYTE, ROW BYTE,
                  NAME(6) BYTE ) PUBLIC DATA (

                    2,7,47,1,     'ARCDT ',
                    1,3,47,2,     'BEMLO ',
                    1,5,47,3,     'BEMOF ',
                    1,4,47,4,     'BEMON ',
                    1,2,47,5,     'BEMRA ',
                    1,7,47,6,     'BEMRL ',
                    0,4,47,7,     'CBTST ',
                    0,7,47,8,     'CPSOF ',
                    2,0,47,9,     'CPSON ',
                    2,5,47,10,    'DRVLO ',
                    2,6,47,11,    'DRVRA ',
                    2,4,47,12,    'FILLO ',
                    2,3,47,13,    'FILRA ',
                    1,6,47,14,    'ILRST ',
                    0,5,47,15,    'MAGLO ',
                    0,6,47,16,    'MAGRA ',
                    0,3,47,17,    'PROGR ',
                    1,0,47,18,    'PMPOF ',
                    1,1,47,19,    'PMPON ',
                    2,1,47,20,    'SYNOF ',
                    2,2,47,21,    'SYNON '  );
```

Fig. 2. Command table

```
142   1       DISPLAY$FORMAT: PROCEDURE;
143   2         DECLARE ANALOG$LABEL(12) STRUCTURE (LBL(11) BYTE ) DATA (
                  'OUTPUT    KW',
                  'BEAM V    KV',
                  'BEAM I     A',
                  'DRIVE     MW',
                  'REFLECT    W',
                  'BODY I    MA',
                  'COLL I     A',
                  'FILA V     V',
                  'FILA I     A',
                  'MAGNET I   A',
                  'VACUUM I  UA',
                  'CROWBAR   US' );
```

Fig. 3. Analog channels

```
            /********** DIGITAL DATA DEFINITIONS 04/22/80 ******/

1           DIGITAL$DEF: DO;

2   1       DECLARE DIGITAL$DAT(72) STRUCTURE (
                BYTE$NUM BYTE, BIT$NUM BYTE,
                COL BYTE, ROW BYTE,
                NAME(6) BYTE,
                DESCRIPT(16) BYTE) PUBLIC DATA (

            /** INTERLOCKS **/

                0,3,54,1,     'ALIHEF',     'ALI HE FLOW I-L ', /* 00 */
                2,4,54,2,     'ALIHET',     'ALI HE O-T I-L  ', /* 01 */
                4,0,54,3,     'ARCDT1',     'ARC DET #1 I-L  ', /* 02 */
                5,7,54,4,     'ARCTD2',     'ARC DET #2 I-L  ', /* 03 */
                2,2,54,6,     'BODYFL',     'BODY FLOW I-L   ', /* 04 */
                4,7,54,7,     'BODYOC',     'BODY O-C I-L    ', /* 05 */
                1,0,54,8,     'CBFIRE',     'C-B FIRED I-L   ', /* 06 */
                3,2,54,9,     'CBLKBF',     'CBL KBF I-L     ', /* 07 */
                3,1,54,10,    'CBLKBS',     'CBL KBS I-L     ', /* 08 */
                1,1,54,11,    'CBLKMS',     'CBL KMS I-L     ', /* 09 */
                2,7,54,12,    'CBLTES',     'CBL TEST I-L    ', /* 10 */
                2,3,54,13,    'COLLFL',     'COLECTR FLOW I-L', /* 11 */
                6,0,54,14,    'COLLOC',     'COLLECTR O-C I-L', /* 12 */
                3,0,54,15,    'DCOCUR',     'DC O-C I-L      ', /* 13 */
                1,7,54,16,    'DCOVLT',     'DC O-V I-L      ', /* 14 */
                5,3,54,17,    'DOORAN',     'DOOR ANTENNA I-L', /* 15 */
                3,5,54,18,    'DOORPE',     'DOOR PEDESTL I-L', /* 16 */
                5,4,54,19,    'DOORVA',     'DOOR VALULT I-L ', /* 17 */
                2,1,54,20,    'DRIFTT',     'DRIFT T FLOW I-L', /* 18 */
                5,2,54,21,    'ELEVAT',     'ELEVATION I-L   ', /* 19 */
                0,7,54,22,    'FILAMA',     'FIL-MAG FLOW I-L', /* 20 */
                4,3,54,23,    'FILATD',     'FILAMENT T-D I-L', /* 21 */
                4,5,54,24,    'FILAUC',     'FILAMENT U-C I-L', /* 22 */
                2,6,61,1,     'GENERA',     'GEN LOCKOUT I-L ', /* 23 */
                1,4,61,2,     'HVZERO',     'H-V ZERO I-L    ', /* 24 */
                3,7,61,3,     'IGNITR',     'IGNITRON PWR I-L', /* 25 */
                4,6,61,5,     'MAGNUC',     'MAGNET U-C I-L  ', /* 26 */
                3,0,61,6,     'MAPOWE',     'MET AMP POW I-L ', /* 27 */
                1,5,61,7,     'MOTORL',     'MOTR LOCKOUT I-L', /* 28 */
                1,3,61,8,     'MOTORS',     'MOTOR START I-L ', /* 29 */
                1,6,61,9,     'RECTPH',     'REC PHAS O-C I-L', /* 30 */
                4,2,61,10,    'REFLP1',     'REFL PWR #1 I-L ', /* 31 */
                4,1,61,11,    'REFLP2',     'REFL PWR #2 I-L ', /* 32 */
                5,6,61,12,    'REFLPM',     'REFL PWR MET I-L', /* 33 */
                5,5,61,13,    'TRFLOW',     'TRN-REC FLOW I-L', /* 34 */
                1,2,61,14,    'TRROIL',     'TRN-REC OIL I-L ', /* 35 */
                0,5,61,15,    'TXRCON',     'TXR CONFIG I-L  ', /* 36 */
                4,4,61,16,    'VACUOC',     'VACUUM O-C I-L  ', /* 37 */
                5,1,61,17,    'VACUPW',     'VACUUM PWR I-L  ', /* 38 */
                2,0,61,18,    'WATRLO',     'WATER LOAD F I-L', /* 39 */
                3,6,61,19,    'WAVPRE',     'WAVE-G PRESS I-L', /* 40 */
                0,6,61,20,    'WAVSWS',     'WAVEGUIDE SW I-L', /* 41 */
```

Fig. 4. Interlocks

```
/** INDICATORS **/

    7,0,54.5,     'AUXHEO',     'AUX H-E           ',  /* 42 */
    2,5,61,4,     'MAINHE',     'MAIN H-E          ',  /* 43 */
    7,4,61.22,    'ALIHEO',     'ALIDADE H-E       ',  /* 44 */
    3,4,61.23,    'ANTENA',     'ANT POSITION IND',    /* 45 */
    7,2,61,24,    'BEAMOF',     'BEAM OFF IND      ',  /* 46 */
    8,5,68.1,     'BEAMLO',     'BEAM LOWER IND    ',  /* 47 */
    8,4,68.2,     'BEAMRA',     'BEAM RAISE IND    ',  /* 48 */
    6,4,68,3,     'BEAMRD',     'BEAM READY IND    ',  /* 49 */
    6,5,68.4,     'CNTROF',     'CONTROL P-S IND   ',  /* 50 */
    6,6,68.5,     'CNTRON',     'CONTROL P-S IND   ',  /* 51 */
    6,2,68.6,     'DRIVLO',     'DRIVE LOWER IND   ',  /* 52 */
    6,3,68.7,     'DRIVRA',     'DRIVE RAISE IND   ',  /* 53 */
    8,3,68.8,     'FILALO',     'FILA LOWER IND    ',  /* 54 */
    6,1,68.9,     'FILARA',     'FILA RAISE IND    ',  /* 55 */
    7,1,68.10,    'GENFIE',     'GEN FIELD PS IND',    /* 56 */
    0,4,68.11,    'HEFANS',     'H-E FANS          ',  /* 57 */
    7,3,68.12,    'ILOPEN',     'I-L OPEN IND      ',  /* 58 */
    0,2,68,13,    'NORMAL',     'NORMAL IND        ',  /* 59 */
    0,1,68.14,    'PROGRA',     'PROGRAM IND       ',  /* 60 */
    8,2,68,15,    'PUMPOF',     'PUMPS IND         ',  /* 61 */
    8,1,68.16,    'PUMPON',     'PUMPS IND         ',  /* 62 */
    6,7,68.17,    'SYNCOF',     'SYNC MOTOR IND    ',  /* 63 */
    8,0,68.18,    'SYNCON',     'SYNC MOTOR IND    ',  /* 64 */
    7,7,68.19,    'V5UAMP',     'V5UA SCALE IND    ',  /* 65 */
    8,6,68,20,    'V50UAM',     'V50UA SCALE IND   ',  /* 66 */
    7,6,68,21,    'V500UA',     'V500UA SCALE IND',    /* 67 */
    7,5,68.22,    'V5MAMP',     'V5MA SCALE IND    ',  /* 68 */
    8,7,68.23,    'V50MAM',     'V50MA SCALE IND   ',  /* 69 */
    3,3,68.24,    'WATRPO',     'WATER-LD POS IND',    /* 70 */
    0,0,61,21,    'SPARE ',                       ');/* 71 */
```

Fig. 5. Indicators

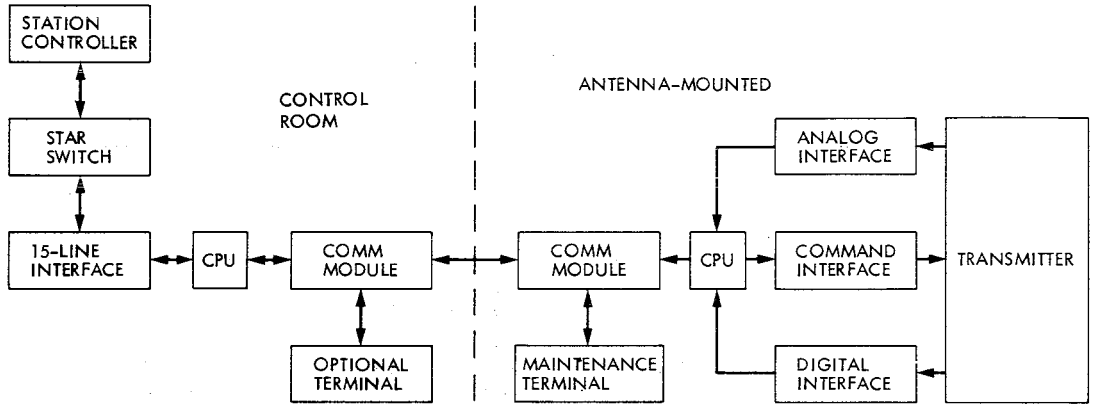

Fig. 6. Transmitter controller block diagram

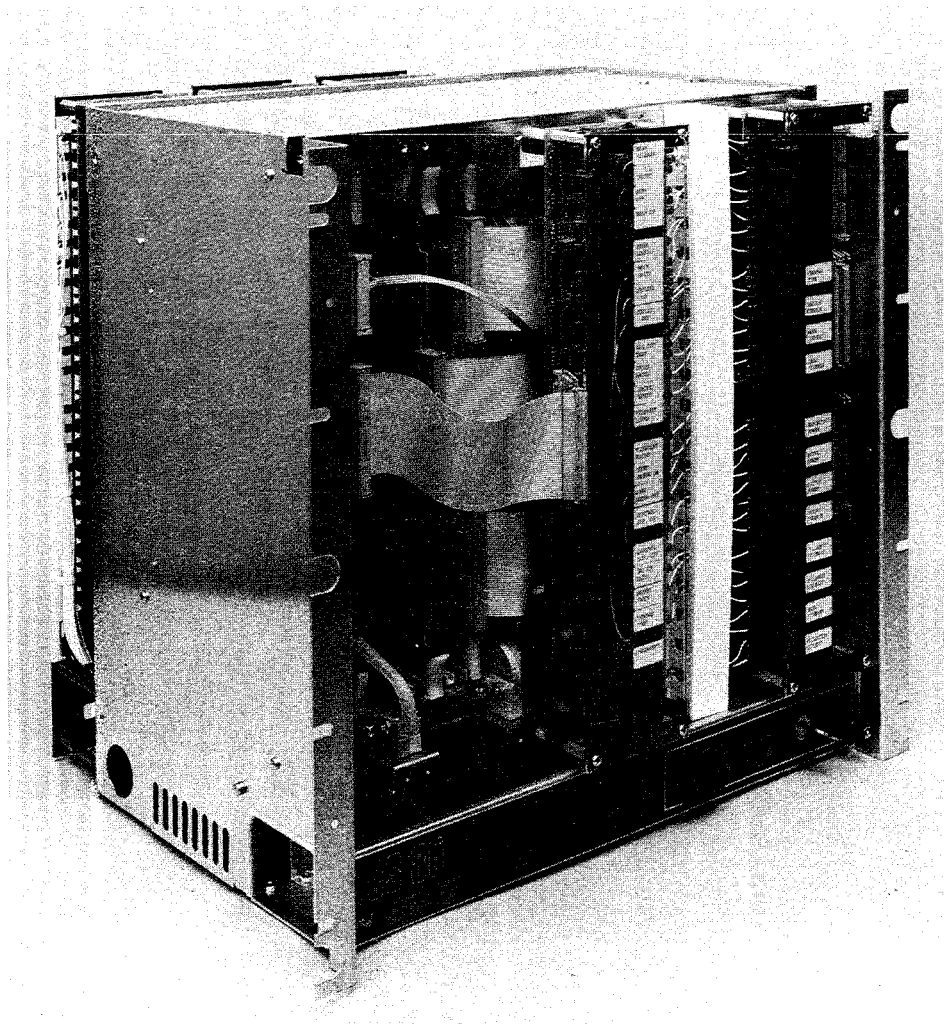

Fig. 7. Transmitter controller

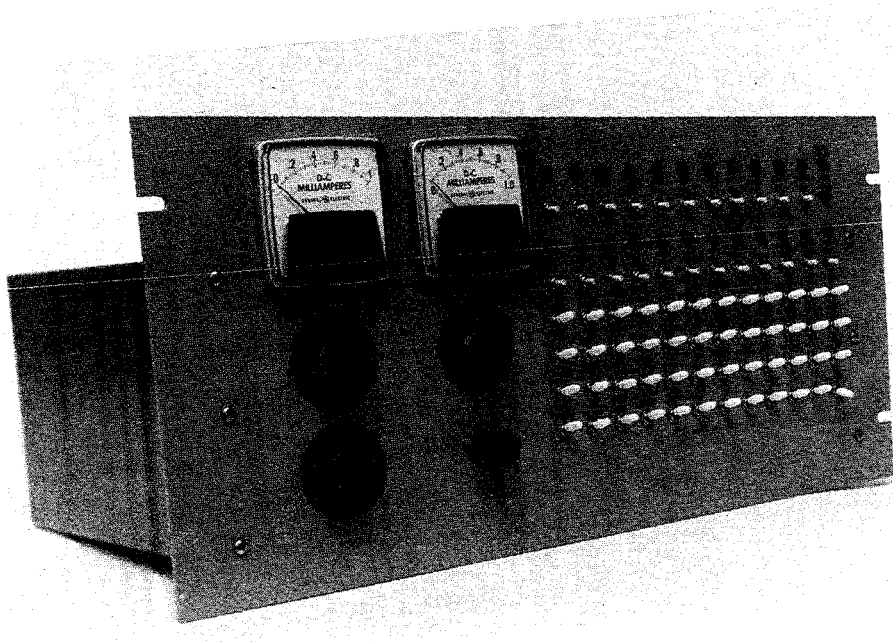

Fig. 8. Transmitter simulator

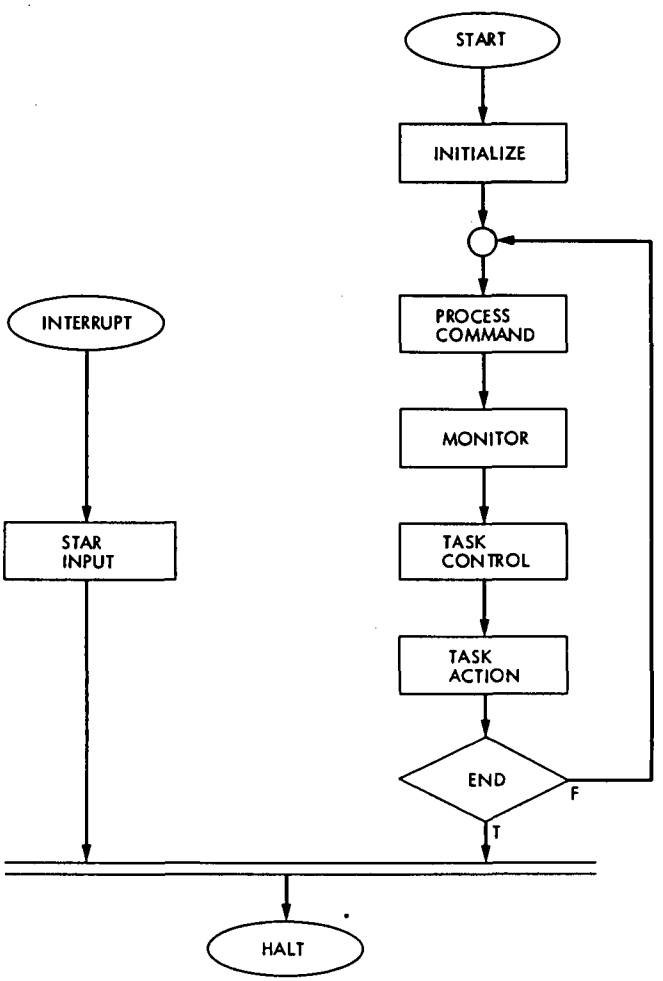

Fig. 9. Transmitter control program top-level flowchart

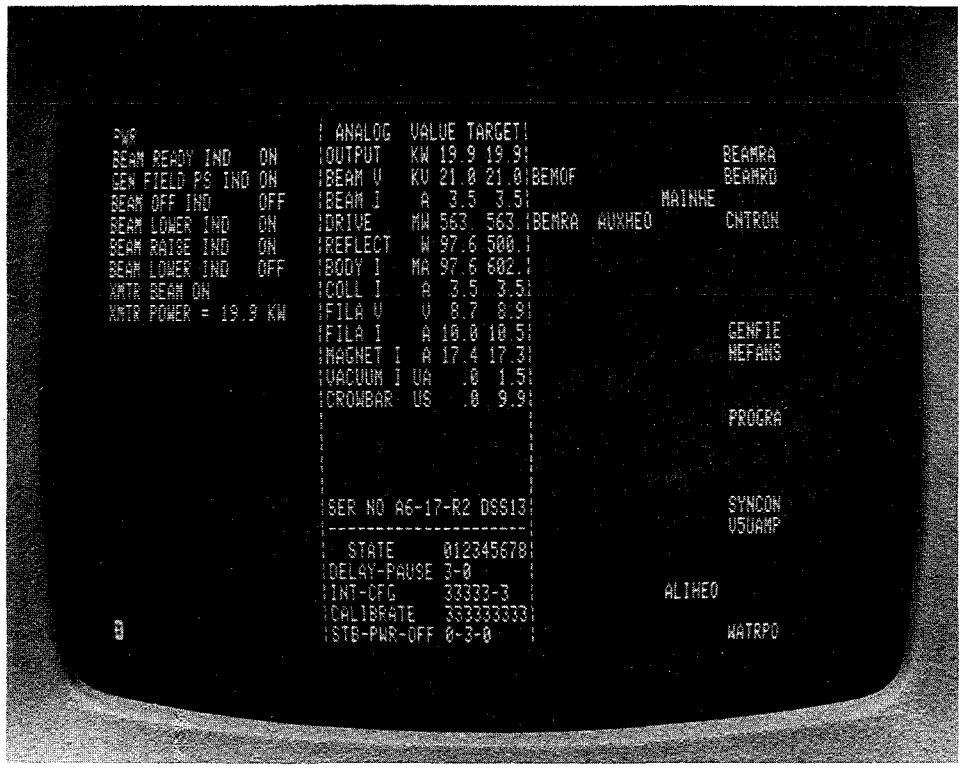

Fig. 10. Maintenance display

RFI Receiver

R. Lay
Radio Frequency and Microwave Subsystems Section

In support of an effort to analyze and identify sources of RFI problems in the DSN tracking stations, an S-band RFI Receiver has been developed that will be upgraded later for S/X-band operation.

I. Introduction

The DSN tracking stations have experienced occasional problems with RF interference because of the extreme sensitivity of its receivers and antennas. The RF surveillance system has been developed as a possible aid to establish the characteristics of the RF environment at the Goldstone DSN Complex.

The RFI Receiver, shown in Fig. 1, is a constant-gain, double-conversion, open-loop receiver with dual sine/cosine channel outputs, providing a total of 20-MHz monitoring capability. This receiver is computer controlled using a MODCOMP II miniprocessor.

II. Design Considerations

The RFI Receiver has been designed to operate at a 150-kelvin system noise temperature accomplished by cascading two low-noise field effect transistor (FET) amplifiers for the receiver front-end. The first stage low-noise FET amplifier will be mounted at the feed horn to minimize any cable losses to achieve a lower system noise temperature. The receiver is tunable over the frequency range of 2150 to 2450 MHz in both sine/cosine output channels with a resolution of 100 kHz.

One output channel contains the IF signal mixed with the sine of the reference frequency of the digital controlled oscillator, and the other output channel contains the IF signal mixed with the cosine of the reference frequency. This is a complex mixer discussed in detail in Ref. 1.

Care was taken in the design of the complex mixer output stage for maintaining good phase and gain tracking between the sine/cosine output channels, thus suppressing unwanted image or ghost response in the power spectrum of the baseband signal.

Measurement data taken on phase tracking between the sine/cosine channel outputs, without the video amplifiers and low-pass filters, is shown in Fig. 2. The data represents the best phase tracking data obtained after a number of trial combinations were made between different manufactured 90-degree hybrids and mixers. The plots shown in Fig. 3 and Fig. 4 are exclusively on the video amplifier and the low-pass filter that track in phase within 6 degrees. As shown in Fig. 3, there is a large phase difference near 300 kHz and 800 kHz. Additional alignment was done to smooth the phase response of the video amplifier and low-pass filter. The phase tracking response of the low-pass filter and the video amplifiers were made to track in phase within 2 degrees across the pass band. The resulting phase tracking response of the video amplifier and low-pass filter, is shown in Fig. 4. The composite plot of the phase tracking between the sine/cosine output channels of the RFI receiver is shown in Fig. 5.

Gain tracking between the sine/cosine output channels of the RFI Receiver tracks within 1 dB across the receiving frequency band.

III. Theory of Operation

A simplified block diagram of the RFI Receiver is shown in Fig. 1 and is a double conversion open-loop receiver. The received S-band signal from the feed horn is converted to an IF signal in the first mixer using a fixed 2000-MHz local oscillator (LO) signal. The second mixer translates the IF signal to video. The LO signal for the second mixer is fed from a digitally controlled synthesizer through a 90-degree hybrid. The RFI Receiver is designed for measuring the S-band environment at the Goldstone DSN Complex using its own S-band feed horn; however, it has the capability of monitoring the Block IV receiver at DSS 14 at the 55-MHz IF or the 325-MHz IF.

IV. Future Plans

The future plan will be to upgrade this S-band Receiver to enable S- and X-band operation. This will be accomplished by providing an additional X-band receiving channel and will provide a total of 80-MHz monitoring capability at either S- or X-band. In addition, investigation of the design of lower system noise temperatures for the receiver will be conducted.

Reference

1. Winkelstein, R., "Complex Mixer Error Analysis," *Deep Space Network Progress Report*, Technical Report 32-1526, Vol. XII, pp. 47-50, Jet Propulsion Laboratory, Pasadena, Calif., Dec. 15, 1972.

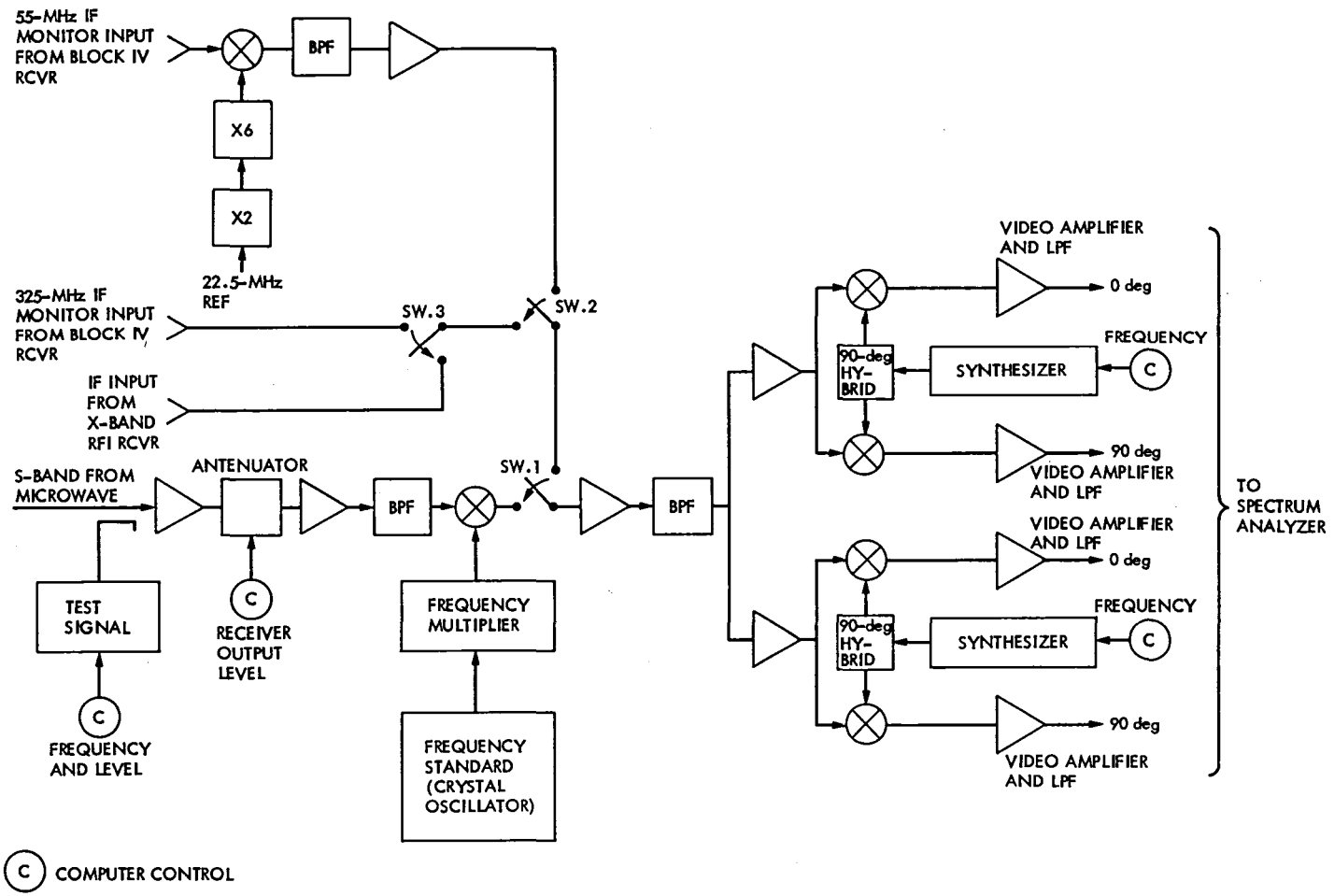

Fig. 1. RFI Receiver block diagram

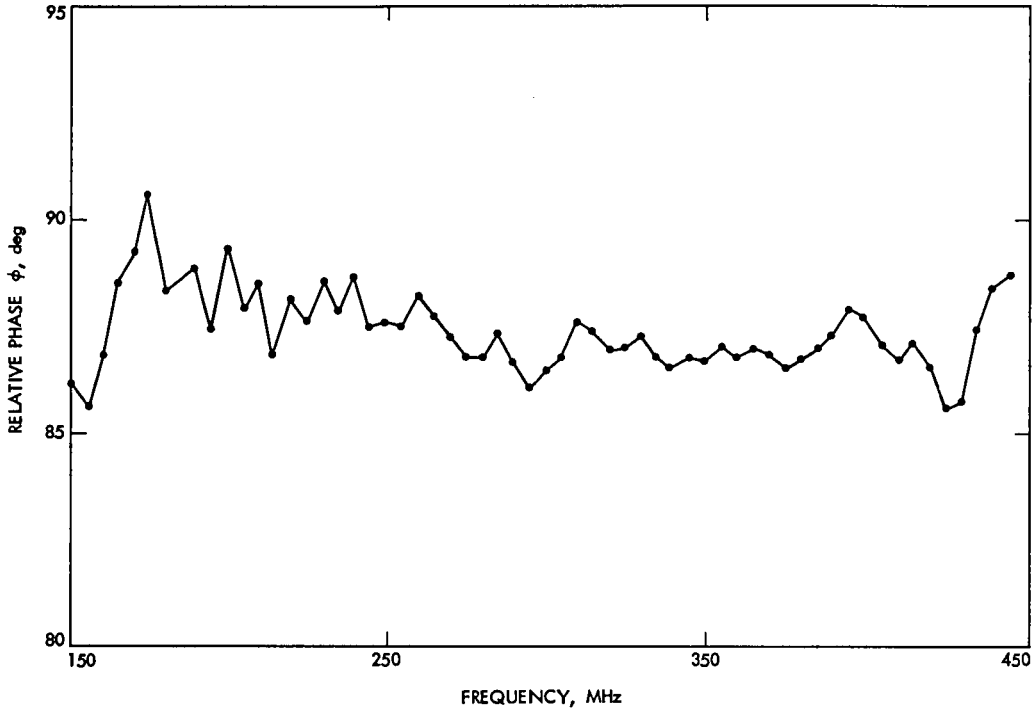

Fig. 2. Phase tracking response between the sine/cosine channels without the video amplifiers and low-pass filters

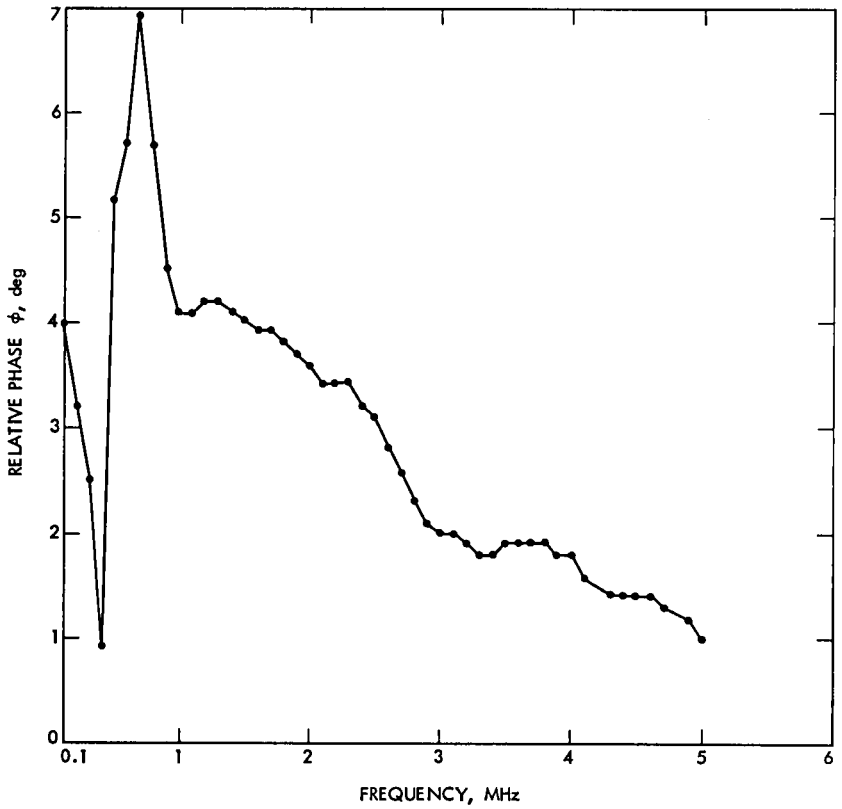

Fig. 3. Phase tracking response between the video amplifier and low-pass filter

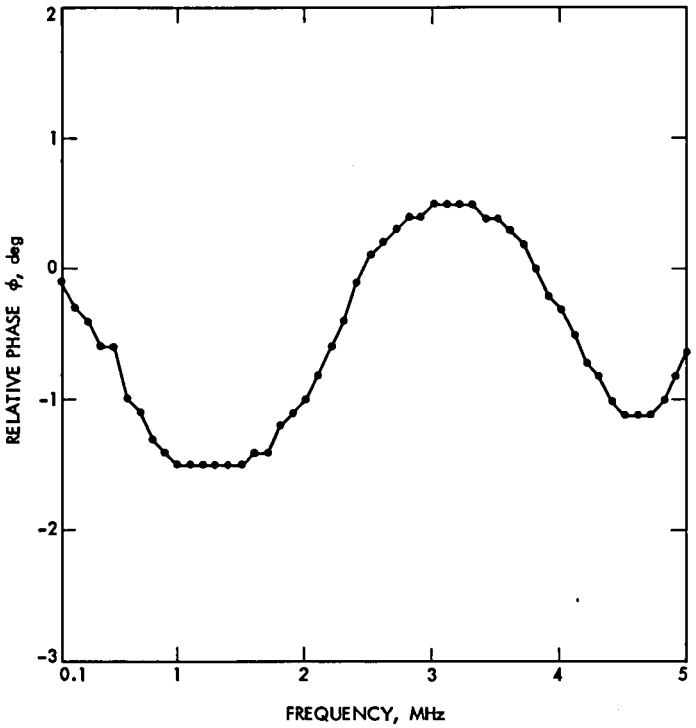

Fig. 4. Phase tracking response of the video amplifier and low-pass filter

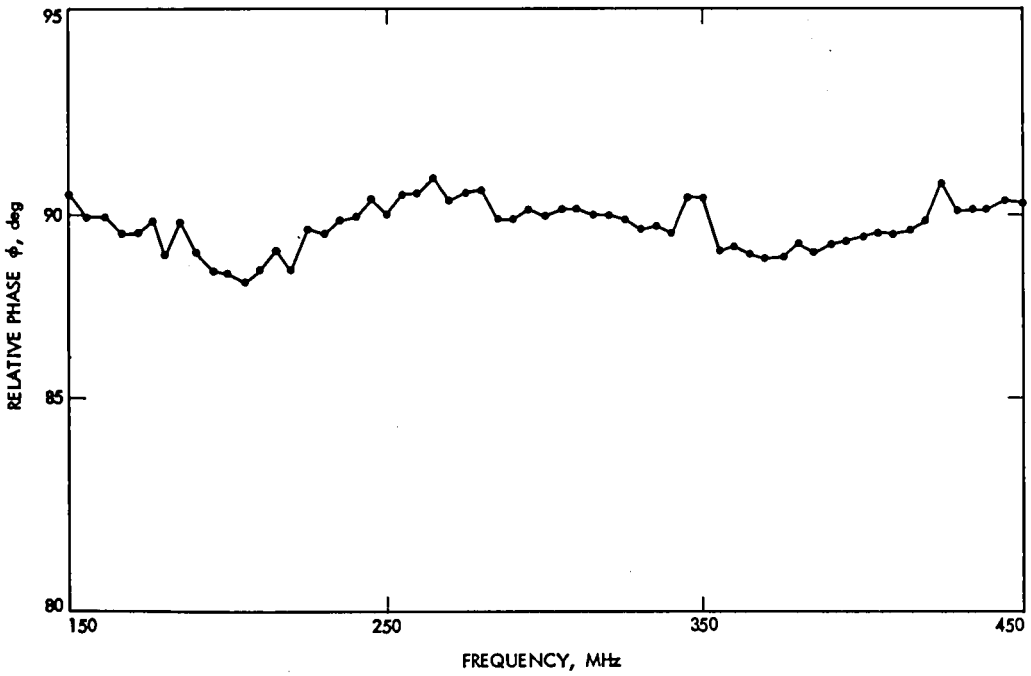

Fig. 5. Composite phase tracking response between the sine/cosine output channels of the RFI receiver

On the Application of a Fast Polynomial Transform and the Chinese Remainder Theorem to Compute a Two-Dimensional Convolution

T. K. Truong and R. Lipes
Communications Systems Research Section

I. S. Reed
University of Southern California

C. Wu
Radar Science and Engineering Section

In this article, a fast algorithm is developed to compute two-dimensional convolutions of an array of $d_1 \cdot d_2$ complex number points, where $d_2 = 2^m$ and $d_1 = 2^{m-r+1}$ for some $1 \leq r \leq m$. This new algorithm requires fewer multiplications and about the same number of additions as the conventional FFT method for computing the two-dimensional convolution. It also has the advantage that the operation of transposing the matrix of data can be avoided.

I. Introduction

Two-dimensional convolutions of two sequences of complex number points can be applied to many areas, in particular to the synthetic aperture radar (SAR) (Refs. 1, 2). In SAR, a two-dimensional cross correlation of the raw echo data of complex numbers with the response function of a point target is required to produce images. When the two-dimensional filter does not change rapidly with the range, one can divide the entire range of echo data into several subintervals. Within each subinterval, one can use a constant filter function. This is accomplished usually by using the conventional fast Fourier transform (FFT). However, the FFT algorithm generally requires a large number of floating-point complex additions and multiplications. Also, the transpose of a matrix is usually required in the computation of such a two-dimensional convolution.

Recently, Rader (Ref. 3) proposed that a number-theoretic transform (NTT) could be used to accomplish two-dimensional filtering. It was shown (Ref. 4) that an improvement, both in accuracy and speed, of two-dimensional convolutions could be achieved by transforms over a finite field $GF(q)$, where q is a prime of the form $45 \times 2^{29} + 1$. However, to compute a two-dimensional convolution of two long sequences of an integer number of points, such a transform over a finite field did not allow for a wide variety of dynamic ranges.

More recently, Nussbaumer and Quandalle (Ref. 5) showed that a type of polynomial transform over the complex numbers could be used to efficiently compute two-dimensional convolutions. A principal advantage of this method over the above mentioned techniques is that the need for computing the transpose of matrix can be avoided. Furthermore, this new method offers a wider variety of dynamic ranges. It was shown recently by Arambepola and Rayner (Ref. 6) that the ideas of Nussbaumer and Quandalle can be generalized to a radix-2 polynomial transform analogous to the conventional radix-2 FET. But they do not make use of the Chinese remainder theorem as it is shown in this article to further reduce the complexity of the algorithm.

In this article, it is shown that a combination of a fast polynomial transform (FPT) and the Chinese remainder theorem (CRT) can be used to very efficiently compute a two-dimensional convolution of a $d_1 \cdot d_2$ complex number array, where $d_2 = 2^m$ and $d_1 = 2^{m-r+1}$ for $1 \leqslant r \leqslant m$. Such a new algorithm requires considerably fewer multiplications and about the same number of additions as the conventional algorithm for the two-dimensional case. Therefore, it has the potential for important application in SAR.

II. The Computation of Two-Dimensional Convolutions

The following algorithm for a two-dimensional digital convolution is based on an important identity. Let d_i be a power of 2 for $i = 1, 2$ and let C be the field of complex numbers. Also let a_{t_1,t_2} and b_{t_1,t_2} be two $d_1 \cdot d_2$ arrays, where $0 \leqslant t_i \leqslant d_i - 1$ for $i = 1, 2$. Then the two-dimensional cyclic convolution of a_{t_1,t_2} and b_{t_1,t_2}, where $a_{t_1,t_2}, b_{t_1,t_2} \in C$, is defined by

$$C_{n_1,n_2} = \sum_{t_1=0}^{d_1-1} \sum_{t_2=0}^{d_2-1} a_{t_1,t_2} b_{(n_1-t_1),(n_2-t_2)}, \quad 0 \leqslant n_i \leqslant d_i \text{ for } i = 1, 2 \tag{1}$$

where $(n_i - t_i)$ denotes the residue of $n_i - t_i$ modulo d_i for $i = 1, 2$.

Define

$$\left.\begin{aligned} A_{t_1}(Z) &= \sum_{t_2=0}^{d_2-1} a_{t_1,t_2} Z^{t_2} \qquad B_{t_1}(Z) = \sum_{t_2=0}^{d_2-1} b_{t_1,t_2} Z^{t_2}; \\ C_{n_1}(Z) &= \sum_{n_2=0}^{d_2-1} c_{n_1,n_2} Z^{n_2}, \quad \text{for } 0 \leqslant n_1, t_1 \leqslant d_1 - 1 \\ &\qquad\qquad\qquad\qquad 0 \leqslant n_2, t_2 \leqslant d_2 - 1 \end{aligned}\right\} \tag{2}$$

Nussbaumer and Quandalle (Ref. 5) expressed the two-dimensional convolution in Eq. (1) as a one-dimensional convolution of polynomials, i.e.,

$$\left.\begin{aligned} C_{n_1}(Z) &= \sum_{t_1=0}^{d_1-1} \left(\sum_{t_2=0}^{d_2-1} a_{t_1,t_2} Z^{t_2} \right) B_{(n_1-t_1)}(Z) \\ &\equiv \sum_{t_1=0}^{d_1-1} A_{t_1}(Z) B_{(n_1-t_1)}(Z) \bmod \left(Z^{d_2} - 1\right) \text{ for } 0 \leqslant n_1 \leqslant d_1 - 1 \end{aligned}\right\} \tag{3}$$

where $C_{n_1}(Z), A_{t_1}(Z), B_{t_1}(Z)$ are defined in Eq. (2) and $(n_1 - t_1)$ denotes the residue of $n_1 - t_1$ modulo d_1.

If $d_2 = 2^m$ and $d_1 = 2^{m-r+1}$ for $1 \leqslant r \leqslant m$, then one can factor $Z^{d_2} - 1$ into pairwise relatively prime factors as follows,

$$Z^{d_2} - 1 = \left(Z^{d_2/2} + 1\right)\left(Z^{d_2/2^2} + 1\right)\cdots\left(Z^{d_2/2^{r-1}} + 1\right)\left(Z^{d_2/2^r} + 1\right)\left(Z^{d_2/2^r} - 1\right)$$

Thus, Eq. (3) is equivalent to

$$C_{n_1}(Z) = \sum_{t_2=0}^{d_1-1} A_{t_1}(Z) B_{(n_1-t_1)}(Z) \bmod \left(Z^{d_2/2} + 1\right)\left(Z^{d_2/2^2} + 1\right)\cdots\left(Z^{d_2/2^r} + 1\right)\left(Z^{d_2/2^r} - 1\right) \tag{4}$$

Since $(Z^{d_2/2} + 1)$, $\cdots, (Z^{d_2/2^r} - 1)$ are pairwise relatively prime, by the Chinese remainder theorem (CRT) for polynomials (Ref. 7), the polynomial congruences

$$C^i_{n_1}(Z) \equiv C_{n_1}(Z) \bmod \left(Z^{d_2/2^i} + 1\right) \quad \text{for } i = 1, 2, \cdots, r \tag{5a}$$

and

$$C^*_{n_1}(Z) \equiv C_{n_1}(Z) \bmod \left(Z^{d_2/2^r} - 1\right) \tag{5b}$$

have a unique solution $C_{n_1}(Z)$ given by

$$C_{n_1}(Z) \equiv \sum_{i=1}^{r} C^i_{n_1}(Z)\left(-\frac{1}{2^i}\right)\frac{Z^{d_2} - 1}{Z^{d_2/2^i} + 1} + C^*_{n_1}(Z)\left(\frac{1}{2^r}\right)\frac{Z^{d_2} - 1}{Z^{d_2/2^r} - 1} \bmod Z^{d_2} - 1 \tag{6}$$

Note that the arithmetic needed to compute Eq. (6) requires only cyclic shifts and additions. The number of real additions needed to compute Eq. (6) is $2rd_2d_1$.

The derivation of $C^i_{n_1}(Z)$ in Eq. (5a) proceeds in the following manner:

$$C^i_{n_1}(Z) \equiv C_{n_1}(Z) \bmod \left(Z^{d_2/2^i} + 1\right)$$

$$\equiv \sum_{t_1=0}^{d_1-1} A_{t_1}(Z) B_{(n_1-t_1)}(Z) \bmod \left(Z^{d_2/2^i} + 1\right)$$

$$\equiv \sum_{t_1=0}^{d_1-1} A^i_{t_1}(Z) B^i_{(n_1-t_1)}(Z) \bmod \left(Z^{d_2/2^i} + 1\right) \tag{7}$$

where $A^{i}_{t_1}(Z)$ is defined by

$$A^{i}_{t_1}(Z) = \sum_{t_2=0}^{(d_2/2^i)-1} \left(a_{t_1,t_2} - a_{t_1,t_2+d_2/2^i} + a_{t_1,t_2+2d_2/2^i} \cdots \right.$$

$$\left. - a_{t_1,t_2+3d_2/2^i} + \cdots - a_{t_1,t_2(2^i-1)d_2/2^i} \right) Z^{t_2}$$

$$= \sum_{t_2=0}^{(d_2/2^i)-1} a^{i}_{t_1,t_2} Z^{t_2} \quad \text{for } 1 \leqslant i \leqslant r$$

and $B^{i}_{t_1}(Z)$ is obtained from the expression $A^{i}_{t_1}(Z)$ on replacing each $a_{i,j}$ by $b_{i,j}$, that is,

$$B^{i}_{t_1}(Z) = \sum_{t_2=0}^{(d_2/2^i)-1} b^{i}_{t_1,t_2} Z^{t_2} \quad \text{for } 1 \leqslant i \leqslant r$$

Note that $A^{i}_{t_1}(Z)$ and $B^{i}_{t_1}(Z)$ are, respectively, $A_{t_1}(Z)$ and $B_{t_1}(Z)$ reduced modulo $(Z^{d_2/2^i} + 1)$.

It was demonstrated in (Ref. 6) that a fast polynomial transform can be used to compute Eq. (7). Let us show this more carefully. Since $d_2 = 2^m$ and $d_1 = 2^{m-r+1}$ for $1 \leqslant r \leqslant m$, then $d_2/2^{i-1} = 2^{m-i+1} = 2^{r-i} \cdot 2^{m-r+1} = 2^{r-i} d_1$ for $i = 1, 2, \cdots, r$. Note the identity

$$Z^{d_2/2^{i-1}} \equiv \left(Z^{d_2/2^i}\right)^2 \equiv (-1)^2 \equiv 1 \bmod \left(Z^{d_2/2^i} + 1\right) \tag{8}$$

Also let $j = 2^{r-i}$ and define the d_1-point j^{th} power polynomial transform of $A^{i}_{t_1}(Z)$ and $B^{i}_{t_2}(Z)$ by

$$\tilde{A}^{i}_{k}(Z) \equiv \sum_{t_1=0}^{d_1-1} A^{i}_{t_1}(Z) (\tilde{Z})^{t_1 k} \equiv \sum_{\ell=0}^{(d_2/2^i)-1} \tilde{a}^{i}_{k,\ell} Z^{\ell} \bmod \left(Z^{d_2/2^i} + 1\right) \quad \text{for } 0 \leqslant k \leqslant d_1 - 1 \tag{9a}$$

and

$$\tilde{B}^{i}_{k}(Z) \equiv \sum_{t_1=0}^{d_1-1} B^{i}_{t_1}(Z) (\tilde{Z})^{t_1 k} \equiv \sum_{\ell=0}^{(d_2/2^i)-1} \tilde{b}^{i}_{k,\ell} Z^{\ell} \bmod \left(Z^{d_2/2^i} + 1\right) \quad \text{for } 0 \leqslant k \leqslant d_1 - 1, \tag{9b}$$

respectively, where $\tilde{Z} = Z^j$ is the j^{th} power of Z. Note by Eq. (8) that

$$\tilde{Z}^{d_1} \equiv Z^{jd_1} \equiv Z^{2^{r-i} d_1} \equiv Z^{d_2/2^{i-1}} \equiv 1 \bmod \left(Z^{d_2/2^i} + 1\right), \quad \text{for } i = 1, 2, \cdots, r$$

The product of the transforms $\tilde{A}_k^i(Z)$ and $\tilde{B}_k^i(Z)$ is given by

$$\tilde{C}_k^i(Z) \equiv \tilde{A}_k^i(Z) \cdot \tilde{B}_k^i(Z) \equiv \sum_{\ell=0}^{(d_2/2^i)-1} \tilde{c}_{k,\ell}^i Z^\ell \bmod \left(Z^{d_2/2^i} + 1\right) \quad \text{for } 0 \leqslant k \leqslant d_1 - 1, \; 1 \leqslant i \leqslant r \tag{10}$$

One needs now to compute the inverse transform of $\tilde{C}_k^i(Z)$. That is, to compute

$$C_{n_1}^i(Z) \equiv \frac{1}{d_1} \sum_{k=0}^{d_1-1} \tilde{C}_k^i(Z) \tilde{Z}^{-kn_1}$$

$$\equiv d_1^{-1} \sum_{k=0}^{d_1-1} \left(\sum_{s=0}^{d_1-1} A_s^i(Z) Z^{sk} \right) \cdot \left(\sum_{r=0}^{d_1-1} B_r^i(Z) Z^{rk} \right) \tilde{Z}^{-kn_1}$$

$$\equiv \sum_{s=0}^{d_1-1} \sum_{r=0}^{d_1-1} \tilde{A}_s^i(Z) \tilde{B}_r^i(Z) \frac{1}{d_1} \sum_{k=0}^{d_1-1} \tilde{Z}^{(s+r-n_1)k} \bmod \left(Z^{d_2/2^i} + 1\right) \tag{11}$$

Now let $t = s + r - n_1$ and note that

$$S \equiv \frac{1}{d_1} \sum_{k=0}^{d_1-1} \tilde{Z}^{tk} \equiv \frac{1}{d_1} \frac{\tilde{Z}^{td_1} - 1}{\tilde{Z}^t - 1}$$

$$\equiv \frac{1}{d_1} \frac{\left(Z^{jd_1}\right)^t - 1}{\tilde{Z}^t - 1} \equiv \frac{1}{d_1} \frac{\left(Z^{d_2/2^{i-1}}\right)^t - 1}{\tilde{Z}^t - 1} \equiv 0 \bmod \left(Z^{d_2/2^i} + 1\right) \quad \text{for } t \not\equiv 0 \bmod d_1$$

It is seen that $S = 1$ for $t \equiv 0 \bmod d_1$ and $S = 0$ for $t \not\equiv 0 \bmod d_1$. Hence Eq. (11) yields the desired result, namely,

$$C_{n_1}^i(Z) \equiv \sum_{t=0}^{d_1-1} A_{t_1}^i(Z) B_{(n_1-t_1)}^i(Z) \bmod \left(Z^{d_2/2^i} + 1\right) \quad \text{for } 0 \leqslant n_1 \leqslant d_1 - 1, \; 1 \leqslant i \leqslant r \tag{12}$$

where $(n_1 - t_1)$ denotes the residue of $(n_1 - t_1)$ modulo d_1.

Since $d_2 = 2^m$ and $d_1 = 2^{m-r+1}$ for $1 \leqslant r \leqslant m$ the analogue of the conventional FFT algorithm can be utilized to realize the needed polynomial transforms Eqs. (9a) and (9b) and its inverse defined by Eq. (11). That is, in Eq. (9a) let the input data to the usual FFT be replaced by a sequence of polynomials over C, and let w, the usual d_1-*th* complex root of unity, be replaced by $\tilde{Z}$, satisfying $\tilde{Z}^{d_1} = 1$, and finally let the arithmetic operations on the complex number field be replaced by arithmetic operations in the field of polynomials. Then the polynomial transforms in Eqs. (9a), (9b), and (11) can be computed by the conventional FFT algorithm. The polynomial transform, obtained in this manner, is called the fast polynomial transform (FPT). The number of

operations needed to perform the polynomial transform defined in Eq. (9a) requires only $(d_2/2) \cdot \log d_1$ cyclic shifts of polynomials and $2(d_2/2)\, d_1 \cdot \log d_1$ real additions.

To compute $\widetilde{C}_k^i(Z)$, given in Eq. (10) for $0 \leqslant k \leqslant d_1 - 1$, one needs to compute a polynomial product mod $Z^{d_2/2^i} + 1$. To do this directly takes a lengthy calculation. Using an idea, based on the work of Arambepola and Rayner (Ref. 6), this equation can be transformed into

$$\widetilde{C}_k^i(cu) = \widetilde{A}_k^i(cu) \cdot \widetilde{B}_k^i(cu) \bmod \left(u^{d_2/2^i} - 1\right) \tag{13}$$

by changing variables from Z to u with the mapping $Z = cu$, where c is *a* $d_2/2$*-th* primitive root of -1, i.e. $c^{d_2/2^i} = -1$. One can verify (Ref. 8) that the above polynomial product mod $u^{d_2/2^i} - 1$ can be obtained as a cyclic convolution of the two $d_2/2^i$-point coefficients of the polynomials $\widetilde{A}_k^i(cu)$ and $\widetilde{B}_k^i(cu)$. This is vastly simpler than finding the product modulo $Z^{d_2/2^i} + 1$.

In Eq. (13), one observes that

$$\widetilde{A}_k^i(cu) = \sum_{\ell=0}^{(d_2/2^i)-1} \widetilde{a}_{k,\ell}^i (cu)^\ell = \sum_{\ell=0}^{(d_2/2^i)-1} \hat{a}_{k,\ell}^i u^\ell$$

$$\widetilde{B}_k^i(cu) = \sum_{\ell=0}^{(d_2/2^i)-1} \widetilde{b}_{k,\ell}^i (cu)^\ell = \sum_{\ell=0}^{(d_2/2^i)-1} \hat{b}_{k,\ell}^i u^\ell \tag{14}$$

and

$$\widetilde{C}_k^i(cu) = \sum_{\ell=0}^{(d_2/2^i)-1} \widetilde{c}_{k,\ell}^i (cu)^\ell = \sum_{\ell=0}^{(d_2/2^i)-1} \hat{c}_{k,\ell}^i u^\ell$$

where $\hat{a}_{k,\ell}^i = c^\ell \widetilde{a}_{k,\ell}^i$, $\hat{b}_{k,\ell}^i = c^\ell \widetilde{b}_{k,\ell}^i$, and $\hat{c}_{k,\ell}^i = c^\ell \widetilde{c}_{k,\ell}^i$ for $0 \leqslant \ell \leqslant (d_2/2^i) - 1$. If one defines

$$\hat{A}_k^i(u) = \sum_{\ell=0}^{(d_2/2^i)-1} \hat{a}_{k,\ell}^i u^\ell, \quad \hat{B}_k^i(u) = \sum_{\ell=0}^{(d_2/2^i)-1} \hat{b}_{k,\ell}^i u^\ell;$$

$$\hat{C}_k^i(u) = \sum_{\ell=0}^{(d_2/2^i)-1} \hat{c}_{k,\ell}^i u^\ell \tag{15}$$

Then Eq. (13) becomes

$$\hat{C}_k^i(u) = \hat{A}_k^i(u)\, \hat{B}_k^i(u) \bmod \left(u^{d_2/2^i} - 1\right) \tag{16}$$

The polynomial multiplication in Eq. (16) can be computed by the cyclic convolution of the two $d_2/2^i$-point sequences, $(\hat{a}^i_{k,0}, \hat{a}^i_{k,1}, \cdots, \hat{a}^i_{k,d_2/2^{i-1}})$ and $(\hat{b}^i_{k,0}, \hat{b}^i_{k,1}, \cdots, \hat{b}^i_{k,d_2/2^{i-1}})$. This cyclic convolution can be written as

$$\hat{c}^i_{k,\ell} = \sum_{n=0}^{(d_2/2^i)-1} \hat{a}^i_{k,n}\, \hat{b}^i_{k,(\ell-n)} \quad \text{for } 0 \leqslant k \leqslant d_1 - 1, \quad 0 \leqslant \ell \leqslant d_2/2^i - 1 \tag{17}$$

where $(\ell - n)$ denotes the residue of $(\ell - n)$ modulo $d_2/2^i$ and $\hat{a}^i_{n,k}$ and $\hat{b}^i_{n,k}$ are the coefficients of the $\hat{A}^i_k(Z)$ and $\hat{B}^i_k(Z)$, respectively. The convolution $\hat{c}^i_{k,\ell}$ in Eq, (17) can be computed by using the conventional FFT (Ref. 9). Thus, the desired quantities in Eq. (15), i.e., $\tilde{c}^i_{k,\ell}$ for $0 \leqslant k \leqslant d_1 - 1$, $0 \leqslant \ell \leqslant d_2/2^i - 1$ are obtained from $\tilde{c}_{k,\ell} = c^{-\ell}\hat{c}^i_{k,\ell}$. The number of real multiplications and real additions needed to compute Eq. (5a) are $d_1(d_2/2^{i-2}) \cdot \log(d_2/2^i) + d_1 d_2/2^{i-2} + 8d_1(d_2/2^i - 1)$ and $2d_1 d_2 + (d_2/2^{i-2})d_1 \cdot \log d_1 + 6d_1(d_2/2^i) \cdot \log(d_2/2^i)$, for $i = 1, 2, \cdots, r$, respectively.

The flow chart for computing $C^i_n(Z)$ is given in Fig. 1.

Consider now the computation of $C^*_{n_1}(Z)$ in Eq. (5b). That is,

$$C^*_{n_1}(Z) = \sum_{t_1=0}^{d_1-1} A^*_{t_1}(Z)\, B^*_{(n_1-t_1)}(Z) \bmod \left(Z^{d_2/2^r} - 1\right) \tag{18}$$

where

$$A^*_{t_1}(Z) = \sum_{t_2=0}^{(d_2/2^r)-1} \left(a_{t_1,t_2} + a_{t_1,t_2+d_2/2^r} + a_{t_1,t_2+2d_2/2^r} + a_{t_1,t_2+3d_2/2^r} + \ldots + a_{t_1,t_2+(2^r-1)d_2/2^r}\right) Z^{t_2}$$

$$= \sum_{t_2=0}^{(d_2/2^r)-1} a^*_{t_1,t_2} Z^{t_2}$$

and $B^*_{t_1}(Z)$ is obtained from the expression $A^*_{t_1}(Z)$ on replacing each $a_{i,j}$ by $b_{i,j}$, that is,

$$B^*_{t_1}(Z) = \sum_{t_2=0}^{(d_2/2^r)-1} b^*_{t_1,t_2} Z^{t_2}$$

Evidently, $C^*_{n_1}(Z)$ in Eq. (18) is in the form of

$$C^*_{n_1}(Z) = \sum_{n_2=0}^{(d_2/2^r)-1} c^*_{n_1,n_2} Z^{t_2}$$

Note here that $A^*_{t_1}(Z)$ and $B^*_{t_1}(Z)$ are, respectively, $A_{t_1}(Z)$ and $B_{t_1}(Z)$ reduced modulo $Z^{d_2/2^i} + 1$.

In order to use the FPT technique to obtain Eq. (18), again use the idea of Arambepola and Rayner (Ref. 6). To compute Eq. (18), let $Z = cu$, where c is a $d_2/2^r$-*th* root of - 1. By an argument similar to that used to obtain Eq. (12), (18) becomes

$$C^*_{n_1}(cu) = \sum_{t_1=0}^{d_1-1} A^*_{t_1}(cu)\, B^*_{(n_1-t_1)}(cu) \bmod \left(u^{d_2/2^r} + 1\right) \quad \text{for } 0 \leqslant n_1 \leqslant d_1 - 1 \tag{19}$$

In Eq. (19), one observes that

$$\begin{aligned} A^*_{t_1}(cu) &= \sum_{t_2=0}^{(d_2/2^r)-1} a^*_{t_1,t_2}(cu)^{t_2} = \sum_{t_2=0}^{(d_2/2^r)-1} a'_{t_1,t_2} u^{t_2} \\ B^*_{t_1}(cu) &= \sum_{t_2=0}^{(d_2/2^r)-1} b^*_{t_1,t_2}(cu)^{t_2} = \sum_{t_2=0}^{(d_2/2^r)-1} b'_{t_1,t_2} u^{t_2} \end{aligned} \tag{20}$$

and

$$C^*_{n_1}(cu) = \sum_{n_2=0}^{(d_2/2^r)-1} c^*_{n_1,n_2}(cu)^{n_2} = \sum_{n_2=0}^{(d_2/2^r)-1} c'_{n_1,n_2} u^{n_2}$$

where $c'_{n_1,n_2} = c^{n_2} c^*_{n_1,n_2}$, $a'_{t_1,t_2} = c^{t_2} a^*_{t_1,t_2}$, and $b'_{t_1,t_2} = c^{t_2} b^*_{t_1,t_2}$ for $0 \leqslant n_1, t_1 \leqslant d_1 - 1, 0 \leqslant n_2, t_2 \leqslant d_2/2^r - 1$

In Eq. (20), define $A'_{t_1}(u) = A^*_{t_1}(cu)$, $B'_{t_1}(u) = B^*_{t_1}(cu)$, and $C'_{t_1}(u) = C^*_{n_1}(cu)$. Then Eq. (19) becomes

$$C'_{n_1}(u) = \sum_{t_1=0}^{d_1-1} A'_{t_1}(u)\, B'_{(n_1-t_1)}(u) \bmod \left(u^{d_2/2^r} + 1\right) \quad \text{for } 0 \leqslant n_1 \leqslant d_1 - 1$$

Using the same procedure used in the computation of Eq. (7), one obtains $C'_{n_1}(u)$. Hence, $c^*_{n_1,n_2}$ in Eq. (18) is obtained from the substitutions, $c^{-n_2} c'_{n_1,n_2}$. The number of real multiplications and real additions needed to compute Eq. (19) are $d_1 d_2/2^{r-2} + d_1 d_2/2^{r-2} \log(d_2/2^r) + 16\, d_1(d_2/2^r - 1)$ and $2d_1 d_2 + d_1(d_2/2^{r-2}) \log d_1 + 3\, d_1(d_2/2^{r-1}) \log(d_2/2^r)$, respectively. Hence the total number of real multiplications and real additions needed to compute Eq. (4) are $8\, d_1[(d_2/2^{r+1})(2^r(\log d_2 + 3) + 4) - (d_2 + r + 2)]$ and $2 \cdot d_1[d_2(2r-4) + d_2(2 \cdot \log d_1 - 1 + 3 \cdot \log d_2) + 6 \cdot d_2/2^r]$, respectively. The flowchart of this new algorithm is shown in Fig. 2.

In the introduction it was stated that transposition of the data matrix, usually required in two-dimensional convolution, can be avoided in this new algorithm. Assume the data matrix for a typical array such as a_{t_1,t_2}, $0 \leqslant t_i \leqslant d_i - 1$ for $i = 1,2$, is arranged with t_1 indexing the row, t_2 indexing the column. Then the polynomial $A_{t_1}(Z)$ of Eq. (2) is the $t_1{}^{th}$ row of this matrix. The FPT of $A_{t_1}(Z)$ can be implemented by a decimation-in-time algorithm analogous to the well-known conventional FFT one. An example is given in the Appendix. This requires that only two polynomials (or rows) need be available for processing at anytime and the resulting two polynomials can replace the input ones. Consequently, no additional storage is required for the FPT, and the

data array need only be accessed by rows with replacement after processing, thus obviating the accessing of individual columns usually done in two dimensional convolution.

In the Appendix, it is shown by an example how fast polynomial transforms can be combined with FFTs to yield a new fast algorithm for computing a two-dimensional convolution. The number of operations needed for this new algorithm to perform the two-dimensional convolutions of a $d_1 \cdot d_2$ array, where $d_2 = 2^m$ and $d_1 = 2^{m-r+1}$ for $1 \leqslant r \leqslant m$, is given in Table 1. In this table, the FPT-FFT algorithm and conventional FFT algorithm for computing the two-dimensional convolutions are compared by giving the number of operations to perform these algorithms.

Table 1. Complexity of new algorithm for two-dimensional convolutions

Convolution size $d = d_1 \times d_2 = 2^{m-r+1} \times 2^m$ for $1 \leqslant r \leqslant m$	FPT-FFT-algorithm			Radix-2 FFT algorithm	
	No. of factors of $z^{d_2-1}=r+1$	No. of real multiplication	No. of real addition	No. of real multiplication $4\,d_1d_2\,(\log d_2 + \log d_1 + 1)$	No. of real addition $6\,d_1d_2\,(\log d_2 + \log d_1) + 2\,d_1d_2$
$2^7 \times 2^9$	4	2,747,392	5,537,792	4,456,448	6,422,528
$2^7 \times 2^{10}$	5	5,892,096	12,288,000	9,437,184	13,631,488
$2^{11} \times 2^{11}$	2	234,831,872	457,179,136	385,875,968	562,036,736
$2^{10} \times 2^{11}$	3	109,019,136	222,298,112	184,549,376	268,435,456
$2^8 \times 2^{12}$	6	55,035,904	118,882,304	88,080,384	127,926,272
$2^8 \times 2^{13}$	7	117,948,416	258,342,912	184,549,376	268,435,456
$2^7 \times 2^{13}$	8	58,842,112	129,073,152	88,080,384	127,926,272

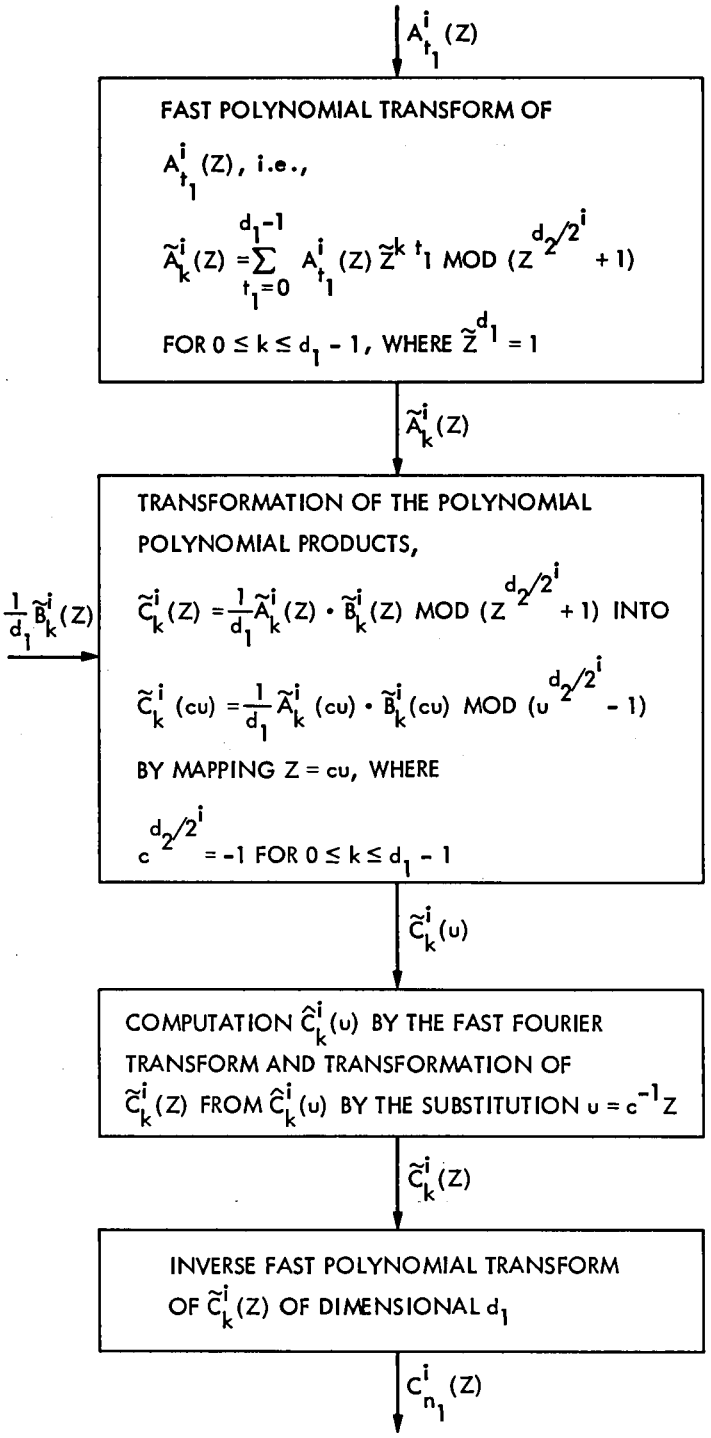

Fig. 1. Computation of the cyclic convolution of two Z-polynomials mod $Z^{d_2/2^i} + 1$, i.e., $C^i_{n_1}(Z)$ given in Fig. 2 by fast polynomial transforms

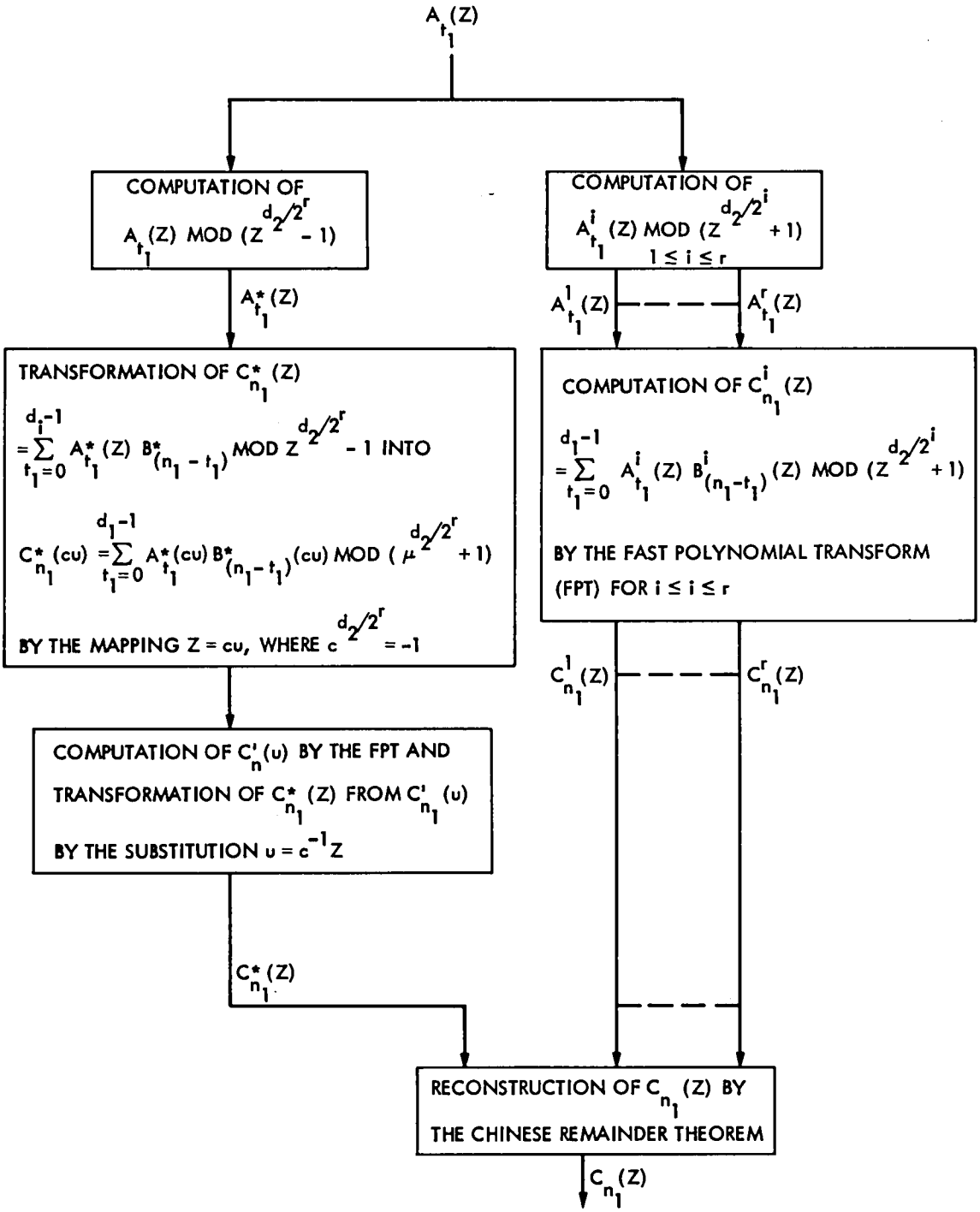

Fig. 2. Computation of a two-dimensional convolution of dimensional $d_1 x d_2$, where $d_2 = 2^m$ and $d_1 = 2^{m-r+1}$ for $1 \le r \le m$

Appendix

Example of a Two-Dimensional Convolution of Dimension Computed by the New Method

Example: Compute the two-dimensional cyclic convolution of two sequences a_{t_1,t_2} and b_{t_1,t_2}, i.e.,

$$c_{n_1,n_2} = \sum_{t_1=0}^{4-1} \sum_{t_2=0}^{4-1} a_{t_1,t_2}\, b_{(n_1-t_2),(n_2-t_2)} \quad \text{for } 0 \leqslant n_1,n_2 \leqslant 3 \tag{A-1}$$

where (x) denotes the residue of x modulo 4 and where $a_{0,0} = y_{0,0} = 1, a_{0,1} = b_{0,1} = 1, a_{0,2} = b_{0,2} = 0, a_{0,3} = b_{0,3} = 0, a_{1,0} = b_{1,0} = 1, a_{1,1} = b_{1,1} = 1, a_{1,2} = b_{1,2} = 1, a_{1,3} = b_{1,3} = 0, a_{2,0} = b_{2,0} = 0, a_{2,1} = b_{2,1} = 0, a_{2,2} = b_{2,2} = 0, a_{2,3} = b_{2,3} = 0, a_{3,0} = b_{3,0} = 0, a_{3,1} = b_{3,1} = 0, a_{3,2} = b_{3,2} = 0, a_{3,3} = b_{3,3} = 0.$

Define

$$A_{t_1}(Z) = \sum_{t_2=0}^{4-1} a_{t_1,t_2} Z^{t_2}, B_{t_1}(Z) = \sum_{t_2=0}^{4-1} b_{t_1,t_2} Z^{t_2};$$

$$C_{n_1}(Z) = \sum_{n_2=0}^{4-1} c_{n_1,n_2} Z^{n_2} \quad \text{for } 0 \leqslant n_1,t_1 \leqslant 3$$

That is, $A_0(Z) = B_0(Z) = 1 + Z, A_1(Z) = B_1(Z) = 1 + Z + Z^2, A_2(Z) = B_2(Z) = 0, A_3(Z) = B_3(Z) = 0$. From Eq. (4), (A-1) becomes

$$C_{n_1}(Z) = \sum_{t_1=0}^{4-1} A_{t_1}(Z)\; B_{(n_1-t_1)}(Z) \bmod (Z^2 - 1)(Z^2 + 1) \tag{A-2}$$

From Eqs. (5a) and (5b) one obtains

$$C^1_{n_1}(Z) = \sum_{t_1=0}^{4-1} A^1_{t_1}(Z)\, B^1_{(n_1-t_1)}(Z) \bmod (Z^2 + 1) \tag{A-3a}$$

where $A^1_0(Z) = B^1_0(Z) = 1 + Z, A^1_1(Z) = B^1_1(Z) = Z, A^1_2(Z) = B^1_2(Z) = 0, A^1_3(Z) = B^1_3(Z) = 0.$

and

$$C^*_n(Z) = \sum_{t_1=0}^{4-1} A^*_{t_1}(Z)\, B^*_{(n_1-t_1)}(Z) \bmod (Z^2 - 1) \tag{A-3b}$$

where $A^*_0(Z) = B^*_0(Z) = 1 + Z, A^*_1(Z) = B^*_1(Z) = 2 + Z, A^*_2(Z) = B^*_2(Z) = 0, A^*_3(Z) = B^*_3(Z) = 0.$

To compute Eq. (A-3a), one takes the Z polynomial transform of $A^1_{t_1}(Z)$ given by

$$\widetilde{A}_k(Z) = \sum_{t_1=0}^{4-1} A^1_{t_1}(Z) Z^{t_1 k} \bmod (Z^2 + 1)$$

The flowgraph of the decimation-in-time decomposition of a four-point polynomial transform computation is given in Fig. 1-A as $\widetilde{A}_0(Z) = 1 + 2Z$, $\widetilde{A}_1(Z) = Z$, $\widetilde{A}_2(Z) = 1$, and $\widetilde{A}_3(Z) = 2 + Z$. Similarly, the Z polynomial transform of $\widetilde{B}_k(Z)$ are $\widetilde{B}_0(Z) = 1 + 2Z$, $\widetilde{B}_1(Z) = Z$, $\widetilde{B}_2(Z) = 1$, and $\widetilde{B}_3(Z) = 2 + Z$.

Let

$$\widetilde{C}_k(Z) = \widetilde{A}_k(Z) \cdot \widetilde{B}_k(Z) \bmod (Z^2 + 1) \text{ for } k = 0, 1, 2, 3 \tag{A-4}$$

If one uses the mapping $Z = iu$, where $i^2 = -1$ then Eq. (A-4) becomes

$$\widetilde{C}_k(iu) = \widetilde{A}_k(iu) \cdot \widetilde{B}_k(iu) \bmod (u^2 - 1) \text{ for } 0 \leqslant k \leqslant 3 \tag{A-5}$$

For $t = 0$, Eq. (A-5) becomes

$$\widetilde{C}_0(iu) \equiv \widetilde{A}_0(iu) \cdot \widetilde{B}_0(iu) \equiv (1 + 2iu)(1 + 2iu) \bmod (u^2 - 1) \tag{A-6}$$

The FFT can be used to compute Eq. (A-6). That is, let $a_0 = 1, a_1 = 2i, b_0 = 1, b_1 = 2i$. The transform of a_n is

$$A_k = \sum_{k=0}^{2-1} a_n w^{nk} = \sum_{n=0}^{2-1} a_n (-1)^{nk} = 1 + 2i(-1)^k \quad \text{for } k = 0, 1 \tag{A-7}$$

The radix-2 FFT algorithm is used to compute Eq. (A-7). The results are $A_0 = 1 + 2i$ and $A_1 = 1 - 2i$. Similarly, one obtains $B_0 = 1 + 2i$ and $B_1 = 1 - 2i$. Let $C_0 = A_0 \cdot B_0 = -3 + 4i$, and $C_1 = A_1 \cdot B_1 = -3 - 4i$. The inverse Fourier transform of C_k is

$$\begin{aligned} c_n &= 2^{-1} \sum_{k=0}^{2-1} c_k w^{-nk} = 2^{-1} \sum_{k=0}^{2-1} c_k (-1)^{-nk} \\ &= 2^{-1} [(-3 + 4i) + (-3 - 4i)(-1)^{-n}] \quad \text{for } n = 0, 1 \end{aligned} \tag{A-8}$$

Again, the radix-2 FFT algorithm is used to compute Eq. (A-8). That is, $c_0 = -3$ and $c_1 = 4i$. Thus, $\widetilde{C}_0(iu) = -3 + 4iu \bmod (u^2 - 1)$. Hence, one obtains $\widetilde{C}_0(Z) = -3 + 4i^{-1}iZ = -3 + 4Z \bmod (Z^2 + 1)$.

Similarly one obtains $\widetilde{C}_1(Z) = -1$, $\widetilde{C}_2(Z) = 1$, and $\widetilde{C}_3(Z) = 3 + 4Z$. The inverse polynomial transform of $\widetilde{C}_k(Z)$ is given by

$$C^1_{n_1}(Z) = 4^{-1} \sum_{k=0}^{4-1} \widetilde{C}_k(Z) \cdot Z^{-n_1 k} \tag{A-9}$$

The FPT is used to compute Eq. (A-9). The results in Eq. (A-3) are $C^1_0(Z) = 2Z$, $C^1_1(Z) = -2 + 2Z$, $C^1_2(Z) = -1$, and $C^1_3(Z) = 0$.

To compute Eq. (A-3b), one needs to use the mapping $Z = iu$. Then Eq. (A-3b) becomes

$$C^*_{n_1}(iu) \equiv \sum_{t_1=0}^{4-1} A^*_{t_1}(iu)\, B^*_{(n_1-t_1)}(iu)$$

$$\equiv c^*_{n_1,0} + i\, c^*_{n_1,1}\, u \mod (u^2+1) \quad \text{for } 0 \leqslant n_1 \leqslant 3 \tag{A-10}$$

where $A^*_0(iu) = B^*_0(iu) = 1 + iu$, $A^*_1(iu) = B^*_1(iu) = 2 + iu$, $A^*_2(iu) = B^*_2(iu) = 0$, $A^*_3(iu) = B^*_3(iu) = 0$.

Let $A'_0(u) = B'_0(u) = 1 + iu$, $A'_1(u) = B'_1(u) = 2 + iu$, $A'_2(u) = B'_2(u) = 0$, $A'_3(u) = B'_3(u) = 0$ and $C'_{n_1}(u) = c'_{n_1,0} + c'_{n_1,0}u$ for $0 \leqslant n_1 \leqslant 3$, where $c'_{n_1,0} = c^*_{n_1,0}$ and $c'_{n_1,1} = ic^*_{n_1,0}$. Hence, Eq. (A-10) becomes

$$C'_{n_1}(u) = \sum_{t_1=0}^{4-1} A'_{t_1}(u)\, B'_{(n_1-t_1)}(u) \bmod (u^2+1) \tag{A-11}$$

Equation (A-11) can be computed by the FPT. This yields $C'_0(u) = 2 + 2iu$, $C'_1(u) = 6 + 6\,iu$, $C'_2(u) = 5 + 4\,iu$, and $C'_3(u) = 0$. Hence

$$C^*_0(Z) = C'_0(i^{-1}Z) = 2 + 2Z,\ C^*_1(Z) = C'_1(i^{-1}Z) = 6 + 6Z;$$

$$C^*_2(Z) = C'_2(i^{-1}Z) = 5 + 2Z,\ C^*_3(Z) = C'_3(i^{-1}Z) = 0 \tag{A-12}$$

From Eq. (6), one obtains

$$C_{n_1}(Z) = \frac{1}{2}\left[C^*_{n_1}(Z)\,(Z^2+1) + C^1_{n_1}(Z)\,(1 - Z^2)\right] \mod (Z^4 - 1)$$

$$\text{for } 0 \leqslant n_1 \leqslant 3$$

where $C^1_{n_1}(Z)$ and $C^*_{n_1}(Z)$ are defined in Eqs. (A-3a) and (A-3b), respectively. Thus, the desired results are $C_0(Z) = 1 + 2Z + Z^2$, $C_1(Z) = 2 + 4Z + 4Z^2 + 2Z^3$, $C_2(Z) = 2 + 2Z + 3Z^2 + 2Z^3$, and $C_3(Z) = 0$. Hence $c_{0,0} = 1, c_{0,1} = 2, c_{0,2} = 1, c_{0,3} = 0, c_{1,0} = 2, c_{1,1} = 4, c_{1,2} = 4, c_{1,3} = 2, c_{2,0} = 2, c_{2,1} = 2, c_{2,2} = 3, c_{2,3} = 2, c_{3,0} = 0, c_{3,1} = 0, c_{3,2} = 0$, and $c_{3,3} = 0$.

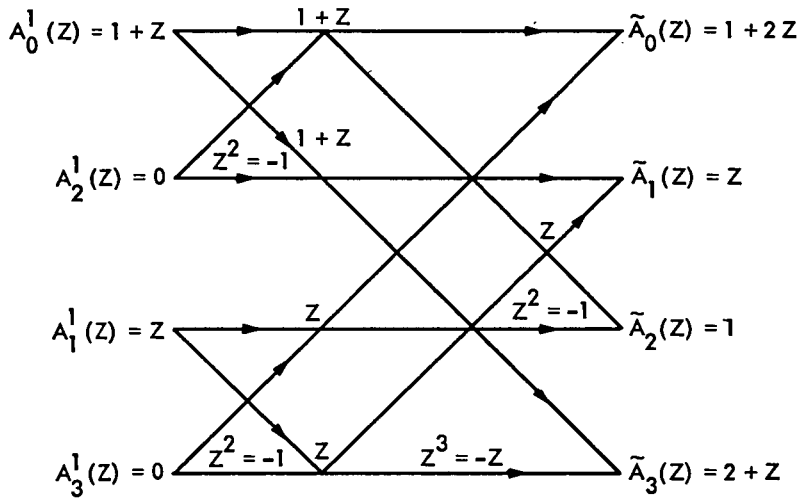

Fig. 1A. Example of four-point fast polynomial transform

References

1. Wu, C., "A Digital System to Produce Imagery from SAR Data," *AIAA Systems Design Driven by Sensors*, Pasadena, California, October 18-20, 1976.

2. Tomiyasu, K., "Tutorial Review of Synthetic – Aperture Radar (SAR) With Applications to Imaging of the Ocean Surface," *Proceedings of the IEEE*, Vol. 66, No. 5, May 1978, pp. 563-583.

3. Rader, C. M., "On the Application of the Number Theoretic Methods of High-Speed Convolution to Two-Dimensional Filtering," *IEEE Trans. Acoust. Speed Signal Processing ASSP-23*, 575 (1975), pp. 575.

4. Reed, I. S., Truong, T. K., Kwoh, Y. S., and Hall, E. L., "Image Processing by Transforms Over a Finite Field," *IEEE Transactions on Computers*, Vol. C-26, No. 9, September 1977, pp. 874-881.

5. Nussbaumer, H. J., and Quandalle, P., "Computation of Convolutions and Discrete Fourier Transforms by Polynomial Transforms," *IBM J. Res. Develop.*, Vol. 22, No. 2, Mar. 1978, pp. 134-144.

6. Arambepola, B., and Rayner, P. J. W., "Efficient Transforms for Multidimensional Convolutions," *Electronics Letters*, 15 March 1979, Vol. 15, No. 6, pp. 189-190.

7. Berlekamp, E. R., *Algebraic Coding Theory*, McGraw-Hill Book Company, New York, 1968.

8. Pollard, J. M., "The Fast Fourier Transform in a Finite Field," *Math Comput.*, Vol. 25, No. 114, April 1971, pp. 365-374.

9. Cooley, J. W., and Tukey, J. W., "An Algorithm for the Machine Calculation of Complex Fourier Series," *Math Comput.*, Vol. 19, April 1965, pp. 297-301.

Deep Space Station (DSS 13) Automation Demonstration

D. S. Remer
Communications Systems Research Section
and Harvey Mudd College

G. Lorden
California Institute of Technology

This article summarizes the data base collected during a six month demonstration of an automated Deep Space Station (DSS 13) run unattended and remotely controlled from JPL in Pasadena. During this period, DSS 13 received spacecraft telemetry data from Voyager, Pioneers 10 and 11, and Helios projects. Corrective and preventive maintenance are reported by subsystem including the traditional subsystems and those subsystems added for the automation demonstration.

Operations and maintenance data for a comparable manned Deep Space Station (DSS 11) are also presented for comparison. The data suggests that unattended operations may reduce maintenance manhours in addition to reducing operator manhours. Corrective maintenance for the unmanned station was about one third of the manned station, and preventive maintenance was about one half.

I. Introduction

Since the mid 1960's there has been a strong effort to reduce the crew size of the Deep Space Stations in order to improve the cost effectiveness of DSN use of NASA resources for tracking and data acquisition. This program has been very successful, as summarized in Fig. 1, where we can see an 80 percent reduction in DSS 12 crew size since 1967.

A research task was started several years ago to extend this effort to running an unattended, fully automated Deep Space Station. It was also hoped that automation would improve network productivity by increasing the time available to the end user. Automation would reduce the time required for check out and calibration, and eliminate the time for operator training. Finally, DSN reliability might be enhanced by reducing the human operator interface. To meet these goals, DSS 13 has been automated and was operated in an unattended mode for telemetry reception during the last half of calendar year 1978. Only downlink capability was available during the demonstration, up-link capability is now being implemented, and further demonstrations are planned for 1980. These demonstrations will provide information useful in determining if automation should be implemented throughout the DSN.

The purpose of this article is to summarize the data taken during the six-month automation demonstration in 1978. Several previous articles (Refs. 1-3) have described the initial data during the early part of this demonstration.

The first article (Ref. 1) was prepared prior to the start of the demonstration in order to outline what data should be collected, how the data would be analyzed, and what we could and could not learn from the unattended operations demonstration at DSS 13.

The second article (Ref. 2) presented an initial 9 week data base of life-cycle cost parameters that were collected at a manned station (DSS 11). This work was started prior to the DSS 13 unattended demonstration in order to debug the data collection procedure and to develop a benchmark for comparison with the results from the unattended operations demonstration at DSS 13.

The third article (Ref. 3) presented the initial results for preventive and corrective maintenance based on the first 15 weeks of the unattended operations demonstration at DSS 13. During this period, DSS 13 had been receiving spacecraft telemetry while being remotely controlled from JPL in Pasadena. The overall maintenance manhours for the manned station (DSS 11) were found to be higher than for the unmanned station (DSS 13).

In this article, we will summarize the results of the entire six months of data collected at both DSS 11 and DSS 13 during the first unattended operations demonstration.

II. Description of the Unattended Deep Space Station

DSS 13, a 26-meter antenna station at Goldstone, is being developed as the test bed for the unattended, automated mode of operation. The on-line telemetry data acquisition capability was implemented in mid 1978. Central control and monitor are exercised by an operator at the Network Operation Control Center (NOCC) at JPL in Pasadena via high-speed data lines to Goldstone. The operator enters configuration control and predicts. Monitor data are also available to the operator. The station is powered up and checked out, spacecraft telemetry is acquired and tracked, and the station is shut down, all by remote control from Pasadena without an operator at the station. There is also automatic antenna shutdown capability in case of high winds or certain servo drive failures.

The DSS 13 telemetry stream is sent to DSS 12 (or DSS 11) for bit detection and then to the flight project at JPL via high-speed data lines. Implementation is now underway so that bit detection can be performed at DSS 13.

The unattended operations design at DSS 13 uses microprocessors or minicomputers on each controlled subsystem for configuration control, monitoring, calibration, and checkout. A central station microprocessor is used for supervision of subsystem monitor and control processors.

At present, the antenna, microwave, and receiver subsystems are under centralized control. The 100-kilowatt S-band transmitter and exciter subsystem are being added now. During the past unattended operations demonstration at DSS 13, telemetry data was provided for the Voyager, Pioneers 10 and 11, and Helios projects.

An overview of the station control and system technology is shown in Fig. 2.

III. DSS 11 Data Base

Data were collected at DSS 11 from May 14, 1978 through December 31, 1978. During the nine-week period of May 14, 1978, to July 9, 1978, a preliminary data base was collected on the operation of DSS 11. This initial data base was described in a previous article (Ref. 2) and served three purposes. First, it allowed us to check the data base requirements outlined in an earlier article (Ref. 1) and make necessary adjustments. Second, it served as a way to check out the data collection procedure, and finally, it was a bench mark to compare to subsequent data obtained from both DSS 11 and DSS 13 during the actual automation demonstration. Data base requirements for this initial test period and for the rest of the demonstration were reduced because no additional station data could be collected or special data sheets introduced at DSS 11 over and above what was normally provided at the station.

Routine data was collected by DSS 11 operations and then screened by the DSS 13 Station Manager, who then culled out the data requested for analysis. This input data was received in a format similar to those shown in Tables 1 and 2. The resulting DSS 11 data base for the 25 week period of July 16, 1978 to December 31, 1978 is summarized below.

A. Station Operating Hours and Telemetry Hours

The station operating hours (SOH) during the entire demonstration period were 160 hours per week at DSS 11. SOH are defined at those hours when a station is required to be available to conduct DSN activities.

Telemetry reception averaged 88.1 hours per week with a standard deviation of 14.1 hours per week. Telemetry hours varied from a low value of 44.6 hours per week to a high value of 102.9 hours per week. During this 25 week period, the telemetry reception hours averaged 55 percent of the SOH with a range of 28 to 64 percent.

Average Station Operating Hours (SOH)/week	160
Average Telemetry Hours/week	88.1
Telemetry Hours as a percent of SOH	55%

For the purposes of this study we defined "good telemetry" reception hours as the data received when the Telemetry Processor Assembly (TPA) was in lock. A summary of the telemetry hours during this period are shown in Fig. 3.

B. Maintenance, Operations, and Training Manhours

The average manhours per week for operations, training, and maintenance is shown below and the week to week variations are shown in Fig. 4. Note that operation manhours are about half of the total manhours. Also, the maintenance manhours are split almost evenly between corrective maintenance and preventive maintenance, as indicated below.

	Average Manhours Per Week	Percent of Total Manhours
Operation Manhours	373.1	51.7
Training Manhours	156.2	21.7
Corrective Maintenance Manhours	97.7	13.5
Preventive Maintenance Manhours	94.2	13.1
	721.2	100.0

An interesting observation is that there are almost three times as many manhours for operations and training as for maintenance. Since automation essentially eliminates operators and therefore operator training, the potential M&O manpower savings is about 70-75 percent.

Although automation has a large impact on reducing operations manhours, the impact of automation on maintenance manhours was not clear before the demonstration. There is the potential for designing automated systems to improve isolation and diagnosis of failures. On the other hand, there is the need to maintain the additional equipment required for automation. As will be seen later, in addition to operations manpower, maintenance manpower also appears to be reduced for an automated station.

In the listing below, note that the coefficient of variation, which is the standard deviation as a percent of the average, increases from 15.9 percent for telemetry hours to a high of 57.7 percent for corrective maintenance manhours. As expected, both preventive and corrective maintenance manhours are more variable than either operating or training manhours.

	Average Per Week	Standard Deviation	Coefficient of Variation
Telemetry Hours	88.1	14.1	15.9%
Operation Manhours	373.1	69.9	18.7%
Training Manhours	156.2	47.2	30.2%
Preventive Maintenance Manhours	94.2	30.5	32.4%
Corrective Maintenance Manhours	97.7	56.4	57.7%

C. Tracking

The number of tracks per week at DSS 11 varied between 6 and 19 with an average of 13.5. The data lost per week varied from a low of 0.6 hours to a high of 5.4 hours with an average loss of 2.4 hours per week or 11 minutes per track. The variation in number of tracks per week is shown in Fig. 5.

Good telemetry data averaged 88 hours per week, and the lost data of 2.4 hours per week represents about 2.7 percent of the data. This is a low number for data lost because it only accounts for lost data when the TPA was out of lock. Additional losses, such as between Goldstone and NOCC via the high-speed data line, are not included in the above data.

The average weekly precal time per track was 54 minutes with a range of 31 to 108 minutes per track. Since the average length of a telemetry track, excluding precal, was 6.5 hours and the average precal per track was 0.9 hours, the time for precal is about 14 percent of the telemetry time. This is a significant amount of time which can be reduced by automation. The variation in precal time per track is shown in Fig. 6.

D. Cost Parameters

Let's now turn our attention from manhours to costs, specifically telemetry hourly M&O cost and station hourly M&O cost. Actual hourly labor costs that included contractor and JPL burden were used. These hourly costs are a weighted composite of the actual straight time and overtime costs.

The following life cycle cost parameters were calculated to compare the maintenance and operations manpower costs at a station per telemetry hour and per station operating hour (SOH). Note that only manpower costs are included in the analysis.

About 70 percent of the total manpower cost is associated with operations and operations training. Thus, for an automated station, about 70 percent of the manpower costs may be eliminated.

	Average Manpower Cost per Telemetry Hour	Average Manpower Cost per Station Operating Hour
Corrective Maintenance	$ 16.41	$ 8.71
Preventive Maintenance	14.56	8.02
Operations	56.71	31.22
Training	23.74	13.07
Total	$111.42	$61.02

In the next section, we will look at data from DSS 13 during the unattended demonstration.

IV. DSS 13 Maintenance Data Base

The maintenance data base for DSS 13 under remote, automated operation from NOCC during the period from 10/1/78 to 12/3/78 is summarized in Tables 3 and 4. A previous article (Ref. 3) summarizes data during the period from 6/18/78 to 9/24/78. The data are tabulated in weekly increments. Corrective maintenance by subsystem is shown in Table 3 and preventive maintenance in Table 4. A footnote designator "a" next to the DSS 13 subsystem (in Tables 3 and 4) indicates that this equipment was added for this unattended demonstration. The data were supplied by the DSS 13 Station Manager on a data sheet shown in Table 5 of Ref. 2.

A. Corrective Maintenance

The corrective maintenance at DSS 13 averaged 24.3 manhours per week during the unattended period of 6/18/78 to 12/31/78. Shown below is the percent of corrective maintenance manhours for each subsystem.

Subsystem	DSS 13 Corrective Maintenance Manhours (%)
Antenna Electronic Systems	50.3
Block III SDA	9.4
Block III Receiver	8.8
Antenna Hydraulic Systems	7.9
Maser Compressor	5.2
Antenna Terminet	5.1
108 KHz Subcarrier Oscillator (microwave link transmission)	4.5
Antenna Clock	2.9
Control Computer (MODCOMP II/25)	2.8
Microwave Link Channel	1.4
Maser Refrigerator	1.3
Other	0.4
	100.0

Note that the antenna electronic systems accounted for half of the total corrective maintenance manhours. The rest of the corrective maintenance is spread over many subsystems. For example, each of the following subsystems accounted for about 5-10 percent of the overall corrective maintenance: the Block III Subcarrier Demodulator Assembly (SDA), the Block III Receiver, the Antenna Hydraulic Systems, the maser compressor, the antenna terminet, and the 108 kHz subcarrier oscillator. Almost half of the subsystems summarized in Table 3 required no corrective maintenance.

B. DSS 13 Preventive Maintenance

The preventive maintenance at DSS 13 averaged 36.7 manhours per week. Shown below is the percent of preventive maintenance manhours for each subsystem during the period of 6/18/78 to 12/31/78.

Subsystem	DSS 13 Preventive Maintenance Manhours (%)
Antenna Hydraulic Systems	49.1
Antenna Electronic Systems	17.8
Maser Compressor	8.0
Control Computer (MODCOMP II/25)	6.8
Block III Receiver	6.0
Block III SDA (Microwave Link Transmission)	4.6
Maser Refrigerator	3.6
108 KHz Subcarrier Oscillator (Microwave Link Transmission)	3.1
Microwave Link Channel	0.6
Station Controller (8080 Based Microcomputer)	0.4
	100.0

The Antenna Hydraulic Systems accounted for almost half of the preventive maintenance manhours. About half of the subsystems received no preventive maintenance during this period, as shown in Table 4.

C. Comparison of Corrective and Preventive Maintenance

The antenna electronic and hydraulic subsystems had vastly different percentages of corrective and preventive maintenance as shown below.

Subsystem	Percent of Total Corrective Maintenance	Percent of Total Preventive Maintenance
Antenna Electronic System	50.3	17.8
Antenna Hydraulic System	7.9	49.1

For example, while the Antenna Electronic System accounted for 50.3 percent of the total corrective maintenance manhours, this system only received 17.8 percent of the total preventive maintenance manhours. On the other hand, the Antenna Hydraulic System received 49.1 percent of the total preventive maintenance manhours and only 7.9 percent of the corrective maintenance manhours. Perhaps there could be a shift in preventive maintenance to reflect corrective maintenance experience in order to optimize the overall maintenance effort.

D. Maintenance for the Traditional Subsystems versus the Subsystems Added for This Demonstration

The subsystems added for this demonstration are shown by the footnote designators "a" in Tables 3 and 4. The percent of preventive maintenance for these subsystems is shown below for the third and fourth calendar quarter of 1978.

	Preventive Maintenance %	
	3Q78	4Q78
Subsystems added for this demonstration	10.6	11.4
Traditional subsystems	89.4	88.6
	100.0	100.0

The subsystems added for this demonstration received only about 11 percent of the total preventive maintenance.

The corrective maintenance for these added subsystems as reported in a previous article (Ref. 3) was 28.9 percent of the total corrective maintenance during the first half of the unattended demonstration. However, there was a very sharp drop to only 6.6 percent of the total corrective maintenance for these subsystems during the second half of the demonstration as shown below.

	Corrective Maintenance %	
	3Q78	4Q78
Subsystems added for this demonstration	28.9	6.6
Traditional subsystems	71.1	93.4
	100.0	100.0

This is a very encouraging result and is evidently due to debugging the new equipment and also to a possible maintenance learning curve.

V. Comparison of Maintenance and Operations Manhours at DSS 11 and DSS 13 for Telemetry Reception

A. Comparison of Maintenance Manhours

The average weekly maintenance manhours for DSS 11 and DSS 13 are shown below for the period of 7/2/78 through 12/31/78.

	Average Weekly Manhours	
	DSS 11	DSS 13
Corrective Maintenance	94.7	24.5
Preventive Maintenance	91.1	35.7
	185.8	60.2

Both the corrective and preventive maintenance manhours at DSS 11 are more than at DSS 13. However, DSS 11 has more equipment than DSS 13. For example, DSS 11 has two receivers, two SDA's, two masers, etc., whereas DSS 13 has only one of each. By doubling the DSS 13 maintenance figures for these subsystems, we arrived at the following comparison.

	Average Weekly Manhours for "comparable" systems	
	DSS 11	DSS 13
Corrective Maintenance	94.7	30.6
Preventive Maintenance	91.1	43.6
	185.8	74.2[a]

[a](39.9% of 185.8)

This comparison is based on the conservative assumption that if DSS 13 had had two SDA's, for example, then the preventive and corrective maintenance for SDA's would have been doubled at DSS 13. In actual practice, this factor should be somewhere between one and two. However, even with this conservative assumption, the corrective maintenance at DSS 13 only increased by 24.7 percent and the preventive maintenance by 22.2 percent. For comparable systems, we see in the above table that the preventive maintenance manhours at DSS 13 are about 1/2 of DSS 11 and the corrective maintenance manhours at DSS 13 are about 1/3 of DSS 11. A weekly comparison of corrective maintenance at DSS 11 and DSS 13 is shown in Fig. 7 and similar data for preventive maintenance is shown in Fig. 8.

B. Comparison of Operations Manhours

The average manpower used for operations at DSS 11 is 373 manhours per week. On the other hand, DSS 13 was run unattended and remotely from NOCC in Pasadena. If we conservatively assume that this remote operation takes 50 percent of the time of one operator at NOCC, then the DSS 13 operations manpower requirement is 80 manhours per week or about 1/5 of the operations manpower at DSS 11. As a result, it would be reasonable to assume a corresponding 80-percent reduction in operator training for an automated station versus current station operation. Operator training averaged 156 manhours per week at DSS 11.

C. Limitation of Results

The data suggests that unattended operations may reduce maintenance manhours. There are other factors, however, that may substantially affect comparisons between the two stations in total maintenance manhours and the split between preventive and corrective maintenance. DSS 13 has substantially different equipment and a different schedule of operations from DSS 11. In addition, the two stations have different types of personnel, whose methods of operation are not the same. For example, DSS 13 station personnel do almost all the corrective maintenance and preventive maintenance at the station, whereas DSS 11 personnel do hardly any corrective maintenance and about 84 percent of the preventive maintenance, leaving the rest to the Maintenance and Integration team for the DSN Complex. Preventive maintenance manhours are particularly hard to compare because preventive maintenance is a discretionary activity which may be handled differently by an operating station like DSS 11 and a research and development station like DSS 13. Furthermore, system performance verification is more stringent at DSS 11 than at DSS 13. These caveats are quite important when viewing the results.

Acknowledgment

We want to thank Earl Jackson for supplying the DSS 11 and DSS 13 data and for providing insight into station operation.

References

1. Remer, D. S., Eisenberger, I., and Lorden, G., "Economic Evaluation of DSS 13 Unattended Operations Demonstration," in *The Deep Space Network Progress Report 42-45*, Jet Propulsion Laboratory, Pasadena, CA, March and April 1978, pp. 165-171.

2. Remer, D. S. and Lorden, G., "Initial Economic and Operations Data Base for DSS 13 Automation Test," in *The Deep Space Network Progress Report 42-49*, Jet Propulsion Laboratory, Pasadena, CA, November and December 1978, pp. 78-85.

3. Remer, D. S. and Lorden, G. "Preliminary Maintenance Experience for DSS 13 Unattended Operations Demonstration," in *The Deep Space Network Progress Report 42-51*, Jet Propulsion Laboratory, Pasadena, CA, March and April 1979, pp. 150-155.

Table 1. DSS 11 operations data sheet

[a]Week Ending Date	_____
[a]Operations Manhours for the Week	_____
Preventive Maintenance Manhours	_____
[a]Maintenance & Integration Team	_____
[a]Station Personnel	_____
Total	_____
Corrective Maintenance Manhours (Requiring no Station Downtime)	
[a]Maintenance & Integration Team	_____
Station Personnel	_____
Total	_____
Corrective Maintenance Manhours (Requiring Station Downtime)	_____
[b]Pre-Calibration Hours for the Week	_____
Post Calibration Hours for the Week	_____
[a]Training Manhours	_____
[a]Downtime hours During Scheduled Operations	_____

[a]Represents data usually received
[b]These numbers are calculated from data in Table 2

Table 2. DSS 11 tracking data sheet

[a]Day of the Year (DOY)	_____
[a]Spacecraft ID	_____
[a]Pre-Cal Start Time	_____
Pre-Cal End Time	_____
Antenna to Point Time	_____
[a]Receiver 1 In-Lock Time	_____
Receiver 2 In-Lock Time	_____
[a]SSAI In-Lock Time	_____
[a]SSA2 In-Lock Time	_____
[a]"Good" Telemetry Start Time	_____
[a]"Good" Telemetry End Time	_____
[a]Data Lost in Minutes	_____
Post Cal Start Time	_____
Post Cal End Time	_____
[b]Tracking for this Pass in Minutes	_____
[a]Scheduled Operating Hours for the Week	_____
[a]End User Hours for the Week	_____
[b]Telemetry Reception Hours for the Week	_____

[a]Represents data usually received
[b]These numbers are calculated from the data in this Table

Table 3. DSS 13 corrective maintenance activities in manhours, 1978

Maintenance	10/1	10/8	10/15	10/22	10/29	11/5	11/12	11/19	11/26	12/3	12/10	12/17	12/24	12/31	Total
26-m Antenna															
Hydraulic Systems	2.0	3.4				3.0			4.0	8.0			0.5		20.5
Electronic Systems	4.0	3.0	2.0	1.0	19.5	37.0	35.5	39	16.0	13.5	39.0	15.0	3.0		227.5
[a]Control Computer (MODCOMP II/25)		11.0													11.0
[a]Clock															
[a]Terminet										4.5	5.5	0.5			10.5
[a]Microprocessor										1.0					1.0
Waveguide Configuration Assembly															
Low Noise Amplifier (Maser)															
Maser Compressor	21.0		1.3		2.0	1.5	0.5	6.5				1.5	0.5		34.8
Refrigerator	1.0			3.0					1.0	3.0	1.5				9.5
Block III Receiver						8.0	16.5	5.0	13.0	3.0	1.0			1.5	48.0
Block III SDA			2.0		0.5	1.5	2.5		1.5	1.0					9.0
[a]108 KHz Subcarrier Oscillator (Microwave Link Transmission)															
[a]Station Controller (8080 Based Microcomputer)							2.0								2.0
Star Switch Controller															
[a]SDA Controller															
[a]Block III Receiver Controller															
[a]Waveguide Configuration Assembly Controller															
High Speed Data Line Data Set Microwave Link Channel															
Total	28.0	17.0	5.3	4.0	22.0	51.0	57.0	50.5	35.5	34.0	47.0	17.0	4.0	1.5	373.8

[a]Equipment added for automation demonstration

Table 4. DSS 13 preventive maintenance activities in manhours, 1978

Maintenance	10/1	10/8	10/15	10/22	10/29	11/5	11/12	11/19	11/26	12/3	12/10	12/17	12/24	12/31	Total
26-m Antenna															
Hydraulic Systems	13.0	7.5	26.0	29.0	27.0	30.0	27.0	25.0	25.0	21.0	18.0	5.0	5.0	4.0	262.5
Electronic Systems	6.5	5.3		12.0	8.5	4.5	4.0	5.0		0.5	7.5	14.0	22.5	8.0	98.3
[a]Control Computer (MODCOMP II/25)	26.2		12.3	1.5	4.0	2.0									46.0
[a]Clock															
[a]Terminet															
[a]Microprocessor															
Waveguide Configuration Assembly															
Low Noise Amplifier (Maser)															
Maser Compressor	2.0	7.0	1.0	1.5	1.0				1.0		0.5	1.0	2.5	2.0	19.5
Refrigerator	1.0	3.5		4.0	0.5			2.5	1.0	3.0					15.5
Block III Receiver	1.5	5.0	0.5	0.5	1.0			2.0		0.5			0.5		11.5
Block III SDA	1.0	0.5	1.5	1.0	1.0	1.5	2.0	1.0					0.5	0.5	10.5
[a]108 KHz Subcarrier Oscillator (Microwave Link Transmission)				1.0		2.5									3.5
[a]Station Controller (8080 Based Microcomputer)															
Star Switch Controller															
[a]SDA Controller															
[a]Block III Receiver Controller															
[a]Waveguide Configuration Assembly Controller															
High Speed Data Line															
Data Set															
Microwave Link Channel					1.5	2.5	0.5								4.5
Total	51.2	28.8	41.3	50.5	44.5	43.0	33.5	35.5	27.0	25.0	26.0	20.0	31.0	14.5	471.8

[a]Equipment added for automation demonstration

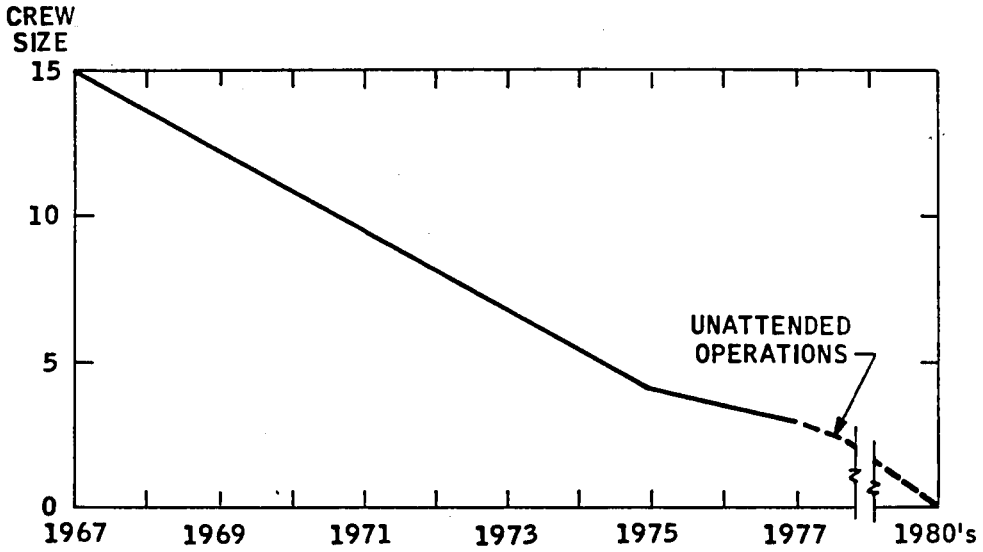

Fig. 1. DSS 12 crew size

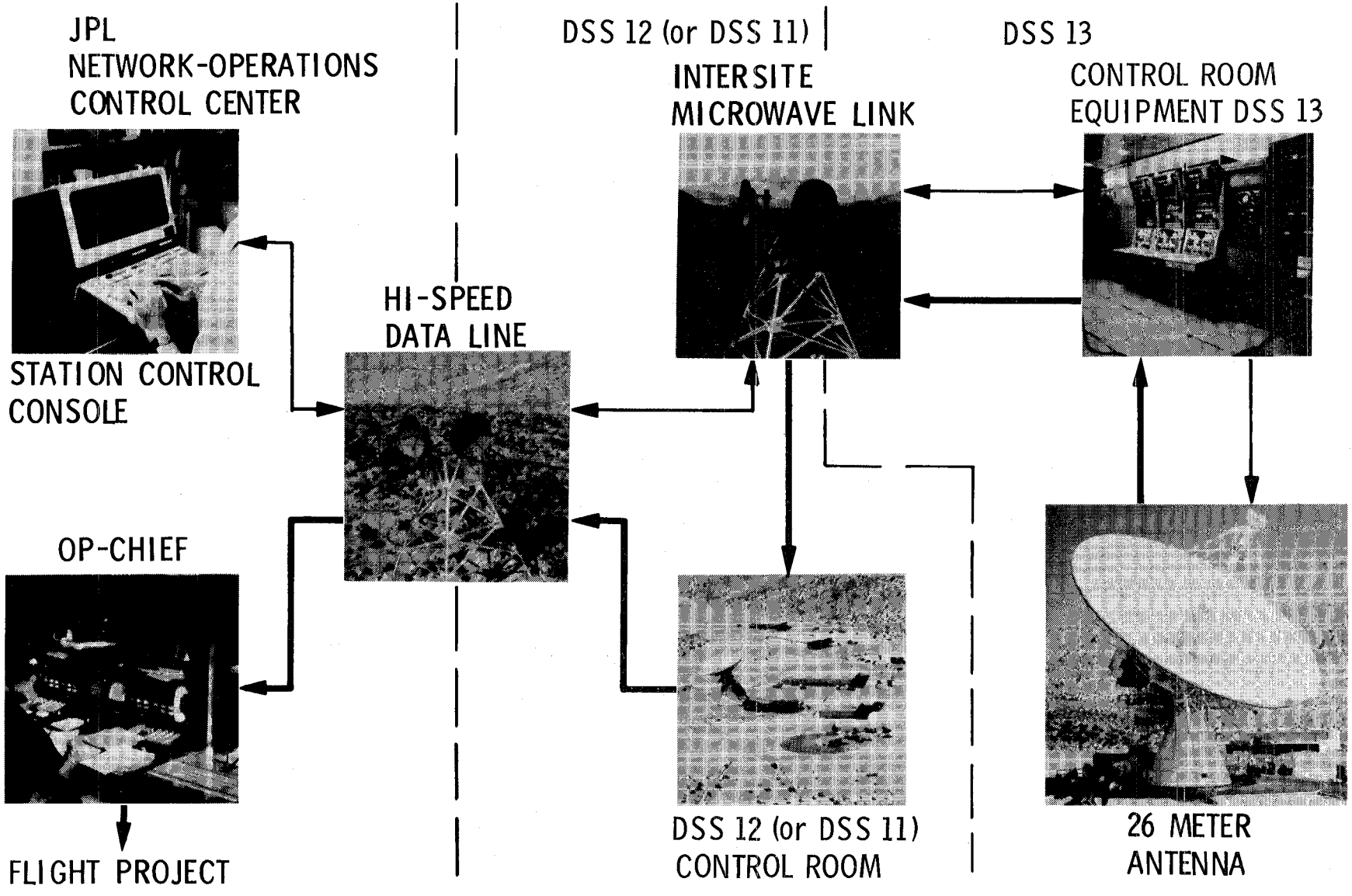

Fig. 2. Station control and system technology overview

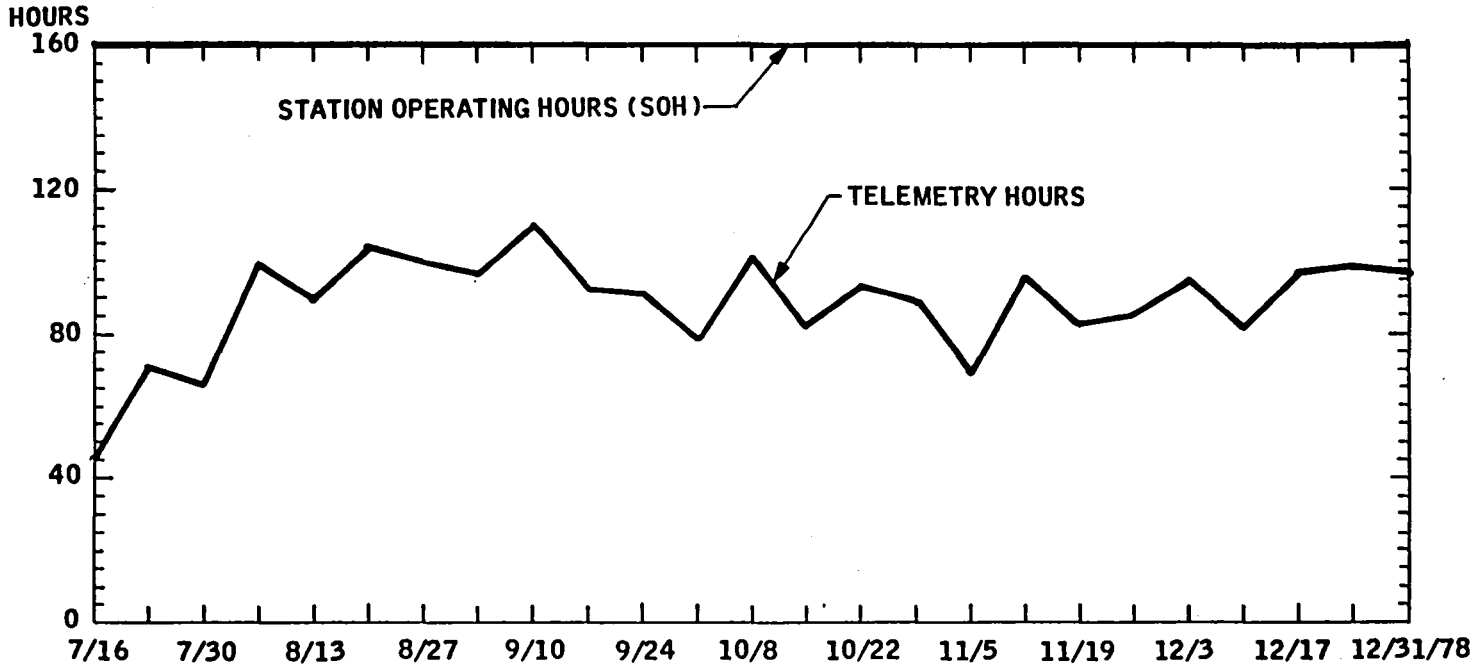

Fig. 3. DSS 11 station operating and telemetry hours (weekly averages)

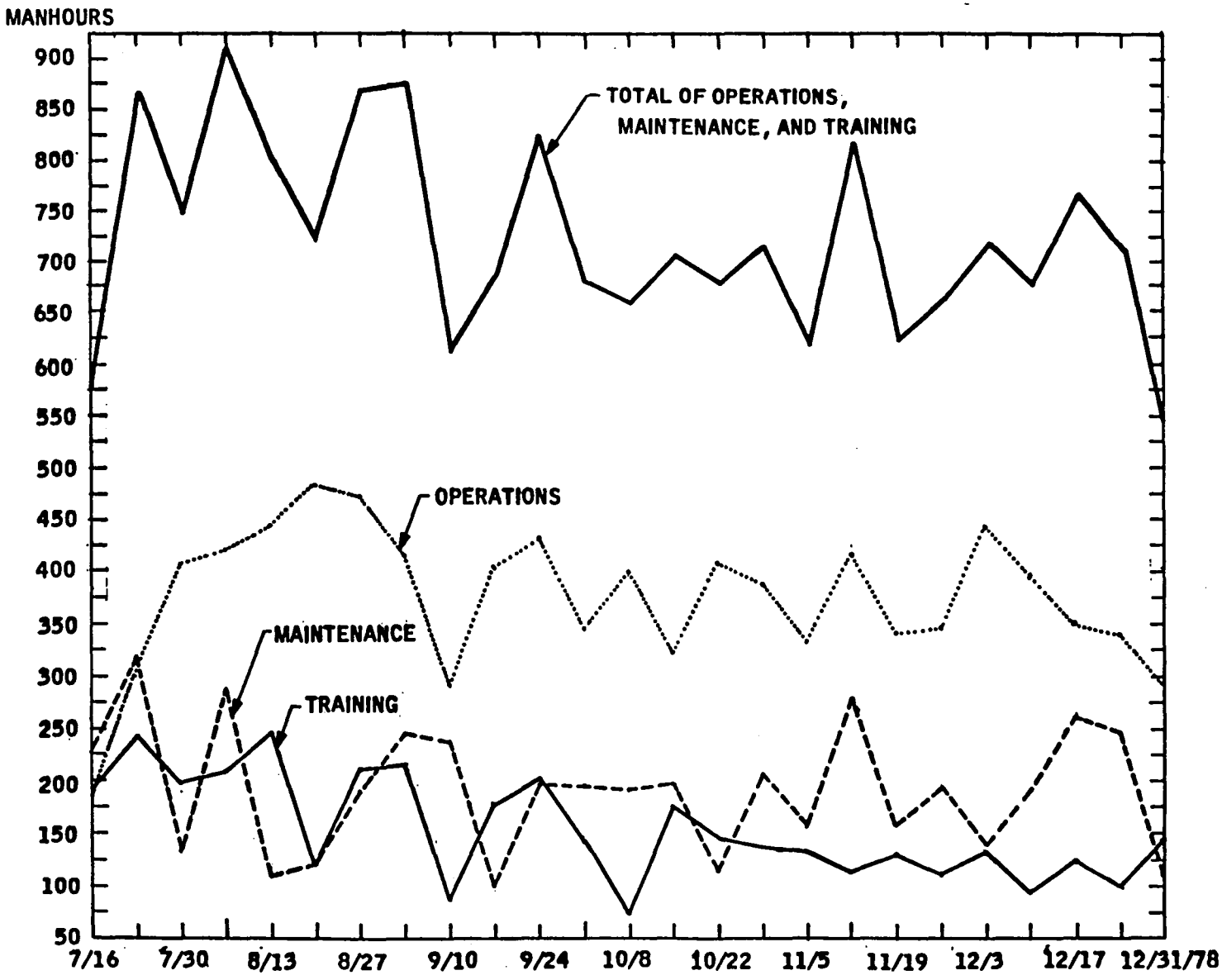

Fig. 4. DSS 11 manhour allocation between operations and maintenance (weekly averages)

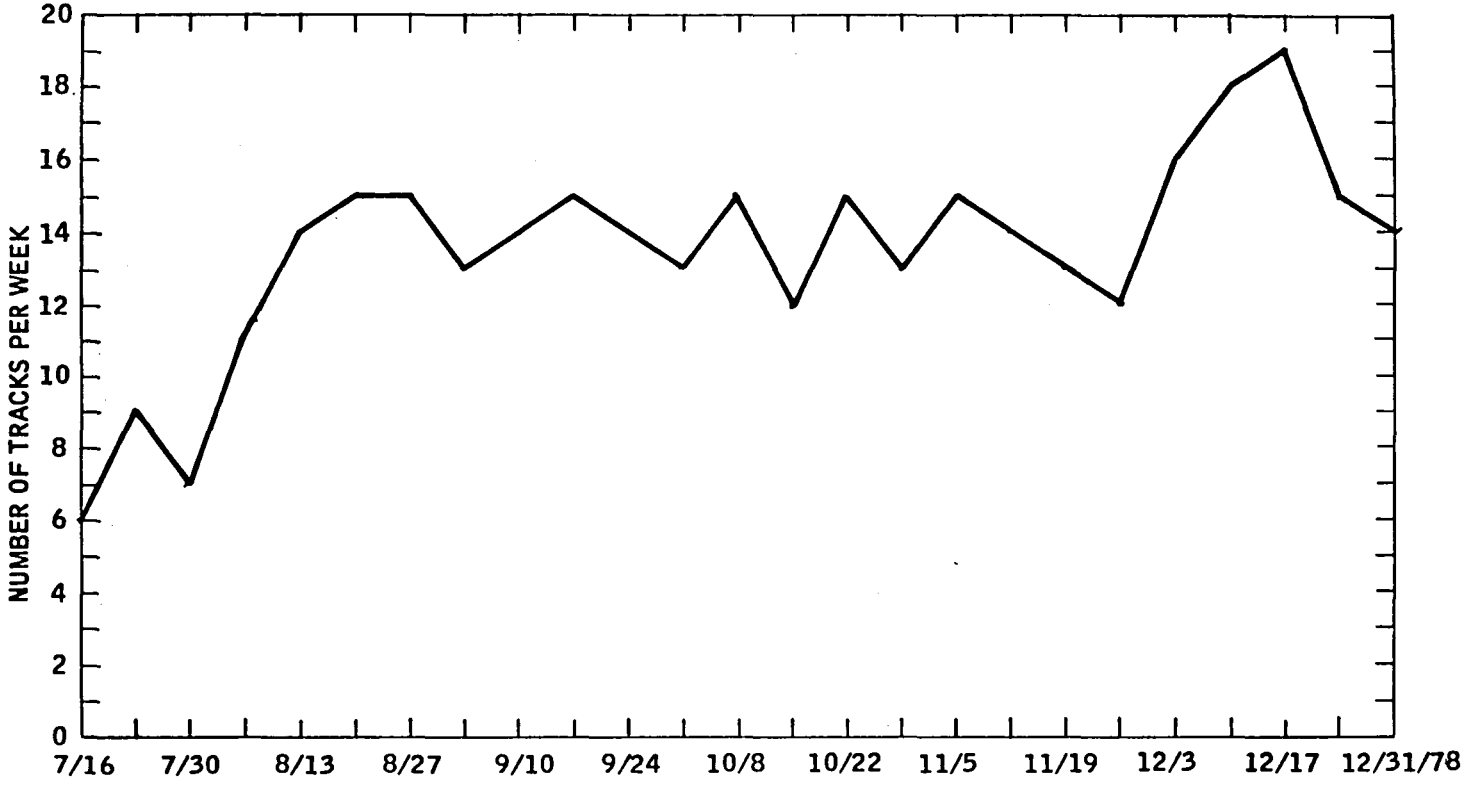

Fig. 5. DSS 11 tracks per week

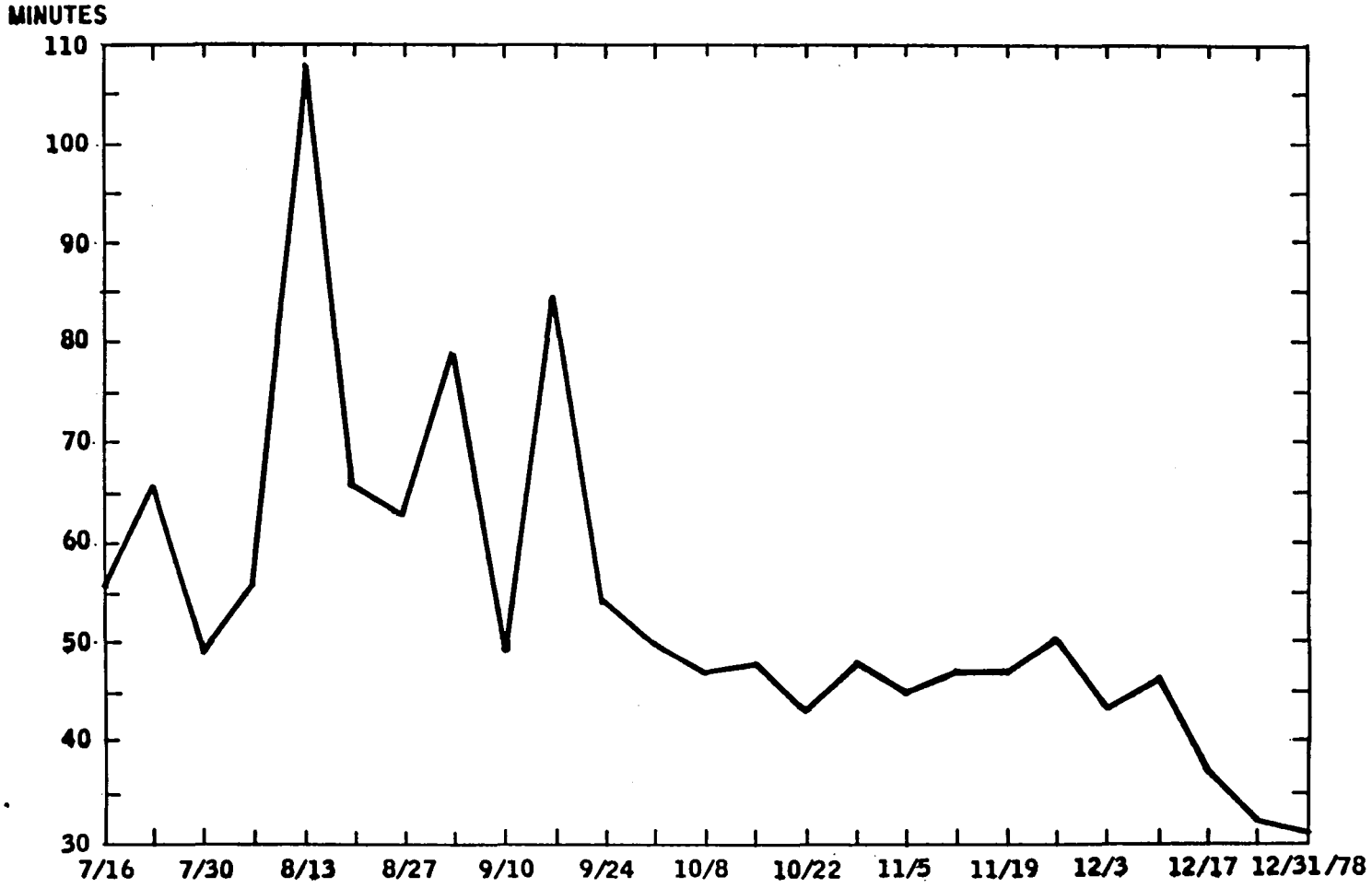

Fig. 6. DSS 11 precal time per track

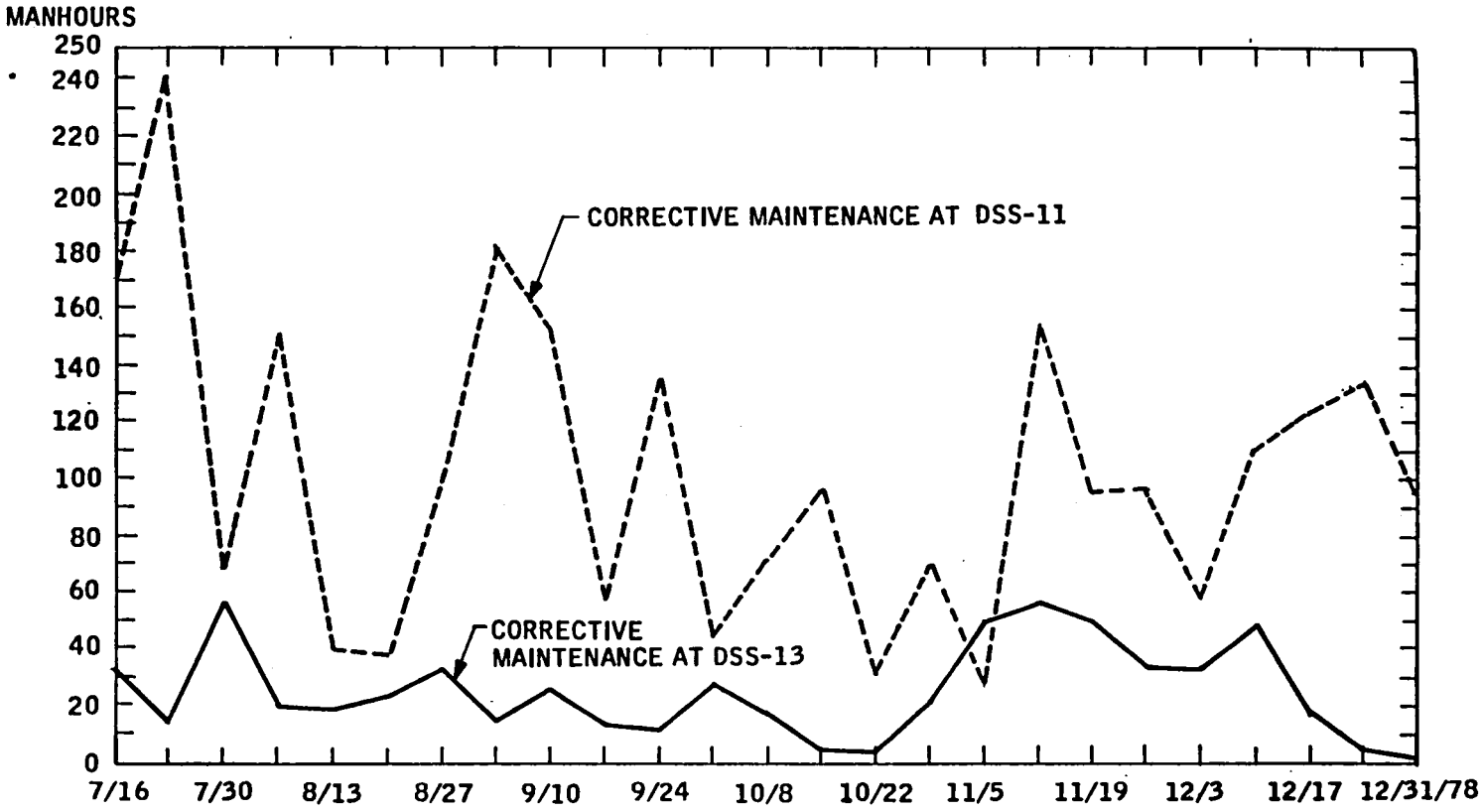

Fig. 7. Comparison of corrective maintenance at DSS 13 and DSS 11

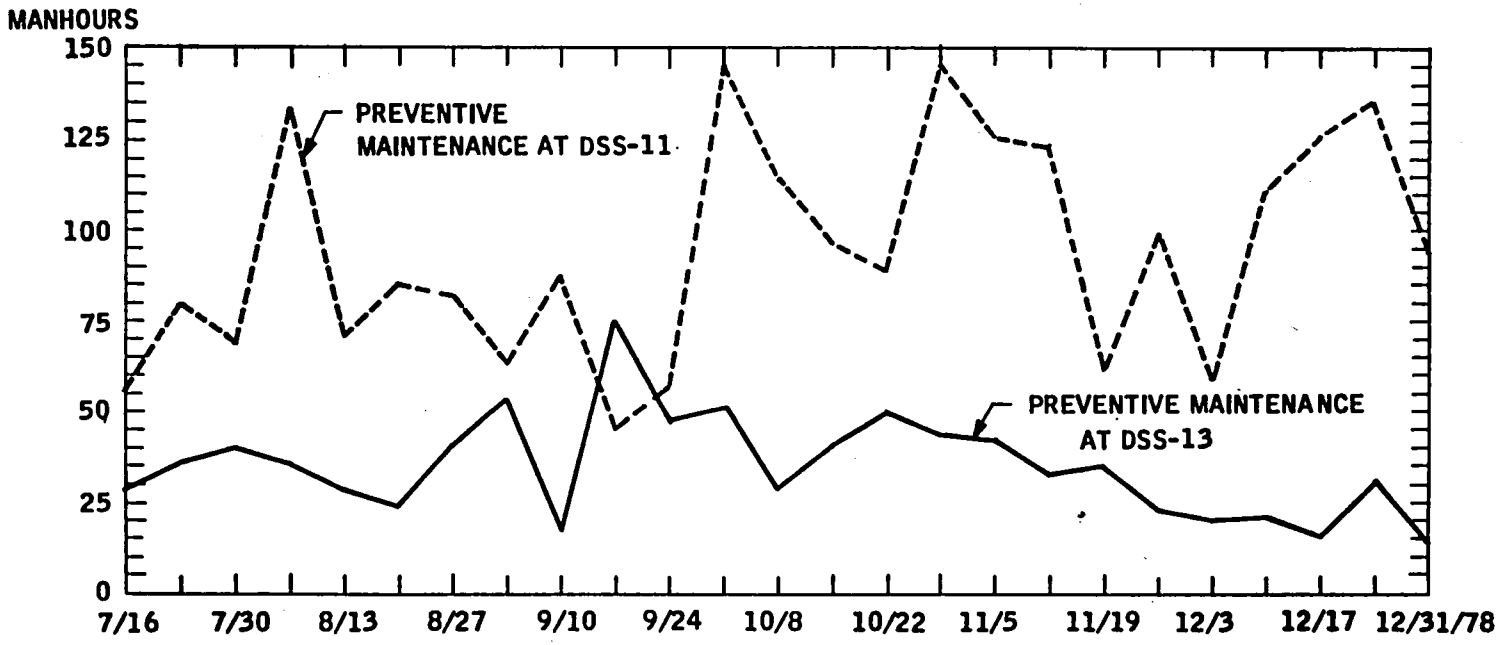

Fig. 8. Comparison of preventive maintenance at DSS 13 and DSS 11

Synchronization of Reed-Solomon Codes

R. L. Miller
Communications Systems Research Section

B. B. Newman
Department of Mathematics
California Institute of Technology

Reed-Solomon codes have recently been suggested for use as an "outer" code on NASA projects, since these codes perform very well on channels prone to burst errors. This article discusses another feature of Reed-Solomon codes, viz, the way in which they can be used to acquire sync.

I. Introduction

A concatenated coding scheme, consisting of an inner $(7, 1/2)$ convolutional code and an outer $J = 8$, $E = 16$ Reed-Solomon code, will be used for the Galileo mission and the International Solar Polar Mission, and is part of the multimission packet telemetry guidelines currently being proposed. This report examines the synchronization capabilities of Reed-Solomon codes when an appropriate coset of the code is used instead of the code itself. In this case an E-error correcting Reed-Solomon code is transformed into a new code capable of determining that there are m symbols out of sync, if e symbol errors occurred, whenever $m + e < E$. In the event that $m = 0$, i.e., the word is in sync, then the decoder will correct any pattern of $E - 1$ or fewer symbol errors.

The key idea to achieving synchronization is to use a coset of the code instead of the code itself. (A coset is obtained by adding the same vector to every code word.) From an error-correcting point of view, the coset is equivalent to the code itself. In addition, synchronization can sometimes be achieved as well. The algorithm to be presented differs from usual coding algorithms in that the information is encoded into one code, but decoded in a larger (different) code. The larger code contains the coset of the smaller code.

II. Synchronization Algorithm

Suppose that C_1 and C_2 are Reed-Solomon codes of length n whose symbols lie in $GF(q)$. Let

$$C_1 = (g_1(x)), \text{ where } g_1(x) = \prod_{i=2}^{2E-1} (x - \alpha^i), \text{ and } C_2 = (g_2(x)),$$

where

$$g_2(x) = \prod_{i=1}^{2E-1} (x - \alpha^i),$$

and α is a primitive n^{th} root of unity. (Observe that $C_2 \subseteq C_1$.) Then the following algorithm will insure that any transmitted

code word of C_2 will be resynchronized if it is received out of sync by m symbols, and e errors were made, provided that $m + e < E$. If $m = 0$, then any combination of $E - 1$ or fewer symbol errors will be corrected.

Algorithm:

Encoder

(1) Encode the information into $w(x) \in C_2$.

(2) Transmit $w(x) + g_1(x)$ (a coset).

Decoder

(1) Receive $r(x)$, which has e errors and is out of sync by m symbols.

(2) Compute $r(x) - g_1(x)$.

(3) Determine m.

(4) If $m = 0$, then correct $r(x)$ using the C_1 - decoder. Otherwise, shift $r(x)$ ahead by $n - m$ symbols to acquire sync.

III. Verification of Algorithm Correctness

Suppose that $w_1(x)$, $w_2(x) \in C_2$ are codewords and that $w_1(x) + g_1(x)$, $w_2(x) + g_1(x)$ are transmitted over a noisy channel. Assume also that the decoder does not know where a codeword begins, and that it begins to decode m symbols out of sync. This can be represented by the following diagram.

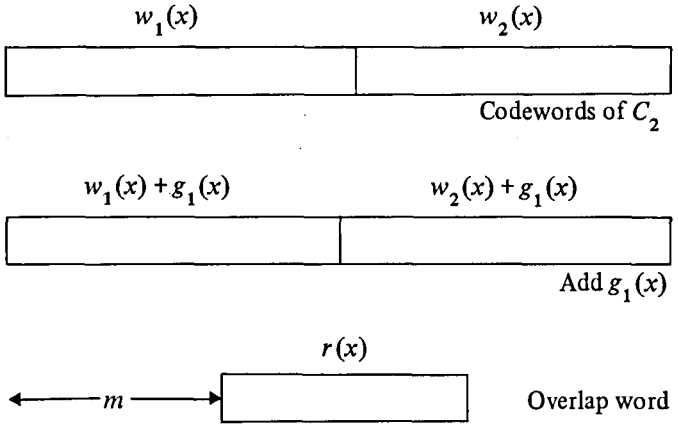

Let $x^{n-m} P_m(x)$ be the prefix of $w_2(x)$ appearing in $r(x)$, where deg $P_m(x) < M$. Also let $q_{n-m}(x)$ be the suffix of $w_1(x)$ appearing in $r(x)$, where deg $q_{n-m}(x) < n$. Finally, denote $x^{n-m} v_m(x)$ as the prefix of $w_1(x)$ preceding $r(x)$. Then the following diagram is useful.

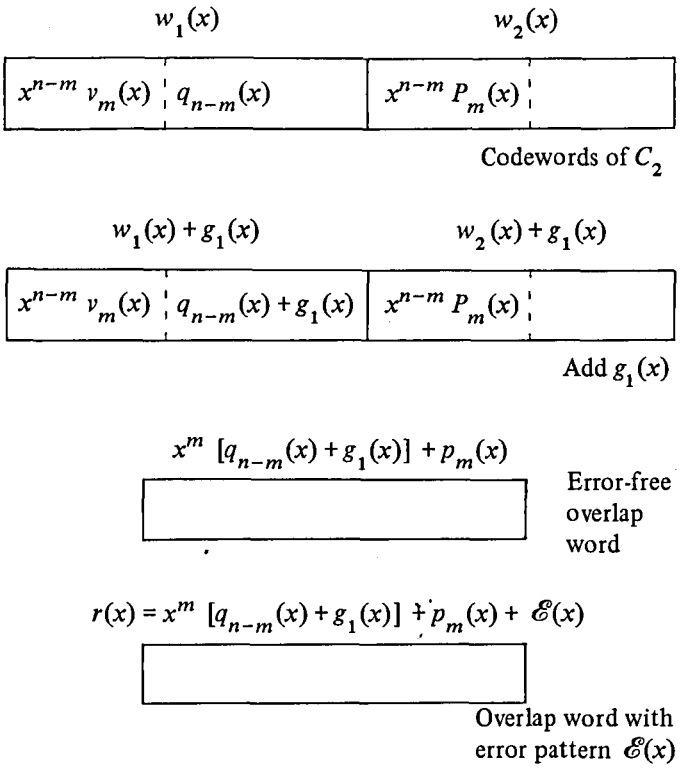

At stage 2, the decoder attempts to strip $g_1(x)$ from the received word by subtraction. This will succeed if the received word is in sync, i.e., if $m = 0$. Otherwise the received word is further perturbed from the originally transmitted word. This is indicated below.

$$r(x) - g_1(x) = (x^m - 1)g_1(x) + x^m q_{n-m}(x) + P_m(x) + \mathcal{E}(x)$$

Subtract $g_1(x)$

Since $w_1(x), g_1(x) \in C_1$, $(x^m - 1)g_1(x) + x^m w_1(x) \in C_1$.

Thus $r(x)$ and $r(x) - [(x^m - 1)g_1(x) + x^m w_1(x)]$ have the same error pattern, $\mathcal{E}(x)$, as far as the C_1 – decoder is concerned. But,

$$\begin{aligned} r(x) - [(x^m - 1)g_1(x) + x^m w_1(x)] &= x^m q_{n-m}(x) + P_m(x) - x^m w_1(x) + \mathcal{E}(x) \\ &= x^m [q_{n-m}(x) - w_1(x)] + P_m(x) + \mathcal{E}(x) \\ &= x^m [-x^{n-m} v_m(x)] + P_m(x) + \mathcal{E}(x) \\ &= [P_m(x) - v_m(x)] + \mathcal{E}(x), \text{ since } x^n = 1. \end{aligned}$$

Now $P_m(x)$ and $v_m(x)$ both have degree $< m$; hence $P_m(x) - v_m(x)$ has at most m nonzero terms. If $\mathcal{E}(x)$ has at most $E - m$ nonzero terms, i.e., if at most $E - m$ transmission errors occurred, then the C_1 — decoder will determine $\hat{\mathcal{E}}(x) = P_m(x) - v_m(x) + \mathcal{E}(x)$ as the error polynomial. Of course, what is desired is to compute $\mathcal{E}(x)$ and m separately. Note that if $m = 0$, then $\hat{\mathcal{E}}(x) = \mathcal{E}(x)$, and $r(x) - \mathcal{E}(x)$ is the desired codeword. Otherwise,

$$r(x) - \hat{\mathcal{E}}(x) = x^m [q_{n-m}(x) + g_1(x)] + v_m(x)$$

$$= x^m q_{n-m}(x) + v_m(x) + x^m g_1(x)$$

$$= x^m [q_{n-m}(x) + x^{n-m} v_m(x)] + x^m g_1(x)$$

$$= x^m [w_1(x) + g_1(x)].$$

Thus

$$r(\alpha) - \hat{\mathcal{E}}(\alpha) = \alpha^m [w_1(\alpha) + g_1(\alpha)]$$

$$= \alpha^m g_1(\alpha), \text{ since } w_1 \in C_2.$$

Since $g_1(x)$ is a fixed polynomial, m can be easily determined by a table look-up. Once m is known, then a shift of n-m symbols will reacquire sunc.

IV. Example

Let C_1 be the Reed-Solomon code, RS(255,225), generated by

$$g_1(x) = \prod_{i=2}^{31} (x - \alpha^i),$$

where α is a primitive 255th root of unity in GF(2^8). Let C_2 be the Reed-Solomon code, RS(255,224) generated by

$$g_2(x) = \prod_{i=1}^{31} (x - \alpha^i).$$

The information is encoded in C_2, and $g_1(x)$ is added to the parity symbols. If $r(x)$ is received out of sync by m symbols with symbol errors, then m will be determined if $m + e < 16$. Moreover, if $m = 0$, then $r(x)$ will be correctly decoded, provided that 15 or fewer symbol errors occurred.

V. System Considerations

The (255,223) 16-error correcting Reed-Solomon code has been given as a quasi-standard by various groups in NASA. If one wants to be able to acquire sync using the Reed-Solomon code alone, then additional system considerations are needed.

First, the information is encoded in one code, but decoded in another. Second, to maintain the same information rate, only 15 errors can be corrected; on the other hand, keeping the same error-correcting capability forces the information rate to drop. This memo alludes to using the former option, since initial performance studies indicate that the (255,225) 15-error correcting code performs better than the (255,223) 16-error correcting code. Of course, what have to be estimated are the expected time to acquire sync, the probability of false sync, and the buffer requirements, assuming that the ratio of the decoder's speed to the data rate is some constant. This work as well as estimating the performance comparison (dB) of using this new Reed-Solomon scheme to acquire sync vs using the (255,223) Reed-Solomon code and a fixed sync pattern should be performed in the future.

Acknowledgment

The authors wish to thank Dr. E. C. Posner for his suggestion to perform this investigation.

Stress Distribution in a Semi-Infinite Body Symmetrically Loaded Over a Circular Area

H. McGinness
DSN Engineering Section

Algorithms are developed for computing stresses in a semi-infinite body when loaded by a uniform pressure acting over a circular area.

I. Introduction

The stress distribution through a semi-infinite body of isotropic material has been obtained in various ways. For the particular case where the loading on the plane surface is one of uniform pressure acting on a circular area, the stress components can be calculated by numerically evaluating the integral expressions presented herein. These integrals can be evaluated by desk calculator programs, thus making it easy to determine any stress component in a semi-infinite body having a known constant Poisson's ratio. The solution of this problem has a direct application to circular columns resting on large footings and can be helpful in estimating stresses in foundations supporting certain vehicle rails.

II. Derivation of the Algorithms

If a concentrated force P is applied perpendicularly to the plane surface of a semi-infinite body, the stress components per Ref. 1 are:

$$\sigma_r = \frac{P}{2\pi}\left\{(1-2\nu)\left[\frac{1}{r^2} - \frac{Z}{r^2}(r^2+Z^2)^{-1/2}\right] - 3r^2 Z\,(r^2+Z^2)^{-5/2}\right\} \tag{1}$$

$$\sigma_\theta = \frac{P}{2\pi}(1-2\nu)\left\{-\frac{1}{r^2}+\frac{Z}{r^2}(r^2+Z^2)^{-1/2} + Z(r^2+Z^2)^{-3/2}\right\} \tag{2}$$

$$\sigma_Z = -\frac{3P}{2\pi} Z^3 (r^2+Z^2)^{-5/2} \tag{3}$$

$$\tau_{rZ} = -\frac{3P}{2\pi} rZ^2 (r^2+Z^2)^{-5/2} \tag{4}$$

where the coordinates are defined as follows: Assume the plane of the semi-infinite body to be horizontal and on the upper side of the body. The coordinate r is the horizontal distance from the point of concern, point 0, to the point directly beneath the force P. The positive coordinate Z is the distance that point 0 is below the plane. The coordinate θ is mutually perpendicular to r and Z. The symbols σ and τ represent the normal and shear stresses, respectively, and ν is Poisson's ratio.

The solution for the case of a uniform pressure acting over a circular area of radius a is obtained by replacing the concentrated load P by pdA where p is the uniform pressure and dA is a differential area, and appropriately summing over the circular area.

Let the point 0 be on a vertical plane which passes through the center of the circularly loaded area, as shown in Fig. 1. The differential area is $rd\theta dr$. It is desired to obtain the stress components along axes R, T, and Z, namely, σ_R, σ_T, σ_Z and the shear stress τ_{RZ}. By symmetry the other shear stresses will be zero.

Thus from these four components, principal stresses can be calculated. By the usual method of resolving two-dimensional stress components the following obtain:

$$\sigma_R = \sigma_r \cos^2\theta + \sigma_\theta \sin^2\theta \tag{5}$$

$$\sigma_T = \sigma_r \sin^2\theta + \sigma_\theta \cos^2\theta \tag{6}$$

$$\tau_{RZ} = \tau_{rz} \cos\theta \tag{7}$$

The stress components σ_R, σ_T, σ_Z, and τ_{RZ} caused by the pressure loading over a differential area are formed by substituting $prdrd\theta$ for P in Eqs. (1), (2), (3), and (4) and substituting the results into Eqs. (5), (6), and (7). The following double integrals represent the desired stress components in terms of the coordinates r, θ, and Z:

$$\frac{\sigma_R}{p} = \frac{1-2\nu}{2\pi}\int_{\phi_1}^{\phi_2}\int_L^U \left\{\cos^2\theta\left[\frac{1}{r} - \frac{Z}{r(r^2+Z^2)^{1/2}} - \frac{3r^3Z}{(1-\nu)(r^2+Z^2)^{5/2}}\right] + \sin^2\theta\left[-\frac{1}{r} + \frac{Z}{r(r^2+Z^2)^{1/2}} + \frac{rz}{(r^2+Z^2)^{3/2}}\right]\right\} dr\,d\theta \tag{8}$$

$$\frac{\sigma_T}{p} = \frac{1-2\nu}{2\pi}\int_{\phi_1}^{\phi_2}\int_L^U \left\{\sin^2\theta\left[\frac{1}{r} - \frac{Z}{r^2(r^2+Z^2)^{1/2}} - \frac{3r^3Z}{(1-\nu)(r^2+Z^2)^{5/2}}\right] + \cos^2\theta\left[-\frac{1}{r} + \frac{Z}{r(r^2+Z^2)^{1/2}} + \frac{rz}{(r^2+Z^2)^{3/2}}\right]\right\} dr\,d\theta \tag{9}$$

$$\frac{\sigma_Z}{p} = -\frac{3}{2\pi}\int_{\phi_1}^{\phi_2}\int_L^U \frac{rZ^3}{(r^2+Z^2)^{5/2}}\, dr\,d\theta \tag{10}$$

$$\frac{\tau_{RZ}}{p} = -\frac{3}{2\pi}\int_{\phi_1}^{\phi_2}\int_L^U (\cos\theta)\frac{r^2Z^2}{(r^2+Z^2)^{5/2}}\, dr\,d\theta \tag{11}$$

Equations (8), (9), (10), and (11) are readily integrated with respect to r to yield:

$$\frac{\sigma_R}{p} = \frac{1-2\nu}{2\pi}\int_{\phi_1}^{\phi_2}\left\{\cos 2\theta\left[\ln\left(Z+\sqrt{r^2+Z^2}\right)\right]_L^U + \frac{\cos^2\theta}{(1-2\nu)}\left[\frac{3Z\left(r^2+\frac{2}{3}Z^2\right)}{(r^2+Z^2)^{3/2}}\right]_L^U - \sin^2\theta\left[\frac{Z}{(r^2+Z^2)^{1/2}}\right]_L^U\right\} d\theta \tag{12}$$

$$\frac{\sigma_T}{p} = \frac{1-2\nu}{2\pi}\int_{\phi_1}^{\phi_2}\left\{-\cos 2\theta\left[\ln\left(Z+\sqrt{r^2+Z^2}\right)\right]_L^U + \frac{\sin^2\theta}{(1-2\nu)}\left[\frac{3Z\left(r^2+\frac{2}{3}Z^2\right)}{(r^2+Z^2)^{3/2}}\right]_L^U - \cos^2\theta\left[\frac{Z}{(r^2+Z^2)^{1/2}}\right]_L^U\right\} d\theta \tag{13}$$

$$\frac{\sigma_Z}{p} = \frac{1}{2\pi}\int_{\phi_1}^{\phi_2}\left[\frac{Z^3}{(r^2+Z^2)^{3/2}}\right]_L^U d\theta \tag{14}$$

$$\frac{\tau_{RZ}}{p} = -\frac{1}{2\pi}\int_{\phi_1}^{\phi_2}\cos\theta\left[\frac{r^3}{(r^2+Z^2)^{3/2}}\right]_L^U d\theta \tag{15}$$

A distinction must be made between Case 1, where point 0 lies under or on the loaded area, as shown in Fig. 1, and Case 2, where point 0 lies outside the loaded area, as shown in Fig. 2.

For Case 1 the point is located distance βa from the boundary of the circle and a distance γa below the surface. The distance from point 0 to point U is OU, where

$$OU = a\left[(1-\beta) + \sqrt{(1+\beta)^2 + \frac{\beta(2-\beta)}{\cos^2\theta}}\right]\cos\theta \quad (16)$$

The distance from point 0 to point L is OL, where

$$OL = -a\left[(1-\beta) - \sqrt{(1+\beta)^2 + \frac{\beta(2-\beta)}{\cos^2\theta}}\right]\cos\theta \quad (17)$$

and the positive roots of the radicals are to be used.

In order for the integration to cover the entire circular area for Case 1, the bracketed terms of Eqs. (12), (13), (14), and (15) must be evaluated for two sets of limits and summed, namely between OU and zero and between OL and zero. The limits of θ are $\pi/2$ and zero provided the integrals are multiplied by 2.

For Case 2 the point 0 is located a distance αa from the boundary of the circle and a distance γa below the surface. The upper and lower limits of the bracketed terms of Eqs. (12), (13), (14), and (15) are respectively:

$$u = a\left[(1+\alpha) + \sqrt{(1+\alpha)^2 - \frac{\alpha(\alpha+2)}{\cos^2\theta}}\right]\cos\theta \quad (18)$$

$$l = a\left[(1+\alpha) - \sqrt{(1+\alpha)^2 - \frac{\alpha(\alpha+2)}{\cos^2\theta}}\right]\cos\theta \quad (19)$$

The limits of θ are arc tan $\sqrt{1/\alpha(\alpha+2)}$ and zero provided the integrals are multiplied by 2.

The results are as follows:

For Case 1

$$\frac{\sigma_{1R}}{p} = \frac{1-2\nu}{\pi}\int_0^{\pi/2}\left\{\cos 2\theta\left[\ln\frac{(\gamma+\sqrt{U^2+\gamma^2})(\gamma+\sqrt{L^2+\gamma^2})}{4\gamma^2}\right]\right.$$

$$+\frac{\cos^2\theta}{1-2\nu}\left[\frac{3\gamma\left(U^2+\frac{2}{3}\gamma^2\right)}{(U^2+\gamma^2)^{3/2}} + \frac{3\gamma\left(L^2+\frac{2}{3}\gamma^2\right)}{(L^2+\gamma^2)^{3/2}} - 4\right]$$

$$\left. - \sin^2\theta\left[\frac{\gamma}{(U^2+\gamma^2)^{1/2}} + \frac{\gamma}{(L^2+\gamma^2)^{1/2}} - 2\right]\right\}d\theta \quad (20)$$

$$\frac{\sigma_{1T}}{p} = \frac{1-2\nu}{\pi}\int_0^{\pi/2}\left\{-\cos 2\theta\left[\ln\frac{(\gamma+\sqrt{U^2+\gamma^2})(\gamma+\sqrt{L^2+\gamma^2})}{4\gamma^2}\right]\right.$$

$$+\frac{\sin^2\theta}{1-2\nu}\left[\frac{3\gamma\left(U^2+\frac{2}{3}\gamma^2\right)}{(U^2+\gamma^2)^{3/2}} + \frac{3\gamma\left(L^2+\frac{2}{3}\gamma^2\right)}{(L^2+\gamma^2)^{3/2}} - 4\right]$$

$$\left. - \cos^2\theta\left[\frac{\gamma}{(U^2+\gamma^2)^{1/2}} + \frac{\gamma}{(L^2+\gamma^2)^{1/2}} - 2\right]\right\}d\theta \quad (21)$$

$$\frac{\sigma_{1z}}{p} = \frac{1}{\pi}\int_0^{\pi/2}\left\{\gamma^3\left[\frac{1}{(U^2+\gamma^2)^{3/2}} + \frac{1}{(L^2+\gamma^2)^{3/2}}\right] - 2\right\}d\theta, \quad (22)$$

$$\frac{\tau_{1RZ}}{p} = -\frac{1}{\pi}\int_0^{\pi/2}(\cos\theta)\left[\frac{U^3}{(U^2+\gamma^2)^{3/2}} - \frac{L^3}{(L^2+\gamma^2)^{3/2}}\right]d\theta \quad (23)$$

where

$$U = \left[(1-\beta) + \sqrt{(1-\beta)^2 + \frac{\beta(2-\beta)}{\cos^2\theta}}\right]\cos\theta \quad (24)$$

$$L = -\left[(1-\beta) - \sqrt{(1-\beta)^2 + \frac{\beta(2-\beta)}{\cos^2\theta}}\right]\cos\theta \quad (25)$$

For Case 2

$$\frac{\sigma_{2R}}{p} = \frac{1-2\nu}{\pi}\int_0^{\phi}\left\{\cos 2\theta\left[\ln\frac{(\gamma+\sqrt{U^2+\gamma^2})}{(\gamma+\sqrt{l^2+\gamma^2})}\right]\right.$$

$$+\frac{(\cos^2\theta)(3\gamma)}{1-2\nu}\left[\frac{U^2+\frac{2}{3}\gamma^2}{(U^2+\gamma^2)^{3/2}} - \frac{l^2+\frac{2}{3}\gamma^2}{(l^2+\gamma^2)^{3/2}}\right]$$

$$\left. - (\sin^2\theta)(\gamma)\left[\frac{1}{(U^2+\gamma^2)^{1/2}} - \frac{1}{(l^2+\gamma^2)^{1/2}}\right]\right\}d\theta \quad (26)$$

$$\frac{\sigma_{2T}}{p} = \frac{1-2\nu}{\pi}\int_0^{\phi}\left\{-\cos 2\theta\left[\ln\frac{(\gamma+\sqrt{u^2+\gamma^2})}{(\gamma+\sqrt{l^2+\gamma^2})}\right]\right.$$

$$+\frac{(\sin^2\theta)(3\gamma)}{1-2\nu}\left[\frac{u^2+\frac{2}{3}\gamma^2}{(u^2+\gamma^2)^{3/2}}-\frac{l^2+\frac{2}{3}\gamma^2}{(l^2+\gamma^2)^{3/2}}\right]$$

$$\left.-(\cos^2\theta)(\gamma)\left[\frac{1}{(u^2+\gamma^2)^{1/2}}-\frac{1}{(l^2+\gamma^2)^{1/2}}\right]\right\}d\theta \qquad (27)$$

$$\frac{\sigma_{2Z}}{p} = \frac{\gamma^3}{\pi}\int_0^{\phi}\left[\frac{1}{(u^2+\gamma^2)^{3/2}}-\frac{1}{(l^2+\gamma^2)^{3/2}}\right]d\theta \qquad (28)$$

$$\frac{\tau_{2RZ}}{p} = -\frac{1}{\pi}\int_0^{\phi}(\cos\theta)\left[\frac{u^3}{(u^2+\gamma^2)^{3/2}}-\frac{l^3}{(l^2+\gamma^2)^{3/2}}\right]d\theta \qquad (29)$$

where

$$u = \left[(1+\alpha)+\sqrt{(1+\alpha)^2-\frac{\alpha(\alpha+2)}{\cos^2\theta}}\right]\cos\theta \qquad (30)$$

$$l = \left[(1+\alpha)-\sqrt{(1+\alpha)^2-\frac{\alpha(\alpha+2)}{\cos^2\theta}}\right]\cos\theta \qquad (31)$$

$$\phi = \arctan\sqrt{\frac{1}{\alpha(\alpha+2)}} \qquad (32)$$

The integrals of Eqs. (20), (21), (22), (23), (26), (27), (28), and (29) can easily be integrated numerically on programmable desk calculators. Angular increments of 1/9 the angular range will produce results sufficiently accurate for most engineering applications. These programs are available on four cards for HP97 calculators.

Principal stresses can be calculated per Ref. 2 as follows:

$$\sigma_{P1} = \frac{1}{2}\left[\sigma_R+\sigma_Z+\left|\sqrt{(\sigma_R-\sigma_Z)^2+4\tau_{RZ}^2}\right|\right] \qquad (33)$$

$$\sigma_{P2} = \frac{1}{2}\left[\sigma_R+\sigma_Z-\left|\sqrt{(\sigma_R-\sigma_Z)^2+4\tau_{RZ}^2}\right|\right] \qquad (34)$$

$$\sigma_{P3} = \sigma_T \qquad (35)$$

III. Discussion of Results

On the plane surface of the semi-infinite body the stresses σ_R, σ_T, and σ_Z are discontinuous at the boundary of the loaded circular area. Even at finite values of γ, that is, for points beneath the plane surface, the algorithms fail when the points are directly beneath the boundary. However, in Ref. 2 it is demonstrated that there are no infinite stress values obtained at the boundary and that all stresses are continuous at the boundary except those at the surface. Therefore, the values at the boundary may be approximated by considering very small values of the parameters α or β. For these reasons it is convenient to plot the calculated stresses on a semi-logarithmic chart with the abscissas α and β extending in opposite directions from a common small value. In Fig. 3 this has been done for a Poisson's ratio of 0.15, starting with α and β values of 0.001. Figure 3 gives the stresses at various distances below the plane surface, that is, at γ values of 0, 0.001, 0.01, 0.10, and 1.00. The ranges are sufficient to show the value and location of the maximum tensile stresses.

The curves of Fig. 3 pertain to a Poisson's ratio of 0.15 because this is a typical value for a Portland cement grout. Such grout has a tensile strength far less than its compressive strength. The curves can be useful in determining what tensile strength is necessary to ensure that surface cracks are not likely to form, and how far below the surface the high tensile stress region extends.

The curves of Fig. 4 pertain to a Poisson's ratio of 0.30, representative of many metals. Only the stress components σ_R and σ_T are shown, since σ_Z and τ_{RZ} are independent of Poisson's ratio and may be taken from Fig. 3. By comparing corresponding curves of Figs. 3 and 4 it is seen that the effect of Poisson's ratio on σ_R and σ_T is large.

Results obtained with the above algorithms, by dividing the angular range into 9 parts, agree with the tabulated values of Ref. 2.

By superposition the stresses can be calculated for any circularly symmetric loading. For example, the real loading could be approximated by a number of uniforms loads of different radii, and the effects of each appropriately summed by the above algorithms.

References

1. Timoshenko, S., *Theory of Elasticity*, McGraw Hill, 1934, First edition, p. 331, Eqs. 196.

2. Love, A. E. H., "The Stress Produced in a Semi-Infinite Solid by Pressure on Part of the Boundary," Phil. Trans. Roy. Soc., London, Series A, Vol. 228, 1929.

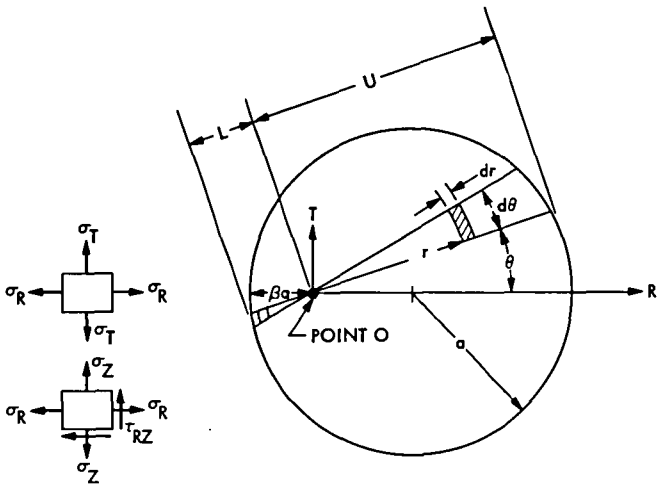

Fig. 1. Integration limits when point 0 lies below loaded circular area

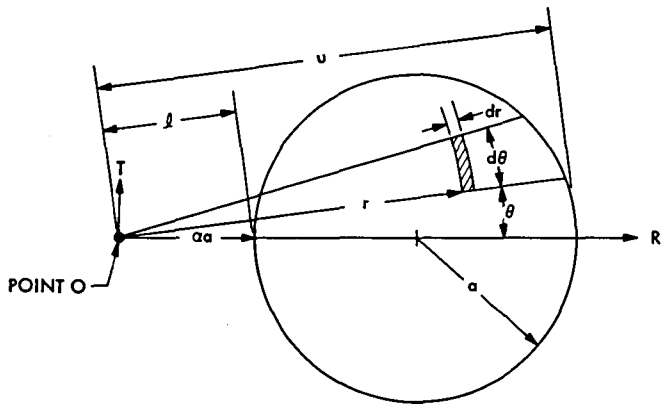

Fig. 2. Integration limits when point 0 lies outside loaded circular area

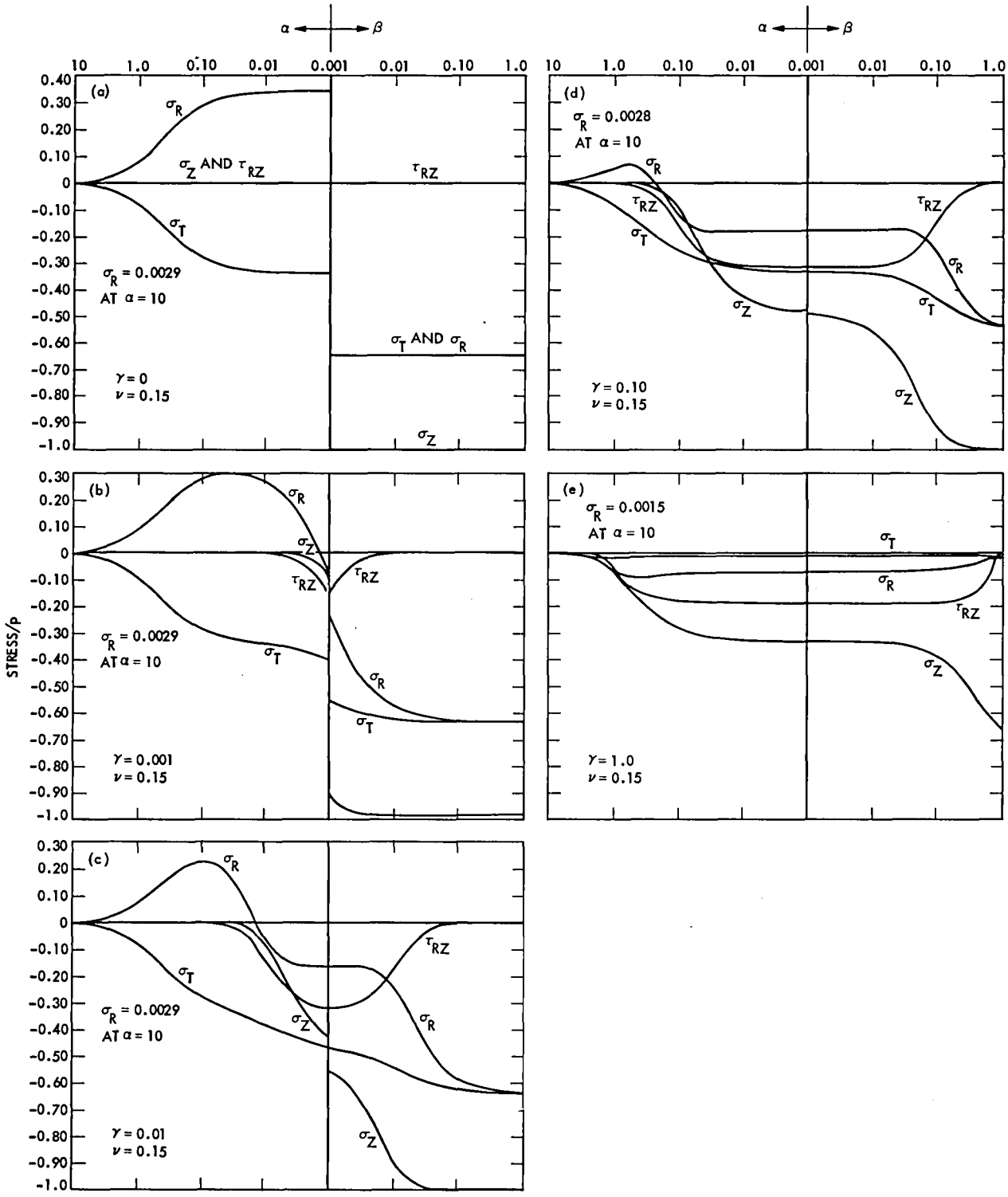

Fig. 3. Stress ratios vs α & β, ν = 0.15

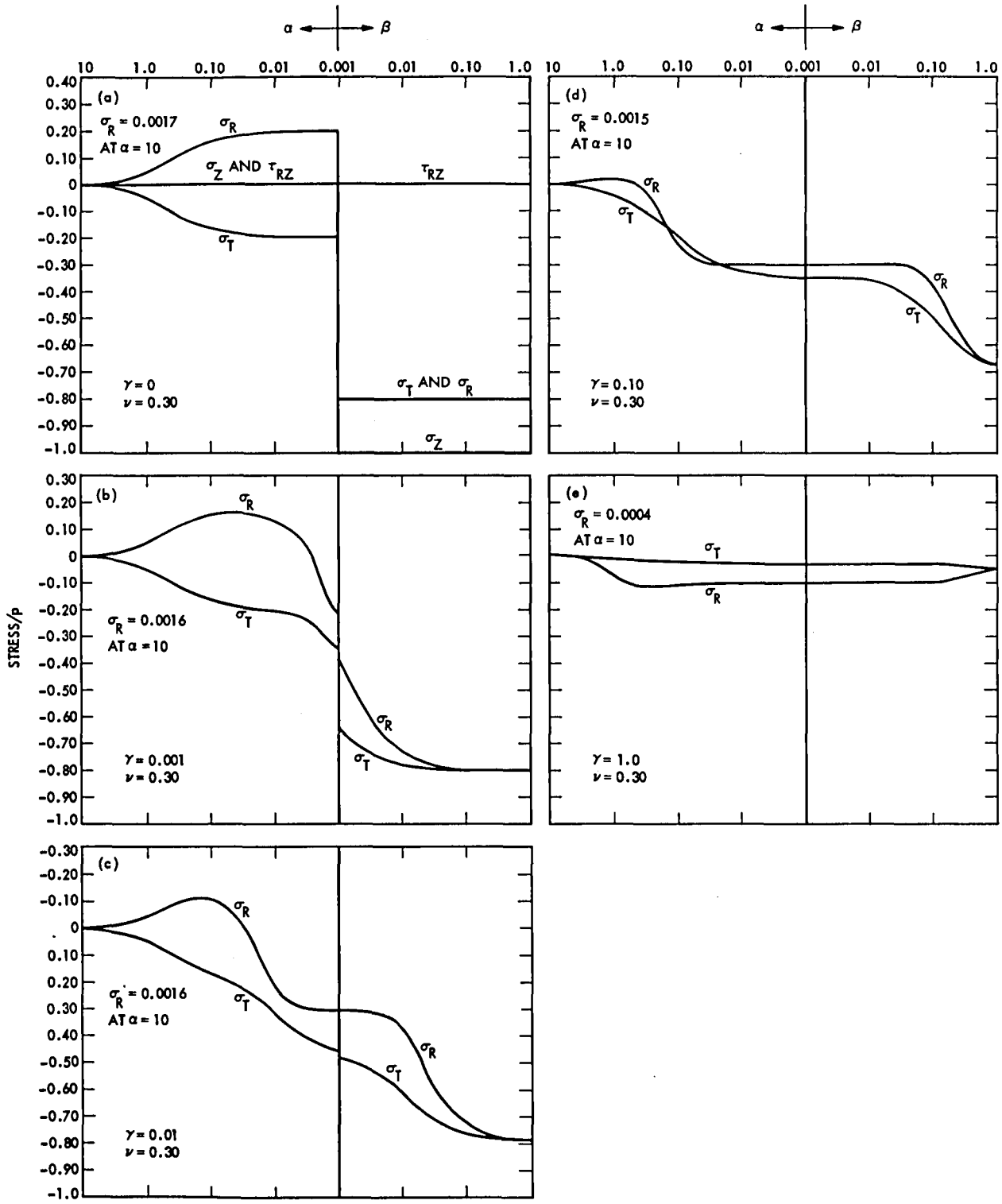

Fig. 4. Stress ratios vs α & β, ν = 0.30

Optimal Periodic Binary Codes of Lengths 28 to 64

S. Tyler and R. Keston
Quality Assurance – Ground Data Systems Section

Computer searches were performed to find repeated binary phase coded waveforms with optimal periodic autocorrelation functions. The best results for lengths 28 to 64 are given. These codes have extensive applications in radar and communications.

I. Introduction

Repeated binary phase coded waveforms with 100 percent duty factors form an important class of signals utilized extensively in radar and communications (Ref. 1).

Some codes with good periodic autocorrelation functions are known. For lengths of 27 and less, the best codes are fairly well known. For lengths of $2^n - 1$, maximal length P-N codes have optimal autocorrelation functions. However, for most lengths there is no practical algorithm for obtaining the best code (Ref. 2).

This article gives codes of lengths 28 to 64. Some of these codes are "optimal," others merely the best the authors have been able to find so far. These codes often represent a marked improvement over what has been reported previously in the available literature. Codes of these lengths are not merely useful in themselves; they can also be combined to give good codes of longer lengths. For instance, our best result for length 52 was obtained by copying the optimal code of length 13 four times and inverting one of the copies.

For codes of lengths above about 40, it is not practical to search exhaustively for the best code (Ref. 3). Smaller searches must be done. In this study, initial guesses were used and then modified until no further modification produced a superior code. Hopefully, methods for determining initial guesses and for modifying these will be improved as experience is gained in this field.

A periodic binary code can have several good features. In this study, we look at just two:

(1) The peak sidelobe in the autocorrelation function is small.

(2) The sum of the squares of the sidelobes in the autocorrelation function is small.

II. Examples

Consider a code of length 7:

+ + + + - + -

To get the elements of the autocorrelation function:

+ + + + - + -	is the original code.
- + + + + - +	is the code shifted one position.
- + + + - - -	is the arithmetic product for each position.
-1	is the sum of these products; it is the first sidelobe element of the autocorrelation function.

Shifting by 2:

```
+ + + + - + -

+ - + + + + -
-----------
+ - + + - + +      +3 is the sum.
```

Shifting by 3:

```
+ + + + - + -

+ - + + + + -
-----------
- + - + - + -      -1 is the next element of the autocorrelation function.
```

Shifts by 4, 5, 6 are equivalent to those of 3, 2, and 1.

The first element of the autocorrelation function is the main lobe. It corresponds to shifting by zero positions. The other elements are the sidelobes (the main lobe is not a sidelobe).

Thus the autocorrelation function of (+ ++ + - + -)

is (7 -1 3 -1 -1 3 -1).

Here P = peak sidelobe magnitude = 3

S = sum of squares of sidelobes = 22

Two simple relationships manifest themselves:

(1) Each element of the autocorrelation function when taken modulo 4, is equal to the length of the code modulo 4.

(2) The sum of the elements of the autocorrelation function equals the square of the sum of the elements of the code (Ref. 4).

An "optimal" code: + + + - - + - would have autocorrelation function

$$7, -1, -1, -1, -1, -1, -1$$

where

P = 1

S = 6

For length 8, the "optimal" code is

+ + + + - + - -

with autocorrelation function

$$8, 0, 0, 0, -4, 0, 0, 0$$

Here P = 4

S = 16.

Two other results are used in determining the optimality of codes:

(1) No code of length greater than 4 has P = 0.

(2) No code has length 1 modulo 4, length greater than 13, and P = 1 (Ref. 5).

III. Results

Table 2 shows the best codes for each lengths 28 to 64. Table 1, showing the results for lengths 3 to 27, is included for completeness.

Length gives the length of the code.

$\Sigma(\text{Sidelobes})^2$ gives the lowest sum of the squares of the sidelobes discovered for any code of that length. When a code which has a lower peak sidelobe is found which has a higher than optimal $\Sigma(\text{Sidelobes})^2$, both codes are given.

When the value for the peak sidelobe or sum of squares is in parentheses, the authors feel that a better but as yet undiscovered code probably exists. When the value is underlined, a better value might exist. In all other cases, the value can be proved to be optimal.

The codes are written in hex notation. The first bit is always a +. For example, the code for 29 is given in hex as 14A7C111. In binary, this would be 0001 0100 1010 0111 1100 0001 0001 0001. By removing the leading zeroes, we get the code:

+ - + - - + - + - - + + + + + + - - - - + - - - + - - - +

In some cases a code from Table 2 was found in an earlier work. In these cases, the reference number is given.

References

1. MacMullen, A., *Radar Antennas, Transmitters, and Receivers*, pp. PC-1-56, Technology Service Corporation, April 1977.

2. Boehmer, A., "Binary Pulse Compression Codes," IEEE Transactions on Information Theory, Volume 13, No. 2, p. 156, April 1967.

3. Lindner, J., "Binary Sequences up to Length 40 with Best Possible Autocorrelation Functions," Electronic Letters, Vol. II, No. 21, p. 507, 16 October 1975.

4. Tyler, S., *Optimum Binary Codes of Lengths* 2^n, Technology Service Corporation Memorandum, 12 July 1978.

5. Turyn, R., *Optimum Codes Study*, Sylvania Electronic Systems Final Report AF19(604)-5473, 29 January 1960.

6. Tausworthe, R., *Correlation Properties of Cyclic Sequences*, JPL Technical Report No. 32-388, 1 July 1963.

7. Tyler, S., *Binary Codes of Lengths* 2^n *with good periodic correlation properties*, Technology Service Corporation Memorandum TSC-PM-A207-26, 7 August 1978.

8. Bailey, J., and Tyler, S., *Periodic Binary Waveforms with Optimum Autocorrelation Functions* (to be published).

Table 1. Optimal codes of length less than 28

Length	Peak Sidelobe	Σ (Sidelobes)^2	Code (hex)
3	1	2	4
4	0	0	E
5	1	4	1D
6	2	20	25
7	1	6	4B
8	4	16	CB
9	3	24	1F4
10	2	36	350
11	1	10	716
12	4	16	941
13	1	12	1F35
14	2	52	36A3
15	1	14	647A
16	4	48	FAC4
17	3	64	19A3D
18	2	68	31EDD
19	1	18	7A86C
20	4	64	F6E8E
21	3	52	117BCE
22	2	84	3D1231
23	1	22	6650FA
24	4	32	DC20D4
25	3	72	18B082E
26	2	100	2C1AEB1
27	3	74	5A3C444

Table 2. Best results for codes of length 28 to 64

Length	Peak Sidelobe	Σ (Sidelobes)^2	Code (hex)	Ref.
28	4	80	B30FDD4	
29	3	92	14A7C111	
30	2	116	33927FAB	(6)
31	1	30	4B3E3750	(6)
32	4	80	89445BC1	(7)
33	3	64	18A5C2401	
34	2	132	24D1F7112	(8)
35	1	34	71F721592	(6)
36	4	64	C6859AE80	
37	3	84	1BD623E316	
38	2	148	3D69144620	(8)
39	(5)	(118)	7C744B905E	
39	3	(134)	5CC00AD278	
40	4	80	918547E90C	
41	3	104	1F0D19DF14A	(8)
42	2	164	33A970D33F4	(8)
43	1	42	653BE2E00D6	(6)
44	4	(144)	A042EA0F334	
45	3	(124)	17473C9B1AD0	
46	2	180	3B9BA0712495	
47	1	46	7BCAE4D82C20	(6)
48	4	112	CBF089223A51	
49	3	(192)	120AF28D1C5E0	
50	2	196	2E92B0050EE1C	
51	(5)	(226)	60B957CC485B0	
52	4	192	F9AFCD7E6A0CA	
53	(5)	(228)	12030BA906D987	
53	3	(260)	196EB81901D769	(6)
54	(6)	(276)	30EA0DB237B100	
55	(5)	(230)	74E705812DC456	(6)
56	4	(272)	DEC4518357C968	
57	(5)	(248)	166EA046116D4F0	
58	(6)	(292)	2C985A631F53A00	
59	1	58	5D49DE7C1846D44	(6)
60	4	224	FA32C756BD9E480	(6)
61	(5)	(268)	18F5981E02FBDBA4	
61	3	(300)	1B89F34A052CF91D	(6)
62	2	244	225746DC22583D20	
63	1	62	4314F4725BB357E0	(6)
64	(8)	(352)	A804EA630D727C2C	
64	4	(384)	EC10845E8B3CB0AC	

Utilization of the Venus Station (DSS 13) 26-Meter Antenna During CY 1979

E. B. Jackson
Goldstone Operations

The various activities for which the Venus Station's 26-m antenna was used are described and the number of manned tracking hours devoted to each activity are given. A brief description of the goal of each activity supported is provided, and, where appropriate, the observing technique is summarized.

I. Introduction

This article describes the activities, both tracking and significant non-tracking, to which the Venus Station (DSS 13) 26-m AZ-EL antenna provided support during January-December 1979. The Venus Station, a non-mission support committed station, is normally staffed for 40 hours each week. Its activities can broadly be classified into:

A. Operations

Activities which either directly supported the spacecraft tracking mission of the DSN or were closely associated with those activities.

B. Advanced Systems Development

Activities, usually funded from the NASA 310 program, which are aimed at development of techniques and equipment with which future DSN needs can be met.

C. Non-Flight Project

Activities, primarily radio astronomy, which are not directly related to DSN spacecraft tracking nor associated with specific development of equipment or techniques.

In the following discussion of activities, grouped as above, the numbers in parentheses immediately following the activity title are the number of hours of antenna support provided, unless otherwise described in the text.

II. Operations

A. Pioneer Venus Radio Scintillation (29-½ h)

This activity, which used the Pioneer spacecraft as a signal source, measured the amplitude and frequency fluctuations in the spacecraft downlink. Later correlation with other data allowed these fluctuations to be related to turbulence characteristics of the solar wind near the Sun.

B. Voyager Telemetry Support (137-¼ h)

During the temporary non-availability of normally scheduled DSN stations, primarily DSS 12, the Voyager Project was provided with downlink telemetry to minimize the data gaps which would otherwise have resulted. These data were primarily provided when DSS 12 was taken out of service for a few days to perform major maintenance and main reflector adjustment.

III. Advanced Systems Development

A. Mark IV Radiometric Tracking Systems Development (238 h)

This activity, which utilized the Voyager spacecraft as signal sources, demonstrated the feasibility of using narrow-band (less than 1 MHz) signals in a delta VLBI technique for spacecraft navigation, particularly during the Jupiter encounter period.

B. Mark IV Differential One-Way Range (DOR) Systems Development (6-¼ h)

This activity is to demonstrate the feasibility of using wideband (greater than 1 MHz) signals in differential VLBI measurements to perform spacecraft navigation. This activity also uses the Voyager spacecraft in cruise mode and at the forthcoming Saturn encounter. The bandwidth employed is approximately 3.6 MHz.

C. Viking Delta VLBI (22 h)

In this activity, VLBI observations are made of the Viking spacecraft and also quasars which are near the spacecraft pointing angles. Using these data from the spacecraft, which is in orbit around Mars, the orbit of Mars can be tied into the nearly inertial reference frame formed by the quasars.

D. Radio Source Catalog Development (42-½ h)

The goal of this activity is to identify, precisely determine locations, and measure the flux densities of a large number of compact radio sources which are usable as part of an intercontinental baseline S- and X-band VLBI network. This is an on-going activity and more than 600 sources with flux densities greater than 0.1 Janskys have been so identified and located.

E. VLBI System Design Analysis (28-¼ h)

This experiment is used to demonstrate the feasibility of using VLBI techniques to measure relative tracking station locations and to effect inter-station clock synchronization to the nano-second level. The pre-implementation work required to prepare the DSN for the Block I VLBI subsystem is also performed under the aegis of this activity.

F. ARIES-VLBI Laser Intercomparison (265-½ h)

In this activity, a comparison is made between the accuracy of Earth vector measurements made using VLBI observations and those made using laser ranging of Earth orbiting satellites.

G. DSS-13 S-X Feed Concepts (41-¼ h)

This activity had as its goal the development of a high illumination efficiency, common aperture, S-X Cassegrain Feed system. The Phase 1 design has been field tested on the DSS 13 26-m antenna to provide design verification of aperture efficiency, bandwidth, impedance match and noise temperature when mounted onto a large Cassegrain parabolic antenna. This feed system has been in routine use on the DSS 13 26-m antenna throughout 1979, being utilized primarily to support simultaneous S-X reception for various VLBI projects which utilize dual band spacecraft as signal sources.

H. DSS 13 S-X Unattended Systems Development (34 h)

This activity is to develop the operations methodology and systems engineering required for an unattended tracking station for the DSN. Specifically, DSS 13 is being developed as a remote-controlled unattended station and the data base thus developed will be used to predict life cycle costs and the feasibility of implementing an automated station.

This is one of the major activities which have been on-going at DSS 13 during 1979, and the 34 h represents only *manned* hours specifically devoted to computer program development and testing, and does not include the large number of hours used in the unmanned mode during nights and weekends.

I. Microwave Phase Center Calibration

The purpose of this activity is to develop techniques to determine time and phase delays in the ground tracking receiving system and relate RF Phase Centers for these measurements to the physical structure and configuration.

The DSS 13 26-m antenna has been fitted with two "outrigger" antennas, six feet in diameter, which transmit and receive with two identical antennas mounted at the near-field collimation tower, 1.6 km distant. By proper choice of antenna polarization, signals can be transmitted "round robin" through this system of four antennas, and measurements made. Signals can also be received on the 26-m antenna after having passed through a portion of this array, and comparison measurements made.

J. Radiometer Performance Monitoring

This activity makes serendipitous use of the times when the 26-m antenna is not being used for tracking, e.g., nights and weekends. During these periods, the antenna is used to demonstrate the utility of a Noise Adding Radiometer (NAR) in making precision total power measurements of the noise output from a low-noise receiver mounted on a large parabolic antenna. The antenna is placed into various fixed azimuth

and elevations and left stationary for periods of time ranging from 8 to 72 hours. During these periods, the Earth's rotation sweeps the antenna beam across the sky and review of the NAR output enables determination of overall gain stability at various antenna attitudes. If the incremental positions are properly chosen, and the number of observations is large enough, a radio map of the sky is also obtained from these data. During 1979 a total of 689-3/4 h were devoted to this activity.

IV. Non-Flight Project

A. VLBI Investigation of Twin Quasi-Stellar Objects 0957 + 561A, B (RAES 176) (8-¼ h)

This activity performs VLBI observations of this unusual pair of objects which are apparently separated by only 6 arc-seconds. Such observations, assuming sufficient source flux density, can determine the nature of the source's compact radio emission and variability in time.

B. Pulsar Rotation Constancy (176-¼ h)

These observations are used to monitor the short term variations in the period of the Vela Pulsar (0833-45). Also, twenty-three additional well behaved pulsars are studied to discover (a) the nature of the events causing the observed pulsar timing noise, (b) the proper motion of the pulsar, and (c) how a young, erratic pulsar evolves into an older, more stable pulsar. The observing program's goal is to measure the phase of the pulse train from each pulsar at intervals of one week to one month.

C. Planetary Radio Astronomy (137-¼ h)

This program studies the properties of the planet Jupiter's radio emission and uses the results of these observations to construct improved models of Jupiter's radiation belt environment. This program also measures and studies the thermal emission from the atmospheres of the outer planets and uses these data to construct atmospheric models.

D. ALSEP-QUASAR VLBI (3-½ h)

This experiment uses VLBI techniques to tie the lunar ephemeris to the nearly inertial extragalactic reference frame formed by the quasars observed. By combination with the lunar laser ranging, the Earth's orbit also may be tied into the quasar reference frame. Such high accuracy observations are also of value to test gravitational theories and to measure the Earth-Moon tidal friction interaction.

V. Conclusion

Since the Venus Station is not committed to provide mission support, long term testing and other developmental and radio astronomy activities can be carried out without significantly impacting the utilization of the DSN to fulfill its primary flight project support requirements. During CY 1979, a total of 1169.75 manned tracking hours were provided by DSS 13 in support of operations, advanced systems development, and non-flight project activities. This utilization is graphically depicted in Fig. 1. In addition to the manned tracking support, a substantial amount of support was provided in the unmanned mode to S-X Unattended Systems Development and Radiometer Performance Monitoring activities.

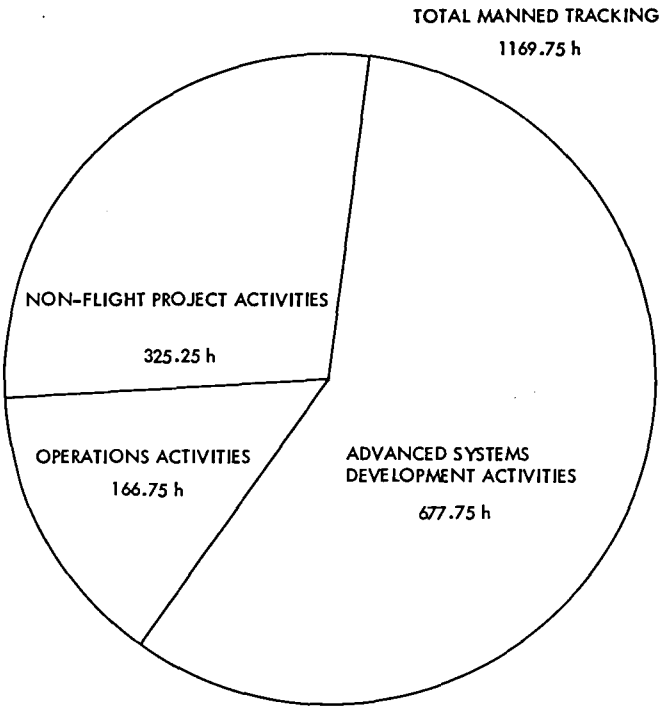

Fig. 1. Tracking utilization of 26-m antenna, Venus Station (DSS 13) during 1979

Data Acquisition for Measuring the Wind on Venus from Pioneer Venus

J. R. Smith
DSN Data Systems Section

R. Ramos
Ames Research Center

The Pioneer Venus Differential Long Baseline Interferometry experiment was designed to measure the motion in three dimensions of the Pioneer probes during their fall to the surface of Venus, using a combination of Doppler and long baseline ratio interferometric methods. The altitude profiles of wind speed and direction that may be deduced from these data are expected to contribute significantly to the understanding of the dynamics of the Venus atmosphere. The design of the experiment and the equipment and software techniques that were developed specially for this experiment are described.

I. Introduction

The Pioneer Venus Differential Long Baseline Interferometry (DLBI) experiment was designed to provide precise measurements of the three dimensional velocity profiles for each of the four Pioneer Venus probes during their descent through the Venus atmosphere. For altitudes below about 65 km, the horizontal components of velocity, if averaged over a few seconds, are substantially equal to those of winds. Interpretation of the horizontal velocities at altitudes above about 65 km and the vertical velocity component at all altitudes requires aerodynamic modeling. The wind velocity information inferred in this way is expected to contribute significantly to the understanding of atmospheric circulation patterns on Venus.

The probe velocity profiles were measured with a combination of direct radial velocity measurements using conventional Doppler velocity measurement technique, and a differential long baseline interferometry technique for the velocity components normal to the line of sight. In a conventional interferometer, the corrupting effects of the transmission media in the vicinity of the spacecraft affect the signal received by both tracking stations almost equally, and therefore largely cancel in the data processing (see Fig. 1). The media in the vicinity of the receiving stations affect the signals independently, and thus the corrupting effects are not reduced by cancellation. In this experiment, the signal from the Bus spacecraft, which remained in ballistic trajectory until after all four probes had impacted the surface of Venus, was used as a reference. Since this Bus signal traversed essentially the same media in the vicinity of the earth stations as did the Probe signals, it was corrupted in essentially the same way. Thus when the interferometric data from the Bus are differenced with the Probe data, the near earth media effects are removed by cancellation. To the extent that the Bus and Probe signals

are processed by the same ground instrumentation and are corrupted by it in the same way, the effects caused by this instrumentation also tend to cancel in the differencing process. The resulting differenced data are sensitive to the motion of the Probes relative to the Bus spacecraft, and are relatively free of errors introduced by the propagation media and the instrumentation.

Four ground instruments were provided for this experiment. Two used facilities of the Deep Space Network (DSN) stations at Goldstone, CA, and Tidbinbilla, Australia. The other two were located at the Spaceflight Tracking and Data Network (STDN) stations at Santiago, Chile, and Guam (See Fig. 2). The three-dimensional velocity measurements required the use of three stations. The fourth station provided a degree of redundancy which improves the confidence in the resulting data and would have permitted the experiment to be completed should one of the stations have failed to function properly. Each of the instruments made use of the existing antennas and receiver preamplifiers at the stations (see Fig. 3). The DSN stations have 64-m diameter antennas and are equipped with cryogenically cooled maser preamplifiers exhibiting an effective system noise temperature of about 24 K; the STDN stations have 9-m diameter antennas and parametric preamplifiers which provide an effective system temperature of about 100 K. All reference frequency signals and all timing signals were synthesized from a single frequency standard at each station; an atomic hydrogen maser standard was used at each DSN station, and a cesium beam frequency standard was used at each STDN station. The receiver at each station was designed to provide a passband from 2291 to 2293 MHz, which was wide enough to include the signals from all four probes and the Bus simultaneously. Additionally, two low-amplitude calibration signals were injected into the receiver, one near each edge of the passband, to permit monitoring of the group delay, the phase delay, and gain of the receiving system. The entire 2-MHz wide passband containing all seven signals was converted by the receiver to a "video" band from 0 to 2 MHz which was then sampled at 0.24-μs intervals (slightly above the Nyquist rate) and digitized with 3 b/sample. The resulting 12.5 Mb/s data stream was then recorded, along with time derived from the local atomic clock, on magnetic tape using a wide-band instrumentation recorder modified for digital recording. A READ-after-WRITE playback capability was then used to provide the data to a fast-Fourier transform spectrum analyzer for verification of overall recording system performance. The signal-to-noise ratio (SNR) that existed at the DSN stations made the unambiguous detection of the Probe signals possible with the spectrum analyzers, but the smaller antenna and higher noise figure of the STDN stations made detection marginal at best, so those stations were operated largely without the benefit of real-time performance verification.

II. Data Acquisition

The data tracking phase of the Multiprobe mission, which extended from carrier turn-on of the first Probe until the Day Probe ceased transmitting from the Venusian surface occupied about 2.5 h during which nearly 10^{12} bits of data were recorded. While these data occupied only a modest number of rolls of instrumentation tape, they were not in a form which would have permitted the required data processing. Had this amount of data simply been copied to computer tapes, several thousand reels would have been required. To reduce this amount of data to a manageable level, the wide-band recordings were transported to the Jet Propulsion Laboratory (JPL) where the data were digitally filtered to extract an approximately 1-kHz-wide spectral window about each of the seven (5 spacecraft and 2 calibration) signals present in the original 2-MHz recorded bandwidth. Conventional tracking data were acquired by the two DSN stations during the encounter, and this was used to obtain an a posteriori estimate of the frequency profile of each spacecraft as observed from each station. Figure 4 illustrates a typical Doppler profile. During the digital filtering process at JPL, the spacecraft signals were multiplied by the estimated frequency to remove the major portion of the Doppler shift and the result filtered to the 1-kHz bandwidth. This bandwidth reduction process reduced the amount of data to about 4×10^9 bits which, although large, was manageable. The computer tapes, containing the bandwidth-reduced data, were shipped to the Massachusetts Institute of Technology (M.I.T.) where the experimenter and his associates are continuing the data processing.

III. Data Processing

The data processing is a multipass process in which the phase history of each signal at each station is determined. These histories are then differenced twice. First the phase for the same spacecraft is differenced for two receiving stations, then these differences for two spacecraft (a Probe and the Bus) are differenced to produce the desired information on the vector component of the velocity of the Probe relative to the Bus. This vector component lies in the plane defined by the two stations and the Probe and is normal to the average line of sight between the stations and the Probe. Further processing, involving knowledge of the Bus trajectory relative to the planet and knowledge of the Probe position relative to Venus, is necessary to define the direction of the local vertical at the Probe. Further discussion here will be concerned only with the determination of the phase history of the Probe signals as observed at the stations.

The signals recorded at the DSN stations exhibit a sufficiently high SNR that they may be phase tracked without difficulty. This is done using a process that is essentially a

digital model of the standard analog phase-locked loop. For the signals recorded at the STDN stations, however, the problem is more difficult because the signals are undetectable with less than a few seconds averaging time, and the rate of change of frequency remaining in the signals after the first step of processing at JPL is too high to permit tracking the signals with a sufficiently narrow loop. To alleviate this problem, the frequency profile observed at a DSN station is adjusted by the expected Doppler difference between that station and a STDN station and then used to remove most of the remaining frequency variation. The resulting data are then digitally filtered to a 20-Hz bandwidth in which the signal can be tracked with a loop utilizing a 10-s time constant.

The SNR in this loop is approximately 10, but the phase error is as large as 0.5 radian and there are phase slips and periods of loss of lock caused by the rapid (relative to the averaging time) fluctuations of signal frequency. The frequency profile thus determined is then removed from the data, and the process is iterated several times. The resulting phase profile is the best available estimate of the phase profile of the signal as observed at the STDN station, but may still contain errors due to cycle slips or loss of lock in the phase-locked loop used. As a check on the quality of the data, the process is repeated, starting with the measured frequency profile from the other DSN station. The results typically agree to within the noise in the DSN data (6 degrees peak to peak) which is much less than the noise in the STDN data. This is, of course, a necessary but not sufficient condition to guarantee correct phase tracking. To gain additional confidence, the data are reprocessed using different integration times for the tracking loop. When a 6-s averaging time is used, the data are degraded by the remaining thermal noise, while for an 18-s averaging time, the actual frequency changes due to the varying Venus winds degrade the quality of the phase tracking. As a final check, the redundancy provided by the fourth observing station is used; the velocity profiles, as determined using data from the two DSN stations and one STDN station, are compared with the profiles using the two DSN stations and the other STDN station. Since the errors will occur largely as a result of attempting to phase track the weak STDN data, this last comparison provides considerable confidence that the profiles are correct to the level of the agreement observed. It is believed that the estimates of the velocity of the probes, relative to Venus and including all significant error sources, will be accurate to 0.3 m/s for all components when averaged over 100-s intervals.

IV. Instrumentation

Much of the equipment used to support the DLBI experiment was standard tracking station equipment. This standard equipment includes the antenna and antenna-pointing equipment, the low-noise receiver preamplifiers, and the frequency standards and clocks. The receivers were a special wide-bandwidth single-sideband design for which phase stability was a major design consideration. A block diagram of the receiving system used at the DSN stations is shown in Fig. 5. Performance requirements for the system are presented in Table I. The receivers used in the STDN stations were similar except that parametric preamplifiers were used rather than maser preamplifiers. The calibration tones were generated by a tunnel diode pulse generator driven by a phase stable 5.4-MHz square wave. The pulse train was then gated at a 1.8-MHz rate to produce a 1.8 million pulse per second pulse train. Harmonics of these pulses at 2291.1 MHz and 2292.9 MHz were then injected into the receiver. At the DSN station, the calibration signals were injected after the distribution amplifier that delivers the signals to the receivers used for telemetry so as to avoid interference with the telemetry recovery process. Provision was made, however, for injecting the calibration signals ahead of the maser preamplifier for test purposes. Since the STDN stations were dedicated to this experiment and were not attempting to recover the telemetry data, the calibration signals were injected ahead of the preamplifiers at those stations. The remainder of the receiver is of conventional design except for the three blocks shown at bottom center of Fig. 5. These blocks provided a local monitor of the phase stability of the receiver that could be used during testing. The amplitude of the calibration tones used during the mission was too low to allow this equipment to function during this time. The mixer and bandpass filter separated the calibration tones present in the receiver output and mixed them together to obtain a signal at the 1.8-MHz tone spacing. The phase meter compared this with a model of the original pulse repetition rate derived from the same source as the original pulses. This comparison provides a good indicator of the phase stability of the receiver.

The output of the receiver, which contained the five spacecraft signals and the two calibration tones all dominated by the thermal noise present in the 2-MHz bandwidth, was then sampled at 0.24-μs intervals and quantized to 3 bits. The quantizer was designed with optimally spaced quantization levels to minimize the degradation in SNR caused by the quantizing. The quantized digital data, together with timing and error detection information, were then recorded on an instrumentation tape recorder which was specially modified for digital recording. The data were distributed across twenty tracks on the tape and recorded at a bit density of 11000 b/cm (28000 b/in). This permitted the recording of the 12.5 Mb/s data at a tape speed of 11.8 cm/s (30 in/s) which provided about 80 min of recording per reel of tape.

As discussed above, the wide-band tapes recorded at the four tracking stations were processed at JPL to produce

narrow-bandwidth records. Each tape contained the signal from one spacecraft or one calibration signal. The processing was entirely digital and was performed using special purpose hardware in conjunction with a general purpose computer. A conceptual block diagram of the process is given in Fig. 6. The a posteriori estimate of the frequency profile for one signal was used by the control computer to control the frequency of the oscillator. The time base for this process was provided by the wide-band data samples, and the oscillator actually produced a sequence of numbers representing the oscillator output. Because this process was fully quantized in both time and amplitude, the phase history of the oscillator was exactly known. The oscillator output was multiplied by the signal samples in the mixer and the result summed in the filter. The running sum was sampled periodically and stored on the output tape. The quadrature channel was provided to allow separation of signals whose frequencies were above the oscillator frequency from those whose frequencies were below. This process was repeated for each of the seven input signals on each wide-band tape from each of the four stations. The resulting narrow-band data, in standard computer tape format, was then sent to M.I.T. for further processing by the experimenter.

Preliminary results reported by the experimenter (Refs. 1 and 2) show that the recording equipment at all four stations functioned perfectly, and that the velocities of the winds on Venus can be estimated from the data.

Note

This article originally appeared in *IEEE Transactions on Geoscience and Remote Sensing*, Vol. GE-18, No. 1, January 1980.

Acknowledgments

The conduct of the DLBI experiment required the dedicated efforts of a great many people for the design, implementation, and performance verification of the many pieces of equipment and computer programs that were required. Many additional people were involved in testing and operating the equipment. We can thank only a few of these. The crews of the four tracking stations performed flawlessly in their execution of these intricate observations; D. W. Johnston of JPL and G. Kronmiller, J. McKenzie, and P. Mitchell of the Goddard Space Flight Center provided the training and operations support for the DSN and STDN; P. Liebrecht of GSFC assisted in overall coordination for the STDN; H. Donnelly and associates (JPL) implemented the receiver and calibrated systems; K. Kimball and associates (JPL) provided the wide-bandwidth recorders; R. Tappan (JPL) implemented the bandwidth reduction assembly; R. Speer and associates (Bendix Field Engineering Corp.) operated the bandwidth reduction assembly. I. I. Shapiro of M.I.T. originally suggested the DLBI experiment in 1971 and G. H. Pettengill, Chairman of the Pioneer Venus Radio Science Team led the effort in 1972 to 1974 to include the experiment in the Multiprobe mission plan. C. C. Counselman, III, of M.I.T. is the experimenter. His exceptional level of interest and enthusiasm contributed enormously to the success of the implementation and operations activities. S. A. Gourevitch, R. W. King, G. B. Loriot, and R. G. Prinn, all of M.I.T., provided the data processing software and are providing the data analysis. R. B. Miller (JPL) is the DSN Tracking and Data Systems Manager for the Pioneer Venus Project; L. Colin (Ames Research Center) is the Project Scientist and C. Hall (ARC) is the Pioneer Venus Project Manager.

References

1. C. C. Counselman, III, S. A. Gourevitch, R. W. King, G. H. Pettengill, R. G. Prinn, I. I. Shapiro, R. B. Miller, J. R. Smith, R. Ramos, and P. Liebrecht, "Wind velocities on Venus: Vector determination by radio interferometry," *Science*, Vol. 203, p. 805, 1979.
2. C. C. Counselman, III, S. A. Gourevitch, R. W. King, G. B. Loriot, and R. G. Prinn, "Venus winds are zonal and retrograde below the clouds," *Science*, Vol. 205, p. 85, 1979.

Table 1. Performance specifications on the DLBI receivers

Parameter	Requirement
Input signal frequency range for probe and calibration signals	2291.1 to 2292.9 MHz
Phase calibrator	
Phase stability (over four hours)	≤1 deg phase variation between calibration signals
Signal level	≥94 dBm into receiver front end via coupler
Frequencies	2291.1 to 2291.15 MHz lower calibration signal; 2292.9 to 2292.95 MHz upper calibration signal
Receiver composite output signal	
Frequency range	0.1 to 1.9 MHz
Phase ripple	2 deg peak-to-peak
Phase linearity	9-pole Tchebycheff response. Phase equalized to within 10% of linear
Amplitude response	≥10 dB down at 2.26 MHz

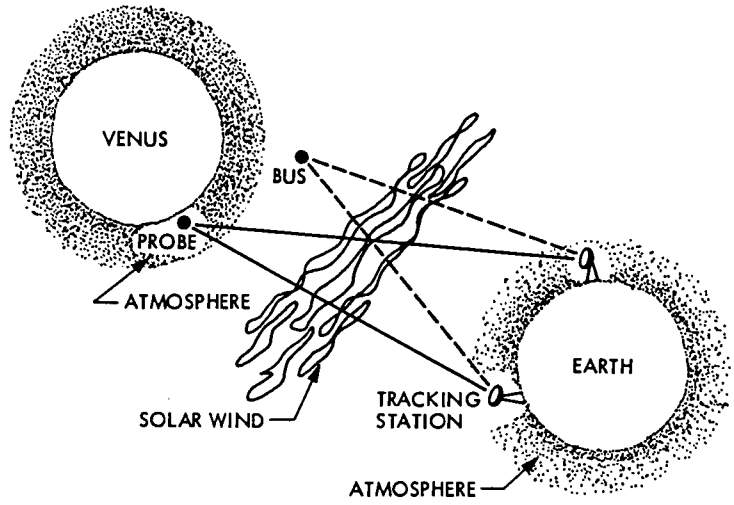

Fig. 1. Geometry of the DLBI observations, with the atmospheric and the interplanetary propagation media indicated. Because the propagation paths are so nearly parallel, and because the DLBI observable is differenced symmetrically with respect to both the transmitting spacecraft and the receiving ground stations, the effects on the observable of both Venus' and the earth's atmospheres cancel to a high degree. The effects of the interplanetary plasma do not cancel so exactly

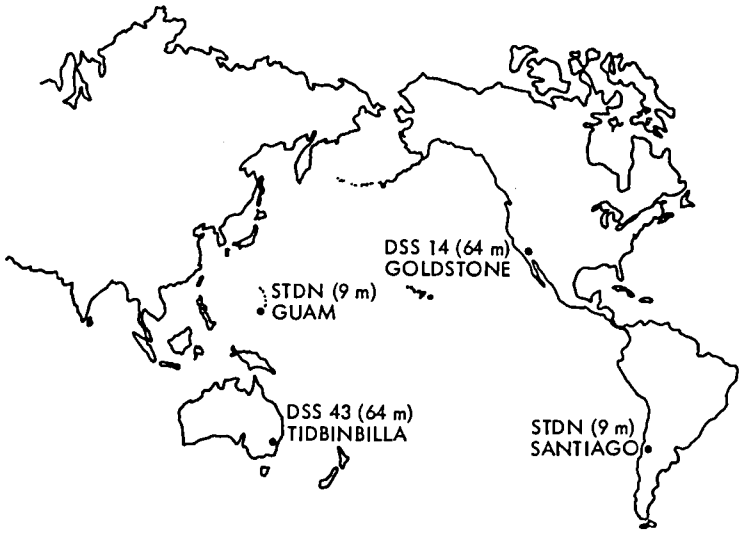

Fig. 2. DSN and STDN station locations, DLBI wind measurement experiment

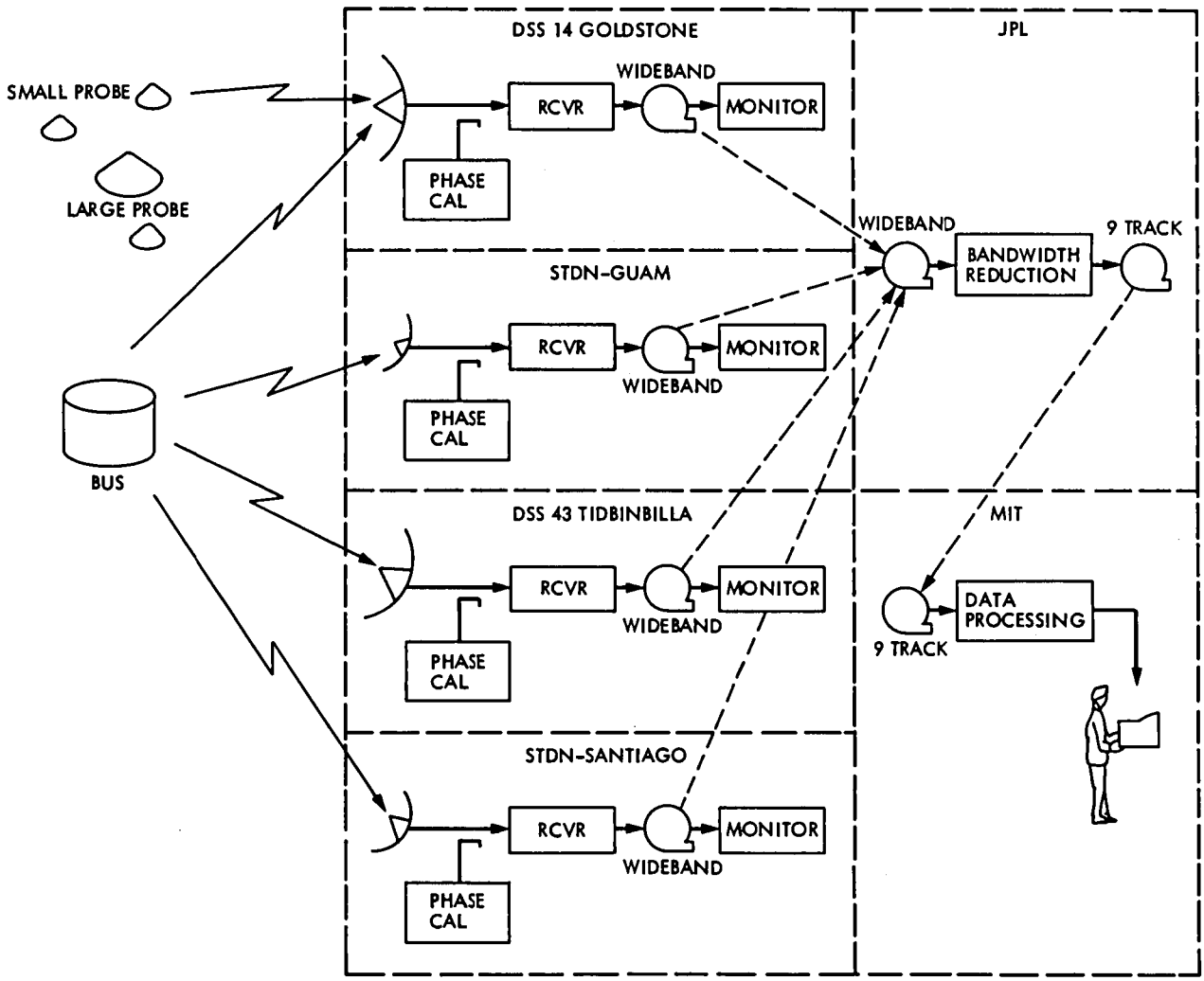

Fig. 3. The DLBI experiment involved the simultaneous reception and recording of the signals from the four Pioneer Probes and the Bus spacecraft, and subsequent processing of the recorded data at JPL and M.I.T.

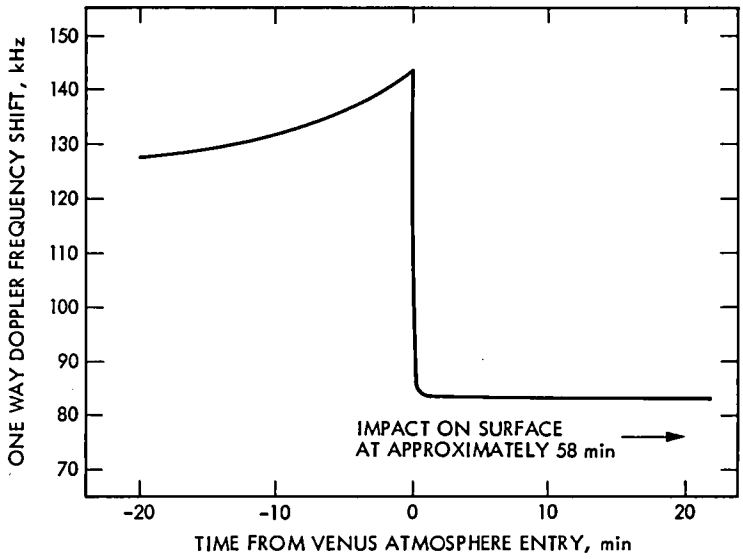

Fig. 4. The Pioneer Venus Probes fell with increasing speed as they approached Venus. Upon reaching the top of the Venus atmosphere, they were quickly slowed by atmospheric friction and then fell through the atmosphere at terminal velocity. This velocity profile results in a Doppler shift in the Probe's S-band radio carrier frequency. A typical frequency profile for the Pioneer Venus Probes is illustrated

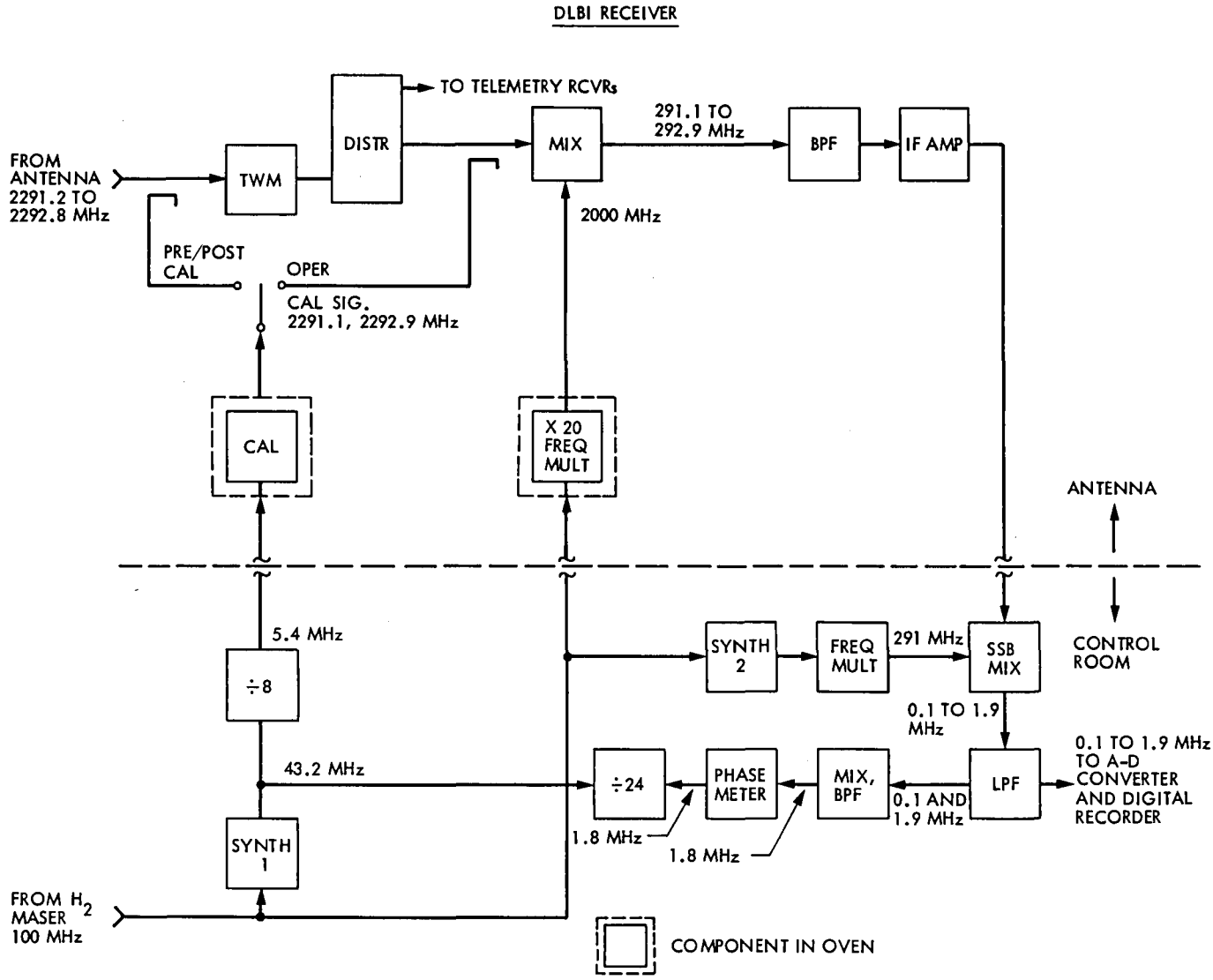

Fig. 5. Simplified block diagram of the receiving system used in the DLBI experiment

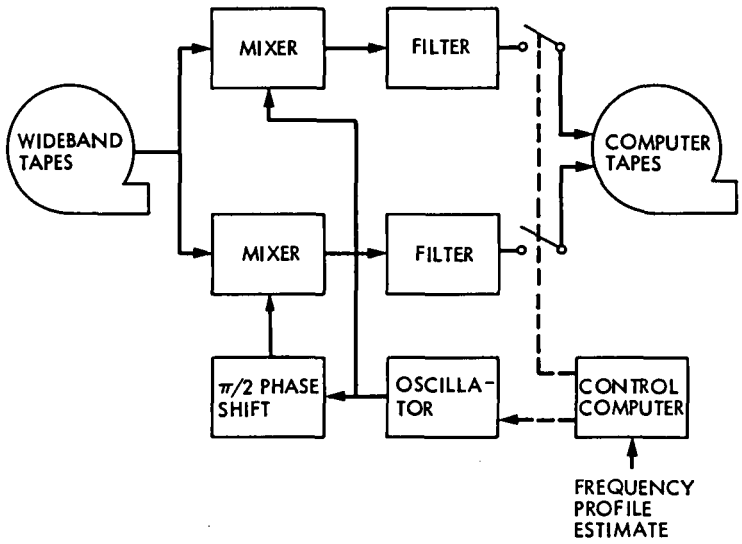

Fig. 6. Simplified functional block diagram of the bandwidth reduction system provided for the DLBI experiment at JPL

Planetary Radar

R. M. Taylor
Deep Space Network Operations Section

G. S. Downs
Communications Systems Research Section

This article reports on the Radar Astronomy activities supported by the Deep Space Network during January, February and March 1980. Data were obtained at both S- and X-band and the observations were 75 percent successful.

The high-power S- and X-band radar transmitters at the Goldstone 64 meter station were used for a radar probe of Mars during January, February and March 1980, which was designed to provide range and doppler data derived from signals reflected from the Martian surface, taking advantage of the planet's nearness during opposition.

Observations were scheduled to provide eight hours of data every three to four days. Complete success would have provided two looks at each surface element and allowed measurement of a continuous topographic profile for slightly more than one full rotation of Mars.

In reality, the observations were 75 percent successful and of high quality. Complete success was not achieved, due to 1) occasional high-voltage problems in the S-band transmitter, 2) some data-acquisition hardware failures and 3) weak back-scattered power from the rougher regions of Mars.

The radar sensitivity is inversely proportional to the fourth power of the Earth-to-Mars distance. This opposition provided a minimum distance of 0.7 Astronomical Units (AU), twice the possible minimum. Hence, the radar sensitivity was about 12 dB below maximum. Nevertheless, the data quality is high enough to provide:

(1) Topographic profiles with 8 km resolution along the latitude parallel at 23° N, thereby adding to the topographic database established at other latitudes between 1971 and 1978.

(2) Additional scattering data for the Martian regolith, with an eye towards differentiating terrain types by remote sensing and correlating the results of the Viking on-board instrumentation.

(3) A basis for extending the Martian ephemeris to 1982 in the event that the Viking Lander spacecraft can no longer provide ephemeris information (the same region will be observed again in 1982).

A Survey of Numerical Models for Wind Prediction

D. Schonfeld
DSN Engineering Section

A literature review is presented of the work done so far in the numerical modeling of wind flows. Pertinent computational techniques are described, as well as the necessary assumptions used to simplify the governing equations. A steady-state model is outlined, based on the data obtained at the Deep Space Communications complex at Goldstone, California.

I. Introduction

In recent years, due to the increasing cost of oil and other fossil fuels, wind-generated electricity has been actively sought as a possible alternate and renewable energy source. At the present time, there exists a national R&D program to test the engineering and economic feasibility of wind-driven turbines.

In determining the site and construction of such turbines, a necessary starting point is the collection of data on wind speed, direction and duration. Since this data collection is limited in scope due to resource restrictions, alternative means must be sought. This siting problem can be stated as follows: for a certain area, given the topography of the terrain and given the wind direction and speed at one or more of the area boundaries, it is desired to predict the wind distribution at all points within the stated boundaries.

The solution of the problem can be quite complex due to *three* main sources of difficulty. First, the problem is complicated by the topography of the terrain, which may be highly irregular, requiring a large amount of data to describe it. Second, the wind data, given at one or more of the boundaries, is highly irregular with respect to temporal variation in magnitude and with changes of direction. Therefore, there are difficulties related to processing the large amounts of data necessary for describing these boundaries. Third, and of equal importance, is the fact that the fluid dynamics and energy equations describing the wind flow are too complicated to be solved by analytic means in closed form. Because of these reasons, any analysis for the prediction of wind velocities over an arbitrary terrain must be treated by numerical, i.e., computer methods.

This article is written with the aim of introducing the reader to various aspects of wind prediction research. The first section presents the results of a literature search made during June – December 1979 into this subject and it also describes the past DSN activities in this field.

The next four sections discuss the physical and computational aspects of pertinent numerical modeling. The article concludes with suggestions for future work.

II. Literature Review

During the period from June – December 1979, a review of the literature pertaining to wind velocity predictions has been conducted in the Energy Group of the DSN Engineering

Section. It became apparent that most of the research effort in this area had been concentrated at only a few laboratories and universities. The results obtained at these centers are presented below.

A. Work Performed at Los Alamos Scientific Laboratory

The Los Alamos Scientific Laboratory (LASL) has a strong tradition of computer modeling dating back to the 1940s. The laboratory possesses some of the most modern computers available and an excellent technical staff. This combination has produced several classic techniques for fluid flow modeling such as the Marker And Cell (MAC) (Ref. 1) and the Particle In Cell (PIC) methods (Ref. 2). In recent years, LASL has published a number of papers dealing with computer programs that model the spread of wind-borne pollutants (Refs. 3-5). These programs are characterized by (1) solutions of the complete, unsteady Navier-Stokes equations, and (2) the application of these solutions to flows past obstacles with a regular geometry, e.g., cubes and rectangular blocks. The results obtained show very good agreement with experimental observations of pollutant dispersion.

A penalty paid for obtaining such good results is the high cost incurred by operating these programs. Nearly all the storage of the 64,000-word fast core memory of a CDC – 7600 computer is taken up by these codes. Within these programs, there are approximately 3300 computational cells, each of them requiring approximately 1.5 sec of computation time per cycle; this means significantly more than 1 hour of computation time for each cycle. Some of the simpler programs developed at LASL (such as SOLA) still require large amounts of computer time and cost. A rough estimate (Ref. 10) shows that these costs are proportional to (N^4), where N is the number of mesh cells into which the length dimension is divided, and with (K^3), where K is proportional to the distance that the mesh boundaries must be kept away from the flow region of interest. Therefore, computational costs can be kept within some reasonable limits by accepting the minimum resolution that will still yield accurate results, that is reducing N and providing realistic boundary conditions, which means minimizing K. It was shown (Ref. 6) that these cost penalties still remain high even when the physical assumptions of the problem are slightly relaxed.

B. Work Performed at Lawrence Livermore Laboratory

A second center which is involved in research on wind field prediction is the Lawrence Livermore Laboratory (LLL). The impetus for their studies is also the desire to predict air pollution dispersion. The papers published by LLL point out both the diversity which can exist in computer modeling and the marginal results that one often encounters when such numerical modeling is applied to wind prediction. In contrast with the LASL efforts, the model used at LLL (Ref. 7) employs variational techniques to obtain a time-independent, three-dimensional wind field model. Despite the sophisticated techniques involved, the comparison of numerical predictions with terrain measurements is not good. "Typically, 60% of the time the calculations of pollutant dispersion were within an order of magnitude (of terrain measurements)." The chief sources of error were found to be, in decreasing order of magnitude, (1) wind direction, (2) topography, (3) diffusion parameters, (4) source strength, and (5) wind speed. Probably because of its time-independent characteristics, the LLL program is shorter to run than corresponding LASL models; the LLL program takes 80% of the large core memory on a CDC – 7600 computer and uses 2 to 3 minutes of CPU time to generate approximately 30,000 grid points above the terrain. There is no documentation as to how many iterations (i.e., sweeps) are needed to achieve the steady-state conditions.

C. Work Performed at Colorado State University

Two university centers have also done important work regarding different aspects of wind modeling. Research done at the Colorado State University, Fort Collins (CSUFC), has centered on experimental wind tunnel modeling of atmospheric flows over various topographies. Specialized meteorological wind tunnels are used in these studies (Refs. 8 and 9). The wind tunnel at Ft. Collins is capable of simulating thermally stratified atmospheric boundary layers. This type of modeling is also being used in France, Australia, and New Zealand (Refs. 10-12). The foremost advantage to this approach is that it lowers costs if the terrain conditions can be reproduced accurately in a wind tunnel. Also, it becomes much cheaper to obtain pertinent data from wind tunnel measurements rather than from instrumentation erected and monitored on the actual terrain. The results published by CSUFC indicate that there exists enough similarity between wind tunnel patterns and actual wind fields to justify this approach (Ref. 13). It is still unknown how adequate this modeling can be in nonspecialized or nonmeteorological wind tunnels, and very little information about it has so far appeared in the literature (Ref. 14). The CSUFC interest in computer modeling seems to be centered on the analysis of atmospheric turbulence. Significantly, the results which were obtained from numerical models were then checked with wind tunnel measurements (Ref. 60).

D. Work at Other Universities and Centers

The other university center which has done long-range, sustained research on wind fields is Pennsylvania State University (PSU), where H. A. Panofsky and his co-workers

have conducted a number of investigations on the effect of terrain roughness on wind profiles (Refs. 15-19). Their data is probably the best record on how different types of terrain roughness such as forests, cropland, and desert can affect the wind profiles. How important this information would be in a numerical model of wind prediction, is not known at the present time. Work has also been done at Sandia Laboratories, Albuquerque, New Mexico on numerical wind modeling (Ref. 58), but the present status of this research is unknown.

The NASA-Lewis Research Center has been involved in designing and building their first 100-kW(e) wind propeller and working in cooperation with the Department of Energy as consultant in implementing similar or larger units at various other locations. However, relative to numerical modeling of wind velocities, it was not evident that NASA-Lewis was involved in detail.

E. JPL Activities

The wind prediction studies at JPL were aimed at determining the feasibility of using wind power as part of an energy system to supply the energy needs for the Deep Space Network at Goldstone, JPL in Pasadena, and Edwards sites. In 1974, a Wind Power Feasibility Study committee at JPL published a preliminary report (Ref. 59), which contained a section related to wind siting. The report limited itself to discussing observed wind speeds at different California sites. This data was based on a comprehensive report of observed wind speeds at 137 California sites (Ref. 42). In parallel to that effort, another program was undertaken to determine the effects of wind loading on the structure of the tracking antennas at Goldstone. For the latter program, continuous records of wind speed and direction were obtained at six Goldstone sites (including different heights at the same site) during the period from October 1974 through July 1976. These records form one of the most comprehensive wind logs available, despite considerable gaps, due mainly to equipment malfunctions. Besides the terrain measurements, a private consulting firm (MRI)[1] developed a computer model for wind prediction at the Goldstone site. The results of this program (Ref. 21) show it to be quite unreliable and very expensive at about $300/run. A possible cause for this poor performance is given as due to "lack of sufficient fineness in the rectangular grid representation of the terrain." At the present time, all of the data taken by the Goldstone wind energy measurement system has been processed and a report is expected to be released shortly.

[1]Meteorology Research, Inc., Box 637, 464 West Woodbury Road, Altadena, CA 91001.

F. Conclusions of Literature Search

From the literature search briefly described above, one can draw the following conclusions:

(1) No numerical model presently available can predict with sufficient accuracy wind speeds and directions over an arbitrary terrain.

(2) Building such a model is feasible; this has been shown by the computer models developed at LASL for pollutant dispersion.

(3) The results of any such model can be checked cheaply and accurately with the aid of wind tunnel experiments.

(4) JPL has one of the best data bases available to serve as an input for such a model. This is extremely important since a computer program is only as good as the inputs that the program starts with.

Building such a numerical model in a simple way would be of great help to the DSN in the decision of wind turbine locations to achieve a sizable reduction in the energy consumption and cost. The sections that follow address themselves to the "mechanics" that enter into writing such a new program. The fluid mechanics, mathematics, and computational bases for such a model are discussed in a tutorial manner starting from elementary notions and briefly touching some state-of-the-art techniques.

III. Mathematical and Physical Description of the Problem

The flow dynamics of many liquids and gases can be described by means of a mathematical expression known as the Navier-Stokes equation. This is a vector equation which relates the forces and accelerations acting on a fluid particle.

In cartesian coordinates, the x, y, and z components of this equation are respectively:

$$\frac{\partial V_x}{\partial t} + V_x \frac{\partial V_x}{\partial x} + V_y \frac{\partial V_x}{\partial y} + V_z \frac{\partial V_x}{\partial z} = - \frac{1}{\rho} \frac{\partial p}{\partial x} + \frac{\mu}{\rho} \left(\frac{\partial^2 V_x}{\partial x^2} + \frac{\partial^2 V_x}{\partial y^2} + \frac{\partial^2 V_x}{\partial z^2} \right) + F_x \quad (1)$$

$$\frac{\partial V_y}{\partial t} + V_x \frac{\partial V_y}{\partial x} + V_y \frac{\partial V_y}{\partial y} + V_z \frac{\partial V_y}{\partial z} =$$

$$-\frac{1}{\rho}\frac{\partial p}{\partial y} + \frac{\mu}{\rho}\left(\frac{\partial^2 V_y}{\partial x^2} + \frac{\partial^2 V_y}{\partial y^2} + \frac{\partial^2 V_y}{\partial z^2}\right) + F_y \tag{2}$$

$$\frac{\partial V_z}{\partial t} + V_x \frac{\partial V_z}{\partial x} + V_y \frac{\partial V_z}{\partial y} + V_z \frac{\partial V_z}{\partial z} =$$

$$-\frac{1}{\rho}\frac{\partial p}{\partial z} + \frac{\mu}{\rho}\left(\frac{\partial^2 V_z}{\partial x^2} + \frac{\partial^2 V_z}{\partial y^2} + \frac{\partial^2 V_z}{\partial z^2}\right) + F_z \tag{3}$$

The first term on the left hand side of these equations represents a temporal acceleration. The remaining terms on the left hand side represent accelerations due to the motion of the fluid (convective accelerations). The right hand side of the equations contains the force terms due respectively to pressure, viscous and bulk effects.

The three Navier-Stokes equations contain five unknowns: the velocity components V_x, V_y, and V_z, the pressure p and the density ρ. Even if the problem is such that ρ can be considered as a known constant, there will still be four unknowns. In order to have as many equations as there are unknowns, an additional equation is needed. The needed relation is the conservation of mass, known as the continuity equation. The continuity equation for an incompressible fluid is:

$$\frac{\partial V_x}{\partial x} + \frac{\partial V_y}{\partial y} + \frac{\partial V_z}{\partial z} = 0 \tag{4}$$

Hence, for the case where ρ is constant (incompressible flow), the continuity and the three components of the momentum equations (Navier-Stokes) will form a well-posed system of four equations and four unknowns.

An important characteristic of the Navier-Stokes equations is the nature of the convective acceleration terms. These accelerations consist of dependent variables (velocities) multiplied by their derivatives, for example V_x multiplied by $\partial V_x/\partial x$. Such terms are called "nonlinear", and the equations that contain these types of terms are called nonlinear equations. Nonlinear equations are very difficult to solve by analytic methods. A limited, if important number of solutions exist for simplified, linearized forms of the Navier-Stokes equations (Ref. 22). These simplified forms occur when the nature of the flow allows the investigator to neglect some of the terms in comparison with other terms. For example, for a flow which has the same axial velocity profile at all locations on the Z-axis, we can neglect terms that contain $\partial V_z/\partial z$.

It is only in the last decade that the advent of large computers has made possible the solution of the *full* Navier-Stokes equations by *numerical* methods. In considering such methods, one needs to know the answers to the following questions:

How are the equations approximated for numerical processing?

What are the numerical errors and instabilities that can arise?

What techniques are available to solve the flow problems of interest by fast, inexpensive, and accurate means?

Some answers to these questions are considered next.

IV. Numerical Procedures

A. Finite Differences and Finite Elements

There are two main numerical techniques available for the solution of fluid flow phenomena. They are the *finite-difference method* and the *finite-element method*. In the first, the differential equations to be solved are transformed into a set of *difference equations*. Difference equations are algebraic in nature. They consist of additions and subtractions of variables at discrete points, in place of the continuous derivatives that occur in differential equations.

In the second technique, *the finite element method*, variational calculus is used to solve the differential equations of the problem converting it to an integral form and following a minimization path. First, the region of interest is divided into discrete elements. The elements are assumed to be connected only at the common nodes of their boundaries, (for example, nodes a, b, c, in Fig. 1). The finite-element method searches for the values of the dependent variables at all these common nodes within the domain. The variational techniques which are used (for example, the Bubnov-Galerkin method) consist of setting up integrals of the differential equations and then minimizing the values of these integrals at each of the nodes in the domain.

There is no clear-cut choice as to which of these two methods is better for the solutions of fluid mechanics problems. Finite differences are easier to set up than finite

elements. In addition, there is a large body of experience dealing with finite difference techniques as applied to numerical fluid dynamics (Ref. 23). This experience has to do with questions of numerical stability and convergence and is very important when writing new numerical schemes. The main disadvantage of the finite-difference method is that it does not lend itself very easily to incorporating irregular physical boundaries.

On the other hand, finite element schemes, originally devised for structural and elasticity problems, have only recently been applied to fluid mechanics problems. Their great advantage is the ease with which the solution domain can be discretized. Therefore, irregular physical boundaries are easily described by this method. However, finite-elements methods suffer from difficulties in dealing with nonlinear terms of the Navier-Stokes equations and with incorporating the incompressibility conditions. While new methods are being devised to overcome these difficulties (Refs. 24, 25), finite elements methods also seem to require slightly more computing time than finite difference methods (Ref. 26).

It can be shown (Ref. 27) that finite differences are written for points in space and finite elements are spatial integrators of point formulas. However, no comparisons have been published regarding the efficiency and cost of these two methods when applied to the same problem. Mainly because of the difficulties still remaining with the finite element methods, we will concentrate our attention to the solution of the Navier-Stokes and continuity equations by means of finite-difference techniques.

B. Derivatives and Computational Meshes

There are a number of ways by which derivatives can be approximated by finite differences. Suppose, for example, that one is interested in computing the changes in the x-component of the velocity vector with respect to the position on the x-axis, that is $\partial V_x/\partial x$. Consider a computational mesh, with equal mesh intervals Δh, in the x-direction, as shown in Fig. 2. Denote by $(n-1)$, (n) and $(n+1)$ a series of three adjacent points at the intersections of the grid lines. These points are on a grid line parallel to the x-axis. In general, the velocity component V_x has different values at each of these points; these values are denoted respectively by V_{n-i}, V_n, and V_{n+i}. The change in V_x with respect to x, *evaluated at the point n*, can be approximated by the differences between the velocity values at these points. For example, for the *forward-difference scheme*:

$$\frac{\partial V_x}{\partial x} \cong \frac{V_{n+1} - V_n}{x_{n+1} - x_n} = \frac{V_{n+1} - V_n}{\Delta h} \tag{5}$$

For the *backward-difference scheme*:

$$\frac{\partial V_x}{\partial x} \cong \frac{V_n - V_{n-1}}{x_n - x_{n-1}} = \frac{V_n - V_{n-1}}{\Delta h} \tag{6}$$

Finally, for the *central-difference scheme*, we can take differences relating points on either side of n and obtain:

$$\frac{\partial V_x}{\partial x} \cong \frac{V_{n+1} - V_{n-1}}{x_{n+1} - x_{n-1}} = \frac{V_{n+1} - V_{n-1}}{2\Delta h} \tag{7}$$

Because all difference formulas are only approximations to derivatives, they will contain some errors when compared with the actual values of the derivatives. The magnitude of the errors depends on the finite difference form used. It can be shown mathematically (Ref. 28) that of all three schemes presented above, the central-differences gives the most accurate result.

In general, velocities and pressures do not vary in one direction only. In rectangular coordinates, two- or three-dimensional computational cells, as those shown in Figs. 3a and 3b, are often used.

For two- or three-dimensional flows, one has to decide how to assign the variables *within* each cell. For the two-dimensional case, the most popular schemes are illustrated in Figs. 4a and 4b.

In Fig. 4a, averages at the *center* of the cell are used to determine fluxes through the cell's edges. The staggered mesh arrangement shown in Fig. 4b is more advantageous for incompressible flows (Ref. 29). Here, the horizontal velocity component V_x is centered on the right and left faces of the cell, while the vertical component V_y is centered on the bottom and top. The pressure and density are cell-center averaged.

In addition to assigning the variables within each cell, one also has to "optimize" the computational grid size. An optimal grid size is one which yields good resolution for the fluid flow phenomena. It is natural to expect that the smaller the grid size, the better the resolution. However, a small grid size also implies a greater number of cells covering the domain of interest. With a larger number of cells, both computational time and cost will increase. Therefore, a good compromise is to use a variable mesh size having small cells in regions of rapid flow changes and larger cells in regions where the flow does not change drastically (Refs. 3 and 36).

In the next section, it will be shown that the selection of mesh size and the way the variables are assigned within each cell are part of the computational stability problem. Meaningful solutions of the Navier-Stokes equations can be obtained only when written in a certain form and when the finite differences are forced to take into account the direction of the flow velocities.

C. Problems of Stability and Convergence

When finite-differences are substituted for the derivatives, it may happen that the numerical solution behaves very differently compared to the solution of the corresponding differential equation. The main causes for such discrepancies are instability and poor convergence.

Since any computer memory is limited, the numbers that are stored and worked with in computers can be represented only by a finite number of digits. Numbers having more digits are "rounded-off" according to algorithms designed into the machine. Any such rounding-off will contribute to errors in the final result. Therefore, it is possible that round-off errors will propagate through a computer program and, as a result, small changes in the initial data will be translated into very large changes in the output. Numerical schemes that suffer from such defects are said to be unstable. The growth of errors due to the presence of possible extraneous solutions to the difference equations, can also cause instability (Ref. 61).

Another possible type of error has to do with the convergence of the algorithm used. In general, finite differences are only approximations to the continuous derivatives that they replace, and therefore, the numerical solution will always be in error compared to the solution of the original differential equation. Mathematically, one defines a *convergent* finite difference scheme as one in which the finite differences solution approaches the continuum differential equation solution, as the mesh size approaches zero (Refs. 23 and 35).

The definitions of stability and convergence can provide only rough guidelines for practical numerical calculations. In particular, stability analysis is still in its infancy. The oldest method for testing the stability of a numerical scheme is due to von Neumann (Ref. 31) and is based on expressing the dependent variables in terms of Fourier series. When the Fourier components are substituted into the finite-difference equation, the decay or growth of each mode in these components will show whether the scheme is stable or unstable, respectively. While this technique works fairly well for linear equations with constant coefficients, it is inaccurate when applied to nonlinear equations such as the Navier-Stokes equations. Hirt (Ref. 32) has introduced another method, based on expanding each term of the finite difference equation into Taylor series and analyzing the higher order terms. Although Hirt's method can be applied to nonlinear equations with variable coefficients, it is uncertain yet whether it can be applied to some of the common complex equations.

It will be shown later that computational stability can be improved by a judicious choice of finite-difference expressions. In particular, a certain scheme of differentiation, called the "upwind" or "donor-cell" method, has been found to greatly improve the stability of the numerical solutions of the Navier-Stokes equations. However, before this method is described further, convergence must be looked at in more detail.

As mentioned earlier, convergence is related to the accuracy of the numerical solution, and it is an indication of how close the numerical solution approximates the solution of the continuous differential equation. The laws of fluid mechanics, as given by Eqs. (1), (2), (3), and (4) can be written in different forms, to which correspond different numerical schemes. Some of these schemes have better convergence than others. In particular, when the momentum equations are written in what is called a "conservative form," it has been argued (Refs. 29, 33 and 34), that the finite difference equations corresponding to this form give more accurate results than when the equations are in a "non-conservative" form.

Although there is no rigorous proof for this statement, and some exceptions have been found (Ref. 23), in general, it is advisable to write the momentum equations in the conservative form (Ref. 35).

D. Conservation: "Upwind-Differencing"

An equation is said to be in "a conservative form" when it can be written as a sum of a time derivative and a spatial flux. For example, the *one-dimensional* momentum equation can be written in conservative form as

$$\frac{\partial(\rho V_x)}{\partial t} + \frac{\partial}{\partial x}\left(\rho V_x^2 + \rho\right) = 0 \tag{8}$$

The corresponding "non-conservative" form of the momentum equation is:

$$\frac{\partial V_x}{\partial t} + V_x \frac{\partial V_x}{\partial x} + \frac{1}{\rho}\frac{\partial p}{\partial x} = 0 \tag{9}$$

Note that Eq. (8) can be obtained from Eq. (9) by adding to the latter the continuity equation multiplied by V_x. The corresponding finite-difference equations for Eqs. (8) and (9) are, respectively,

$$\frac{(\rho V_x)_j^{t+\Delta t} - (\rho V_x)_j^t}{\Delta t} - \frac{1}{\Delta x}\left[(\rho V_x^2 + p)_{j+1} - (\rho V_x^2 + p)_{j-1}\right] = 0 \tag{10}$$

and

$$\frac{(V_x)_j^{t+\Delta t} - (V_x)_j^t}{\Delta t} + (V_x)_j^t \frac{(V_x)_{j+1}^t - (V_x)_{j-1}^t}{\Delta x} + \frac{1}{\rho_j}(P_{j+1} - P_{j-1}) = 0 \tag{11}$$

In the above equations, the superscripts refer to the time step and the subscripts refer to the computational cell (see Fig. 5).

Note than in Eq. (10), the change of momentum with respect to time is given by the difference of cell edge fluxes. In the second equation, neither the velocity nor the pressure are written in a conservative form, because the cell-edge difference fluxes, that is $(p_{j+1} - p_{j-1})$ and $(V_x)_{j+1}^t - (V_x)_{j-1}^t$, are multiplied by $(1/\rho_j)$ and $((V_x)_j^t)$, respectively.

In particular, for the velocity term, Fig. 5 and Eq. (11) indicate that the flux out of the right side of cell j and which enters cell $j+1$, is $((V_x)_j(V_x)_{j+1/2})$. However, the flux *into* cell $(j+1)$, *from* cell j, is $((V_x)_{j+1}(V_x)_{j+1/2})$. Therefore, at the interface between two cells, the outgoing flux is different than the incoming one and it is for this reason that the numerical scheme in Eq. (11) is called "non-conservative."

It has been shown that the finite difference form of the Navier-Stokes equations is frequently unstable, even when the equations are written in conservative forms (Refs. 4, 36-38). However, these equations can be made stable, by replacing the central differences scheme by the "upwind" or "donor-cell" differencing scheme (Ref. 39). In this method, the boundary values for any dependent variable are a function of the direction of the flow velocity. For example, labeling this dependent variable by Q, the upwind (donor-cell) scheme gives:

$$Q_{j+1/2}^t = \begin{cases} Q_j^t & \text{if } (V_x)_{j+1/2}^t \geq 0 \qquad (12) \\ Q_{j+1}^t & \text{if } (V_x)_{j+1/2}^t < 0 \qquad (13) \end{cases}$$

This is illustrated in Figs. 6a and 6b.

V. Simplification of the Governing Equations for Wind Modeling

The Navier-Stokes equation, as written in Section III, is very complicated and its numerical solution would require a great deal of computer time and money. Therefore, in constructing a numerical scheme, it is useful to see if the equations can be simplified in any way. For example, in the problem of wind prediction, by using order-of-magnitude analysis one can use wind speed and direction measurements to check if any of the force and/or acceleration terms are significantly smaller than the other terms. As indicated in Section I, such measurements do exist for the Goldstone area and this data can be used to answer the following questions: (1) Is it necessary to keep the temporal acceleration (transient term) in the Navier-Stokes equation? (2) Are all the convective acceleration terms significant, or can the flow in one direction be neglected in comparison with the other two? (3) Can viscous effects be neglected and the problem be treated as inviscid flow? (4) How can thermal heating and stratification be entered into the equations? (5) Are the flow conditions laminar or turbulent? This section attempts to answer these questions, based on the Goldstone data and on other measurements.

A. Variations in Wind Speed and Direction at Goldstone

The data taken at Goldstone were processed by calculating hourly averages of wind speed and direction. Changes in this average are illustrated in Fig. 7 for an arbitrarily selected week in October 1974. A trend of stronger afternoon winds may be discerned, but this trend is not reproducible enough to be incorporated in any numerical model. It seems that on a diurnal basis there is no steady state for wind velocity, and the best approach is to accept an hourly quasi steady state, with values given by the averages processed from the Goldstone data. Although this means that such a model will have to be run for every hour, the model itself will be much simpler to run than a transient model and thus the cost per run will be lower. The usefulness of this approach has been recognized by other investigators who have built models based partially on this assumption (Ref. 40). An additional advantage of this quasi-steady state approach is that temporary variations in turbulent eddy structures will be averaged out; this will also contribute in decreasing the complexity of the model. (A note on turbulence and its effects appears in Section C.)

B. Convective Accelerations in Wind Fields

In the rectangular coordinate system, there are three mutually perpendicular velocity components: V_x, V_y, and V_z. Spatial changes in these components (e.g., $\partial V_x/\partial x$, $\partial V_y/\partial x$, $\partial V_z/\partial y$) multiplied by the velocities themselves make up the

convective accelerations. The Goldstone data indicate that wind magnitudes do change from location to location, but that velocity changes with height area are, in general, much smaller than those in the horizontal plane (see Fig. 8). Such an observation is also supported by measurements taken at the Savannah River Plant, Georgia (see Fig. 9)(Ref. 41). Note, however, that this data represents speed, a scalar, and not velocity, a vector. Indeed, Fig. 10 indicates that the wind direction changes with height, this change in direction remaining nearly constant with time. Other data, however, indicate a logarithmic distribution of the horizontal velocity components (Refs. 8, 42, 43 and 57).

$$\overline{U}_Z = \frac{U^*}{K} ln\left(\frac{Z}{Z_0}\right) \tag{14}$$

In this formula, $\overline{U}_Z$ is the mean speed (m/s) at height Z above the ground, U^* is the friction velocity[2] (m/s), K is von Karman's constant ($\simeq$0.04), and Z_0 is the roughness length (m). This last quantity is terrain dependent and is related to the height of the roughness elements in a given terrain, such as trees, buildings, crops, etc. Examples of Z_0 are:

Terrain	Roughness length Z_0, m
Sand, desert	0.0003
Grass	0.003 - 0.01
Agricultural crops	0.04 - 0.20
Forests	1.0 - 6.0
City	1.5
Snow	0.00005 - 0001

It is possible that these conflicting data sets result from different wind velocity profiles occurring at different wind speeds, and that these changes may also depend on the surface roughness. In the model proposed, the acceleration normal to the terrain will be taken into account so as to allow the model to exhibit terrain sheltering and some aspects of flow separation (Ref. 40).

C. Viscous Effects, Turbulence

The problems of viscous effects are tied to the velocity profiles. If normal accelerations are to be allowed as indicated in the previous paragraph, then a full three-dimensional model is needed. Such a model must take into effect the influence of viscosity, i.e., the boundary layer that is developed between the main air flow and the ground. Tied to the nature of boundary layers is the problem of turbulence, one of the most complex in fluid dynamics. The modeling of turbulence in any numerical code is not only difficult, but of uncertain accuracy also. Because of this, at least in the preliminary program, turbulence effects will not be taken into account.

[2] U^* is a measure of surface shear stress.

D. Thermal Heating

It was mentioned in Section II that body forces are important in the setup of the Navier-Stokes equations. In the problem of air flow, body forces due to gravitational effects must be coupled with buoyancy effects. The latter are due to thermal heating or, more precisely, to differences in the temperature between the air close to the ground (warmer air) and air higher up (cooler air). These differences in temperature cause differences in density and thus buoyancy forces. The Boussinesq parameter accounts for these forces and also incorporates the effect of gravity. This parameter can be written in either of the two forms:

$$\left(\frac{\rho}{\rho_0} - 1\right) g = -\beta(T - T_0)g \tag{15}$$

In these expressions, g is the gravitational acceleration, ρ_0 and T_0 are reference density and temperature, respectively, and β is the volumetric expansion coefficient.

Note that the second form involves temperatures, which must be considered as unknowns for the momentum and continuity system of equations; this implies that an additional equation, the *energy equation*, must be added to the system.

It is not immediately apparent how important the effect of density stratification is on the prediction of wind speeds. Most wind model studies, (e.g., Ref. 44) do not compare predicted results that include stratification with results that do not. As a compromise between accuracy and computational complexity, the effect of density stratification will be retained, but instead of adding the energy equation to our previous system, the new model proposed will incorporate a subroutine giving the explicit dependence between density and temperature. The advantages of such an approach are also discussed in Ref. 45.

E. Simplified System of Equations

As a result of the above discussions, the system to be solved is composed of the following equations:

Continuity:

$$\frac{\partial V_x}{\partial x} + \frac{\partial V_y}{\partial y} + \frac{\partial V_z}{\partial z} = 0 \tag{16}$$

Momentum:

$$V_x \frac{\partial V_x}{\partial x} + V_y \frac{\partial V_x}{\partial y} + V_z \frac{\partial V_x}{\partial z} =$$

$$-\frac{1}{\rho}\frac{\partial p}{\partial x} + \frac{\mu}{\rho}\left(\frac{\partial^2 V_x}{\partial x^2} + \frac{\partial^2 V_x}{\partial y^2} + \frac{\partial^2 V_x}{\partial z^2}\right) \tag{17}$$

$$V_x \frac{\partial V_y}{\partial x} + V_y \frac{\partial V_y}{\partial y} + V_z \frac{\partial V_y}{\partial z} =$$

$$-\frac{1}{\rho}\frac{\partial p}{\partial y} + \frac{\mu}{\rho}\left(\frac{\partial^2 V_y}{\partial x^2} + \frac{\partial^2 V_y}{\partial y^2} + \frac{\partial^2 V_y}{\partial z^2}\right) \tag{18}$$

$$V_x \frac{\partial V_z}{\partial x} + V_y \frac{\partial V_z}{\partial y} + V_z \frac{\partial V_z}{\partial z} =$$

$$+\frac{1}{\rho}\frac{\partial p}{\partial z} + \frac{\mu}{\rho}\left(\frac{\partial^2 V_z}{\partial x^2} + \frac{\partial^2 V_z}{\partial y^2} + \frac{\partial^2 V_z}{\partial z^2}\right) + g\left(\frac{\rho}{\rho_0} - 1\right) \tag{19}$$

This system contains four equations and four unknowns: V_x, V_y, V_z, p. As it stands, the system also needs explicit relationships between the density and temperature:

$$\rho = \rho(T) \tag{20}$$

and the viscosity and temperature

$$\mu = \mu(T) \tag{21}$$

A final point worth mentioning is the problem of compressibility. In the equations presented above, air is treated as an incompressible fluid. Airflows at moderate temperatures, say between 50 and 100°F, and at speeds less than about 100 m/s (225 mph), can be considered incompressible (Ref. 46). Since these limits are well beyond the situations expected in this study of winds, the numerical analysis will be based on an incompressible flow.

VI. Steady-State Models

The differential equations given in the previous section describe steady, fully developed, three-dimensional flows. Effective numerical procedures for the solution of these equations have been worked out by a group of investigators led by D. B. Spalding (Refs. 34, 47 and 48).

The main variables in these procedures are the velocities and the pressures. The domain of interest is overlaid by a rectangular mesh which can contain cells of different size. The differential equations are then approximated by finite differences applied to this mesh. Figure 11 illustrates the placement of the variables within the computation grid.

Note that in this scheme, the variables are staggered, meaning that the pressure and velocities are stored at different locations; the pressure is stored at the intersection of the grid lines, e.g., at P, and the velocities at the locations indicated by the arrows, i.e., midway between the grid lines. (In this figure, the velocity components for point P are V_x and V_y).

The reason for using a "staggered-grid" arrangement is that momentum fluxes can be easily computed from the *integration* of the velocity components over the areas A_x and A_y, and such integrations form the basis of these methods (Ref. 62).

From the integration of the momentum differential equations, and by using a combination of central and upwind difference schemes, algebraic equations are obtained involving the velocity components and/or any scalar quantity that might be needed such as effluent concentration, radiation flux, etc. Together with the finite difference form of the continuity relation, this set of equations is solved by a semi-implicit[3] method.

The steps in this method are first to establish guessed pressures (either as pure guesses or as values from a previous calculation sweep), and then to obtain a field of intermediate velocities. In general, these intermediate velocities do not satisfy the continuity equation and a pressure correction term must then be introduced. The process of finding this pressure correction field reduces to solving a Poisson equation, a problem for which there exist many rapid and economical methods of solution (Ref. 49).

The algorithm used in these papers has been applied to problems such as that of laminar flow over a slab-sided "build-

[3]The terms explicit and implicit appear quite often in the description of solutions for partial differential equations. Explicit methods are those in which the unknown quantity, say a velocity at a time t, V, is determined in terms of previously found quantities, say V^{t-1}, $V^{t-2}, \ldots, V^{t-n}$. In the implicit methods, *two or more* values of the unknown quantity are specified in terms of known values on a previous data line. For example, the values of say the velocity at time t *and* at different locations can be described as a function of the velocities at these locations at a time $(t-1)$. Implicit methods are often used in time-dependent heat conduction problems.

ing" (Ref. 48), flow with heat transfer in three-dimensional ducts (Ref. 50), and boundary layer flows (Ref. 5). The results are quite good and the methods appear economical, although no figures are given.

There exist some restrictions imposed on these steady programs. These limitations are of three kinds:

(1) All the papers cited above deal with problems involving low Reynolds number laminar flows. At higher Reynolds numbers, which might be expected in wind fields, *turbulence may become a factor*. In this case, one would have to incorporate a turbulence model such as those outlined by Gawain and Pritchett (Ref. 52) or by Deardorff (Ref. 53).

(2) The boundaries of the domain of integration are rigid and impermeable to fluid flow. This simplifies the boundary conditions. In a real situation, however, topographical variations will affect the wind field at the boundaries.

(3) Finally, all the problems under consideration have dealt with regular geometrics: tubes, rectangular blocks, etc. In the wind flow problem, the topography is highly irregular and storing the necessary terrain description can be a significant problem.

None of the difficulties described above represent insurmountable obstacles. As mentioned above, numerical schemes that describe turbulence already exist in the literature. The problem of irregular topography has been attacked by Viecelli (Ref. 54) and also by Mason and Sykes (Ref. 55). Extrapolation formulas can be used to describe the boundary flows; an example of this approach appears in Clark (Ref. 56). It seems possible, therefore, to build on these works and write an accurate wind-field prediction model.

VII. Conclusions and Plans for Future Work

The present report has surveyed various numerical methods which can be used to predict the wind field over an arbitrary terrain, together with an overview of modeling activities by various centers. Several conclusions can be drawn from this review.

Writing such a numerical code is feasible. Numerous papers have been cited which successfully predict the dispersal of pollutants and the velocity vectors over slablike, cuboidal and bell-shaped obstacles. There is no intrinsic and impenetrable difficulty in predicting the velocities over an irregular, three-dimensional terrain such as one would encounter in real life. No claim is made that the problem is simple and that all one has to do is to slap together previously worked out techniques; however, writing such a numerical code is perfectly feasible.

Due to the nature of the problem which requires the manipulation of large amounts of data, any wind prediction numerical model must be economical to run. This economy can be gained by various means – the most obvious one being good programming. Beyond this purely technical aspect, however, the physical data of the problem can also be used to reduce the computational load. For example, by assuming an incompressible and steady-state flow, the governing equations can be simplified considerably and the computational complexity is reduced. The only limit in this simplification process is that the resulting physical model must give a wind field prediction reasonably close to terrain measurements.

A numerical wind model along the lines described above is in the process of being written in the DSN Advanced Engineering and Energy Conservation Group. This model will take advantage of the existing Goldstone Wind Data Base. The results of the computer program will be checked both against terrain measurements and the wind tunnel simulations.

References

1. Harlow, F. H., and Welch, J. E., "Numerical Calculation of Time-Dependent Viscous Incompressible Flow of Fluid with Free Surface," *Phys. Fluids*, Vol. 8, No. 12, pp. 2182-2189, 1965.

2. Harlow, F. H., "The Particle-in-Cell Computing Method for Fluid Dynamics," *Methods in Computational Physics*, Vol. 3, p. 318 ff, 1964.

3. Hirt, C. W., Ramshaw, J. D., and Stein, L. R., "Numerical Simulation of Three Dimensional Flow Past Bluff Bodies," *Comp. Methods Appl. Mech. Engr.*, 14: 93-124, (1978).

4. Hirt, C. W., and Cook, J. L., "Calculating Three-Dimensional Flows Around Structures and over Rough Terrain," *J. Comput. Phys.*, 10: 324-340, 1972.

5. Nichols, B. D., and Hirt, C. W., "Transient Three-Dimensional Fluid Flow in the Vicinity of Large Structures," in Lectures Notes in Physics V. 19, Proc. of the Third Int. Conf. in Numerical Methods in Fluid Mechanics, Springer-Verlag (1972).

6. Nakayama, P. I., and Romero, N. C., "Numerical Method for Almost 3D Incompressible Fluid Flow and a Simple Internal Obstacle Treatment," *J. Comput. Phys.*, 8: 230-240, 1971.

7. Sherman, C. S., "MATHEW – A Mass Consistent Wind Field Model," Lawrence Livermore Laboratory, Report UCRL-52479, May 1978.

8. Cermak, J. E., "Laboratory Simulation of the Atmospheric Boundary Layer," AIAA Paper No. 70-751, 1970.

9. Hsi, G., Binder, G. J., and Cermak, J. E., "Topographic Influences on Wind Near Green River, Utah," Colorado State Univ., Fort Collins, Fluid Mechanics Program, Report No. CER-67-68GH-GJB-JEC54, 1968.

10. Mery, P., "Scale Reproduction of Atmospheric Boundary Layer Diffusion," La Houille Blanche, No. 3, 1969.

11. Mulhearn, P. J., "Turbulent Flow over a Very Rough Surface," 6th Tech. Conf. of Australian Hydraulics and Fluid Mechanics, Adelaide, Australia, 1977.

12. Raine, J. K., "Simulation of a Neutrally Stable Rural Atmospheric Boundary Layer in a Wind Tunnel," 5th Tech. Conf. of Australian Hydraulics and Fluid Mechanics, Christchurch, New Zealand, 1974.

13. Cermak, J. E., and Peterka, J., "Simulation of Wind Fields over Point Arguello, Calif., by Wind-Tunnel Flow over a Topographic Model," Colorado State Univ., Fort Collins, Rept. CER65 JEC-JAP 64, Nov. 1966.

14. Boutwell, F. K., and Porter, R. E., "Industrial Applications of Wind Tunnel Investigations" AGARD Rept. 314 Oct. 1960.

15. Blackadar, A. K., and Panofsky, H. A., "Effects of a Change of Terrain on Wind Profiles," Final Report, July 1, 1965 – August 15, 1968, Pennsylvania State Univ., Dept. of Meteorology, Univ. Park, Penn. 1970.

16. Panofsky, H. A., and Townsend, A. A., "Change of Terrain Roughness and the Wind Profile," Quart. J. of the Royal Meteorological Society, 90 (384): 147-155, April 1964.

17. Panofsky, H. A., and Petersen, E. L., "Wind Profiles and Change of Terrain Roughness at Riso," Quart. J. of the Royal Meteor. Soc. 98 (418): 845-854, Oct. 1972.

18. Peterson, E. W., "On the Relation Between the Shear Stress and the Velocity Profile After a Change in Surface Roughness," *J. Atmos Sci.*, 26 (4): 773-774, July 1969.

19. Blackadar, A. K., Glass, P. E., and Panofsky, H. A., "Effect of Stability on the Wind Profile Under Conditions of Inhomogeneous Terrain Roughness," Symposium on the Theory and Measurement of Atmospheric Turbulence and Diffusion in the Planetary Boundary Layer, Albuquerque, N.M., Dec. 5-7, 1967.

20. Wolte, C. G., Rhody, T. R., Goodridge, J. D., and Powers, J. B., "Office Report on Wind in California," State of California Dept. of Water Resources, Division of Resources Planning, Climatology Group, August 1960.

21. Levy, R., and McGinness, H., *Wind Power Prediction Models*, TM 33-802, Jet Propulsion Laboratory, Pasadena, Calif., Nov. 1976.

22. Berker, R., "Integration Des Equations Du Movement D'un Fluide Visqueux Incompressible," *Handbuch der Physik*, Band VIII/2, Springer, Berlin, 1963.

23. Roache, P. J., *Computational Fluid Mechanics*, Hermosa Publishers, Albuquerque, N.M., 1972.

24. Hughes, T. J. R., Liv, W. K., and Brooks, A., "Finite Element Analysis of Incompressible Viscous Flows by the Penalty Function Formulation," *J. Comput. Physics*, 30: 1-60, 1979.

25. Schneider, G. E., Raithby, G. D., and Yovanovich, M. M., "Finite Element Solutions Procedure for Solving the Incompressible Navier-Stokes Equations Using Equal Order Variable Interpolation," *Numerical Heat Transfer*, Vol. 1, pp. 433-451, 1978.

26. Engleman, M., "A Finite Element for the Numerical Solution of Viscous Incompressible Flows," *J. Comput. Phys.*, 30: 181-201, 1979.

27. Gray, W. G., and Pinder, G. F., "On the Relationship Between the Finite-Element and Finite Difference Methods," *Int. J. for Numerical Methods in Engineering*, 10: 893-923, 1976.

28. Forsythe, G. E., and Wasow, W. R., *Finite-Difference Methods for Partial Differential Equations*, J. Wiley and Sons, N.Y. (1960).

29. Harlow, F. W., and Amsden, A. A., "Fluid Dynamics," Los Alamos Scientific Laboratory Report, LA-4700, Los Alamos, N.M., June 1971.

30. Kalnay de Rivas, E., "On the Use of Nonuniform Grids in Finite-Difference Equations," *J. Comput. Phys.*, 10: 202-210, 1972.

31. O'Brien, G. G., Hyman, M. A., and Kaplan, S., "A Study of the Numerical Solution of Partial Differential Equations," *J. Math Phys.*, 29: 233-251, 1950.

32. Hirt, C. W., "Heuristic Stability Theory for Finite Difference Equations," *J. Comput. Phys.*, 2: 339-355, (1968).

33. Cheng, S. I., "A Critical Review of Numerical Solution of Navier-Stokes Equations," in Lecture Notes in Physics, V. 41, "Progress in Numerical Fluid Dynamics," ed. H. J. Wirz, p. 146, 1974.

34. Runchal, R. K., "Convergence and Accuracy of Three Finite Difference Schemes for a Two-Dimensional Conduction and Convection Problem," *Int. J. Num. Methods Engr.*, 4: 541-550, 1972.

35. Ames, W. F., *Numerical Methods for Partial Differential Equations*, 2nd. ed., Academic Press, N.Y. (1977).

36. Hirt, C. W., Nichols, B. D., and Romero, N. C., "SOLA – A Numerical Solution Algorithm for Transient Fluid Flows," Los Alamos Scientific Laboratory Report, LA-5852, Los Alamos, N.M., April 1975.

37. Daly, B. J., and Pracht, W. E., "Numerical Study of Density-Current Surges," *Phys. Fluids*, 11(1): 15-30, (1968).

38. Roache, P. J., "On Artificial Viscosity," *J. Comput. Phys.*, 10:169-184, 1972.

39. Gentry, R. A., and Martin, R. E., "An Eulerian Differencing Method for Unsteady Compressible Flow Problems," *J. Comput. Phys.*, 1:87-118, 1966.

40. Ball, J. A., and Johnson, S. A., "Physically Based High Resolution Surface Wind and Temperature Analysis for EPAMS," Mission Research Corporation, Santa Barbara, Calif., Rept. MRC-R-7731-1-278.

41. Sherman, C. S., "MATHEW: A Mass-Consistent Wind Field Model," Lawrence Livermore Laboratory Report, UCRL – 52479, May 1978.

42. Oke, T. R., *Boundary Layer Climates*, Methuen & Co., Ltd., London, 1978.

43. Bietry, J., Sacre, C., and Simiu, E., "Mean Wind Profiles and Change of Terrain Roughness," Proceedings of the ASCE, J of the Struct. Division, V. 104, No. ST 10, Oct. 1978, pp. 1585-1593.

44. Agopian, K. G., and Crow, S. C., "The Effect of Atmospheric Density Stratification on Wind Turbine Siting," DOE Report RLO-2444-78/1, Jan. 1978.

45. Ball, J. A., "A Concept for a High-Resolution Toposcale Wind Model to Estimate Surface Wind in Complex Terrain," Mission Research Corporation (MRC) March 15, 1979, Santa Barbara, Calif.

46. Mironer, A., *Engineering Fluid Mechanics*, McGraw-Hill Book Co., N.Y., 1979.

47. Spalding, D. B., "A Novel Finite Difference Formulation for Differential Expressions Involving Both First and Second Derivatives," *Int. J. Num Meth. Engr.*, 4: 551-559, 1972.

48. Caretto, L. S., Gosman, A. D., Patankar, S. V., and Spalding, D. B. "Two Calculation Procedures for Steady, Three-Dimensional Flows with Recirculation," in Proceedings of the 3rd Int. Conf. on Numerical Methods in Fluid Mechanics, Vol. II, 1972, Springer-Verlag, New York.

49. Burridge, D. M., and Temperton, C., "A Fast Poisson – Solver for Large Grids," *J. Comput. Phys.* 30: 145-148, 1979.

50. Pratap, V. S., and Spalding, D. B., "Fluid Flow and Heat Transfer in Three Dimensional Duct Flows," *Int. J. Heat Mass Transfer*, 19:1183-1188, 1976.

51. Caretto, L. S., Curr, R. M., and Spalding, D. B., "Two Numerical Methods for Three-Dimensional Boundary Layers," *Comput. Meth. in Appl. Mech. Engr.*, I: 39-57, 1972.

52. Gawain, T. H., and Prichett, J. W., "A Unified Heuristic Model of Fluid Turbulence," *J. Comput. Phys.*, *5*, 1970.

53. Deardorff, J. W., "On the Magnitude of The Subgrid Scale Eddy Coefficient," *J. Comput. Phys.*, 7: 120-133, 1971.

54. Viecelli, J. A., "A Computing Method for Incompressible Flows Bounded by Moving Walls," *J. Comput. Phys.*, 8: 119-143, 1971.

55. Mason, P. J., and Sykes, R. I., "Three Dimensional Numerical Integrations of the Navier-Stokes Equations for Flow Over Surface-Mounted Obstacles," *J. Fluid Mech.*, 91 (3): 433-450, 1979.

56. Clark, T. L., "A Three Dimensional Small Scale Dynamic Model Using a Terrain Following Co-ordinate Transformation," *J. Comput. Phys.*, 24: 186 ff, 1977.

57. Simiu, E., "Logarithmic Profiles and Design Wind Speeds," *J. of Engr. Mech.*, Division, ASCE Vol. 102, No. ST. 4 Proc. Paper 10100, Oct. 1973, pp. 1073-1083.

58. Gartling, D. K., "NACHOS: A Finite Element Computer Program for Incompressible Flow Problems. Part I. Theoretical Background, SANDIA Laboratories, Report SAND-77-1333, NTIS ACCESS, N78-33395, 1977.

59. Clements, P., McGinness, H., and Lutes, G., "Wind Study," Appendix C to the JPL Wind Power Feasibility Study Committee, August 1974 (an internal document).

60. Huang, C. H., and Nickerson, E. C., "Numerical Simulation of Wind, Temperature, Shear Stress and Turbulent Energy Over Nonhomogeneous Terrain," Colorado State Univ., Fort Collins, Rept. CER71-72CH-ECN 23 March 1972.

61. Hornbeck, R. W., "Numerical Marching Techniques for Fluid Flow with Heat Transfer," NASA SP-297, 1973.

62. Gosman, A. D., Pun, W. M., Runchal, A. K., Spalding, D. B., and Wolfshtein, M., *Heat and Mass Transfer in Recirculating Flows*, Academic Press, 1969.

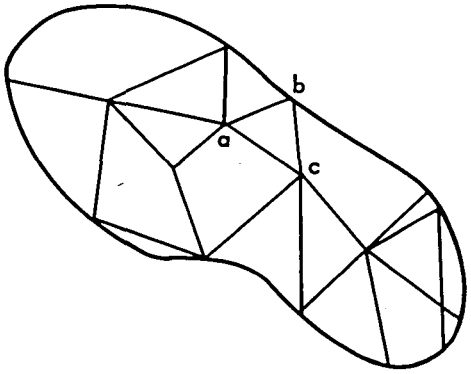

Fig. 1. Finite elements

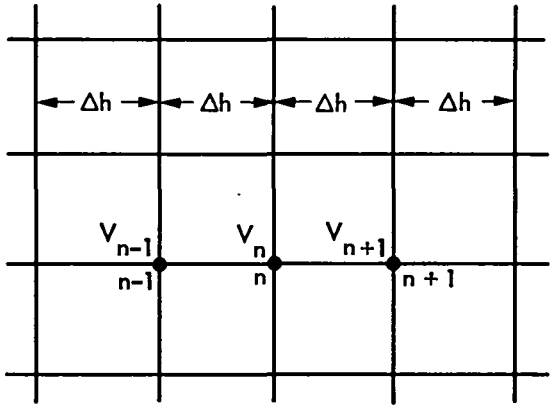

Fig. 2. Computational mesh for one-dimensional velocity derivative

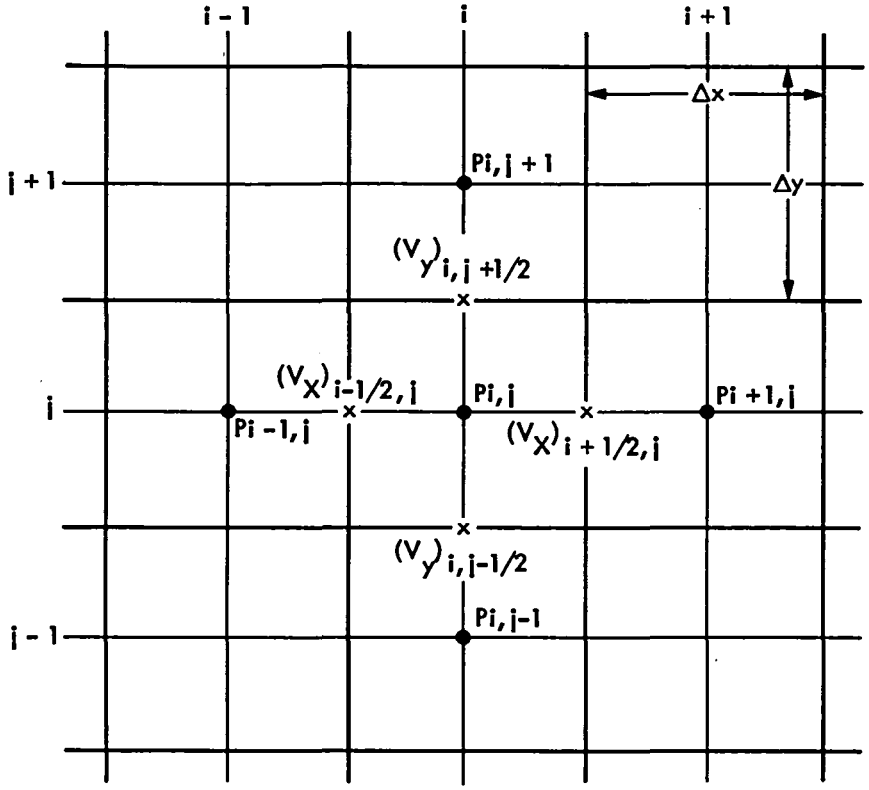

Fig. 3a. Two-dimensional case

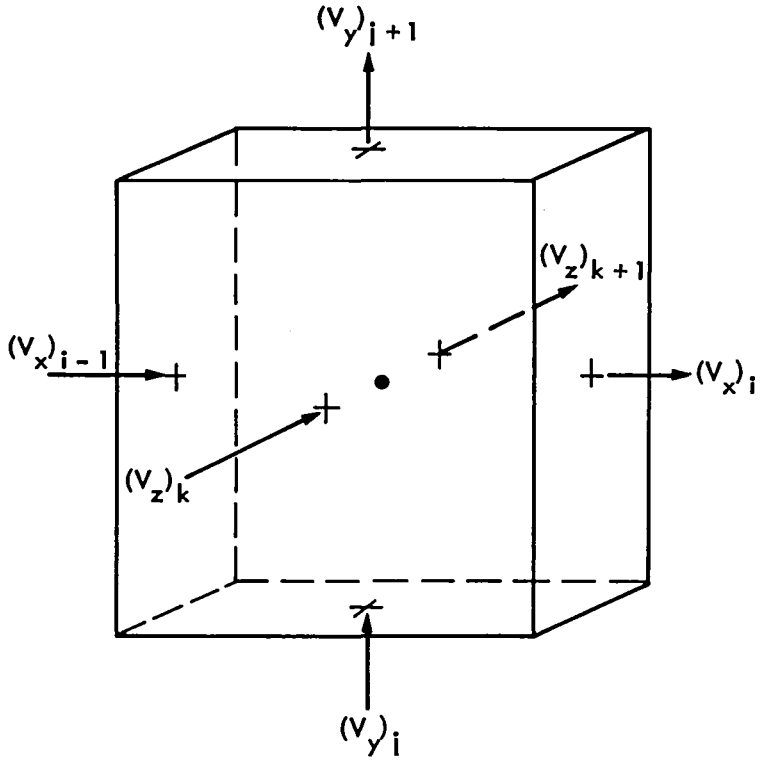

Fig. 3b. Three-dimensional case

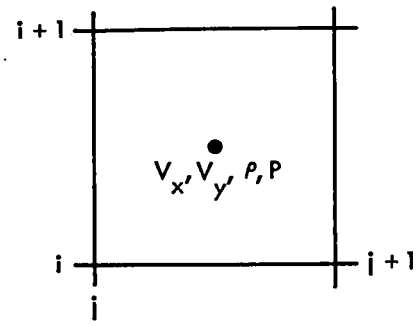

Fig. 4a. Cell centered variables

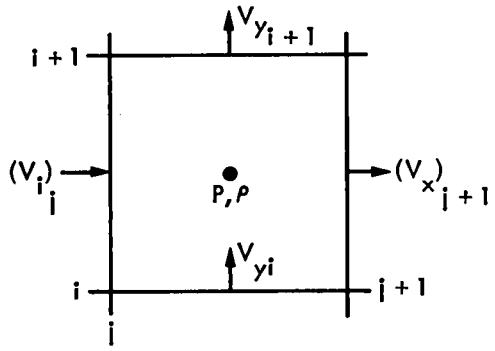

Fig. 4b. Staggered computational mesh

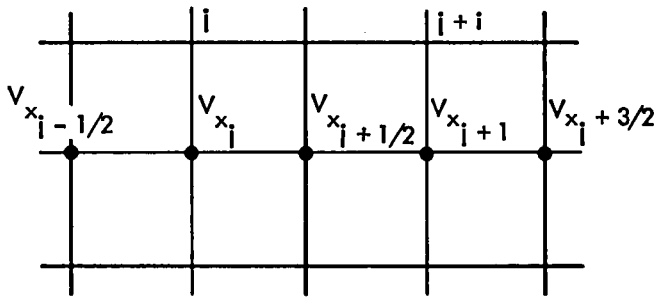

Fig. 5. Velocity fluxes between adjacent cells

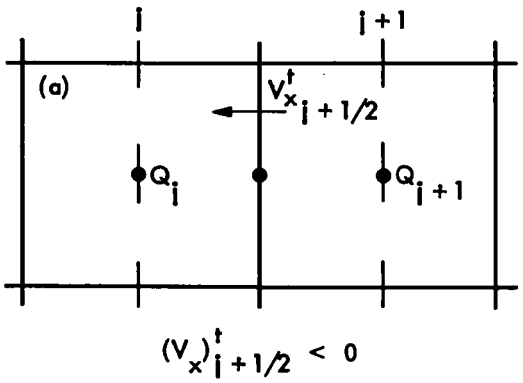

Fig. 6a. Donor cell method, case I

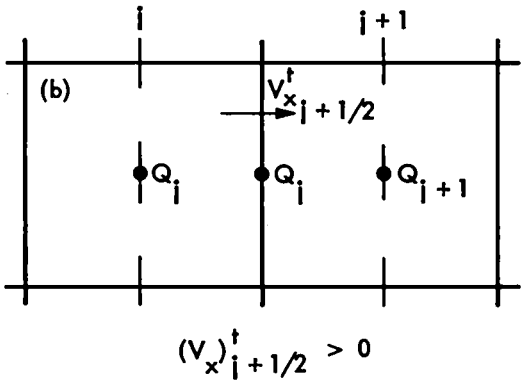

Fig. 6b. Donor cell method, case II

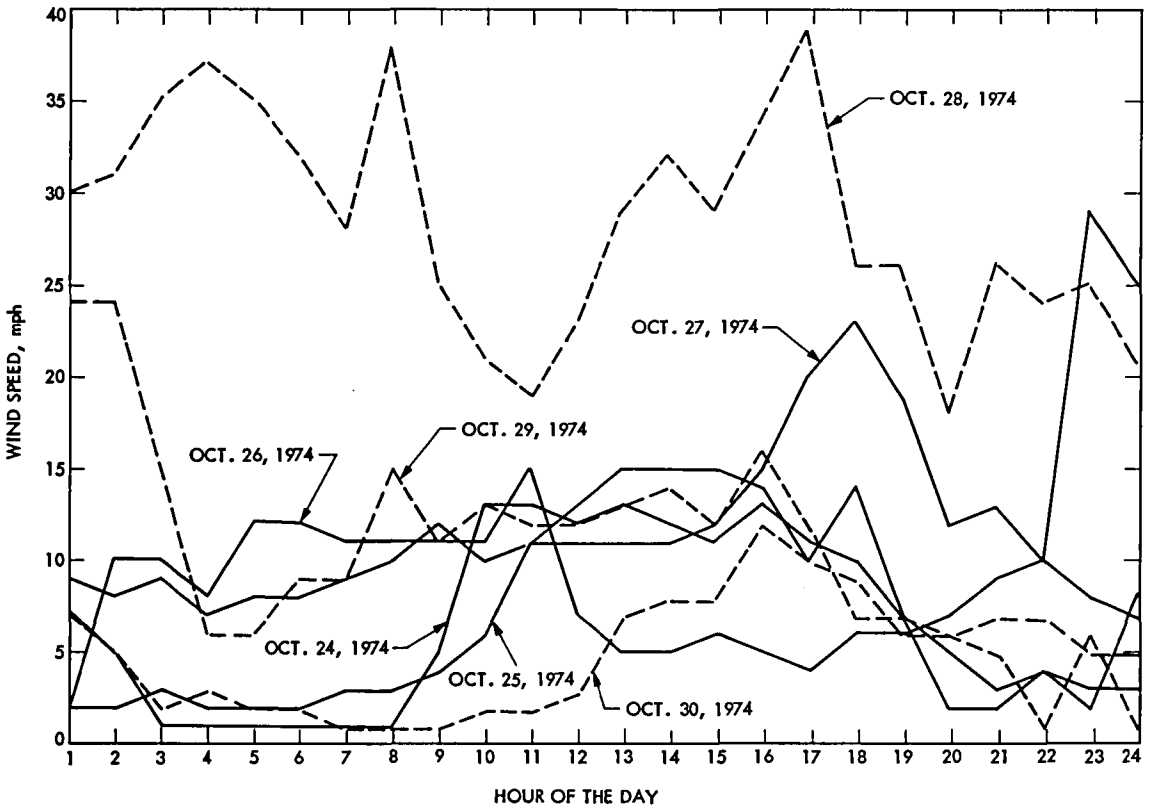

Fig. 7. Wind speed vs time (Goldstone data)

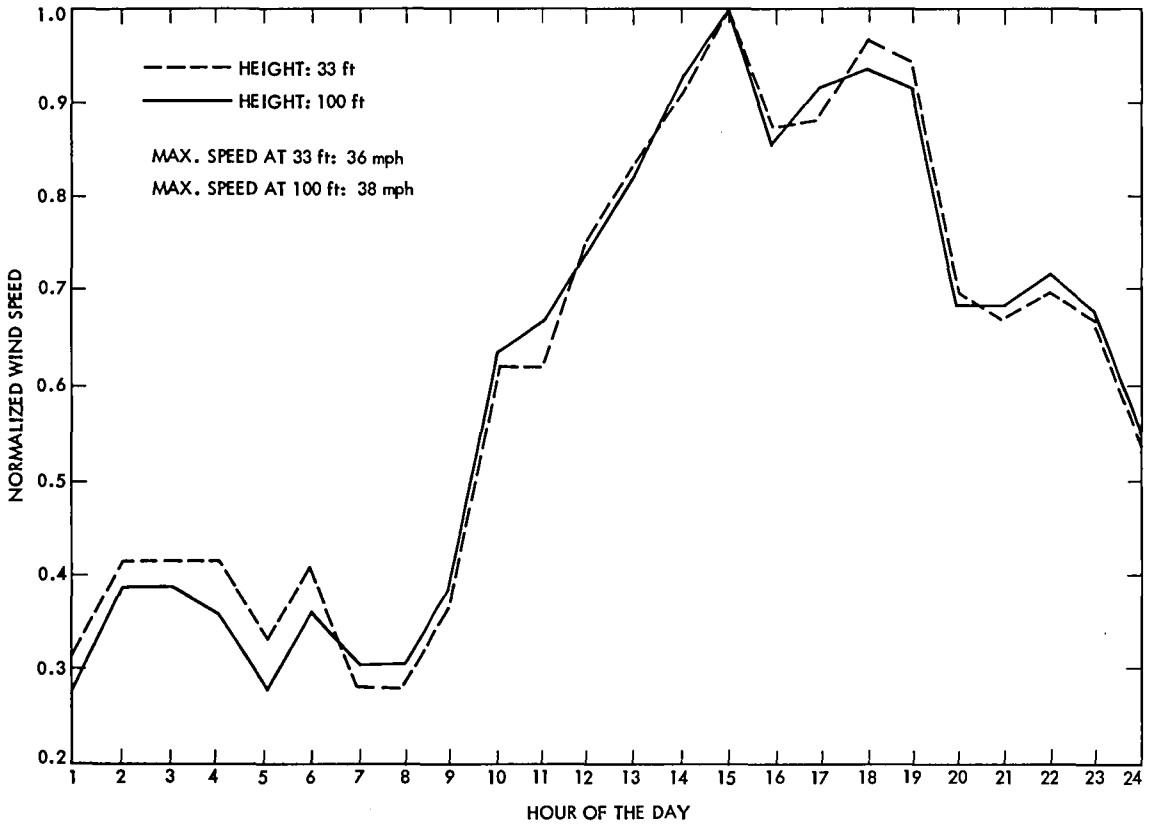

Fig. 8. Comparison of wind speeds at different heights

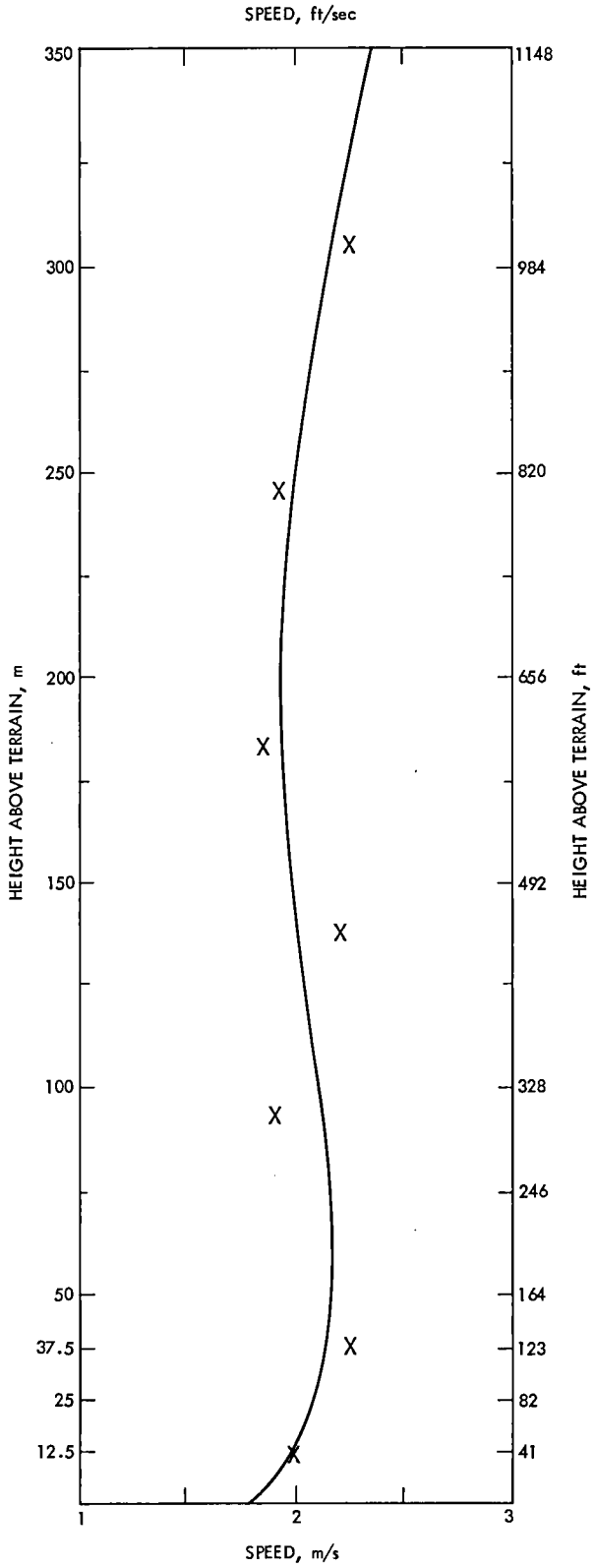

Fig. 9. Wind profile at Savannah River Plant, Ga.

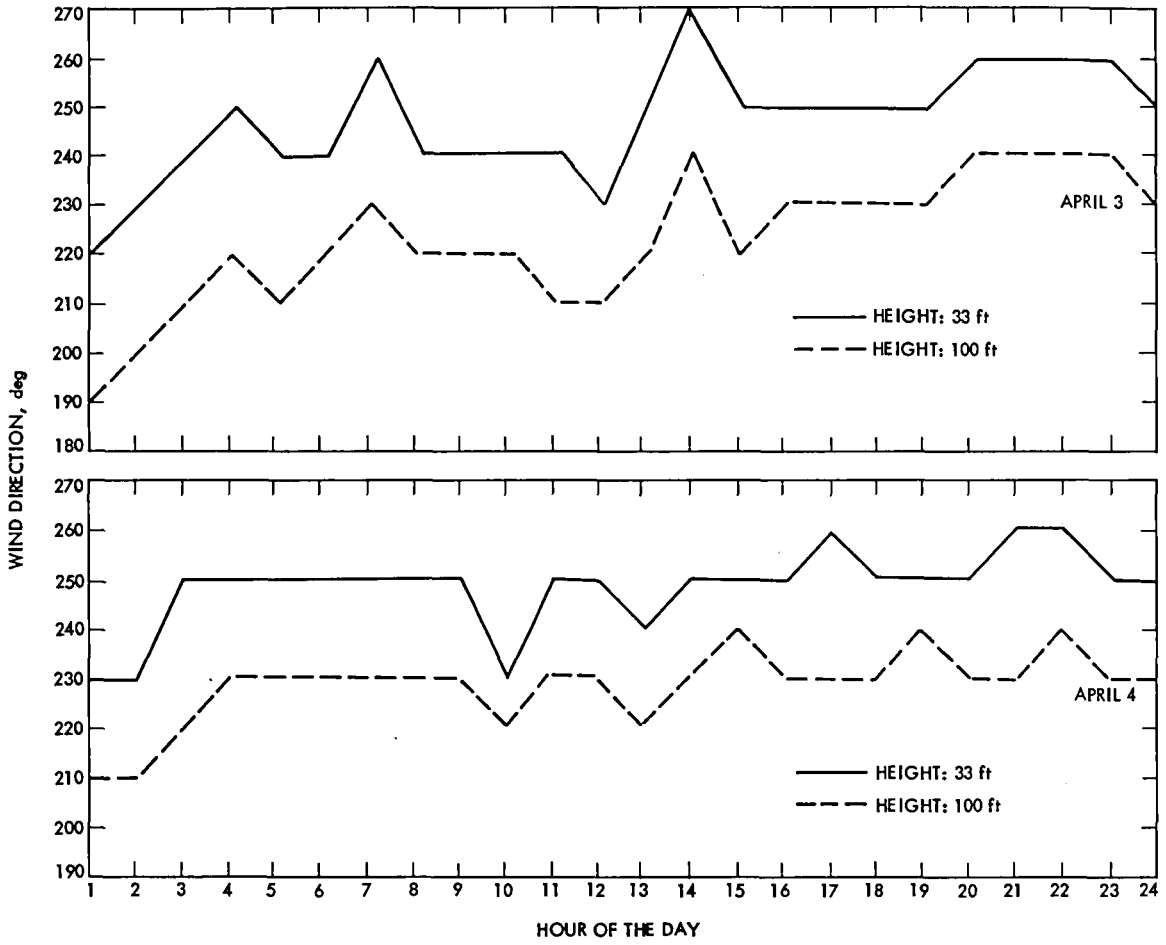

Fig. 10. Comparison of wind directions at different heights

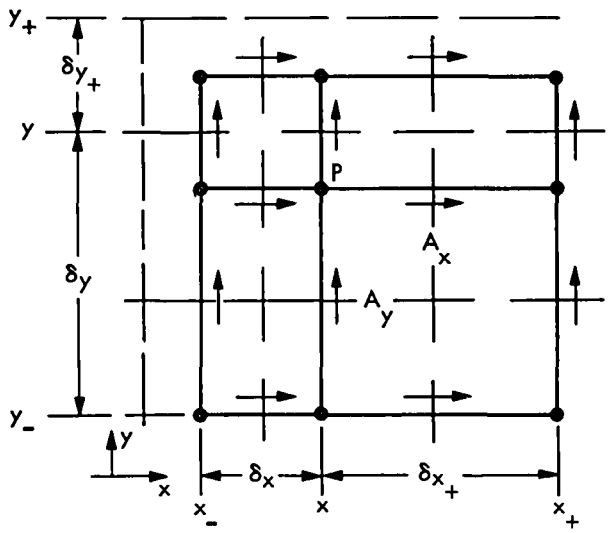

Fig. 11. The staggered grid used in the steady-state model

NASA—JPL—Coml., L.A., Calif.

End of Document